

Integrated Electronics to Control and Readout Electrochemical Biosensors for Implantable Applications

THÈSE N° 6600 (2015)

PRÉSENTÉE LE 1^{ER} JUIN 2015

À LA FACULTÉ INFORMATIQUE ET COMMUNICATIONS
LABORATOIRE DES SYSTÈMES INTÉGRÉS (IC/STI)
PROGRAMME DOCTORAL EN GÉNIE ÉLECTRIQUE

ÉCOLE POLYTECHNIQUE FÉDÉRALE DE LAUSANNE

POUR L'OBTENTION DU GRADE DE DOCTEUR ÈS SCIENCES

PAR

Seyedeh Sara GHOREISHIZADEH

acceptée sur proposition du jury:

Prof. A. P. Burg, président du jury
Prof. G. De Micheli, Dr S. Carrara, directeurs de thèse
Prof. C. Dehollain, rapporteuse
Prof. P. Georgiou, rapporteur
Prof. R. Thewes, rapporteur



ÉCOLE POLYTECHNIQUE
FÉDÉRALE DE LAUSANNE

Suisse
2015

Acknowledgements

I owe my deepest gratitude to my advisors, Professors Giovanni De Micheli and Sandro Carrara for all their guidance and constant help and encouragement during the last five years.

I would like to thank Professors Roland Thewes and Pantelis Georgiou for their acceptance to be the reporters of my thesis. They pointed out many typos and gave me many helpful comments which highly improved the thesis. It is my great honour to thank Professors Catherine Dehollain and Andreas Burg to be the members of the jury.

I wish to thank Prof. Pantelis Georgiou for his constant guidance, and encouragement during my stay as an exchange PhD student at Imperial college London.

I am indebted to many people for their kind help in the course of my PhD studies. I would like to thanks Prof. Wayne Burluson for teaching me the basics of Cryptography and for showing so much interest in my research. I very much appreciated the technical discussions I had with Federico, Hassan, Jaume, and Ivan about the software, hardware and digital circuits that I designed or tested. Cristina, Camilla, Irene, and Andrea showed me different aspects of electrochemical sensors. I learned from Camilla and Irene how to be patient with the sensors. With Cristina I had many insightful discussions especially in the final integration of the implantable devices. I wish to thank Sanjiv for the time he spent to provide me with data that I needed to design DIRIC; Stefano for helping me with testing my ICs; Ermis for all the effort he made to prepare and fabricate Optimus Prime; Pierre-Emmanuel, for his comments on my work and presentations; Jack, for his help- even after his graduation -with the test and measurement of the IMDs; Tolga for his help in writing the chapter of my thesis on Crypto-system.

Many thanks goes to Christina Govoni for all the time she spent, with so much care and patience, helping me with the documents, organizing meetings, events, and in particular my PhD thesis defense.

I would also like to thank all of my friends who supported me in writing, encouraged me to strive towards my goal, and for all the happy times we spent together. Mitra and Arash for supporting me all the time especially when I first arrived in Switzerland; Banafsheh for her unlimited kindness; Alena, for her encouragement and for memorable biking trips we had together; Mahsa, for our afternoon tea breaks and our many discussions on the circuit design; Mohadeseh, for keep encouraging me to come to the sport center; Samira, for all the time that we spent together jogging, walking, talking, and dining; Irene, for being a wonderful friend and officemate. I wish to thank many other friends: Hassan, Julien, Wenqi, Somayyeh, Nima, Andrea in Lausanne and Melina, Mohammad, and Peter in London for all lunches and coffee

Acknowledgements

breaks we have had together.

A special thanks goes to my family. Words cannot express how grateful I am to my mother and my father for all the sacrifices that they have made on my behalf. I would also like to thank my sisters, Marjan and Mahsa, and my brother, Ehsan, for the heart-warming encouragement and confidence they give me. At the end I would like to express appreciation to my beloved husband Davoud who was always my guide and support in the most challenging moments.

17 May 2015

S. G.

Abstract

Biosensors can effectively be used to monitor multiple metabolites such as glucose, lactate, ATP and drugs in the human body. Continuous monitoring of these metabolites is essential for patients with chronic or critical conditions. Moreover, this can be used to tune the dosage of a drug for each individual patient, in order to achieve personalized therapy. *Implantable medical devices* (IMDs) based on biosensors are emerging as a valid alternative for blood tests in laboratories. They can provide continuous monitoring while reduce the test costs.

The potentiostat plays a fundamental role in modern biosensors. A potentiostat is an electronic device that controls the electrochemical cell, using three electrodes, and runs the electrochemical measurement. In particular the IMDs require a low-power, fully-integrated, and autonomous potentiostats to control and readout the biosensors.

This thesis describes two *integrated circuits* (ICs) to control and readout multi-target biosensors: LOPHIC and ARIC. They enable chronoamperometry and cyclic voltammetry measurements and consume sub-mW power. The design, implementation, characterisation, and validation with biosensors are presented for each IC. To support the calibration of the biosensors with environmental parameters, ARIC includes circuitry to measure the pH and temperature of the analyte through an Iridium oxide pH sensor and an off-chip *resistor-temperature detector* (RTD). In particular, novel circuits to convert resistor value into digital are designed for RTD readout.

ARIC is integrated into two IMDs aimed for health-care monitoring and personalized therapy. The control and readout of the embedded sensor arrays have been successfully achieved, thanks to ARIC, and validated for glucose and paracetamol measurements while it is remotely powered through an inductive link. To ensure the security and privacy of IMDs, a *lightweight cryptographic system* (LCS) is presented. This is the first ASIC implementation of a cryptosystem for IMDs, and is integrated into ARIC. The resulting system provides a unique and fundamental capability by immediately encrypting and signing the sensor data upon its creation within the body.

Nano-structures such as Carbon nanotubes have been widely used to improve the sensitivity of the biosensors. However, in most of the cases, they introduce more noise into the measurements and produce a large background current. In this thesis the noise of the sensors

Acknowledgements

incorporating CNTs is studied for the first time. The effect of CNTs as well as sensor geometry on the signal to noise ratio of the sensors is investigated experimentally. To remove the background current of the sensors, a differential readout scheme has been proposed. In particular, a novel differential readout IC is designed and implemented that measures input-currents within a wide dynamic range and produces a digital output that corresponds to the -informative- redox current of the biosensor.

Key words: CMOS, electrochemical sensors, sensor control and readout, amperometric sensors, differential readout, multi-target sensing, resistor measurement, implantable medical devices.

Résumé

Les bio-senseurs peuvent être efficacement utilisés pour détecter une variété de métabolites comme le glucose, l'acide lactique ou les substances actives de différents médicaments dans le corps humain. Cette détection continue de ce type de métabolites est essentielle pour les patients avec des conditions critiques ou chroniques. De plus, elle peut être utilisée pour adapter le dosage d'un médicament de manière à obtenir un thérapie personnalisée pour chaque patient. Les dispositifs médicaux implantables (IMD) basés sur la technologies des bio-senseurs sont de plus en plus en train de se positionner comme une alternative viable aux tests sanguins fait en laboratoire. Ils sont capables de fournir un contrôle continu tout en limitant les coûts.

Le potentiostat joue un rôle fondamental pour les bio-senseurs modernes. Un potentiostat est un dispositif électronique capable de contrôler la cellule électrochimique à trois électrodes et d'effectuer la prise de mesures électrochimiques. En particulier les IMDs nécessitent l'utilisation de circuits électroniques de contrôle à faible consommation, intégrés et autonomes pour contrôler les bio-senseurs et effectuer les mesures requises.

Ce travail de thèse détail deux circuits intégrées (CI) spécialisés dans le contrôle de bio-senseurs multi-cibles : LOPHIC et ARIC. Ils sont capables de faire des mesures chrono-ampérométriques et voltampérométriques cycliques tout en consommant un puissance inférieure au milliwatt. Le développement, l'implémentation, la caractérisation et la validation de ces deux circuits sont présentés en utilisant des bio-senseurs. Pour supporter la calibration des bio-senseurs avec les paramètres environnementaux, ARIC intègre un circuit spécialisé pour la mesure du pH et de la température des analytes grâce d'une part à un capteur de pH à l'oxyde d'iridium et d'autre part à une thermistance. En particulier, de nouveaux circuits ont été développés pour mesurer de manière numérique la valeur de la thermistance.

ARIC est intégré dans deux IMDs destinés au domaine de la santé et a l'établissement de thérapies personnalisées. Grâce à l'ARIC, le contrôle et la lecture d'ensembles de bio-senseurs ont été réalisés avec succès et validés pour la mesure du taux de glucose et de paracétamol tout en utilisant une alimentation à distance via un lien inductif. Pour assurer la sécurité des IMDs ainsi qu'assurer la vie privée des patients, un système léger de cryptographie (LCS) est présenté. Tel qu'intégré à l'ARIC, il constitue la première implémentation sur un ASIC d'un système de cryptographie appliqué aux IMDs. Le système résultant offre une possibilité unique et fonda-

Acknowledgements

mentale en cryptant et signant numériquement les données à la source, au niveau du senseurs.

Les nano-structures comme les nanotubes de carbone (CNTs) ont beaucoup été utilisés pour améliorer la sensibilité des bio-senseurs. Cependant, le rapport signal à bruit est amoindri et le courant d'offset de base est non négligeable dans la plupart des cas. Dans cette thèse, le bruit introduit par les senseurs utilisant des CNTs est étudié pour la première fois. L'effet des CNTs ainsi que de la géométrie des senseurs sur le rapport signal à bruit est étudié expérimentalement. Pour éliminer le courant d'offset de ces senseurs, une approche utilisant la signalisation différentielle pour la prise des mesures est proposée. En particulier, un nouveau circuit de prise de mesures utilisant une transmission différentielle a été mis en place et implémenté pour la mesure de courant avec une dynamique importante et générant des valeurs numériques traduisant l'intensité de la réaction oxydoréduction se produisant au niveau du senseur.

Mots clé : CMOS, capteurs électrochimiques, électronique de contrôle et de prise de mesures, capteurs ampérométriques, mesure différentielle, bio-senseur mutli-cibles, mesure de résistance, dispositifs médicaux implantables

List of abbreviations

ADC	Analog to digital converter
ARIC	Autonomous reconfigurable IC
CA	Chronoamperometry
CDS	Correlated double sampling
CE	Counter electrode
CGTIA	Common-gate TIA
CIC	Cascaded integrator-comb
CNT	Carbon nanotube
CV	Cyclic voltammetry
CYP	Cytochrome P450
D2SC	Differential to single converter
DAC	Digital to analog converter
DDS	Direct digital synthesizer
DIRIC	Pseudo-differential readout IC
ETO	Etoposide
EIS	Electrochemical impedance spectroscopy
EXER	External reader
GE	Gate equivalents
GOD	Glucose oxidase
HEM	Health-care monitoring
HEM-IMD	health-care monitoring IMD
HEM-PMIC	HEM power management IC
IMD	Implantable medical devices
ISFET	Ion sensitive field effect transistor
IV	Initialization vector
JTAG	Joint Test Action Group
LCS	Lightweight cryptographic system
LOD	Limit of detection
LOPHIC	Low-power hybrid IC
mSNR	Modified SNR
MWCNT	Multi-walled CNT
PSRR	Power supply rejection ratio

Acknowledgements

NIST	National Institute of Standards and Technology
OCP	Open circuit potential
OOK	On-off keying
PBS	Phosphate-buffered saline
PET	Personalized therapy
PET-IMD	personalized therapy IMD
PET-PMIC	PET power-management IC
PGA	Programmable gain amplifier
PSD	Power spectral density
PSRR	Power supply rejection ratio
PTAT	Proportional to absolute temperature
R2PC	Resistance to pulse-width converter
R2VC	Resistance value into voltage
RE	Reference electrode
RTD	Resistive temperature detector
SC	Switch capacitor
SEM	Scanning electron microscope
SH	Sample and hold
SNR	Signal to noise ratio
SPE	Screen printed electrodes
SPCH	Serial to parallel converter and hold
TIA	Trans-impedance amplifier
VCM	Common mode voltage
WE	Working electrode
ZTC	Zero temperature coefficient

List of Figures

1.1	Glucose detection with chronoamperometry for bare (black rhombus) and CNT-covered (grey squares) sensors. Reprinted from [1].	2
1.2	The conceptual diagram of HEM-system. The implanted device measures multiple metabolites in the interstitial tissue and sends the results to the patch. The patch communicates the results to a more powerful device for processing, storage and display.	3
1.3	The conceptual diagram of HEM-IMD	4
1.4	Scheme of PET-system: an intelligent system with the data transmission via Bluetooth to an Android interface (left), and the scheme of the implantable device (right).	5
1.5	An implantable device for multiple-metabolite detection	5
1.6	Voltammogram acquired using a potential scan rate of 20 <i>mV sec</i> during the detection of etoposide with multi-walled CNTs. Reprinted from [2].	6
2.1	Simplified principle of the P450 biosensor: the electrons needed for the catalysis are supplied by the electrode, allowing substrate detection. Reprinted from [3].	12
2.2	Diagram of a three-electrode based electrochemical cell with a potentiostat to apply the voltage to the cell and a current-meter to measure the sensor current.	15
2.3	The HEM-biointerface: An example of a platform with multiple WEs. it consists of five WEs, a common RE, a common CE, and pH and temperature sensors. The black dashed line defines the section of the platform that is diced to be integrated in the HEM-IMD reported in Chapters 1 and 6. The red dashed line define the space for bonding the IC; B) SEM image of CNTs drop-cast on a WE; C) at higher magnification; D) SEM image of CNTs and glucose oxidase drop-cast on a WE.	19
2.4	The introduction of CNTs on the electrode surface enhances the electron transfer between the chemical and the electrode surface.	21
2.5	peak voltage shift with pH. Reprinted from [3].	21
2.6	Peak current variation with temperatures. Error bars represent the inter-electrode variation. Reprinted from [3].	22
2.7	Photograph of the pH sensor coated with iridium oxide (red insert). Reprinted from [3].	23

List of Figures

2.8	Open circuit voltage of the Iridium-oxide coated electrode to different solutions pH. Error bars are due to the instrument noise. Reprinted from [4].	24
2.9	Photograph of the temperature sensor. Reprinted from [3]	24
3.1	The conceptual diagram of a readout IC for amperometric electrochemical sensors.	27
3.2	The RC-equivalent model of a three-electrode based electrochemical sensor used for circuit simulations	28
3.3	The simplified structure of a CGTIA. The voltage V_{in} is applied to the WE and the current flows through the transistor. The current at node X can be converted into digital or to voltage and then digital. Reprinted from [5].	29
3.4	CGTIA with a DC offset current to allow bidirectional current measurement. . .	29
3.5	A CGTIA with a current to frequency converter. Reprinted from [6].	30
3.6	Backscattering can be simply implemented by a single NMOS to short-circuit the load of the powering-inductive-link for each bit in the chip output that is equal to “1”. The reader detects the modulated load and reconstructs the data.	30
3.7	A relaxation oscillator to convert the sensor current into frequency.	31
3.8	A CGTIA with a resistor in the path of the current. Reprinted from [7].	32
3.9	A voltage mode readout circuit based on resistive-feedback TIA. The circuit enables both CV and CA control and readout. Reprinted from [8].	33
3.10	The switched-capacitor current integrator to convert the bidirectional input current into voltage. The capacitor is reset in every clock cycle. Φ_1 , Φ_2 , and Φ_3 are non overlapping clocks. V_{ref2} is applied to the WE through OP1 to stimulate the sensor for CA or CV measurements. OP_2 , C_3 and the capacitor array for the PGA.	34
3.11	A typical switched-capacitor readout chain consists of an integrator followed by a PGA followed by a sample and hold. Reprinted from [9].	34
4.1	Schematic view of LOPHIC. It consists of four main circuits: waveform generator, CA readout, CV readout, and potentiostat. Reprinted from [10].	41
4.2	The block diagram of the triangular waveform generator in LOPHIC. Reprinted from [2].	43
4.3	Schematic view of two-stage opamp with NMOS and PMOS input stages, and a class-A output stage, compensated for a wide range of load capacitance. This structure is used for both OP_1 and potentiostat in Fig. 4.1. Reprinted from [10].	44
4.4	Schematic view of the <i>Adder</i> , the last stage of the CV readout circuit. It consists of OP_4 and poly resistors. It amplifies the difference between V1 and V2 by a factor of 10 and shifts the resulted voltage up by $V_{DD}/2$	44
4.5	Layout of LOPHIC in 0.18 μm technology. Reprinted from [10].	46
4.6	The measured sub-Hertz triangular waveform to control the sensor in CV by the on-chip waveform generator. Its min, max and frequency are 0.2 V, 1.6 V, and 5.5 mHz, respectively. Reprinted from [10].	47

4.7	Measured characteristics of the circuits for CA (A) and CV (B) readout. The input current is converted to voltage in CV and to pulse width in CA. The internally generated sub-Hertz triangular waveform is applied to control CV measurement. Reprinted from [10].	48
4.8	Biosensor: A) micro-fabricated sensor that hosts five WEs, a common counter and reference electrode. The black dashed line defines the section of the platform that is diced to be integrated in the implantable sensor. The red dashed line define the space for bonding the IC; B) SEM image of MWCNTs drop-cast on a WE; C) at higher magnification; D) SEM image of MWCNTs and GOx drop-cast on a WE. Reprinted from [10].	49
4.9	Comparison of the calibration curves for glucose (A) and lactate (B) obtained with the IC (in red) and Autolab (in black). The error bars for the case of IC are due to the variations of the measured average frequency. In the case of Autolab, the error bars are standard deviation of the measured current. Reprinted from [10].	52
4.10	CV with the bare electrode in PBS, Etoposide (ETO) 200 μM and ETO 400 μM obtained with the IC (A) and the Autolab (B). The slope of the applied voltage is 68 mV/s . Reprinted from [10].	53
4.11	Comparison between the IC and the Autolab for the CV obtained in presence of ETO 400 μM . Reprinted from [10].	53
4.12	The schematic view of ARIC. The blocks in green and yellow are implemented in full-custom analog and semi-custom digital circuits, respectively.	55
4.13	The schematic view of the circuit for CV, CA and pH readout. A fixed or triangular waveform is applied to the WEx and the resulting current is measured through R_{meas} and amplified before going through the ADC. Reprinted from [11].	57
4.14	The schematic view of the compensated opamp for CV and CA readout (OP_1 in Fig. 4.13). It remains stable for $C_{load} \geq 500 pF$	58
4.15	The gain (20dB) in green and phase in blue of OP_1 for $C_L = 1 nF$	59
4.16	Schematic view of OP_2 in the unified circuit for CV, CA and pH measurement	60
4.17	The schematic view of the second order $\Sigma\Delta$ modulator. The capacitors are chosen such that the modulator gives 14-bit accuracy. Reprinted from [11]	61
4.18	The opamp of the integrators in the $\Sigma\Delta$ modulator. A switched-capacitor common-mode-feedback is implemented to set the differential bias point. The bias circuits is similar to the one showed in Fig. 4.14.	61
4.19	Schematic view of the three-stage current starved ring oscillator	62
4.20	PSD of the $\Sigma\Delta$ modulator output (post-layout simulation). Reprinted from [11].	63
4.21	Three different commands for ARIC: (A) Configuration; (B) Execution; (C) Read.	64
4.22	The pattern of the data as ARIC prepares it for communication. P[8:0] corresponds to the applied voltage to the WE. Data 1st to 4th are the output of the CIC filter.	64
4.23	The microphotograph of ARIC in 0.18 μm technology.	65
4.24	Generated voltages on the WE1 (purple), WE2 (blue), and WE3 (orange) by the voltage generator on ARIC.	66

List of Figures

4.25	The slow triangular waveform on WE1 (purple), and the fixed voltage on RE (orange) generated by ARIC for CV measurement. In this measurement ARIC is configured in CA mode and the applied voltage is changed at each voltage step by sending a command. (The glitch in V_{WE1} is due to the communication error between the FPGA and ARIC.)	66
4.26	The PSD of the output bit stream of the $\Sigma\Delta$ modulator. The noise floor in the signal bandwidth of 1 kHz is $-109dB$ when the input voltage is zero (i.e. the differential inputs of the modulator are short connected).	67
4.27	SNR of the $\Sigma\Delta$ modulator versus input voltage amplitude. The input voltage is at DC frequency. By connecting the input voltage source, the noise floor changes by 14dB. This can be attributed to the injected noise at the input by the power supply equipment. Correcting for this effect gives the effective number of bits of the $\Sigma\Delta$ modulator which is 14.3.	67
4.28	The measured input-output characteristics of the current readout chain which includes the TIA, the gain stage, and the $\Sigma\Delta$ ADC (black), and the simulated characteristics (red). In both lines the offset is removed.	68
4.29	The measured input-output characteristics of the pH readout chain which consist of the Gain stage and the $\Sigma\Delta$ ADC (black), and the simulated characteristics (red). In both lines the offset is removed.	69
4.30	Cyclic voltammetry of potassium ferricyanide at different concentrations with ARIC. Reprinted from [12].	70
4.31	Chronoamperometry of hydrogen peroxide using the proposed IC. Successively injections of 0.2 mM and 0.4 mM of H_2O_2 show that the IC is able to correctly readout the current. Reprinted from [12].	71
4.32	The measured output of the pH readout circuit for different values of the pH. The same measurement repeated three times.	72
4.33	The circuit to measure the open circuit potential between an Ion sensor and a reference electrode.	72
5.1	The schematic view of the R2PC circuit for temperature measurement using an off-chip Pt-RTD. The circuit converts the resistance difference into pulsewidth and then into digital.	76
5.2	Characteristics of the temperature sensor in fast (ff), typical (tt), and slow (ss) corners. The markers represent the simulated points and the lines are interpolated characteristics of the circuit for each corner.	79
5.3	The measured output of the temperature readout in nine different ICs versus the difference between the off-chip RTD, R_{RTD} , and the on-chip R_{REF}	79
5.4	The schematic of the resistance to voltage converter (R2VC) circuit. A PVT independent current source is designed through a PTAT voltage generator and a quasi-constant beta-multiplier.	81
5.5	The variation of I_{out} with temperature when $V_r = 310 mV$	82
5.6	The V_r change in temperature that cancels the effect of μ_n in I_{out}	83

5.7	The variation of I_{out} with temperature when V_r is generated through the PTAT voltage generator.	84
5.8	Simulated I_{coarse} in different process corners including Temperature= 30, 100; V_{Supply} = 3, 3.3, 3.6 V; CMOS model= ws wo wp wz; and resistor model= wp, ws.	85
6.1	The conceptual diagram of the health-care monitoring system. The HEM-IMD measures multiple metabolites in the interstitial tissue and sends the results to the patch. The patch communicates the results to a more powerful device for processing, storage and display.	88
6.2	The wearable patch to transmit power and commands to the HEM-IMD and to receive measured data from it. It is powered by two lithium batteries. A blue-tooth module on the patch transmits the data to a more powerful device.	89
6.3	The conceptual diagram of the HEM-IMD for health-care monitoring. It includes five biomolecular sensors, a pH and temperature sensor for biomolecular calibration, a multi-layer inductor for power and data transmission, and front-end electronics to readout the sensors.	89
6.4	The schematic view of the front-end electronics of the HEM-IMD. The blocks coloured in blue are fully-integrated in ARIC and HEM-PMIC where HEM-PMIC includes the load modulator and the regulator. The rest of the blocks are realized by off-the-shelf components.	90
6.5	The measured signals in HEM-IMD and the patch. In orange: The induced voltage at the multi-layer receiving coil after it is rectified and regulated. In green: the data bit-stream at the output of ARIC. This data is given to the load modulator and is transmitted to the patch via backscattering. In blue: The received signal on the patch.	91
6.6	The photograph of the fully-integrated HEM-IMD with two main parts: the sensing area on the left and the front-end electronics on the right. The multi-layer inductor is placed on the bottom of the device and wire-bonded to the pads on the top.	92
6.7	Scheme of the PET system with the data transmission via Blue-tooth to an Android interface (left), and the scheme of PET-IMD (right). PET-IMD is implanted in a laboratory mice and is powered through the inductive link. The external inductor is placed on a robot arm controlled with a servo-controlled system which moves it according to the position of mice to ensure constant powering of PET-IMD while the mice is moving.	93
6.8	Block diagram of the PET system. It consists of PET-IMD on the top, the external reader (EXER) on the bottom and the tablet on bottom-left. The external reader sends power to PET-IMD at 13.56 MHz, and receives the OOK-modulated data at 869 MHz. The data is validated and sent to an Android device by the EXER.	94
6.9	The micro-fabricated sensing platform of the PET-IMD. Reprinted from [13].	95
6.10	fully-integrated PET-IMD covered with bio-compatible glue. PET-IMD is a battery-less IMD for multiple-metabolite detection in laboratory animals.	96

List of Figures

6.11 (a) Transmitted data out of ARIC on PET-IMD; (b) received data at the output of the logarithmic amplifier on the EXER (in green) and on the EXER comparator (in orange).	97
6.12 Continuous bio-monitoring application on the Android interface during the measurement of Paracetamol with PET-IMD. Two injections of Paracetamol are distinguishable.	98
6.13 The in-vitro test set-up for the measurement of Paracetamol and glucose with PET-IMD and the servo-controlled system.	100
6.14 Calibration curve obtained during the in-vitro measurements of paracetamol with PET-IMD.	100
6.15 Calibration curve obtained during the in-vitro measurements of glucose with PET-IMD.	101
7.1 Fully implantable subcutaneous medical device powered by a patch located on top of the skin. The patch is wirelessly connected to a smart phone for further data analysis and decision-making.	104
7.2 The block diagram of ARIC including LCS. The analog blocks are coloured in yellow and the digital blocks in blue, reprinted from [14].	106
7.3 DUPLEXSPONGE construction for authenticated encryption, reprinted from [14].	108
7.4 The implementation of the biosensor security module: permutation based authenticated encryption, reprinted from [14]	108
7.5 Layout of ARIC in $0.18 \mu m$ technology. LCS is synthesized together with other digital blocks of ARIC.	110
8.1 The screen printed electrode functionalized with CNTs. Reprinted from [15].	114
8.2 Chronoamperometry measurement using MWCNT- functionalized SPE at $300 mV$ with five subsequent additions of $0.5 mM$ Ferrocyanide in PBS with the indication of the noise and signal level.	115
8.3 The PSD of noise at low frequencies in the presence of flicker noise	115
8.4 Noise PSD in chronoamperometry measurement with bare and MWCNT-functionalized electrodes and a $10 k\Omega$ resistor. The H_2O_2 concentration is kept at $2 mM$ and the applied voltage is $650 mV$. The dashed lines represent the fits to Eq. 8.1. Reprinted from [16].	116
8.5 Estimated values of parameters A (left) and α (right) in Eq. 8.1 versus concentration in H_2O_2 measurement with both bare electrodes and MWCNT-functionalized electrodes. The applied voltage is $650 mV$ in these measurements. Reprinted from [16].	117
8.6 The qualitative change of SNR in bare (left) and MWCNT-functionalized (right) sensors for different concentrations of H_2O_2 . The SNR increases with concentration.	118
8.7 Estimated values of parameters A (left) and α (right) in Eq. 8.1 versus the applied voltage. H_2O_2 concentration is $2 mM$ and both bare and MWCNT-functionalized electrodes are used for comparison. Reprinted from [16].	118

8.8	Estimated values of parameters A (left) and α (right) versus concentration in H_2O_2 and Ferrocyanide measurement. MWCNT-functionalized electrode is used and the applied voltage is 650 mV . Reprinted from [16].	118
9.1	The measured voltammogram during the measurement of Mitoxantrone in different concentration [13] with a WE incorporating CNTs. The small current peak at around $+400\text{ mV}$ represents the redox current that should be measured in presence of the large background current.	122
9.2	The readout circuit in DIRIC to measure the sensor currents differentially. Two integrators at the front integrate the current of the sensors and transforms them into voltages. The difference of these two voltages is amplified through the PGA and given to the ADC. A serializer is designed and placed after the ADC to reduce the PAD-cost.	123
9.3	The switch-capacitor current integrator. This is the first stage of the readout chain. S_{LL} is a low leakage switch that enables accurate readout of pA-currents.	124
9.4	The low leakage switch, S_{LL} , consists of three complementary sub-switches. When S_{LL} is open (i.e. $\phi_1 = 0$), the voltage drop across the the left sub-switch is zero ($V_{IN} = V_{CM}$) to prevent the off-state leakage current.	125
9.5	The differential voltage to single voltage converter circuit (D2SC)	126
9.6	The clock generator circuit	127
9.7	The programmable gain amplifier based on opamp, switches and a programmable capacitor array	127
9.8	The programmable capacitor array	128
9.9	The Potentiostat generates the voltage to apply to the RE. It is driven from a serial port to generate arbitrary waveform like: triangular, square wave and fixed voltages. An off-chip micro-controller controls the voltage level of V_{RE}	129
9.10	The serial to parallel converter an hold	129
9.11	The schematic of the single-stage folded-cascode amplifier used in the integrator, D2SC, PGA, and the potentiostat. The given transistor sizes are valid for the opamps used in the integrators.	130
9.12	Two multiplexers integrated to DIRIC to configure the interface of the readout circuit in Fig. 9.2 with the internal sensors ($WE_{1,int}$, $WE_{2,int}$, $WE_{3,int}$, $WE_{C,int}$, ISFET, REFET, MOSFET) or external sensors ($WE_{1,ext}$, $WE_{2,ext}$, $WE_{C,ext}$).	131
9.13	The plot of the on-chip sensors. The array includes three main WEs (WE_1 , WE_3 , WE_3), a common WE_C , a common RE, and a common CE, as well as a set of ISFET, MOSFET and REFET for pH measurement	132
9.14	The ISFET. Reprinted from [17].	133
9.15	The ISFET fabricated in unmodified CMOS technology.	134
9.16	The simulated I_{DS} - V_{GS} characteristics of the ISFET with $(W/L)_{elec} = 20/10$ and $(W/L)_{chem} = 100/100$. The source is grounded and V_{DS} is fixed at 1.65 V . V_G is the voltage of the external reference electrode.	136
9.17	The layout of the readout IC with the on-chip sensors	137

List of Figures

9.18 The input-output characteristics of the readout circuit for a wide range of input currents in different frequency settings. The whole range of 0.1 nA to $100\text{ }\mu\text{A}$ can be covered by three clock frequencies: 200 Hz , 20 kHz , and 2 MHz 139

9.19 The simulated voltages of different nodes in the readout circuit for $I_{in} = 10\text{ }\mu\text{A}$, $\Delta I_{in} = 0.5\text{ }\mu\text{A}$, $f_{clk} = 2\text{ MHz}$, and $PGA = 15$ 140

9.20 The simulated voltages of different nodes in the readout circuit for $I_{in} = 100\text{ nA}$, $f_{clk} = 20\text{ kHz}$, and $PGA = 4$ 141

9.21 The microphotograph of the $3.3 \times 3.3\text{ mm}$ IC fabricated in AMS $0.35\text{ }\mu\text{m}$. It includes DIRIC and the on-chip sensor array in the middle. 142

List of Tables

2.1	List of oxidases used to develop biosensors.	13
2.2	List of cytochromes used to developed biosensors and their electrochemical parameters.	14
2.3	Performance of different metabolite biosensors	25
3.1	Comparison of state-of-the-art ICs for amperometric electrochemical measurement	35
3.2	Comparison of state-of-the-art ICs for differential current measurement	36
3.3	Comparison of state-of-the-art ICs for low-frequency waveform generation	37
3.4	Comparison of state-of-the-art circuits for resistor measurement	38
4.1	Power consumption of different blocks of the IC form simulations.	45
4.2	Measured specifications of LOPHIC	46
4.3	Comparison of sensitivity and LOD between the IC and the Autolab for glucose and lactate detection.	51
4.4	Comparison between the IC and the Autolab for the peak attributed to the oxidation of Etoposide.	51
4.5	The specifications of the opamps in ARIC	59
4.6	Simulation results on the circuit for CV, CA, and pH readout	60
4.7	Measured Specifications of ARIC	70
5.1	The characteristics of R2PC and R2VC circuits in the worst case scenario and comparison with state-of-the-art	84
7.1	Design parameters	109
7.2	Design specifications and performance	110
9.1	Design specifications of the amplifiers	129
9.2	Design specifications of the ISFET	137
9.3	Design specifications and performance of the amplifier	139

Contents

Acknowledgements	iii
Abstract (English/Français)	v
List of abbreviations	ix
List of figures	ix
List of tables	xviii
1 Introduction	1
1.1 Motivation	1
1.1.1 HEM-system	2
1.1.2 PET-system	4
1.2 Research objective	6
1.3 Research contribution	7
1.4 Assumption and limitations	8
1.5 Organization of the thesis	8
2 Electrochemical sensing: background	11
2.1 Electrochemical sensing principles	12
2.2 Physical design of the sensor	15
2.2.1 Sensor design for multiple targets	16
2.3 Sensing Properties	17
2.4 An example: biointerface of HEM-system	19
2.4.1 Sensor development	20
2.4.2 Sensor calibration	20
2.4.3 Measurements	24
2.5 Chapter summary	25
3 Integrated electronics for electrochemical sensing: state-of-the-art	27
3.1 Electrochemical sensor model	28
3.2 Readout IC architecture: state-of-the-art	28
3.2.1 Current-mode circuits	28
3.2.2 Voltage-mode circuits	33

Contents

3.2.3	Differential readout circuits	35
3.3	Waveform generator	36
3.4	Integrated electronics for resistor measurement	36
3.5	Chapter summary and conclusions	38
4	ASICs to control and readout amperometric and potentiometric sensors	39
4.1	LOPHIC to readout amperometric sensors	40
4.1.1	Circuit architecture	40
4.1.2	Electrical measurement	45
4.1.3	Electrochemical measurement	47
4.1.4	Discussion on LOPHIC	54
4.2	ARIC to readout amperometric and potentiometric sensors	54
4.2.1	The control and readout chain	56
4.2.2	Commands	63
4.2.3	Data transmission	64
4.2.4	Electrical measurements	64
4.2.5	Electrochemical measurements	68
4.3	Chapter contributions and summary	71
5	ASICs to readout resistance-temperature-detectors	75
5.1	Resistance to pulsewidth converter (R2PC)	77
5.1.1	Circuit architecture	77
5.1.2	Simulation results	78
5.1.3	Measurement results	78
5.2	Resistance to voltage converter (R2VC)	80
5.2.1	Circuit architecture	80
5.2.2	Simulation results	83
5.3	Chapter contributions and summary	86
6	Application of ARIC in remotely-powered implantable medical devices	87
6.1	Application of ARIC in IMDs for HEM	87
6.1.1	The patch	87
6.1.2	HEM-IMD	88
6.2	Application of ARIC in IMDs for PET	92
6.2.1	PET-IMD	93
6.2.2	EXER and Android interface	96
6.2.3	Servo-controlled system for wireless power transfer	99
6.2.4	Measurement results	99
6.3	Chapter contributions and summary	101
7	A lightweight cryptographic system for implantable medical devices	103
7.1	Threat models	104
7.2	System overview	105

7.3	Background	106
7.4	Security module	107
7.5	Simulation results	110
7.6	Chapter contributions and summary	111
8	Measurement of noise in amperometric electrochemical sensors	113
8.1	Material and methods	113
8.1.1	Preparation of electrodes	113
8.1.2	Apparatus	114
8.2	Results	117
8.2.1	Effect of the analyte concentration and MWCNT	117
8.2.2	Effect of the applied voltage	117
8.2.3	Effect of the target Molecule	119
8.3	Chapter contributions and summary	119
9	Differential readout IC for amperometric sensors	121
9.1	Motivation	121
9.2	DIRIC architecture	122
9.2.1	The integrator	123
9.2.2	Differential to single converter (D2SC)	125
9.2.3	Clock generator	126
9.2.4	Programmable gain amplifier	127
9.3	Potentiostat	128
9.3.1	SPCH	128
9.4	Amplifiers	130
9.5	Sensor array	131
9.5.1	ISFET Design	132
9.6	Simulation results	138
9.7	Chapter contributions and summary	142
10	Conclusions and future work	145
10.1	Thesis summary and contribution	146
10.2	Future work	147
	Bibliography	163
	Curriculum Vitae	165

1 Introduction

Electrochemical detection of biological agents is important in several domains, including the medical practice, the discovery of biological mechanisms and monitoring the environment. To date, several medical devices use electrochemical detection. A notable case is the family of FDA-approved devices for glucose monitoring.

Monitoring human metabolism is of crucial importance for personalized medicine. Many metabolic diseases may be monitored by means of different endogenous metabolites such as glucose, lactate and ATP. On the other hand, metabolism of exogenous compounds, such as drugs can enhance the specificity of a therapy according to the individual patient, since the response rate of different patients to the same pharmacological treatment and dose typically varies in the range from 20% to 50%. Bio-monitoring can be effectively used to tune the dosage of a therapy.

1.1 Motivation

Since clinical analysis in laboratories are time-consuming and expensive processes, research is focused on the development of methods to perform rapid measurements of analytes in point-of-care testing, *e.g.* by patients at home [18]. Electrochemical sensors are ideally suited for these applications by providing rapid, accurate and quantitative detection of analytes with an inexpensive and simple to use set-up [19]. The real-time monitoring of metabolites in the blood enables us to understand the patient's health condition, whereas the real-time drug monitoring enables the individual adjustment of the drug dosage in order to increase the accuracy and efficacy of the treatment and to reduce dangerous adverse drug reactions, especially for patients with critical or chronic conditions [18,20]. Endogenous molecules (*e.g.*, glucose, lactate, ATP) and exogenous molecules (*e.g.* drugs) are among the most important biomolecules to be monitored.

Fully-implantable medical devices (IMDs) are emerging as a valid alternative for blood testing in laboratories that provide continuous monitoring. They eliminate the need for blood

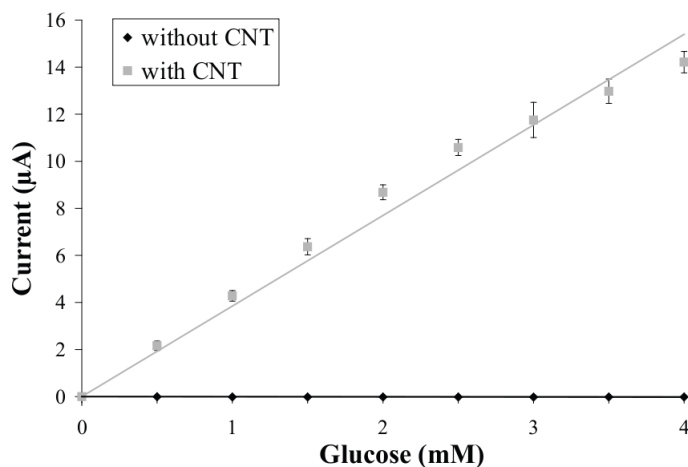


Figure 1.1: Glucose detection with chronoamperometry for bare (black rhombus) and CNT-covered (grey squares) sensors. Reprinted from [1].

sampling and decrease the test costs. The construction of a fully implantable and wireless biosensor requires the integration of three main building blocks: (i) a sensor array to detect and measure the target compounds, (ii) an interface electronics (i.e. a potentiostat) to control and readout the biosensor, and (iii) a power management unit.

The implantable device has to be small to be minimally invasive, and low power. Moreover, it should be able to detect a specific group of key metabolites and/or drugs within a single platform, to accurately monitor the health condition of the patient and to enable personalized therapy. HEM and PET are two heterogeneous systems that include IMDs for *health-care monitoring* (HEM) and *personalized therapy* (PET), respectively. In this section these two systems are described and their different parts and requirements are presented.

1.1.1 HEM-system

The HEM-system includes a fully-implantable and remotely-powered platform for the real-time monitoring of human metabolites. The target molecules are principally but not limited to glucose, lactate, ATP, arachidonic acid, and bilirubin.

Devices dedicated to the continuous monitoring of human metabolites, such as glucose [21] and lactate [22], are already present in the market. Furthermore, experimental prototypes have been reported in the literature for the detection of glutamate [23], and ATP [24]. The HEM-system integrates these metabolite sensors, in a modular way, into a miniaturized biosensing platform to enable minimally-invasive and low-cost human health-care monitoring. Continuous monitoring of human metabolites (such as glucose, lactate and ATP) is of great benefit for patients with critical or chronic conditions as well as for professional sportsmen training.

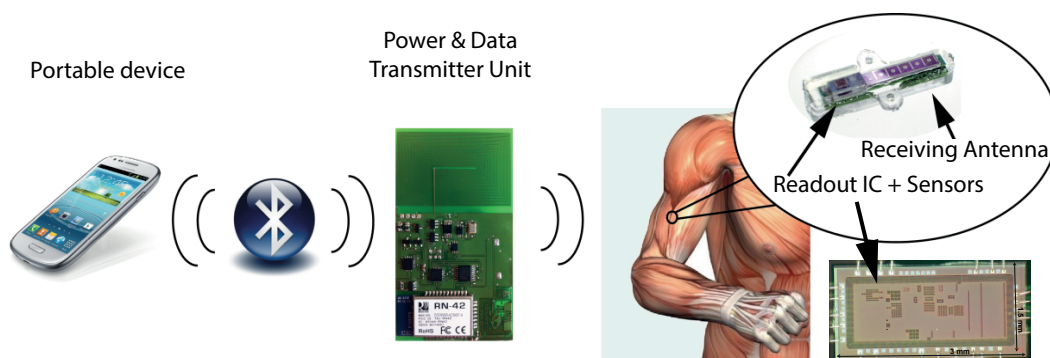


Figure 1.2: The conceptual diagram of HEM-system. The implanted device measures multiple metabolites in the interstitial tissue and sends the results to the patch. The patch communicates the results to a more powerful device for processing, storage and display.

Chronoamperometry (CA) is a common electrochemical technique to measure the concentration of endogenous (i.e. glucose, lactate) molecules in the human body [25]. In a CA measurement, a fixed voltage (for oxidation or reduction) is applied between the cell electrodes and the current is measured. The asymptotic value of the current, when a steady-state is reached, is directly related to the compound concentration (See Fig. 1.1). The sensor sensitivity is improved by using nano-structured materials. The *Carbon nano tubes* (CNTs) are widely used to enhance the performance of electrochemical biosensors in terms of sensitivity and detection limit [26] (See Fig. 1.1). However, they also increase the measurement noise [2] and their effect on the SNR measurements is not yet fully understood. CNTs are potentially toxic [27] which requires careful design to ensure the biocompatibility of devices incorporating nano-materials, while at the same time the contact with biological fluids should not significantly affect the sensor performance [28].

The final HEM-system consists of three devices: a fully implantable sensors array for the metabolite detection, a wearable patch for the remote powering and data acquisition, and an interface dedicated to display the measurements on tablets and smart-phones. The sketch of the HEM-system is depicted in Fig. 1.2. The wearable patch is a power and data transmitter unit that sends power to the implanted device, powers-on the electronics in it, and receives data from the implant, and sends it via blue-tooth to a smart-phone or tablet.

A conceptual diagram of HEM-IMD is shown in Fig. 1.3. The implanted device receives power from the patch via the inductive link. To reduce the total size of the implant, a multi-layer inductor is placed at the bottom of the device. The implanted device consists of the sensor array controlled by an autonomous fully-integrated readout IC. The readout IC reads out the multi-target sensor array and digitizes the data within a very limited energy- and area- budget.

Temperature and pH sensibly affect the results obtained by measurements [29]. Thus, temperature and pH sensors have been included in the sensor array to calibrate the obtained results.

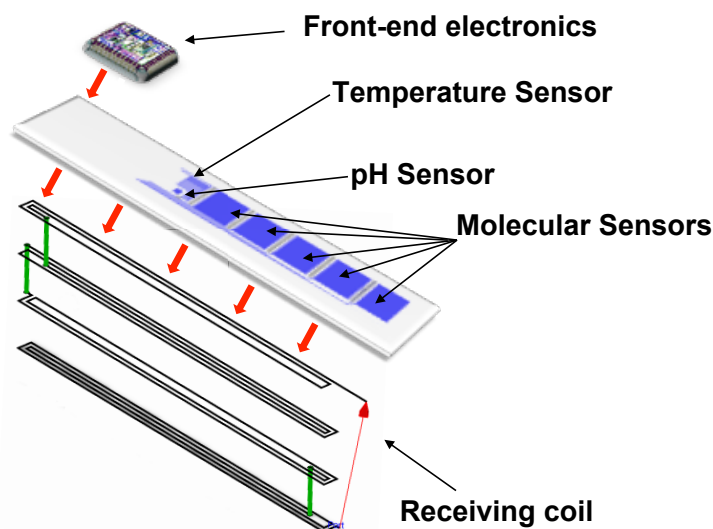


Figure 1.3: The conceptual diagram of HEM-IMD

The temperature sensor is implemented by a custom-designed platinum *resistor temperature detector* (RTD) which is placed close to the sensor array to ensure accurate measurement of the analyte temperature. The pH sensor is implemented with an Iridium oxide coated electrode with its open circuit voltage linearly proportional to the pH of the analyte. The circuits for pH and temperature sensors are also integrated into the readout IC. The detailed presentation of the biointerface of HEM-system is given in Chapter 2 (Section 2.4).

1.1.2 PET-system

The development of an implantable device for monitoring exogenous substances, such as drugs, would represent a big step towards personalized medicine. It enables the individual adjustment of the drug dosage and, therefore, increases the accuracy and efficacy of the treatment which reduces dangerous adverse drug reactions, especially for patients with critical or chronic conditions [19].

The PET-system includes a fully-implantable device for the continuous monitoring of drugs and metabolite concentration in laboratory animals such as mice. Small animal models are increasingly being used in the first phase of clinical trials for drug development. The living conditions of these animals are of primary importance because the stress level can affect the measurement results. This means that the animal must be in a comfortable environment and capable to freely move. Therefore, the final aim of PET-system is to monitor the animal in a living space, such as a cage, where the power must be continuously transferred to the implantable. The conceptual diagram of PET-system is depicted in Fig. 1.4.

The fully-integrand PET-IMD is shown in Fig. 1.5. It consists of three different layers: (i)

1.1. Motivation

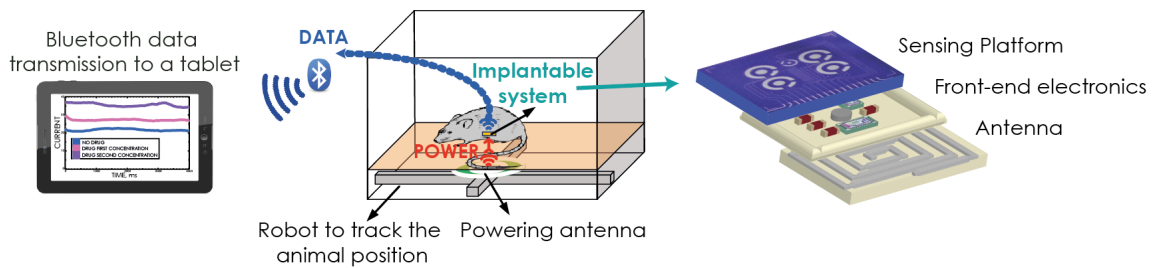


Figure 1.4: Scheme of PET-system: an intelligent system with the data transmission via Bluetooth to an Android interface (left), and the scheme of the implantable device (right).

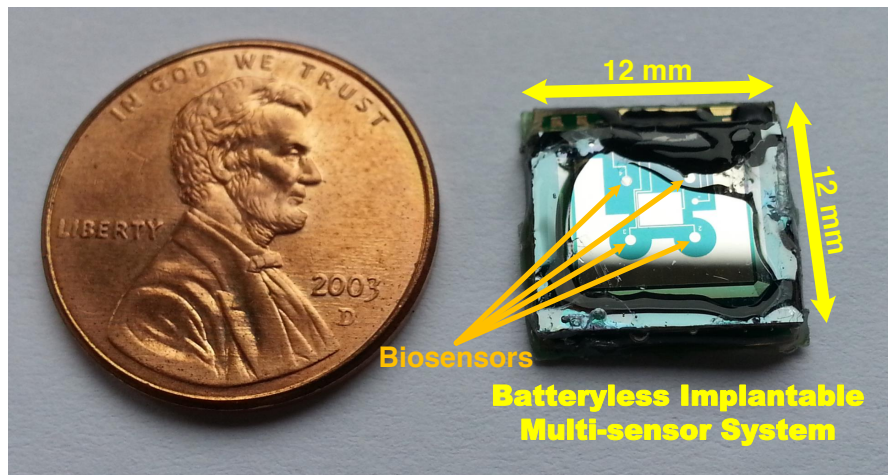


Figure 1.5: An implantable device for multiple-metabolite detection

the sensor array; (ii) the front-end electronics (iii) the antenna for power transmission. The multi-target detection needs the integration of different detection methods within the front-end IC. In addition to CA, *cyclic voltammetry* (CV) is also needed to detect exogenous metabolites such as drugs. In a CV measurement, a very slow triangular voltage is applied to the cell. By changing the applied voltage, a point is reached in which oxidation (loss of electrons by the compound) takes place. The oxidation of the compound generates a current that is continuously monitored by the readout IC in the front-end electronics. The plot of current versus the applied voltage (named voltammogram) shows a peak in the current at the oxidation voltage. In case of reversible reactions, as the voltage sweeps back, the oxidized species starts to be reduced giving a negative current peak at the reduction voltage. An example of voltammogram is reported in Fig. 1.6. The peak values can be translated into the compound concentration, whereas the peak position and their distance are related to the species involved in the reaction.

Therefore, in addition to CA measurement and calibration (as for HEM-IMD), the readout IC in PET-IMD generates a sub-Hertz triangular waveform to perform CV on the sensors and reads the bidirectional current at the same time.

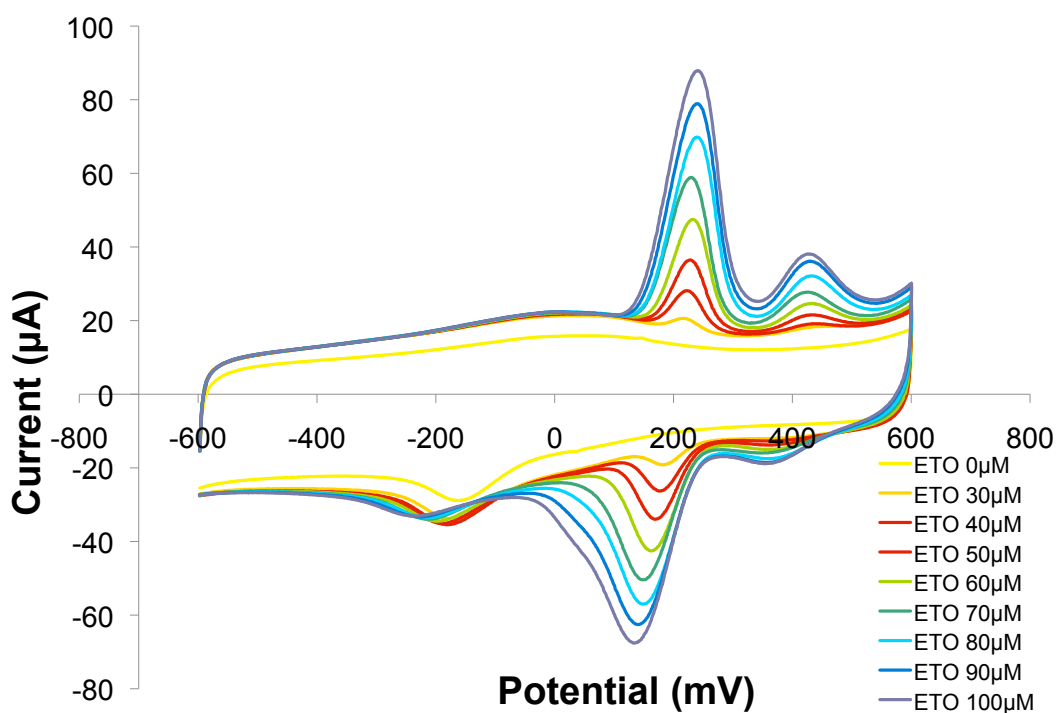


Figure 1.6: Voltammogram acquired using a potential scan rate of 20 mVsec during the detection of etoposide with multi-walled CNTs. Reprinted from [2].

1.2 Research objective

Today's state-of-the-art of integrated circuits for electrochemical detection still suffers from the lack of autonomy and the limited chemical specificity in a complex biological matrix (i.e. multiple metabolite detection) hindering their use for health-care monitoring and personalized therapy studies.

The main objective of this work was to develop fully-integrated and low-power electronics to control, readout and calibrate electrochemical sensors. This is to design and implement integrated circuits and systems that perform multiple measurement techniques such as chronoamperometry, cyclic voltammetry, pH and temperature measurements on multi-target sensor arrays. The readout IC provides all the necessary voltage and current waveforms to stimulate the sensors, in order to make an autonomous and minimally invasive implantable system.

The design of accurate control and readout electronics requires a thorough knowledge of the biosensor. The intrinsic time-varying nature of the biosensors together with emerging use of nano-structures to improve their performance requires the development of new circuit architectures that also enable the calibration of the sensors. The emerging sensing concepts such as multi-metabolite sensing within a single miniaturized biosensor necessitates the co-design of the biosensors and the electronics and opens the door to fully-integrated and autonomous heterogeneous devices for point of care diagnostics and implantable applications

in complex environments (e.g. in blood). A modern potentiostat for implantable applications is therefore a full system made of several circuit blocks to control, readout, and calibrate the biosensors.

1.3 Research contribution

This PhD thesis covers the design, implementation, characterization, and validation of sub-mW reconfigurable and fully-integrated electronics to control and readout electrochemical sensors. The ICs extend significantly the state-of-the-art of potentiostat for multi-metabolite sensing. They are integrated into tiny, battery-less, and wireless implantable devices (i.e. PET- and HEM-IMDs) and successfully measured a number of metabolites. The developed heterogeneous devices provide real-time and continuous monitoring of several metabolites and are a big step forward in health care monitoring and personalized therapy.

Moreover, this thesis presents innovative research on other important aspects of sensors, potentiostats, and implantable medical devices as explained below.

- A better understanding of noise sources in electrochemical sensing is necessary to design the next generation devices for high sensitivity bio-sensing applications. Such understanding is also very useful to develop new models for the electrochemical sensors that can improve chip design simulations. To this aim, the low frequency noise in electrochemical sensors in the presences of CNTs is studied in this research. The noise in CNTs and sensors were already characterised separately in [30–32] and [33, 34], respectively. This is the first time that the noise in sensors incorporating CNTs is studied. The promising results proves the efficacy of CNTs in improving the signal-to-noise ratio of the sensor.
- Novel circuit architectures are designed and implemented to measure *resistor temperature detectors* (RTD). The circuits measure a single off-chip RTD which can later be translated into temperature. The circuits proposed in this research are the first circuits for single custom-designed RTD measurement.
- A fully on-chip waveform generator is designed to provide *ultra-low frequency* (ULF) control voltages to stimulate the sensors in CV measurement. The waveform generator is designed to provide various waveforms at the same time to enable multiple sensing functions.
- By the introduction of the nano-structures such as CNTs to the sensors, the background current of the sensor increases drastically. To remove this from the measured current, a fully-integrated pseudo-differential readout circuit has been designed. The system is the first fully integrated differential readout circuit that samples the differential inputs at the same time. This is also the first circuit that offers the possibility to amplify only the -informative- redox current.

- A lightweight cryptographic system for implantable medical devices has been implemented for the first time in this research. The proposed crypto-system provides security and privacy for the sensor data by encrypting the data upon its creation inside the body. The cryptographic system is integrated into the interface electronics and prevents some low-level attacks on data communication in both HEM- and PET-systems.

1.4 Assumption and limitations

The selected CMOS technology for the fabrication of the readout ICs involved in PET- and HEM-systems was UMC 0.18 μm . The 0.18 μm technology with 1.8 V supply-voltage was chosen over other technologies to make trade-offs between the power consumption and the required supply-voltage: The inductively-powered IMDs have a power budget of only 2 to 3 mW which makes the use of a low supply-voltage favourable. However, reducing the size of the technology and the supply-voltage below 1.8 V is not sufficient to control the biosensors.

The pseudo-differential IC (presented in Chapter 9) is instead implemented in AMS 0.35 μm technology. This technology was chosen because, together with the IC, *ion-sensitive field effect transistors* (ISFET) for pH sensing were also designed and fabricated, and AMS 0.35 μm proved to be one of the best for the development of ISFETs [17]. However, the implementation of the IC in this technology lead to higher area and power consumption compared to a more recent technology.

The less-known nature of the biosensors limited the accuracy of the circuit simulations. To simulate the circuits in contact with the biosensors and to ensure their stability, the simplified models for the electrochemical sensors that are widely used in literature were used. The models consist of a network of resistors and capacitors (as described in Chapter 2) in which the resistor values were calculated from the sensor current range. However, the capacitor values could only be estimated from *electrochemical impedance spectroscopy* (EIS) measurements, which were not available. Therefore, the readout ICs are designed to be stable for a wide range of capacitor values in the equivalent-RC-network of the biosensors.

1.5 Organization of the thesis

Following the Introduction, this thesis is organized as follows:

Chapter 2 gives an overview on the electrochemical sensing strategies for human metabolite monitoring. Nano-materials such as CNTs used in biosensing are introduced, as well as sensor development and calibration for multi-metabolite sensing.

Chapter 3 gives an overview on the control and readout circuits and systems for amperometric electrochemical sensors that have been developed over the last two decades. The chapter is focused on the integrated circuits for CA and CV measurements. A classification of these

circuits is given together with the limitation and advantages of each considering their application in implantable devices. This chapter also gives an overview on the integrated circuits and systems for resistance measurement.

Chapter 4 describes the design, implementation, characterization and validation of two ICs to control and readout multi-target biosensor arrays. These are the *low-power hybrid IC* (LOPHIC) and the *autonomous reconfigurable IC* (ARIC). LOPHIC controls and reads out up to five biomolecular sensors and has an ultra-low-frequency waveform generator to control the sensors in CV. ARIC is a fully-integrated and autonomous system that in addition to provide sensor control and readout, offers a digital output and can be commanded from outside to perform different types of measurement on different sensors. The full characterisation and validation of LOPHIC and ARIC with electrochemical sensors are presented in this chapter.

Chapter 5 describes the design of two novel circuits to measure off-chip RTDs. These are unique circuits that can be coupled to a single off-chip RTD and measure its resistance which can later be translated into temperature. The first circuit provides coarse resolution within a wide dynamic range and the second circuit offers fine resolution within a narrow range. The simulation and measurement results on these circuits are also presented.

Chapter 6 describes the integration and validation of ARIC in the HEM- and PET-systems. Different parts and aspects of the projects are described with a focus on the integration of heterogeneous systems, data and power transmission and finally full system validation with glucose and drug measurements.

Chapter 7 describes a lightweight cryptographic system that is integrated into ARIC to provide security and privacy for the measured data. The system encrypts the data before it is transmitted out of ARIC. The characteristics and the simulated performance of the cryptographic system is also presented.

Chapter 8 presents the empirical study of noise of electrochemical sensors in presence and absence of CNTs. Moreover, the effect of target molecule and the cell control voltage on the signal over noise ratio of the biosensors is shown.

Chapter 9 describes a *pseudo-differential readout IC* (DIRIC) together with a programmable control circuit that are designed to perform differential measurements on amperometric sensors. An on-chip sensor array is designed together with the readout circuit to measure up to three different metabolites as well as pH measurement through an ISFET.

Chapter 10 summarizes the contributions of this research on control, readout and calibration circuits for biosensors and gives an outlook on the future of implantable sensors and systems for biomedical applications.

Within the frame of this research, five ICs (several prototypes of the above mentioned ones) were designed to create autonomous and implantable micro-systems for health-care monitoring and personalized therapy. The implantable medical application is currently an exciting

Chapter 1. Introduction

research field that both academia and the international medical devices industry are just beginning to exploit. In addition to medical applications, these ICs can be applied in other fields and applications such as environmental monitoring through electrochemical gas sensors [35,36].

2 Electrochemical sensing: background

To date, several medical devices use electrochemical detection through biosensors. Biosensors are used to monitor patients in critical and/or chronic conditions, where often the concentration of molecules, typically metabolites, is important. A notable case is the commercialized glucose sensors for diabetes which uses the enzyme glucose oxidase to break down the blood glucose. An electron is then released which is measured as a current by a potentiostat, and translated into blood glucose concentration [37].

Among endogenous metabolites the most interesting are glucose, lactate, glutamate, and cholesterol. Glucose amount in the human blood is a marker for diabetes. Lactic acidosis is one of the effect of Von Gierke's disease which occurs when mitochondria cannot satisfy cell demand of ATP, especially during physical efforts or diseases. Glutamate is a neurotransmitter, which can be found in neuronal and glial membranes. In brain injury or brain diseases, glutamate can accumulate outside cells, leading to neuronal damage and, eventually, cell death. Cholesterol is a lipid, and it is one important building block in the structure of cells. However, high levels in the blood are strongly associated to atherosclerosis.

Many exogenous metabolites are relevant molecules commonly used in drug therapy. Etoposide, ftorafur, cyclophosphamide, ifosfamide, etc. are well known molecules typically used in chemotherapy treatments. The measure of their level in the blood during pharmacological treatment allows doctors to monitor how the patient is metabolising the supplied drugs.

There are several architectures and technologies for integrated biosensors, and most devices are designed with *ad hoc* methods. Moreover the current need of multiple-target biosensing requires an extension of the existing techniques. Thus, the proliferation of electronic monitoring techniques would benefit from a systematic design space exploration, in the search of the most cost-effective solution (e.g., small, low energy consumption, low-cost) to a given problem [8].

This chapter introduces the principle of electrochemical sensing for metabolite sensors through two types of enzymes: oxidases and cytochrome p450. Moreover, an example of

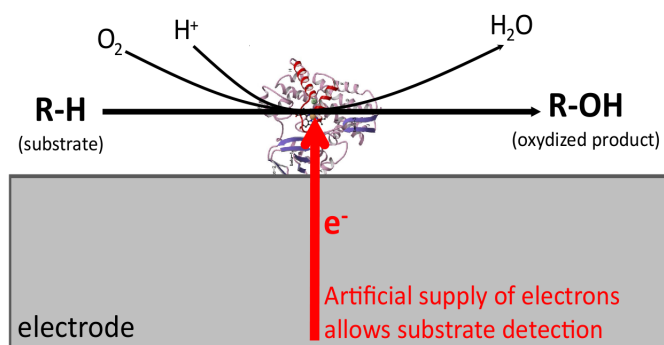


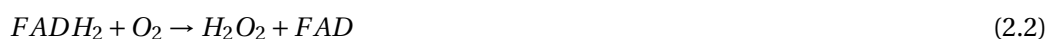
Figure 2.1: Simplified principle of the P450 biosensor: the electrons needed for the catalysis are supplied by the electrode, allowing substrate detection. Reprinted from [3].

a multiple-sensing platform is given, for which the sensor development and calibration are presented.

2.1 Electrochemical sensing principles

Enzymes are very useful proteins, which may be used as probes to monitor metabolites in case of both endogenous and exogenous molecules. In particular, the protein class of *oxidases* may be used for sensing endogenous metabolites, while *cytochromes P450* may be used for sensing drug compounds. The term oxidase is referred to a large family of enzymes that catalyse an oxidation-reduction reaction, involving molecular oxygen (O₂) as the electron acceptor. In these reactions, the final product is typically hydrogen peroxide (H₂O₂) which further splits in water and oxygen.

Oxidases are typically characterized by a prosthetic group integrated within the enzyme, which is the group directly involved in the redox reaction. For such enzymes like *glucose oxidase* (GOD), *L-glutamate oxidase* (GLOD), and *cholesterol oxidase* (COD), the prosthetic group is the *flavin adenine dinucleotide* (FAD) group [8]. FAD can be reduced to FADH₂ by accepting two hydrogen atoms. Then, the reduced form can be oxidized to restore the initial structure, combining hydrogen (H₂⁺) with O₂ and losing two electrons to produce hydrogen peroxide. The redox reaction for all these types of enzyme with FAD as prosthetic group is the following:



Another subclass of enzymes (lactate oxidase, for example) employs *flavin mononucleotide* (FMN) group, which works in the same way as FAD. For both the prosthetic groups, the final

2.1. Electrochemical sensing principles

Table 2.1: List of oxidases used to develop biosensors.

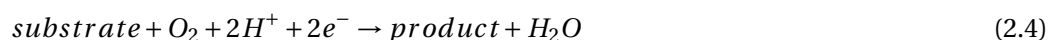
Oxidase species	Target molecule	Description	Applied voltage (vs reference electrode)
GLUCOSE OXIDASE	glucose	Metabolic compound as energy source	+550 mV [38]
LACTATE OXIDASE	lactate	Metabolic compound as marker of cell suffering	+650 mV [39]
CHOLESTEROL OXIDASE	cholesterol	Metabolic compound that establishes proper membrane permeability and fluidity	+700 mV [40]
L-GLUTAMATE OXIDASE	glutamate	Excitatory neurotransmitter	+600 mV [41]

product of the reaction is the hydrogen peroxide, which is an electrochemical active species. The following reaction



is promoted by applying a voltage to the electrochemical cell.

Cytochrome P450 (CYP) belongs to a family of heme proteins which metabolize over 200,000 chemicals, including drugs [8]. Since the liver is the main biotransforming organ for drugs, CYPs and other metabolising enzymes reside in the hepatocytes. As FAD and FMN were the active groups involved in the electron exchange for oxidase, the heme group has an analogous role for cytochromes. The most common redox reaction for this family of proteins is described as follows (see Fig. 2.1):



where the supplier of electrons is the heme functional group that presents in the cytochrome. Thus, it is possible to follow the catalytic cycle of cytochrome by monitoring the electron transfer between the electrode and the enzyme by using an amperometric biosensor. On this basis, it is possible to determine the concentration of the target molecule by measuring the current generated in the electrochemical cell.

There are two main electrochemical techniques to measure target concentration, according to the biological agent used in the sensing mechanism. The common product of oxidases is H_2O_2 , as mentioned before. The oxidation of hydrogen peroxide is well known [52] and can be measured by setting the electrode voltage at +650 mV. For this reason it is possible to apply a constant voltage, corresponding to the oxidation voltage, and recording the current generated, which is directly proportional to the concentration of the target molecule metabolised by the

Chapter 2. Electrochemical sensing: background

Table 2.2: List of cytochromes used to developed biosensors and their electrochemical parameters.

CYP species	Target drug	Description	Reduction voltage (vs Ag/AgCl)
CYP1A2	clozapine	Antipsychotic used in the treatment of schizophrenia	-265 mV [42]
CYP3A4	erythromicin	Broad-spectrum antibiotic	-625 mV [43]
	indinavir	Used in the treatment of HIV infection and AIDS	-750 mV [44]
CYP11A1	cholesterol	Metabolite able to establish proper cell membrane permeability and fluidity	-400 mV [45]
CYP2B4	benzphetamine	Used in the treatment of obesity	-250 mV [46]
	aminopyrine	Analgesic, anti-inflammatory, and antipyretic drug	-400 mV [47]
CYP2B6	bupropion	Antidepressant	-450 mV [48]
	lidocaine	Anesthetic and antiarrhythmic	-450 mV [49]
CYP2C9	torsemide	Diuretic	-19 mV [50]
	diclofecan	Anti-inflammatory	-41 mV [50]
CYP2E1	p-nitrophenol	Intermediate in the synthesis of paracetamol	-300 mV [51]

oxidase. This technique is called *chronoamperometry*, because the current is monitored as a function of time. With screen-printed electrodes, the current decays over time, and it reaches an approximately steady-state after a certain time.

Another technique used in electrochemistry is called *cyclic voltammetry* (CV), and it is more suitable in the case of CYT P450, where it is possible to identify more target molecules with the same biological probe protein. In fact, by using CV it is possible to identify multiple targets and their concentration at the same time. Cyclic voltammetry applies a linear-sweep voltage forward and backward within a voltage window to the electrochemical cell, and monitoring continuously the current. The resulting graph will rise very slowly at the beginning. As soon as the voltage approaches the reduction voltage, the electron transfer from the protein to the electrode increases its rate, which causes cell current to increase. At a certain point, the current will start to decrease again, due to the decreasing rate of diffusion of the target from the bulk of the solution. Typically, the current is plotted as function of the voltage and the plot

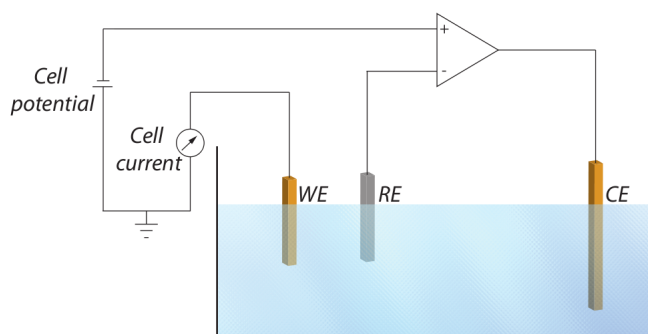


Figure 2.2: Diagram of a three-electrode based electrochemical cell with a potentiostat to apply the voltage to the cell and a current-meter to measure the sensor current.

is characterized by some peaks, whose height is proportional to the target concentration, while position gives information on the type of molecules that are oxidized, like an electrochemical signature. Table 2.1 summarizes some examples of oxidases used to develop biosensors, where chronoamperometry is used as the electrochemical technique used for the detection of hydrogen peroxide. Hydrogen peroxide oxidizes at $+650\text{ mV}$, but depending on the electrode type the oxidation voltage may change by $\pm 100\text{ mV}$. Table 2.2 reports some target molecules, detectable by CYP and their typical reduction voltage.

2.2 Physical design of the sensor

To conduct such experiments at least two electrodes are required. The *working electrode* (WE), which makes contact with the analyte, applies the desired voltage and facilitate the transfer of charge to and from the analyte. A second electrode acts as the other half of the cell. It must have a known potential with which the voltage of the working electrode is determined. Moreover, it must balance the charge added or removed by the working electrode. While this is a viable set-up, it has a number of shortcomings. Most significantly, it is extremely difficult for an electrode to maintain a constant voltage while passing current to counter the redox events at the working electrode.

To solve this problem, the roles of supplying electrons and providing a reference voltage are divided between two separate electrodes. The *reference electrode* (RE) to act as reference in measuring and controlling the working electrode's voltage while it does not pass any current. The *counter electrode* (CE) passes all the current needed to balance the current at the working electrode. To achieve this current, CE oxidizes or reduces the solvent or supporting electrolyte. These electrodes, WE, RE, and CE make up the modern three electrode system. A potentiostat circuit keeps the electric voltage of the WE to a value that can be fixed or variable with respect to RE. The current that flows between WE and CE is collected and measured. Fig. 2.2 shows the simplified diagram of the cell and the potentiostat.

When considering sensing multiple targets, it is possible to consider various bio-electrical

interfaces. The simplest physical structure is a single sensor, made of 3 electrodes, with WE that is functionalized with enzymes to sense one or more targets. An extension of this sensor for n targets, is to use $n + 2$ electrodes, out of which there are n WEs each functionalized for a given target. An underlying assumption for this sensor to be useful is that the targets can be present in the same volume surrounding the probe without interfering. A one-dimensional (or two-dimensional) sensor array consists of k (or $k \times j$) such sensors, each with 3 or more electrodes. Finally, when the electrochemical reactions must be kept separated to prevent cross-talk and interferences, each sensor in an array must have its own chamber [8].

2.2.1 Sensor design for multiple targets

In this section we want to consider jointly: (i) the choice of the probe and (ii) the choice of the sensor structure. We start from the choice of the probe, as this is typically dictated by the target, and the target is often the objective of the biomedical investigation.

Let us consider first oxidase-based sensing. In this case, measures are obtained from the current generated by the oxidation of hydrogen peroxide. In a first approximation it is possible to combine more oxidases in the same chamber to detect different metabolites, even if all the oxidases generate current by oxidation of the hydrogen peroxide. Since the diffusion coefficient of H_2O_2 is really low, we can assume negligible cross-talk among the different sensors [8]. Otherwise, we should consider separate chambers, where an array of electrochemical cells achieve the multi-target sensing.

Next, let us consider CYP-based sensing. As mentioned before, the simplest CYP measure consists in a cyclic voltammetry, i.e., by cycling the voltage of the fluid interposed between the RE and WE, and by measuring the current flowing out of the WE. According to the cytochrome isoform chosen, one or more targets can be detected by current peaks corresponding to the related electrochemical voltages. Thus, a single probe can sense multiple targets, if the I/V plot can be recorded in correspondence with current maxima.

An alternative approach to multiple target detection can be achieved by sensors with more than one WE, each characterized by a different probe. In this case, cyclic voltammetry sweeps the voltage of the fluid between RE and WE, and currents stemming out of the WEs will display peaks in correspondence with the related voltammetric voltages. A circuit sensing the corresponding currents - possibly multiplexed - is then needed. It is important to remark that the collected currents relate to the amount of target interacting with the probe, and thus multiple measures can be done in a single chamber.

The use of sensor arrays - with or without multiple chambers - is a straightforward extension. From an electronic standpoint, an issue is the ability to share hardware resources (such as voltage generators) and current sensors, possibly by multiplexing. In chapter 5 a scheme is shown to multiplex the measurement of the currents coming from various probes, to sense concentrations of different molecules.

2.3 Sensing Properties

We list here the desirable properties of a biosensing acquisition chain.

- *Limit of detection* (LOD). A very general definition of LOD is “the smallest signal that can be distinguished from the background noise associated with the instrumental measurement”. Formally, the Limit-of-Detection is defined as the concentration of analyte required to give a signal equal to the background (blank) plus three times the standard deviation of the blank. The limit of detection in terms of current (y_{LOD}), was calculated as the minimum detectable signal, from the IUPAC definition [53]:

$$y_{LOD} = y_B + k \cdot \sigma_B \quad (2.5)$$

where y_B is the mean value of replicates of blank measurements, σ_B is the standard deviation of the blank signal (that can be substituted with the residual standard error), and $k = 3$ ensures, with a confidence level of 99.86%, that the LOD signal is equal or bigger than the background (blank) plus three times the standard deviation of the blank signal. In case of background-subtracted data (corrected by the same blank value), the standard deviation (or the standard error) should be corrected by multiplying for a factor ($\sqrt{\frac{1}{n} + \frac{1}{n_B}}$) that depends on the number of replicate observations (n) and the number of blank measurements (n_B). The LOD in terms of concentration is then calculated from the equation of the regression line ($y = mx + q$). In case of background subtraction and when the value of the intercept (q) does not significantly differ from the mean blank value (y_B), the LOD can be calculated with the equation:

$$LOD = k \cdot \frac{\sigma_B}{S_{avg}} \quad (2.6)$$

where S_{avg} is the slope of the calibration line (the sensitivity) defined in the following way.

- *Sensitivity*. It is the slope of the calibration line, i.e. ($y_{ss} - y_b$) versus the analyte concentration, c , or its logarithm [54], where y_{ss} is the steady-state response. Global sensitivity is due to the cascading effects of the (i) electrochemical reaction, (ii) electron collection, (iii) current amplification and conversion. The average global sensitivity, S_{avg} can be defined as:

$$S_{avg} = \Delta V / \Delta C \quad (2.7)$$

where ΔC is the measured range of analyte concentration and ΔV is the corresponding change in the output signal of the system.

- *Linear concentration range and linearity*. On the biosensor side, linear range is directly related to the biocatalytic or biocomplexing properties of the biochemical or biological

receptor [54]. In the system level, the effects of the bioprobes membrane and electronics readout should be considered as well in limiting the linearity. The maximum non-linearity of a measurement platform can be defined as:

$$NL_{max} = \max|V_C - V_{C_0} - S_{avg} \cdot (C - C_0)| \quad (2.8)$$

where C_0 refers to a reference concentration, V_C and V_{C_0} are the output signals corresponding to C and C_0 concentrations.

- *Selectivity.* It measures the ability to discriminate between different substances. Such behavior is principally a function of the recognition element, i.e. the enzymes [52].
- *Steady-state response time.* It is the time necessary to reach 90% of the steady-state response. Transient response time corresponds to the time necessary for the first derivative of the output signal to reach its maximum value $(dV/dt)_{max}$ following the analyte addition. Both response times depend upon the analyte, co-substrate and product transport rates through different layers or membranes. They also depend upon the activity of the molecular recognition system and the mixing conditions of the sample into the batch measurement cell [54]. Since the biochemical sensing is a very slow process, the readout circuitry would not limit the response times of the output signal.
- *Sample throughput.* It is a measure of the number of individual samples per unit of time. This parameter takes into account both the transient response time and the recovery time, i.e. the time needed for the signal to return to its baseline [54].
- *Reproducibility, stability and lifetime.* The definition of reproducibility is the same for electrochemical biosensors as for any other analytical device: reproducibility is a measure of the scatter or the drift in a series of observations or results performed over a period of time. It is generally determined for the analyte concentrations within the usable range.

The operational stability of a biosensor response may vary considerably depending on the sensor geometry, method of preparation, as well as on the transducer. Furthermore, it is strongly dependent upon the response rate-limiting factor, i.e. a substrate external or inner diffusion or biological recognition reaction. Finally, it may vary considerably depending on the operational conditions [54].

Although some biosensors have been reported to be usable under laboratory conditions for more than one year, their practical lifetime is either unknown or limited to days or weeks when they are incorporated into industrial processes or into biological tissue, such as glucose biosensors implanted in vivo. For storage stability assessment, significant parameters are the state of storage, i.e. dry or wet, the atmosphere composition, i.e. air or nitrogen, pH, buffer composition and presence of additives [54].

Finally, the mode of assessment of lifetime should be specified, i.e. by reference to initial sensitivity, upper limit of the linear concentration range for the calibration curve, accuracy or reproducibility. The recommended definition of lifetime, denoted t_L , is the

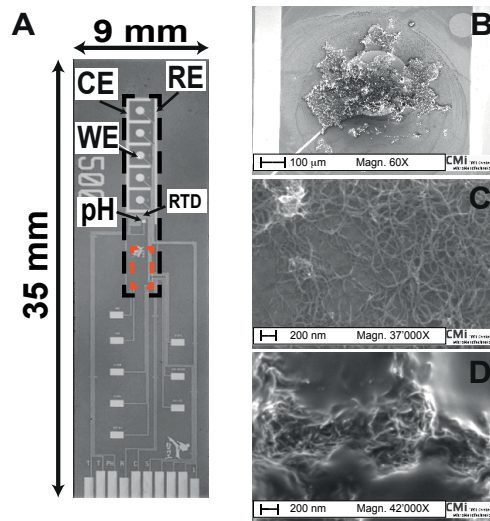


Figure 2.3: The HEM-biointerface: An example of a platform with multiple WEs. It consists of five WEs, a common RE, a common CE, and pH and temperature sensors. The black dashed line defines the section of the platform that is diced to be integrated in the HEM-IMD reported in Chapters 1 and 6. The red dashed line defines the space for bonding the IC; B) SEM image of CNTs drop-cast on a WE; C) at higher magnification; D) SEM image of CNTs and glucose oxidase drop-cast on a WE.

storage or operational time necessary for the sensitivity, within the linear concentration range, to decrease by a factor of 10% ($tL10$) or 50% ($tL50$) [54]. Biosensor stability may also be quantified as the drift, when the sensitivity evolution is monitored during either storage or operational conditions. The drift determination is especially useful for biosensors whose evolution is either very slow or studied during a rather short period of time.

We concentrate on the limit of detection, sensitivity, and linearity parameters because they affect the design of the electronic building blocks.

2.4 An example: biointerface of HEM-system

Fig. 2.3 shows the biointerface of HEM-system. It consists of five WEs, one CE and one RE. The inclusion of common RE and CE simplifies the interconnections with the readout circuit, minimizing at the same time the total sensor area. In the PET-biointerface, the electrode area is minimized. Scaling down the electrodes has several advantages: the background current is smaller, due to different double-layer capacitance phenomena [52]; time response of the biosensor is shorter, enabling much shorter measurements [52].

The sensors were fabricated at the Centre of Micronano Technology of EPFL (CMI). Choice of materials and design was done considering biocompatibility and simplicity of fabrication

as of primary importance. As substrate, silicon has been chosen over glass for its better thermal conductivity, in order to improve the dissipation of heat generated by the integrated circuit. Electrodes are made of a thin film of Pt for three main reasons: (i) biocompatibility and resistance to corrosion, (ii) pseudo- reference electrode behaviour, (iii) employment in the fabrication of resistive thermal devices with a linear range suitable to measure physiological temperatures [55]. Finally the metal passivation was made with Al_2O_3 which is a biocompatible material already used in biomedical coatings [56].

2.4.1 Sensor development

To achieve multi-panel metabolite detection, we can functionalize the five working electrodes to detect glucose, lactate, glutamate, benzphetamine, or aminopyrine, and cholesterol. Oxidases can be the probe for the first three compounds, while cytochromes are able to detect the other compounds (as already discussed in Table 2.2). Note that with the same agent (CYP2B4) it is possible to detect different compounds (benzphetamine and aminopyrine) at the same electrode, due to the fact that the two molecules oxidize at different voltage. The height of the two corresponding peaks gives information about their concentration. This is possible only if the target molecules give a current peak at different voltage locations which is usually the case. Exceptional examples are bupropion and lidocaine that have the same peak location at +450 mV

In addition to the sensor selectivity which should be provided when the sensor is operating in complex solutions (like plasma or interstitial fluid), metabolites biosensing present other challenges: (i) the electrochemical measures are affected by local pH and temperature [57], that need to be constantly monitored in order to obtain reliable data; (ii) concentration of target compounds in the body are often in the nano and micro molar range [58] and difficult to detect; To address this problem, the CNT are introduced to the sensor surface to improve the sensitivity and detection limit of sensors [59, 60] and proved effective in sensing physiological concentrations of analytes in human plasma [61]. Fig. 2.4 shows the conceptual sketch of a sensor incorporating the CNT to improve electron transfer between the chemical and the electrode.

2.4.2 Sensor calibration

According to the electrochemical theory, pH and temperature variations change the peak position in CV and, if not properly considered, can twist the results. In case of a solution with unknown substrates, this may lead to false-positives. Therefore, monitoring pH and temperature is required to guarantee precise electrochemical detection when multiple drugs are present in the sample. Moreover, it extends the applicability of the sensor to biological fluids with different pH and temperature levels like blood, urine and interstitial liquid. In particular for implantable applications, it is important to account for temporal variations in the host environment, like fever.

2.4. An example: biointerface of HEM-system

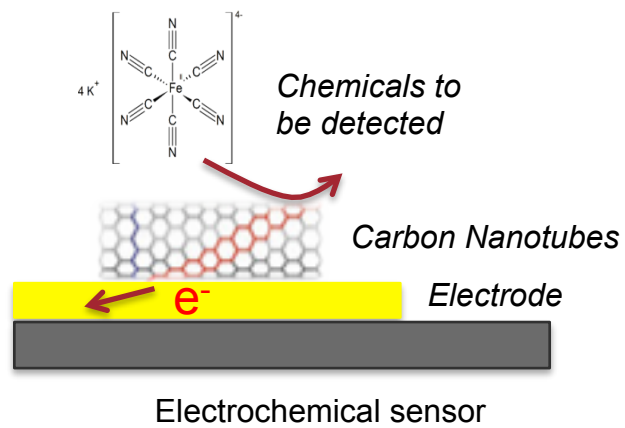


Figure 2.4: The introduction of CNTs on the electrode surface enhances the electron transfer between the chemical and the electrode surface.

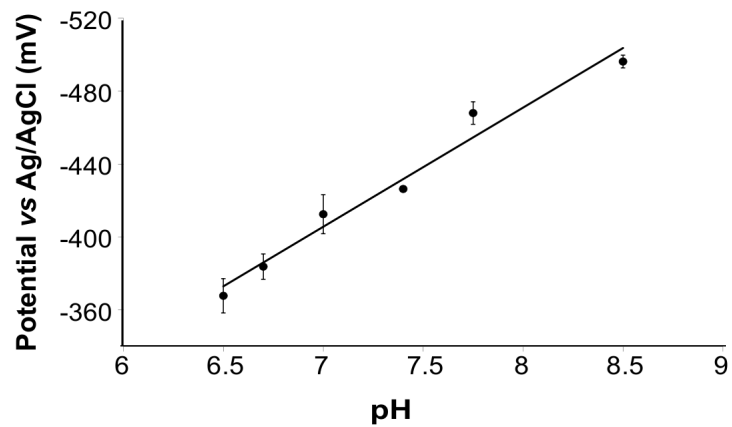


Figure 2.5: peak voltage shift with pH. Reprinted from [3].

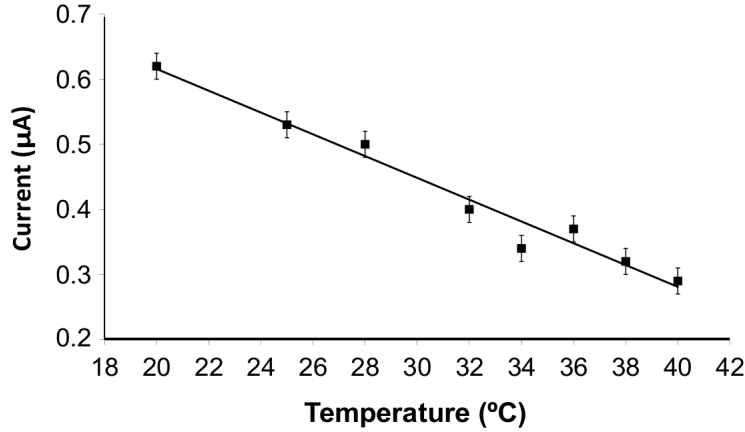


Figure 2.6: Peak current variation with temperatures. Error bars represent the inter-electrode variation. Reprinted from [3].

In order to see the effect of pH and temperature on the biosensor response, cyclic voltammograms of a CYP3A4 biosensor in PBS at different temperature and pH values were acquired [3]. Fig. 2.5 shows the peak voltage changes linearly with the pH. Such linear behaviour is explained by the Nernst equation [25]:

$$E = E_0 - \frac{RT}{nF} \ln\left(\frac{C_r}{C_0}\right) - \frac{RT}{F} pH \quad (2.9)$$

where E is the peak voltage, E_0 is the standard voltage, R is the gas constant, F is the Faraday constant, n is the number of electrons involved in the redox reaction, C_r and C_0 are the concentrations of the reduced and oxidized species at the interface, respectively.

Fig. 2.6 shows the effect of temperature on the peak current value. We can see that the current decreases by heating the sample. The relationship between the peak current and temperature is explained by the Randles-Sevcik equation [25]:

$$i \propto nFAD\left(\frac{nFvD}{RT}\right)^{1/2} C_r \quad (2.10)$$

where v is the scanning velocity, A is the working electrode area, and D is the diffusion coefficient, the equation shows an inverse relationship with the square of temperature, which is approximated by a linear curve for small windows in temperature.

As demonstrated by these experiments the biosensor response should be calibrated for the pH and temperature. To this aim a pH sensor and a temperature sensor are integrated into the HEM-biointerface. According to Fig. 2.6, to ensure a better than 1% accuracy in measuring

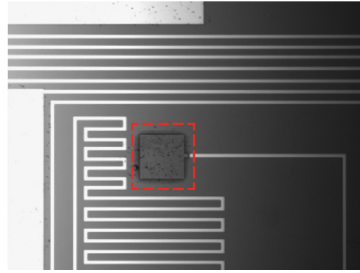


Figure 2.7: Photograph of the pH sensor coated with iridium oxide (red insert). Reprinted from [3].

the real peak voltage, pH variations as low as 0.06 units should be detected. On the other side, according to Fig. 2.6, to ensure a better than 1% accuracy in translating the sensor current into concentration, temperature variations as low as 0.2°C should be detected. These pH and temperature resolutions are also considered enough for accurate sensing of other metabolites with the Hem-biointerface.

Iridium oxide pH sensor

Iridium oxide is chosen as the pH sensing membrane over other pH-sensitive materials due to few reasons: (i) it provides a wide linear pH response range, with negligible interference of ions and complexing agents; (ii) It has a fast and stable response in aqueous, non-aqueous, non-conductive, and even corrosive media; (iii) it has a high conductivity, low temperature coefficient, and no requirement for pretreatment [62].

pH detection with IrO_x films is based on the reversible redox reduction of the Ir/IrO_2 couple, according to the relation described in [63]:



Differences in pH affect the stoichiometry of the equation and change the equilibrium potential of the Ir/IrO_2 couple. By monitoring the open circuit potential between the IrO_x electrode and the reference electrode it is therefore possible to sense the solution pH.

The pH sensor is realized with a platinum-electrode coated with a film of iridium oxide (see Fig. 2.7). Iridium oxide is deposited on the platinum electrode by evaporation [4]. It is a biocompatible material already used in the creation of implantable electrodes [64, 65]. The open circuit voltage between the iridium oxide film and a reference electrode changes linearly with the pH of the solution [66]. Fig. 2.8 shows the measured open circuit voltage decreases linearly with pH with a slope of $0.7 \mu\text{V}/(\text{pH unit} \cdot \mu\text{m}^2)$.

Pt-RTD temperature sensor

The temperature sensor consist of a platinum resistor (See Fig. 2.9) which is commonly used in the production of *resistive temperature detectors* (RTD). Among other metals commonly used for RTDs such as Cu and Ni, Pt was chosen because of its biocompatibility and higher

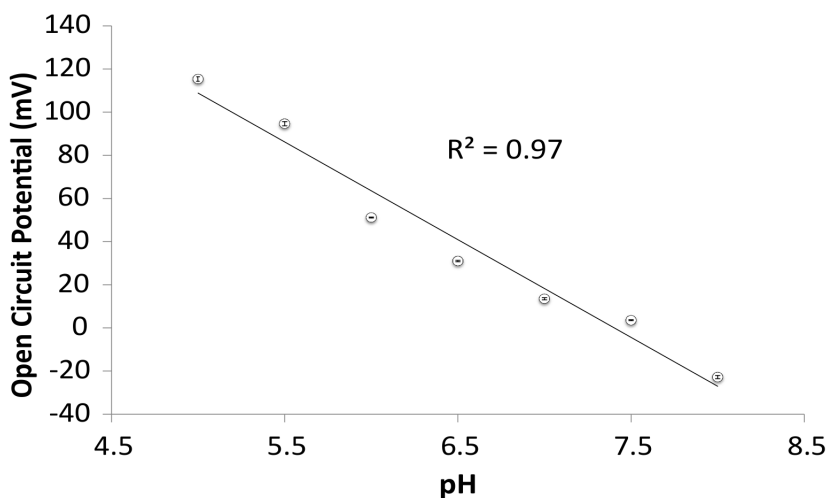


Figure 2.8: Open circuit voltage of the Iridium-oxide coated electrode to different solutions pH. Error bars are due to the instrument noise. Reprinted from [4].

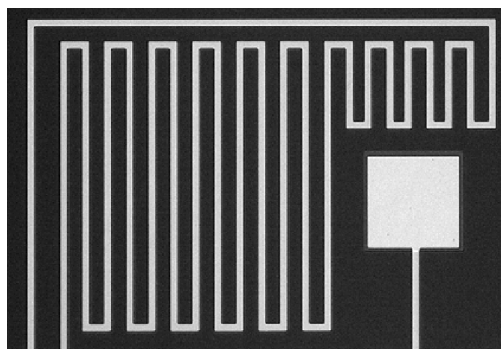


Figure 2.9: Photograph of the temperature sensor. Reprinted from [3]

metal resistivity, which allow to reduce the sensor dimensions [67].

2.4.3 Measurements

Table 2.3 resumes the main properties of each functionalized electrode. Regarding glucose and lactate detection, the values reported in the table are obtained with the PET-biointerface with the WEs nano-structured with CNTs and functionalized with glucose and lactate oxidases, respectively. Benzphetamine and aminopyrine are measured on rhodium graphite electrodes [46], while cholesterol onto CNT-based electrode [45].

With the presented configuration of the HEM-biointerface, it is necessary to employ a fixed or variable voltage generator, according to the functionalization of each electrode. We also need a multiplexer, which switches the readout circuit among different working electrodes. The readout electronics depends also on the type of functionalization. Oxidases produce a unidirectional current during CA while cytochrome p450 produces a bidirectional current

Table 2.3: Performance of different metabolite biosensors

Target	Probe	Sensitivity ($\mu\text{A}/(\text{mM cm}^2)$)	Limit of detection (μM)	Linear range (mM)
GLUCOSE	glucose oxidase	27300	17.5	0.5 - 3
LACTATE	lactate oxidase	322000	4.1	0.05 - 0.2
BENZPHETAMINE	CYP2B4	0.28	200	0.2 - 1.2 [46]
AMINOPYRINE		2.8	400	0.8 - 8 [46]
CHOLESTEROL	CYP11A1	112	—	0.01 - 0.08 [45]

during CV measurement. In Chapter 3, an overview is given on the integrated circuits designed to readout CV and CA over the last two decades. In chapter 4, two ICs for this purpose are presented that were designed within the context of this research.

2.5 Chapter summary

In this chapter different aspects for the development of a fully integrated platform for the detection of endogenous and exogenous metabolites for advanced diagnostics are presented. The electrochemical principles for oxidases and cytochromes are presented which are two enzyme families able to detect the majority of human metabolites. As an example of a sensing platform for multiple-metabolite detection, the biointerface of the HEM-system is described. The advantages of using CNTs in the sensor development were presented as well as the need for sensor calibration with pH and temperature.

3 Integrated electronics for electrochemical sensing: state-of-the-art

A simplified sketch of the readout electronics for an electrochemical amperometric sensor is shown in Fig. 3.1. The readout IC is expected to amplify the sensor current using a low-noise *trans-impedance amplifier* (TIA) and to digitize it through an analog to digital converter (ADC) before transmitting it outside, while it keeps the voltage of the sensor at a known value.

Several integrated circuits for electrochemical sensing have been reported in recent years. In this chapter, a review on the state-of-the-art of ICs for CV and CA measurement techniques is presented. They are categorized and the advantages and disadvantages of each category are discussed with respect to an autonomous multi-target sensing application. The few existing readout circuits for differential measurement are presented. To achieve an autonomous microsystem, the design of an integrated waveform generator for electrochemical stimulation in CV measurement is also discussed. Finally, a part is dedicated to the state-of-the-art circuit for resistance measurement. The resistance measurement circuit is required to readout the RTD in the IMD's biointerface for temperature monitoring.

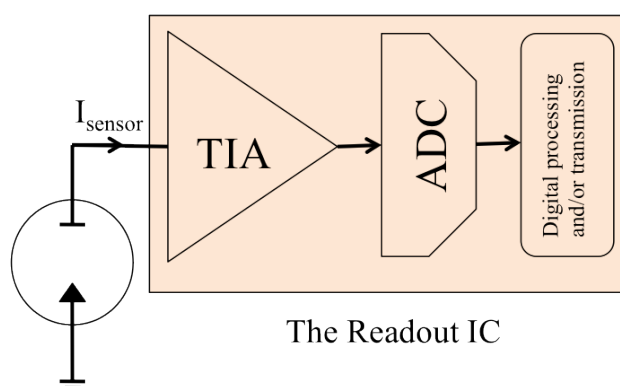


Figure 3.1: The conceptual diagram of a readout IC for amperometric electrochemical sensors.

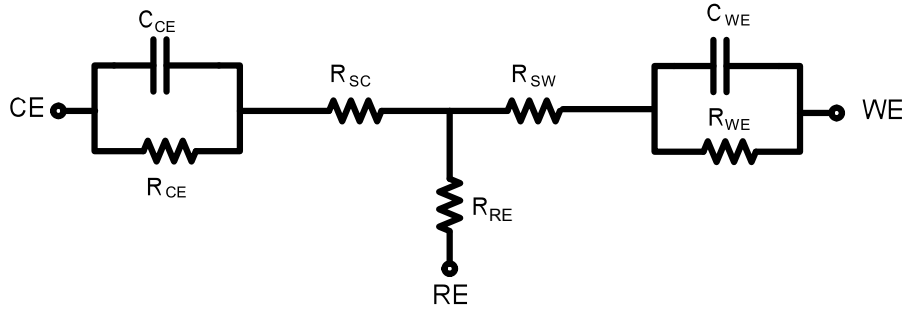


Figure 3.2: The RC-equivalent model of a three-electrode based electrochemical sensor used for circuit simulations

3.1 Electrochemical sensor model

To simulate the system behaviour and the stability of the readout IC when it is operated with the sensor, the small-signal circuit model of the electrode–electrolyte interfaces in an electrochemical cell is used [25]. Fig. 3.2 shows a generic small-signal equivalent circuit of an electrochemical cell. In this model R_{SC} and R_{SW} denote the solution resistance between the working and counter electrodes. The capacitances C_{WE} and C_{CE} model the double-layer capacitance at the WE-electrolyte interface and CE-electrolyte interface, respectively. Finally, the charge transfer resistance at the electrode-electrolyte interface are modelled by R_{WE} , R_{CE} , and R_{RE} .

The equivalent circuit of an electrochemical cell is more complex than that shown in Fig. 3.2 and can be found with electrochemical impedance spectroscopy (EIS) measurements. However, the circuit shown in Fig. 3.2 is a good starting point for hand calculation and simulation purposes.

3.2 Readout IC architecture: state-of-the-art

The readout ICs for amperometric electrochemical sensors are divided into two categories: (i) current-mode and (ii) voltage-mode circuits. The charge-mode circuits are here considered as a subset of voltage-mode circuits. The description of each category is presented in this section.

3.2.1 Current-mode circuits

A number of current mode designs for amperometric sensing applications have been reported [5, 68–74]. Among the current mode input front-ends, the simplest one is the *common-gate trans-impedance amplifier* (CGTIA) which is used in almost all reported current mode circuits as the first stage to keep a fixed voltage on WE while reading its current. The simplified structure of a CGTIA is shown in Fig. 3.3. The voltage V_{in} is applied to the WE and the current

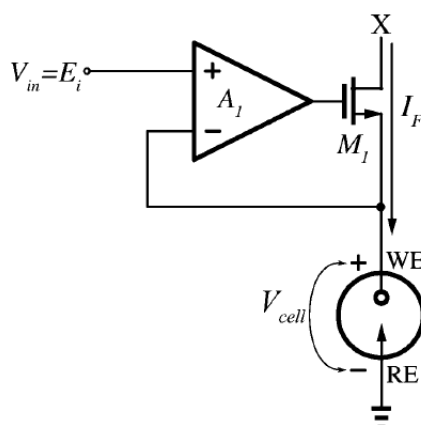


Figure 3.3: The simplified structure of a CGTIA. The voltage V_{in} is applied to the WE and the current flows through the transistor. The current at node X can be converted into digital or to voltage and then digital. Reprinted from [5].

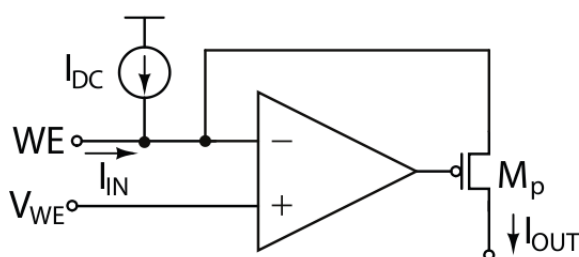


Figure 3.4: CGTIA with a DC offset current to allow bidirectional current measurement.

flows through the transistor M_I to the high impedance node X. From node X the current can be converted into voltage [69, 70, 72, 74], into frequency [5, 73], or into time [68].

The drawback of the CGTIA is the lack of bidirectional current support, which means that it can be used only for CA measurement and not for CV measurement. A solution to acquire a bidirectional current readout with CGTIA is to add a DC offset, I_{DC} , current to its input as shown in Fig. 3.4 [75, 76]. This requires high resolution in the subsequent ADC and adds noise to the redox current. Also, depending on the WE impedance, a portion of the DC offset current can leak into the electrochemical cell and disturb the measurement.

Fig. 3.5 shows the case which current is converted into frequency [5, 73]. A fixed voltage is applied to the three-electrode based sensor and the current goes through a current mirror where a copy of the current is generated and sent to a current starved ring oscillator [73] or a relaxation oscillator [5]. The resulted square waveform is directly used to back-scatter the data through load-modulation of the inductive link [5, 73], resulting is a simple circuit for data communication between the IC and an external reader or the test equipment (See Fig. 3.6) .

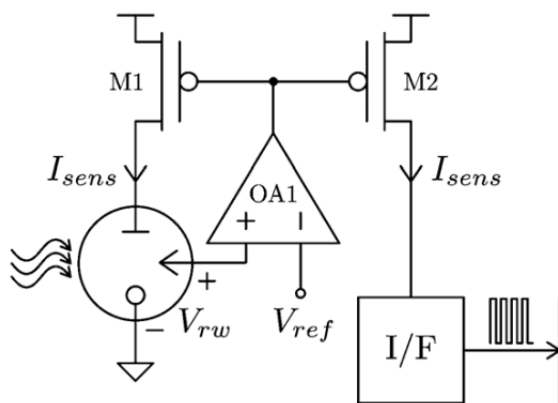


Figure 3.5: A CGTIA with a current to frequency converter. Reprinted from [6].

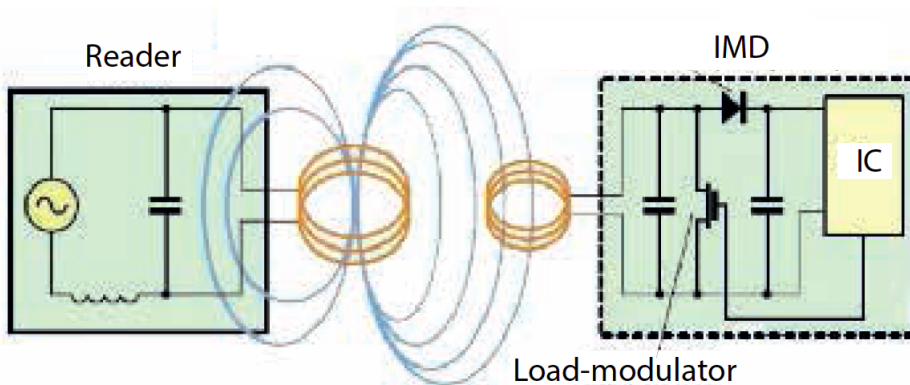


Figure 3.6: Backscattering can be simply implemented by a single NMOS to short-circuit the load of the powering-inductive-link for each bit in the chip output that is equal to “1”. The reader detects the modulated load and reconstructs the data.

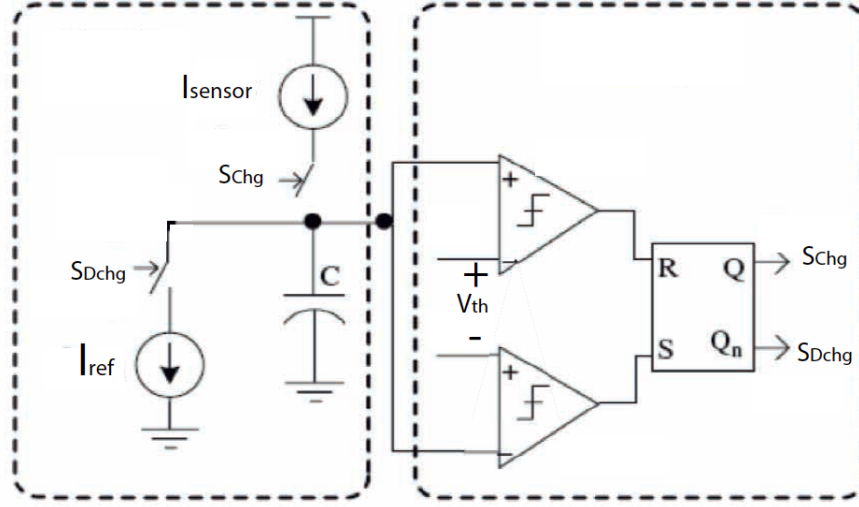


Figure 3.7: A relaxation oscillator to convert the sensor current into frequency.

The current-to-frequency-converter circuits are consuming minimum power among all the other types of current-mode or voltage-mode circuits. This is mainly due to the elimination of the ADC, and the fewer opamps in the circuit structure. However, the main drawback of converting the current into frequency is the limited achievable resolution at the measurement time with the test equipment (e.g. the oscilloscope). To show this, let us assume C_{osc} is the oscillator capacitance and I_{Sensor} is the sensor current we want to measure, and V_{th} is the threshold voltage of the relaxation oscillator (See Fig. 3.7). In order to measure the generated pulse-width in the receiving-end with a resolution of n bits, the sampling frequency of the measurement equipment must be:

$$f_{sampling} \geq \frac{T_{pulserelax.}}{2^n} = \frac{C_{osc} V_{th}}{I_{Sensor} 2^n} \quad (3.1)$$

There, $T_{pulserelax.}$ is the generated pulse-width at the output of the oscillator due to the sensor current I_{sensor} . This means that for example with 1 pF capacitor and 1 V threshold voltage, measuring $1 \text{ }\mu\text{A}$ current with 10-bit resolution, needs a measurement equipment with a sampling frequency of 1 GHz , which is beyond the operating frequency of test PCBs with usual micro-controllers. An alternative solution is to add a digital counter on-chip after the current to frequency converter. But the same sampling frequency is now needed on-chip to drive the counter. Although an on-chip oscillator can generate this frequency, it consumes high power. Moreover, this solution eliminates the simplicity of transmission which was the main advantage of this class of circuits.

Jafari et al [72] introduced a current-mode input-stage that allows bidirectional current acqui-

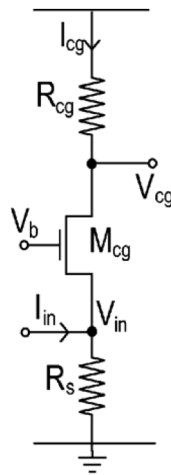


Figure 3.8: A CGTIA with a resistor in the path of the current. Reprinted from [7].

sition and validated it with CV measurement. However, they stimulated the sensor by applying an externally generated triangular waveform to the RE and kept the WE at a fixed voltage. This is fine for single metabolite measurement. But for multiple-target measurement (e.g. for HEM- and PET- IMDs) the RE needs to be fixed with respect to ground and the voltage at WEs vary to provide the required voltage profile for the detection of each individual metabolite.

Enz et al [7] proposed a “noise cancellation and chopper stabilization technique” for the CGTIA to enable low current acquisition and they manage to measure pA-range current. However, they presented CA measurements in which the control voltage is applied to the CE instead of the WE which is not a common practice in electrochemical sensing [25]. Moreover, the voltage of the WE changes with the sensor current, due to an immediate resistor in the path of the current (See Fig. 3.8) which affects the linearity of the measurements.

$\Sigma\Delta$ modulator based circuits

Another class of current mode readout circuits are presented in literature that directly digitize the current through current mode [6, 77], or voltage mode [78, 79] $\Sigma\Delta$ ADCs. The main advantage of this class of readout circuits is wide input dynamic-range [77–79].

While the circuits in [78, 79] detect a wide input dynamic-range, they allow only fixed control voltage (i.e. only CA measurement). The same is true for the voltage-mode ADC in [6]. Moreover, the circuit presented in [6] requires to be disconnected from the sensor for a portion of each clock period which may cause instability problem for the measurement with enzymes [25]. Roham et al [77] presented a current-input $\Sigma\Delta$ ADC enabling both CA and fast-scan CV. However, they do not comment on sensor calibration.

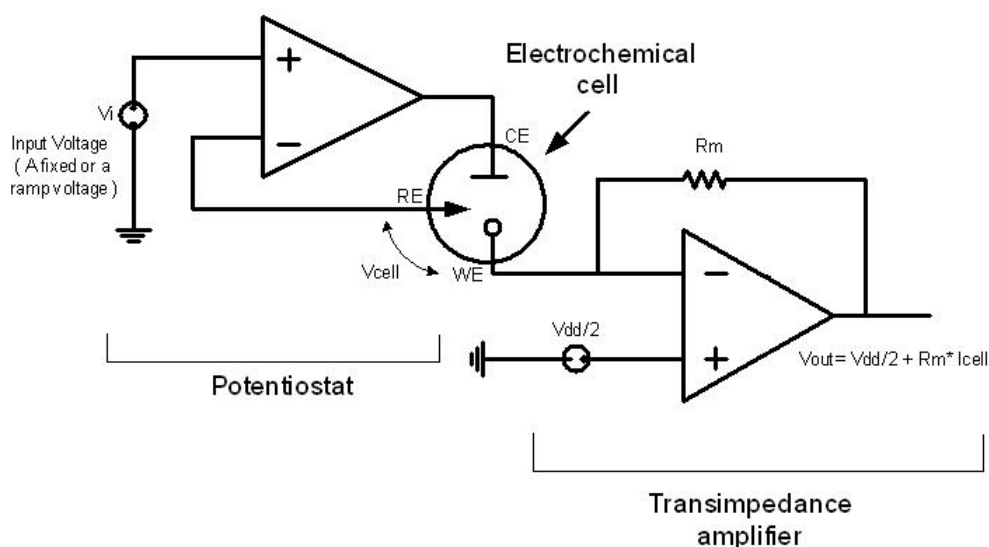


Figure 3.9: A voltage mode readout circuit based on resistive-feedback TIA. The circuit enables both CV and CA control and readout. Reprinted from [8].

3.2.2 Voltage-mode circuits

The use of voltage-mode circuits is the most common approach to redox current acquisition [9, 72, 80–84]. In this approach the TIA sets a virtual voltage at the working electrode and at the same time generates an output voltage that is proportional to the redox current (See Fig. 3.9). This can be implemented by a resistive feedback TIA [10, 84–89] or a *switched-capacitor* (SC)-integrator [9, 72, 80–83]. An SC-integrator is shown in Fig. 3.10 where the charge accumulates on the capacitor and discharges through the switch driven by a clock. The SC TIA configuration is a common choice for arrayed implementations.

A possible configuration for the readout IC based on SC-integrator is shown in Fig. 3.11 and works as follow. The SC-integrator converts the biosensor current response into voltage, which then goes through a programmable gain amplifier (PGA). The PGA can be implemented using a capacitor array. The output of the PGA is sampled, held, and fed to an analog-to-digital converter (ADC). The entire readout chain utilizes the correlated double sampling (CDS) technique to reduce $1/f$ noise, offset, and non-ideal effect inherent to CMOS amplifiers.

However, the effect of switching noise on the sensor is not completely known. For a thorough understanding of this effect, time- and frequency- domain simulations have to be done with the complete model of the sensors based on impedance spectroscopy. For a multi-target sensor in our application such model does not exist yet. Therefore, a resistive feedback TIA is chosen for CV control and readout in both LOPHIC and ARIC. Table 3.1 summarized the functionalities and key specifications of the state-of-the-art ICs for amperometric electrochemical sensing. Only the ICs that provide both CV and CA measurements are presented in this table.

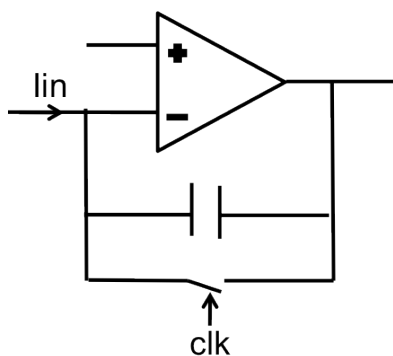


Figure 3.10: The switched-capacitor current integrator to convert the bidirectional input current into voltage. The capacitor is reset in every clock cycle. Φ_1 , Φ_2 , and Φ_3 are non overlapping clocks. V_{ref2} is applied to the WE through OP1 to stimulate the sensor for CA or CV measurements. OP_2 , C_3 and the capacitor array for the PGA.

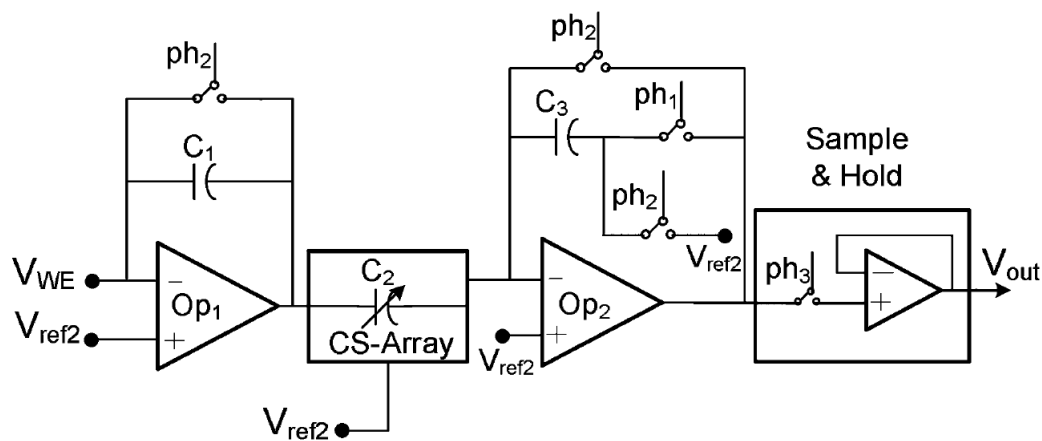


Figure 3.11: A typical switched-capacitor readout chain consists of an integrator followed by a PGA followed by a sample and hold. Reprinted from [9].

3.2. Readout IC architecture: state-of-the-art

Table 3.1: Comparison of state-of-the-art ICs for amperometric electrochemical measurement

	ARIC	LOPHIC	[9]	[72]	[81]	[6]
CV/CA readout	Yes	Yes	Yes	Yes	Yes	Yes
Digital output	Yes	Yes(CA)/No(CV)	Yes	Yes	Yes	Yes
Waveform generator	Yes	Yes	Yes	Yes	No	No
Calibration with pH	Yes	No	No	Yes	No	No
Calibration with Temperature	Yes	No	No	No	No	No
Technology (μm)	0.18	0.18	0.5	0.13	0.25	2.5
Power (μW)	933	220	22500	1150	NA	24
Linear current range (μA)	± 1.7	± 1	± 47	± 0.35	± 0.25	± 2.5
Input dynamic range (dB)	48	46	99	93	54	60

3.2.3 Differential readout circuits

Few differential readout ICs for multi-channel recording to remove the large background current from the measurements have been reported [90–92]. An IC with pseudo-differential architecture is presented in [90] which is not fully-integrated as it needs external loads and off-chip control signals. A differential IC for amperometric DNA detection is presented in [91] in which the charge generated at the electrodes is converted into analog voltages. However, the current of the two electrodes are sampled at different phases of the clock. Moreover, differences of the output voltages is calculated off-chip as well as the generation of the stimulating triangular waveform for the CV.

In [92] a circuit is proposed for fully-differential measurement through two WEs with a SC-integrator. However, the authors did not present any simulation or measurement for a real differential measurement. Indeed, re-simulated the circuit and learned about a problems of the circuit in [92]: The proposed differential TIA can not provide two currents (i.e. to feed the two differential sensors) with same direction (i.e. sign) at its differential outputs, simultaneously. Therefore, since both input currents have the same direction, they can not be measured at the same time by that circuit. The pros and cons of each circuit are summarized in Table 3.2.

Within the context of this research, DIRIC is designed which is a pseudo-differential circuit to measure the redox current and remove the background current from the sensor current. The circuit consists of two SC-integrators to convert the input current from two WEs into voltage. The voltages are sent to a difference amplifier with a unity gain and then to a programmable gain amplifier (PGA) with a digitally programmable on-chip gain. The output of the PGA is sampled and held and then fed to an analog-to-digital converter (ADC). The IC enables wide-dynamic-range current acquisition thanks to the CDS method, as well as background current elimination thanks to differential measurement scheme. DIRIC is the first readout IC that is fully-integrated, samples the differential input current at the same time, and provide a digital output that corresponds only with the redox current.

Table 3.2: Comparison of state-of-the-art ICs for differential current measurement

Paper	Pros	Cons
[90]	Programmable	Pseudo-differential; external components and signals needed
[91]	compact; fully-differential	output is analog; inputs are sampled at different time
[92]	Digital output	IC is not simulated nor measured in differential mode

3.3 Waveform generator

A waveform generator is an important component of an autonomous electrochemical instrumentation system that requires different input waveforms for different voltammetry techniques. A multi-mode waveform generator is desired to produce signals of various shapes, amplitudes (scan range) and frequencies (scan rates). Programmable analog circuits could be constructed to generate continuous waveforms, but different analog circuits would be needed for each desired signal shape (triangle, sawtooth, etc.) with an undesirable impact on power consumption and chip size. In particular, for CV, it is important to generate a high amplitude sub-Hertz triangular waveform for the transducer. The usual method to charge and discharge a capacitor with a fixed current is not applicable, because the desired frequency requires too large capacitors.

In this thesis a *direct digital synthesizer* (DDS) is designed to generate sub-Hertz triangular waveforms. DDS is a mixed-mode circuit consisting of a DAC a digital controller to implement all shapes and generates a quantized output. The DDS is integrated into LOPHIC and generates sub-Hertz triangular waveform to control the sensor in CV measurement. The only on-chip sub-Hertz waveform generators in literature are reported in [77] which consumes 28 times more power; and in [9] which is indeed published after this research and the power consumption is not reported. The pros and cons of each circuit with respect to waveform generation needs in multi-target IMD application (described in Chapter 2) are summarized in Table 3.3.

The DDS in ARIC is further improved to generates different voltage profiles at the same time to control the WEs in CV, CA, conditioning, etc.

3.4 Integrated electronics for resistor measurement

According to the discussion in Section 2.4.2, the sensor calibration necessitates the use of a single off-chip *resistor temperature detector* (RTD) to accurately monitor the temperature of

3.4. Integrated electronics for resistor measurement

Table 3.3: Comparison of state-of-the-art ICs for low-frequency waveform generation

Paper	Pros	Cons
[77]	programmable	high scan rates (100 V/s); high power consumption (99 μW)
[9]	low voltage steps (2 mV)	power is not-reported; limited peak-to-peak voltage $0.4 \times V_{DD}$

the biointerface, and a fully-integrated circuit to readout the RTD.

So far RTDs have been used within two categories: (i) to measure the temperature of the environment, in particular non-accessible places like a dam or an oil well [93–97]; In this category, a common method for RTD measurement is to generate a constant current source and convert the resistor into voltage. This has been adopted in literature using off-the-shelf components [93–97]. (ii) to measure the temperature of the chip to monitor it or to calibrate the clock generator or other circuit blocks with it [98–101].

The sensor described in [98] employs a bridge consisting of a temperature-dependent resistor and an adjustable reference resistor. The latter is actually a switched capacitor resistor, whose resistance can be controlled via its switching frequency. A feedback loop balances the bridge by adjusting the switching frequency via a fractional-N divider, whose division ratio is then a measure of temperature. The circuit achieves 0.1 mK but it consumes 13 mW.

In [99, 100] fully integrated circuits are presented to readout the phase shift of a Wien-bridge filter. The Wien filter consists of three on-chip resistors and few capacitors and shows a linear phase shift due to the temperature dependency of the resistors used. This phase shift is then digitized by a phase domain sigma-delta modulator. The method could be adjusted for our application by replacing the three on-chip RTDs with off-chip RTDs. However, this requires four more connections between the biointerface and the IC which is not desirable.

In [101], a temperature-dependent current generated by an on-chip n-well resistor is used to drive a ring oscillator, resulting in a temperature-dependent output frequency. This results in an equivalent resolution of 40 mK in a 7.5 msec conversion time with a base clock frequency of 1 MHz, while consuming 30 μW . This is the only IC among the second category mentioned above that can be modified to be used with a single off-chip RTD. However, it does not match with the design of the readout ICs. The pros and cons of each circuit with respect to temperature sensing needs in the IMD application (described in Chapter 2) are summarized in Table 3.4.

In Chapter 5, two integrated circuits are presented for off-chip RTD measurement that match with the resources and the architecture of ARIC. In particular a circuit is proposed that gives

Table 3.4: Comparison of state-of-the-art circuits for resistor measurement

Paper	Pros	Cons
[98]	high resolution (0.1 <i>mK</i>)	high power (13 <i>mW</i>)
[99, 100]	low power (36 μW); high resolution (2.8 <i>mK</i>)	based on three RTDs
[101]	low power (30 μW); high resolution (40 <i>mK</i>)	based on on-chip RTD

an equivalent resolution of 10 *mK* which outperforms the circuit in [101].

3.5 Chapter summary and conclusions

For an autonomous microsystem, the CMOS chip includes all necessary electronics and a communication interface to allow user control of measurement operations and reporting of measurement results. For the multi-function amperometric instrumentation chip, this requires an IC to control the sensor, a multi-function waveform generator to produce the stimulus signals necessary for different techniques, a highly sensitive amperometric readout circuit to measure the current resulting from the stimulus voltage, and a temperature and pH readout circuit to enable sensor calibration.

However, today's state-of-the-art integrated circuits for electrochemical detection still suffer from the lack of autonomy and the limited chemical specificity in a complex biological matrix (i.e. multiple metabolite detection), hindering their use for health-care monitoring studies.

The main objective of this research is to develop fully integrated and autonomous ICs for an autonomous microsystem that can precisely and continuously monitor the health-care and enable personalized therapy through the measurement of multiple-metabolites. To this aim, three ICs are presented: LOPHIC, ARIC in Chapter 4 and DIRIC in Chapter 9.

LOPHIC enables multiple measurements with a fully on-chip waveform generator to provide ULF waveforms to stimulate CV and CA measurements. A current to frequency converter is realized to output the data for CA measurement.

ARIC - to the best of our knowledge- is the first complete and integrated realization to support multiple molecular measurements and it addresses several challenges, including, but not limited to, low-power, low-noise realization, slow electrostatic control (to match molecular dynamics) small current sensing, programmability, and sensor calibration.

DIRIC is the first implementation of fully-integrated differential readout that samples the inputs at the same time and gives a digital output proportional to the redox current.

4 ASICs to control and readout amperometric and potentiometric sensors

The construction of a biosensor requires the integration of two main building blocks: (i) a sensor array to detect and measure the target compounds, (ii) interface electronics to control and readout the biosensor. For the portable, point of care, and implantable applications, the biosensor is desired to be fully-integrated and low-power. Moreover, to be small to be minimally invasive.

Moreover, the biosensing device should be able to detect a specific group of key metabolites within a single platform, to accurately monitor the health condition of the patient and to enable personalized therapy. Endogenous molecules (e.g., glucose, lactate, ATP) and exogenous molecules (e.g. drugs) are among the most important biomolecules to be monitored. *Chronoamperometry* (CA) and *cyclic voltammetry* (CV) are two commonly-used electrochemical detection techniques for both endogenous and exogenous molecules [25]. CA and CV measure the current of the sensor when a fixed or variable voltage is applied to the sensor, respectively. The readout of the current and the control of the voltage have to be carried out by the interface electronics.

The interface IC has to address several challenges, including, but not limited to, low-power, low-noise, high accuracy realization, slow electrostatic control (to match molecular dynamics), and small current sensing. In particular, for CV, it is required to generate a high amplitude sub-Hertz triangular waveform to control the transducer. Moreover, as discussed in Chapter 3, monitoring of environmental variables such as pH and temperature is essential for calibrating the biosensors. Thus the interface IC has to enable the measurement of pH and temperature as well.

In this chapter two sub-mW fully-integrated implementations of CA and CV control and readout are presented. Both ICs support CA and CV measurements for biosensor arrays with up to five sensing sites. In the following section a *low-power hybrid IC* (LOPHIC) is described in which a current to frequency converter is implemented for CA readout and a *transimpedance amplifier* (TIA) performs CV readout. The second IC is the *autonomous reconfigurable IC* (ARIC) that uses a universal circuit to perform CA, CV and potentiometry measurements.

ARIC is autonomous and reconfigurable through a serial command line. To reduce the power consumption of the ICs techniques such as block sharing and clock gating are utilized. The electrical and electrochemical measurements are presented for each circuit.

4.1 LOPHIC to readout amperometric sensors

In this section LOPHIC is described that supports both CA and CV for a biosensor array with five sensing sites. In this IC a mixed-mode circuit block generates sub-Hertz triangular waveform for the transducer by means of a *direct digital synthesizer* (DDS) to control CV. The CV readout circuit applies the triangular waveform to the WE of interest and reads the bidirectional sensor current at the same WE. A current to pulse-width converter is realized to output the data for CA measurement directly in digital form.

LOPHIC has been implemented in 0.18 μm technology and successfully tested. The architecture of LOPHIC is described in the following section. A micro-fabricated sensing platform is used to test it for electrochemical measurements. CA and CV measurements acquired with the fabricated LOPHIC are then presented. The results are compared with the commercial equipment in terms of sensitivity, linearity, and limit of detection.

4.1.1 Circuit architecture

LOPHIC consists of four main parts: (i) sub-Hertz triangular waveform generator; (ii) CV readout; (iii) CA readout; (iv) potentiostat. Fig. 4.1 shows different parts of LOPHIC. LOPHIC interfaces two sensors for CV measurement and three sensors for CA. This is because we detect five molecules with our platform: glucose, lactate, ATP, and two anti-cancer drugs: Etoposide and Mitoxantrone. The first three molecules in this list are measured by CA and the last two by CV [10, 102]. A multiplexer is used to select the sensor and the readout type.

Two different circuits for CV and CA are designed in LOPHIC because of the following reasons. The CA current is unidirectional while CV current is bidirectional. Moreover the direction of CV current does not always agree with the applied voltage. For a positive applied voltage, the current might be negative. Therefore, the current to frequency converter can be used only for CA readout, and not for CV. But the CV readout circuit can be used (potentially) for both CA and CV. Nevertheless the CA readout circuit is kept because it provides a digital output while consuming only 63 μW . On the other hand, CV readout consumes 117 μW and still needs an ADC (to implement the communication with outside the implantable). The other benefit of having a separate CA readout circuit is that the CV readout can be shut down while doing CA readout to save energy and vice versa.

4.1. LOPHIC to readout amperometric sensors

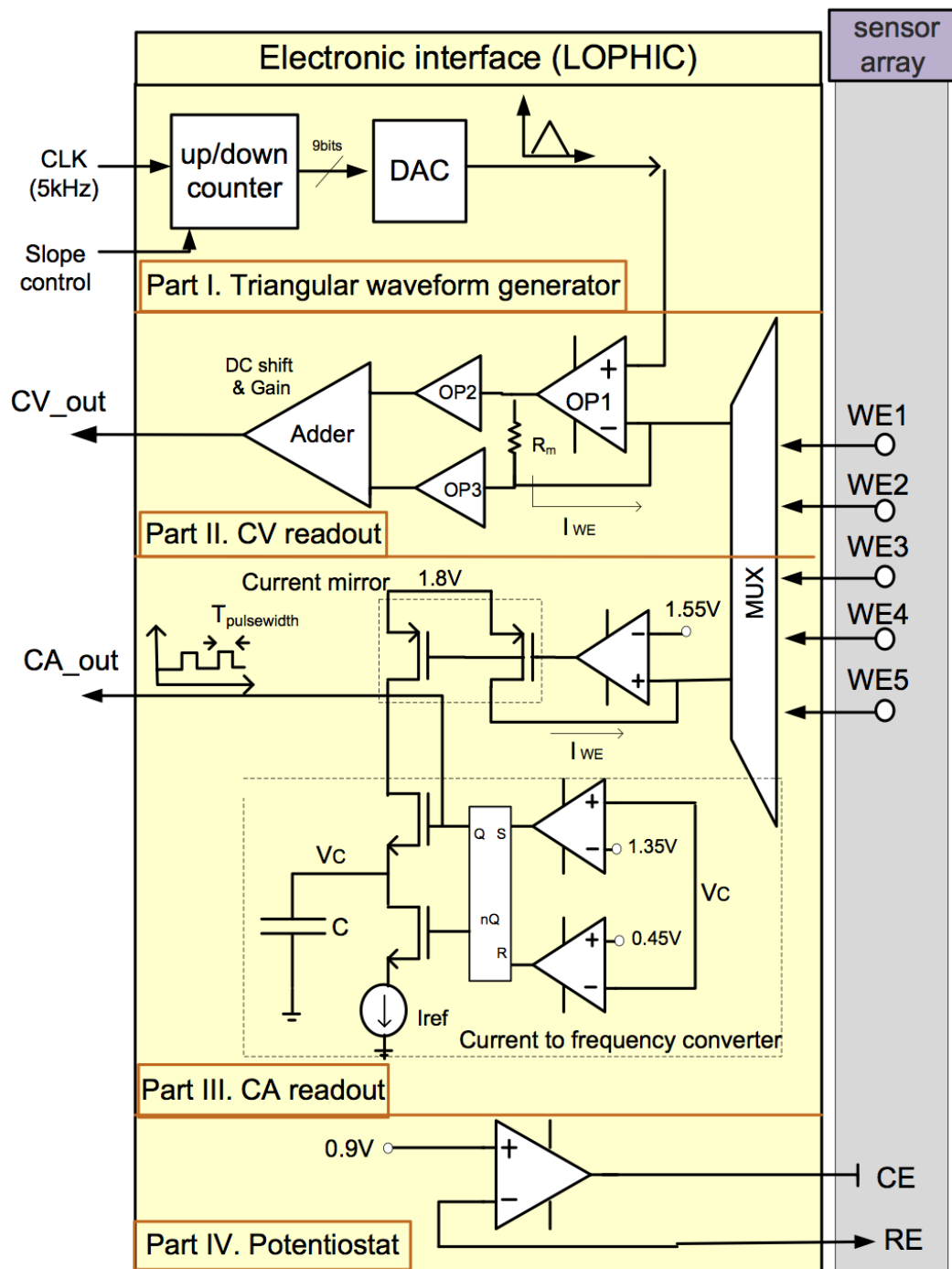


Figure 4.1: Schematic view of LOPHIC. It consists of four main circuits: waveform generator, CA readout, CV readout, and potentiostat. Reprinted from [10].

Triangular waveform generator

A fully-on-chip DDS is designed to generate sub-Hertz triangular waveform from a 5 kHz clock frequency. The DDS is realized by mixed-mode design methods. Generally a DDS waveform generator includes a numerically controlled oscillator and a digital to analog converter (DAC) (see part I in Fig. 4.1). The former produces at its output a discrete-time, quantized version of the desired output waveform whose period is controlled by the digital word contained in the frequency-control-register (FCR). The sampled, digital waveform is converted to an analog waveform by the DAC. Fig. 4.2 shows the block diagram of DDS designed to generate the triangular waveform.

An addition/subtraction block is used to add/subtract the FCR to/from the accumulator in every clock pulse. The FCR value determines the slope of the ramp. The FCR size and also the add/sub number of bits are carefully designed to provide different scan rates with different ramp slopes.

We chose the clock frequency to be 5kHz and considered 4 steps in the given scan rate of 10 to 100 mV/s to cover the needs in different voltammetric measurements. The sizes of the register and add/sub block are 14 bits. Add/Sub block is realized using 14 full adders. The control unit is designed to generate the signals that are required for changing the operation from addition to subtraction and vice versa, to provide the positive and negative slopes of the triangular wave.

The M (here is equal to 9) most significant bits of the counter are converted into analog voltage by the DAC. The DAC is implemented by a resistor ladder scheme. To provide different slopes needed for electrochemical sensor conditioning and measurement, the waveform generator is designed to be configurable. The conditioning is a process in which the sensor is prepared for the measurement through applying a voltage on it. The sensor conditioning is necessary to ensure that the baseline current (i.e. zero concentration of the target analyte) is settled to a fixed value prior to the measurement. The applied voltage during conditioning and the conditioning time depend on the type of the sensor and the measurement to be done afterwards. For example for a chronoamperometry on the glucose sensor described in this chapter, a fixed voltage of +650 mV is applied to the sensor for almost one hour to stabilize the sensor.

CV readout

To control the sensor in CV mode, a fixed voltage at $V_{DD}/2$ is applied to the RE through the potentiostat while the triangular waveform is applied to the WE. Therefore, the cell voltage ($V_{WE} - V_{RE}$) sweeps both negative and positive voltages. The bidirectional sensor current, I_{WE} , is read through a TIA as shown in part II of Fig. 4.1. OP_1 applies the triangular waveform to the WE selected by the multiplexer and the resulted current flows through R_m . OP_1 is a folded cascode with NMOS and PMOS input stage and class-A output stage as shown in Fig. 4.3. Indeed, Folded cascode structure is chosen for the first stage of all opamps in both LOPHIC and ARIC because of it has high gain, which is also desirable for good noise performance; Can

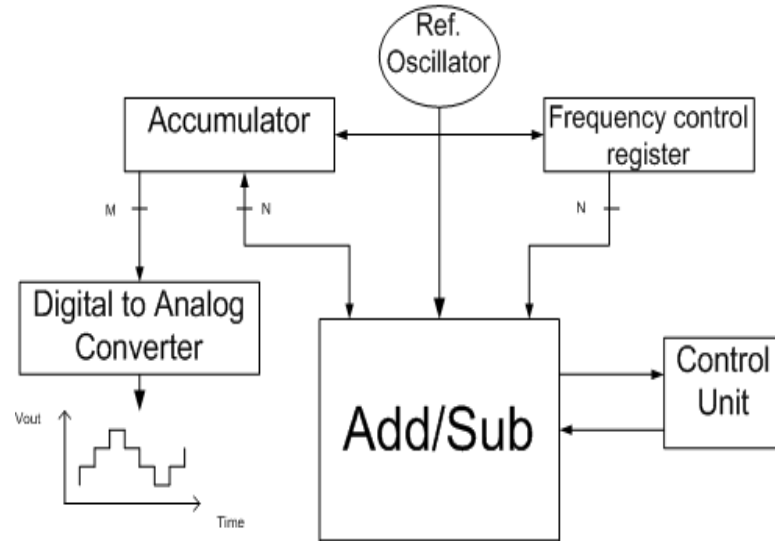


Figure 4.2: The block diagram of the triangular waveform generator in LOPHIC. Reprinted from [2].

cascade an output stage to get extremely high gain with lower output resistance; Has wide input dynamic range and can be used as a buffer with rail-to-rail input; Has good PSRR, which is necessary for implantable applications where power is transferred to the IMD wireless and hence the ground is not so robust.

Its gain, $-3dB$ bandwidth, power consumption and phase margin are $70 dB$, $100 Hz$, $28 \mu W$, and 75° (for load capacitance of $1 nF$), respectively. The load of OP_1 is the electrochemical sensor. Since the RC-equivalent model of an electrochemical sensor is time and concentration dependent [25], OP_1 is compensated using the method in [103] to have a phase margin of higher than 45° for any load capacitance larger than $100 pF$.

The voltage across R_m is buffered through OP_2 and OP_3 . The last stage in CV readout circuit is a common difference amplifier, *Adder*, shown in Fig. 4.4. It consists of OP_4 which is designed similar to OP_1 , and poly resistors with low temperature coefficient. This block amplifies the buffered voltage across the resistor R_m , and adds a DC voltage of $\frac{V_{DD}}{2}$ to it so that its output stays within the supply voltage range. The output voltage of the CV readout is:

$$V_{CV_{out}} = G \times R_m \times I_{WE} + V_{shift} \quad (4.1)$$

where G and V_{shift} are the gain and DC shift voltage by the last stage in CV readout, respectively. G is equal to 10 and V_{shift} is $V_{DD}/2$.

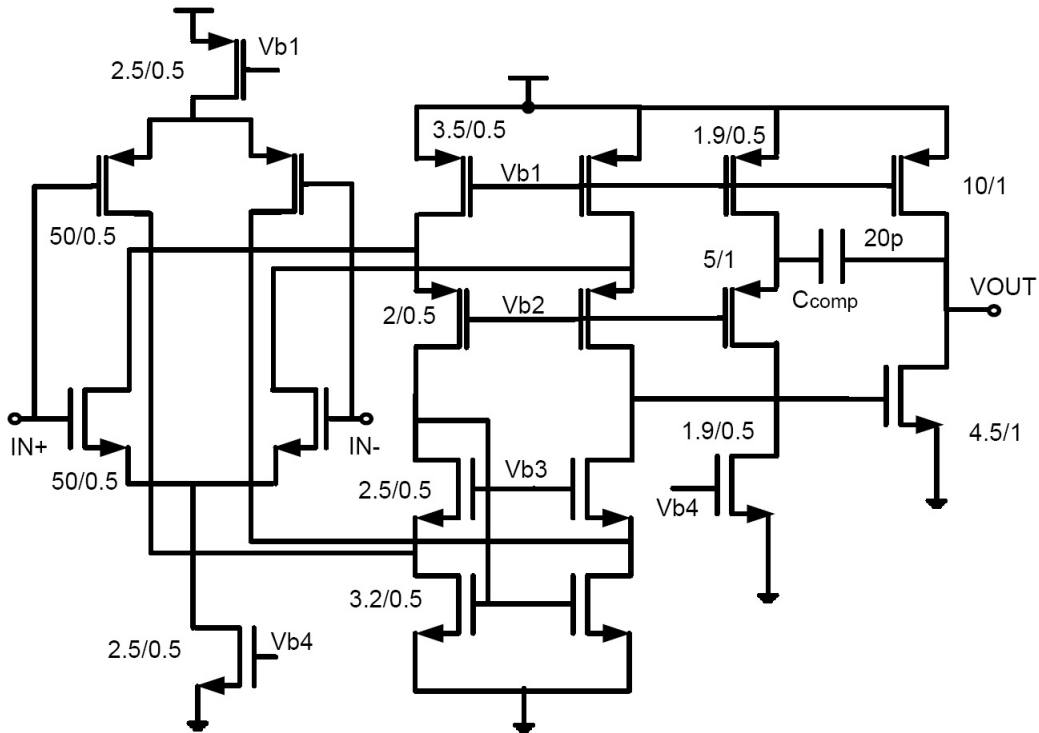


Figure 4.3: Schematic view of two-stage opamp with NMOS and PMOS input stages, and a class-A output stage, compensated for a wide range of load capacitance. This structure is used for both OP_1 and potentiostat in Fig. 4.1. Reprinted from [10].

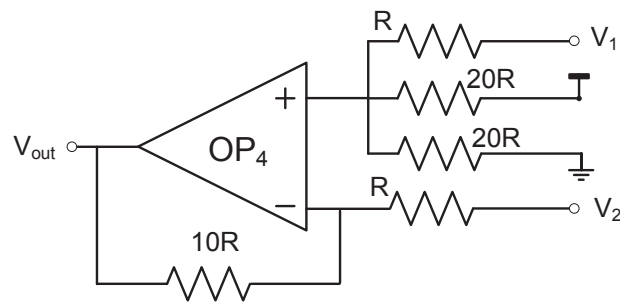


Figure 4.4: Schematic view of the *Adder*, the last stage of the CV readout circuit. It consists of OP_4 and poly resistors. It amplifies the difference between V_1 and V_2 by a factor of 10 and shifts the resulted voltage up by $V_{DD}/2$.

4.1. LOPHIC to readout amperometric sensors

Table 4.1: Power consumption of different blocks of the IC form simulations.

<i>Block name</i>	<i>Power consumption (μW)</i>
Waveform generator	3.5
CV readout	117
CA readout	63
Potentiostat	36.5
Total	220

CA readout

In CA, a fixed voltage is applied to the sensor and the resulted unidirectional current is measured. The circuit for CA measurement is shown in part III of Fig. 4.1. It consists of two main blocks: (i) a circuit to apply a fixed voltage to the WE and current mirrors to generate a copy of the sensor current; (ii) a current to pulse-width converter similar to [5]. The pulse width is inversely proportional to the sensor current and can be calculated by:

$$T_{pulse-width} = \frac{C(V_1 - V_2)}{I_{WE}} \quad (4.2)$$

where V_1 and V_2 are the threshold voltages of the comparators in the current to frequency converter in Fig. 4.1 part III which are $3V_{DD}/4$ and $V_{DD}/4$, respectively

The CA readout circuit converts the sensor current into a digital waveform which can easily be transmitted outside the implantable (e.g. by backscattering) without any need to an ADC. However, as discussed in Chapter 3 it suffers from a limited dynamic range. This problem became clear to us only after the measurement of LOPHIC.

Potentiostat

The potentiostat applies a fixed voltage to the RE using a negative feedback around RE and CE and provides current for the CE (See part IV in Fig. 4.1). The implemented potentiostat is a two stage folded-cascode amplifier with class-A second stage. It is compensated using the method in [103] and its phase margin remains greater than 45° for any load capacitance higher than $400 pF$. The gain, $-3dB$ bandwidth, and power consumption of the potentiostat are $65 dB$, $175 Hz$, $37 \mu W$, respectively.

4.1.2 Electrical measurement

LOPHIC is fabricated in $0.18 \mu m$ technology. Its layout is shown in Fig. 4.5. It measures $3.2 \times 1.5 mm$ and consumes $220 \mu W$ power from $1.8 V$ supply voltage. The power consumption of different blocks are reported in Table 4.1.

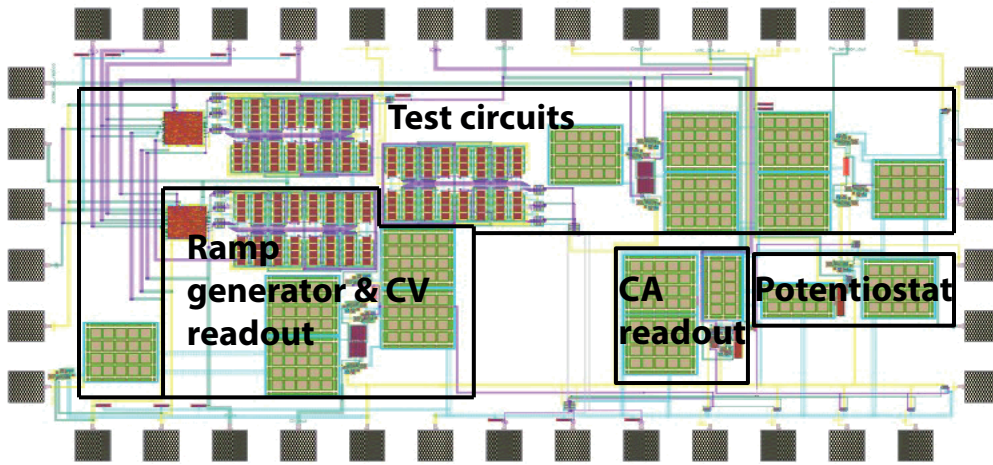


Figure 4.5: Layout of LOPHIC in $0.18 \mu m$ technology. Reprinted from [10].

Table 4.2: Measured specifications of LOPHIC

<i>Parameter</i>	<i>Value</i>
Input current range	$\pm 1 \mu A$
Input current dynamic range	46 dB
Triangular voltage step size	3.2 mV
Triangular voltage range (min-max)	0.2 V – 1.6 V
Triangular voltage slope	15 mV/s to 130 V/s
Input Clock frequency	5 kHz
Technology	0.18 μm
Supply voltage	1.8 V
Total power consumption	0.22 mW
Active area	1.225 mm ²

The measured sub-Hertz triangular waveform generated by the on-chip waveform generator is shown in Fig. 4.6. The slope of the triangular waveform is adjustable to 64 different values from 15 mV/s (Fig. 4.6) to 130 V/s to address different needs in sensor measurement and conditioning. The measured maximum, minimum and the step size of the triangular waveform are 1.6 V, 0.2 V and 3.2 mV, respectively and are independent from the slope of the triangular waveform. To ensure linear operation of the OP_1 and subsequently sharp edges in the triangular waveform, the digital counter is given a fixed offset of 0.2 V from the ground and V_{DD} rails.

CA readout circuit is tested by applying a current between 40 nA and 1 μA to the WE connected to the circuit and a reference current (I_{ref} in Fig. 4.1) of 1.93 μA . The resulted pulse-width is measured, using a Tektronix TDS2014B digital oscilloscope, for different input currents. The inverse of the pulse-width versus the input current is plotted in Fig. 4.7A. The measurements show excellent linearity in sub- μA current range.

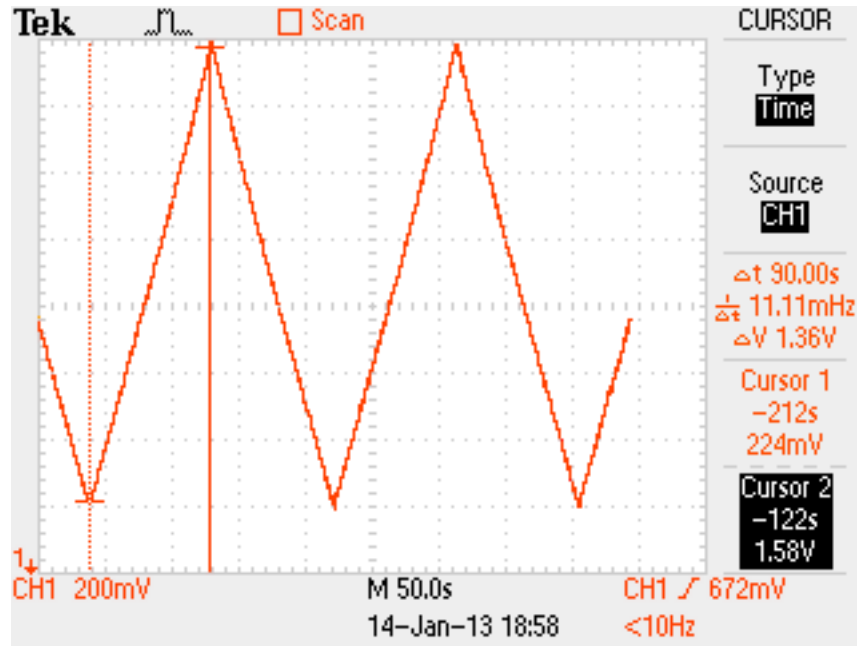


Figure 4.6: The measured sub-Hertz triangular waveform to control the sensor in CV by the on-chip waveform generator. Its min, max and frequency are 0.2 V, 1.6 V, and 5.5 mHz, respectively. Reprinted from [10].

In order to test the CV readout circuit, the internally generated triangular waveform with the slope of 130 V/s is applied to the positive terminal of OP_1 , while the negative terminal of OP_1 (*i.e.* WE) is connected to a resistor R_{test} . The other terminal of R_{test} is connected to CE terminal of the potentiostat, while the potentiostat is connected as a unity gain buffer (*i.e.* RE and CE are short connected) and a voltage of $V_{DD}/2$ is applied to its positive terminal. Therefore the input current of the CV readout circuit can be calculated by:

$$I_{res} = \frac{V_{ramp} - V_{DD}/2}{R_{test}} \quad (4.3)$$

The measured voltage at the output of CV readout circuit is plotted versus the input current in Fig. 4.7B for a R_{test} of 987 k Ω . The measured characteristics of LOPHIC are summarized in Table 4.2.

4.1.3 Electrochemical measurement

The fabricated circuit is electrochemically tested with the sensor array described in Chapter 2 (Section 2.4) and re-sketched in Fig. 4.8. The sensor array has five WEs with a diameter of 500 μm , a common RE and a common CE, all made in platinum. The black dashed line in this

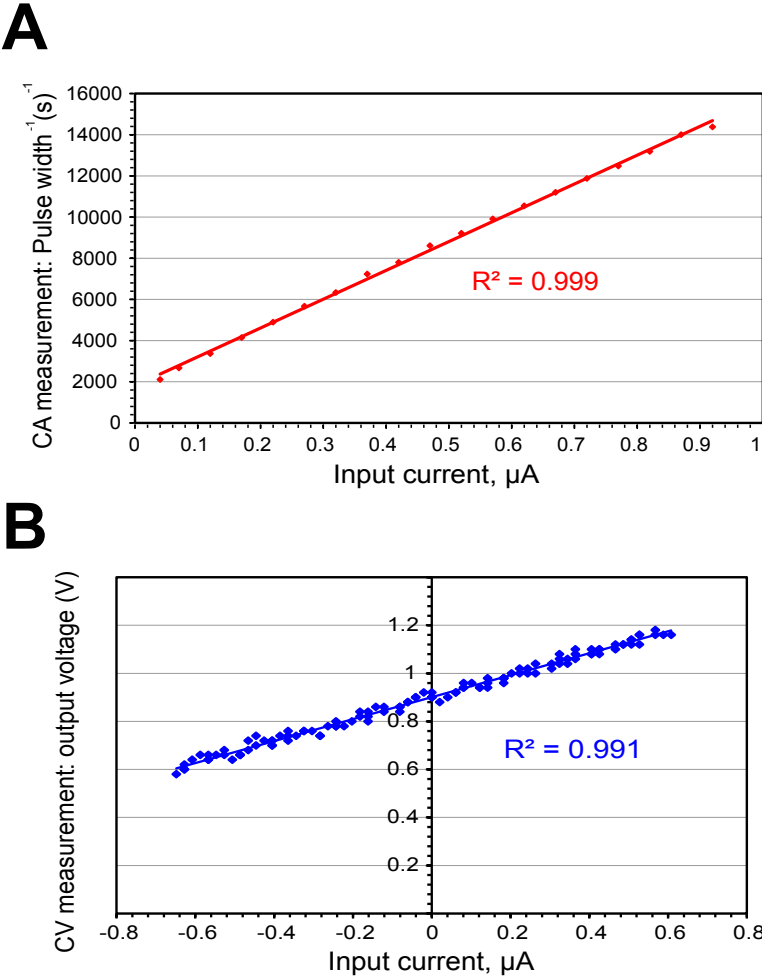


Figure 4.7: Measured characteristics of the circuits for CA (A) and CV (B) readout. The input current is converted to voltage in CV and to pulse width in CA. The internally generated sub-Hertz triangular waveform is applied to control CV measurement. Reprinted from [10].

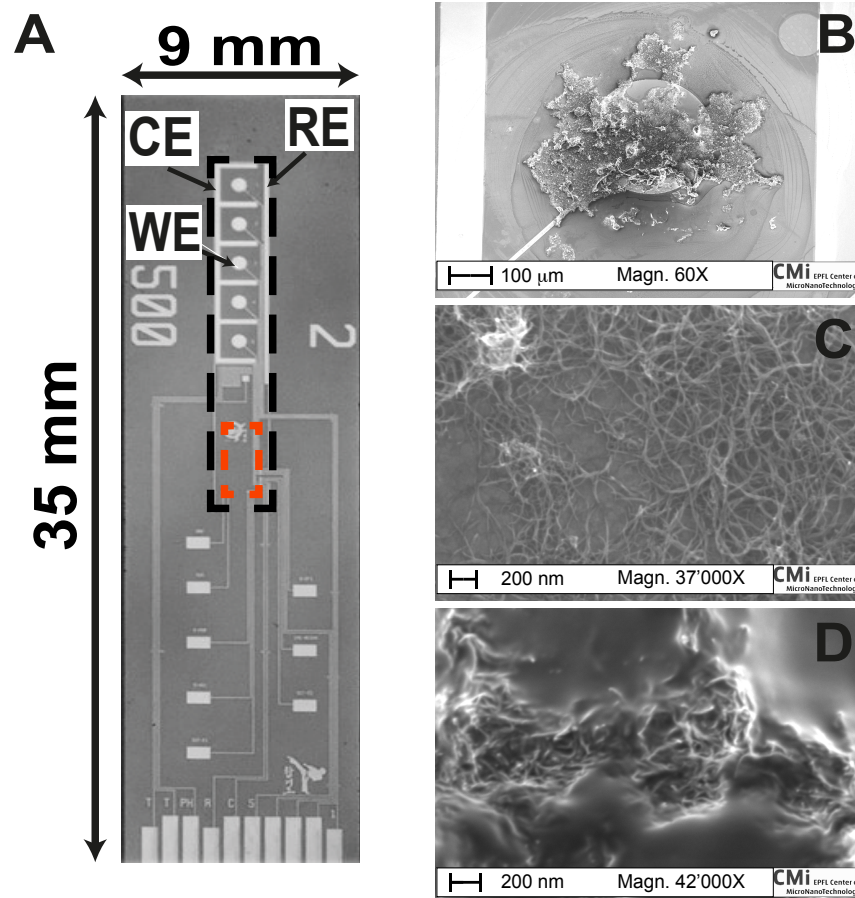


Figure 4.8: Biosensor: A) micro-fabricated sensor that hosts five WEs, a common counter and reference electrode. The black dashed line defines the section of the platform that is diced to be integrated in the implantable sensor. The red dashed line define the space for bonding the IC; B) SEM image of MWCNTs drop-cast on a WE; C) at higher magnification; D) SEM image of MWCNTs and GOx drop-cast on a WE. Reprinted from [10].

figure defines a section of the platform which is $2.2 \times 15 \text{ mm}$ and is diced to be integrated in the implantable sensor. The CA and CV measurements acquired with the sensor array and LOPHIC are presented in this section.

Electrode preparation

The selected target molecules to test the circuits were glucose, lactate and anti-cancer drug Etoposide. The first two molecules were measured with CA and the Etoposide was measured with CV technique. For the glucose and lactate detection, WEs were nanostructured with $0.2 \mu\text{g}$ of MWCNTs and a drop of 15 mg/ml GOx and 33 mg/ml LOx respectively. All the samples were freshly prepared and used the same day. When not in use, electrodes were

stored at 4°C. For the CV measurements, the electrodes were used without modifications. In Fig. 4.8B a *Scanning Electron Microscope* (SEM) image of a WE after the drop-cast of MWCNTs is shown. Fig. 4.8C shows a larger magnification in which the three-dimensional structure of CNTs on the electrode surface is visible. Fig. 4.8D shows the difference when the protein (GOx) is cast on the WE with MWCNT. The SEM images were acquired using a SEM LEO 1550 manual microscope.

Results

Electrochemical measurements were performed using the IC and repeated with an Autolab (Metrohm) electrochemical workstation, on the same day, for comparison. The very same sensing sites of the sensor array were used for the measurements with the IC and Autolab. Electrodes were tested for glucose and lactate sensitivity with CA at +650 mV. The sensors were first dipped in 8 ml PBS (100 mM, pH 7.4) under stirring conditions, and conditioned for one hour at +650 mV. Then they are tested with successive injections of glucose 500 μ M or lactate 50 μ M.

CV was used to identify the oxidation/reduction peaks of Etoposide. Measurements performed by applying a triangular waveform with a minimum of -300 mV, maximum of +900 mV between WE and the RE with a slope of 68 mV/s. Indeed any slope within 15 to 100 mV/sec is good enough for this electrochemical measurement. The sensor was dipped into 8 ml of 100 mM PBS (pH 7.4) and Etoposide was injected at concentrations of 200 μ M and 400 μ M after an initial 5 minute conditioning.

Chronoamperometry

The CA measurements at +650 mV for glucose and lactate obtained with LOPHIC are reported in Fig. 4.9A and Fig. 4.9B respectively. Measurements acquired with the Autolab are also shown for comparison. In these graphs, the vertical axis is the measured sensor current which is calculated using the calibration line in Fig. 4.7A. Table 4.3 reports the sensitivity and LOD for glucose and lactate obtained with the IC and the Autolab calculated according to the formulas presented in Chapter 2 (Section 2.3).

The differences in biosensor sensitivities when measured with the IC and Autolab are 0.4% for glucose and 11% for lactate. This can be fully attributed to the nature of the biosensors as it is widely demonstrated that the sensitivity of the biosensor changes considerably when measured at different times [104–107].

The higher LOD in the measurements with the IC is due to the limited accuracy of and higher noise in the measurement set-up with the IC.

With LOPHIC we were able to detect glucose and lactate in low concentration ranges (500 – 3000 μ M for glucose and 50–200 μ M for lactate), that are relevant in many clinical applications [108, 109]. The detectable glucose concentration is less than 3 mM in this measurement which

4.1. LOPHIC to readout amperometric sensors

Table 4.3: Comparison of sensitivity and LOD between the IC and the Autolab for glucose and lactate detection.

Metabolite	Sensitivity ($\frac{\mu A}{mM \times cm^2}$)		LOD (μM)	
	IC	Autolab	IC	Autolab
Glucose	27.2±5.2	27.3±0.5	87.9±22	17.5±1.4
Lactate	286±42.9	322±48.3	21.4±5.1	4.1±0.9

Table 4.4: Comparison between the IC and the Autolab for the peak attributed to the oxidation of Etoposide.

[Etoposide]	Peak current location (mV)		Peak Current (nA)	
	IC	Autolab	IC	Autolab
200 μM	613±18.4	617±18.5	39.6±6.7	45.4±3.2
400 μM	610±18.3	631±18.9	79.3±3.2	71.2±4.3

corresponds to the hypoglycaemia condition and the glucose level in the tear. Indeed, the functionalized glucose sensor in this measurement saturates at higher concentration. The addition of a selective and biocompatible membrane to the sensor expands the linear range of the detectable glucose concentration into the physiological range [110].

Cyclic voltammetry

The anti-cancer drug Etoposide was chosen for CV measurement because it is an electro-active compound that gives well-defined oxidation peaks at around +600 mV and +300 mV [111].

Fig. 4.10 compares the CVs for Etoposide at the concentration of 0 μM , 200 μM and 400 μM , obtained with LOPHIC (Fig. 4.10A) and Autolab (Fig. 4.10B). In both cases, two peaks at +300 mV and +600 mV are increasing with Etoposide concentration. For a better comparison Fig. 4.11 shows the CV at Etoposide 400 μM acquired with the IC (in red) and with the Autolab (in black). A low pass filter is applied to the data from the measurements with IC to reduce the noise. To keep the voltage of CE within the supply voltage range (0 to 1.8 V) an extra CE is used with an effective size of $\sim 0.126 \text{ cm}^2$. A bigger CE electrode decreases the resistance between CE and RE, and consequently the voltage drop between CE and RE. So, we conclude from these tests that the area of CE need to be increased for CV measurements in the next sensor array fabrication.

Table 4.4 reports the voltage and the current value of the Etoposide oxidation peak at +600 mV calculated from the CV measurements shown in Fig. 4.10. The measured peak position with the IC is less than 3.5% different from the same measurement with Autolab, that compares quite well with measurements errors of about 3% registered with both the IC and the Autolab.

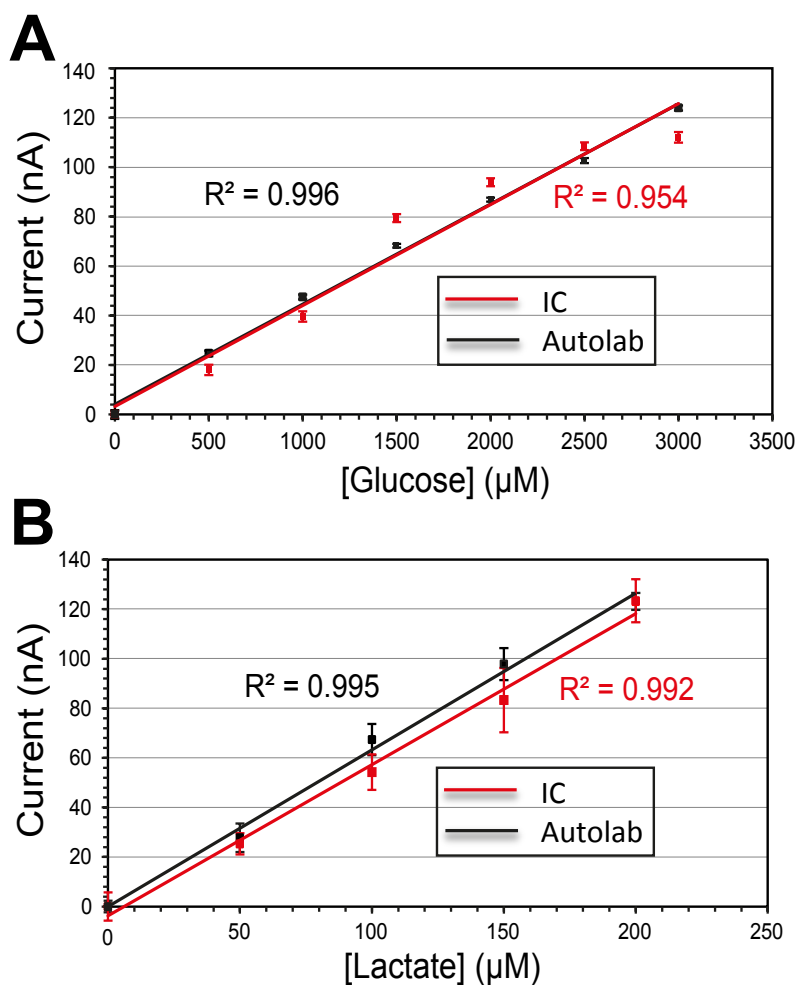


Figure 4.9: Comparison of the calibration curves for glucose (A) and lactate (B) obtained with the IC (in red) and Autolab (in black). The error bars for the case of IC are due to the variations of the measured average frequency. In the case of Autolab, the error bars are standard deviation of the measured current. Reprinted from [10].

4.1. LOPHIC to readout amperometric sensors

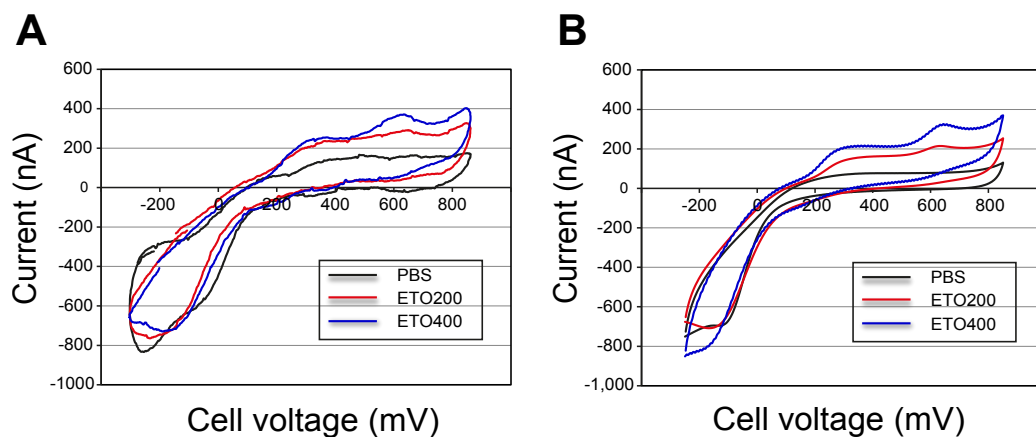


Figure 4.10: CV with the bare electrode in PBS, Etoposide (ETO) 200 μM and ETO 400 μM obtained with the IC (A) and the Autolab (B). The slope of the applied voltage is 68 mV/s . Reprinted from [10].

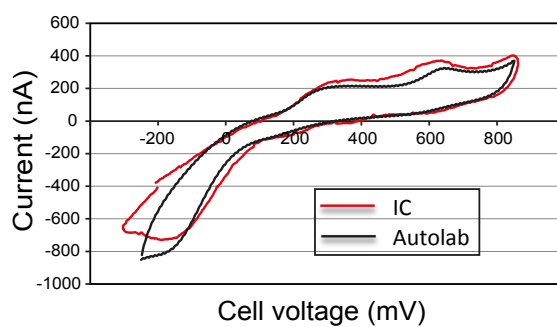


Figure 4.11: Comparison between the IC and the Autolab for the CV obtained in presence of ETO 400 μM . Reprinted from [10].

4.1.4 Discussion on LOPHIC

LOPHIC includes a current to frequency converter for CA readout and a resistive TIA for CV measurement. It consumes only $220 \mu W$ while provides several functions: Mixed-mode ramp generator; bidirectional current measurement; high-stability for different sensors. Measurements show excellent linearity of the current to frequency converter in sub- μA range.

However, few modifications and improvement are needed with respect to IMD application: (i) The current to frequency converter provides limited dynamic range; This is already discussed in Chapter 3; (ii) An ADC is needed for the autonomy of the data communication; (iii) The voltage and current bias circuits as well as the clock generator should be integrated on-chip to provide a fully-integrated and autonomous IC; (iv) The waveform generator which already provides different slopes, must be configurable in a way that requires fewer wire connections. The next section is dedicated to an IC that addresses all the limitations of LOPHIC.

4.2 ARIC to readout amperometric and potentiometric sensors

In this section ARIC is presented to control and read out bimolecular sensors in CA, CV, and potentiometry techniques. The potentiometry, or *open circuit potential* (OCP) measurement is needed to readout the Iridium oxide pH sensor as discussed in Section 2.4.

ARIC works with a $1.8 V$ supply voltage and has a single readout circuit for both CV and CA. It configures the sensor array and performs CV or CA based on the received commands. The control and readout circuits are implemented fully on-chip without any need of external clock or bias generator. The measured signal of all the electrochemical sensors is digitized through a fully-on chip $\Sigma\Delta$ *analog to digital converter* (ADC).

The block diagram of the mixed-mode ARIC is shown in Fig. 4.12, where the analog and digital blocks are shown in green and yellow, respectively. The digital blocks are implemented in collaboration with Antonio Pullini at EPFL. ARIC is in contact with five bio-molecular sensors. The measurement or readout core can be connected to any of the WEs or pH sensor through the multiplexer. The sensor current is converted into voltage by the resistive-TIA and then amplified and given to the $\Sigma\Delta$ ADC. The output of the ADC is given to the Tx/Rx interface block to be encoded and serialized. This block also includes our novel lightweight cryptographic system that is presented in details in Chapter 7. Two conditioning circuit apply the voltage (either fixed or triangular) to the sensors to be conditioned. The potentiostat applies a fixed voltage to the RE while closes the loop for the sensor current by providing the current for the CE.

ARIC receives commands from an standard interface (such as an FPGA board) and configures the sensor interface and the measurements. According to the commands a waveform generator is set to generate the desired voltage profile for different parts of ARIC.

In the following subsections three main parts of ARIC are described: (i) the readout chain; (ii)

4.2. ARIC to readout amperometric and potentiometric sensors

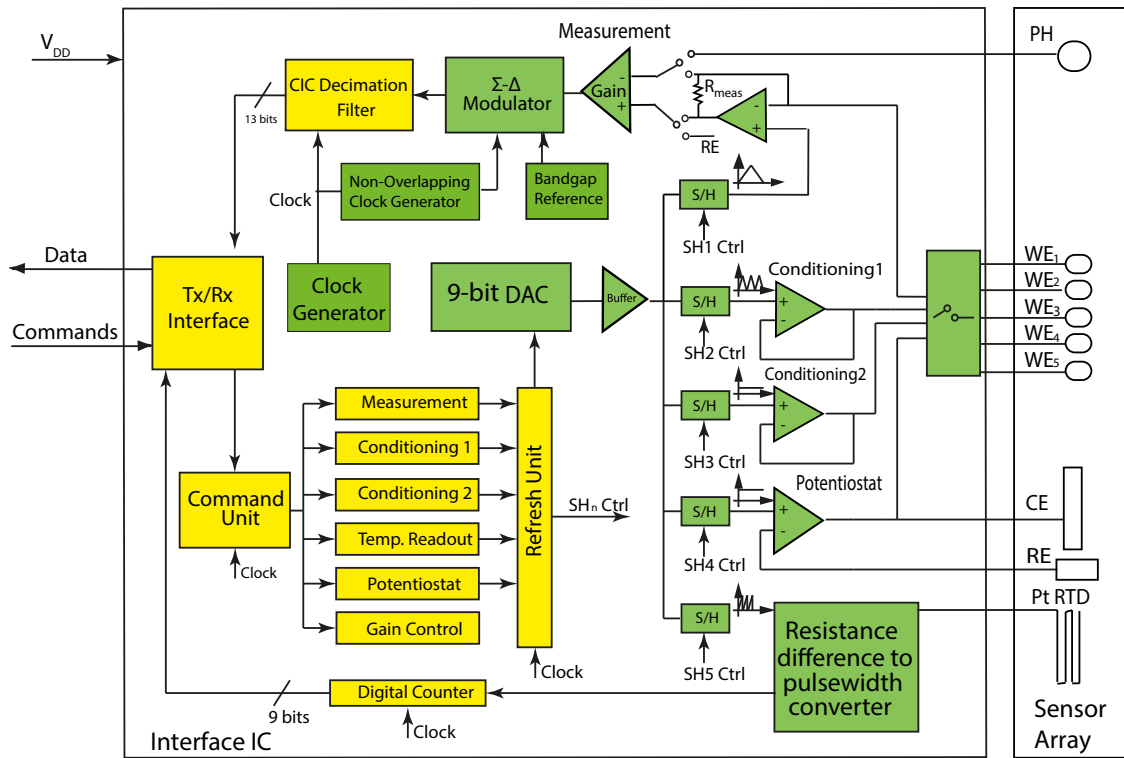


Figure 4.12: The schematic view of ARIC. The blocks in green and yellow are implemented in full-custom analog and semi-custom digital circuits, respectively.

the *Commands*; and (iii) the *Data* transmission. To validate ARIC, CV and CA measurements are performed on the electrochemical sensors by using potassium ferricyanide and hydrogen peroxide as models of target molecules. Hydrogen peroxide is especially useful as a model of the target molecules in metabolites detection because many metabolites are detected by using oxidases that have hydrogen peroxide as reaction side product.

4.2.1 The control and readout chain

The sensor control and readout are achieved through a chain of analog and digital circuit blocks. To control the sensors a fixed or triangular voltage waveform is generated internally by a direct digital synthesizer (DDS). To reduce the power consumption and the area of the IC, the DDS is shared among different circuits to generate five different voltage profiles needed in different parts of the IC: (i) Triangular waveform for CV measurement; (ii) Fixed voltage for CA measurement; (iii) Fixed or (iv) Triangular voltage for parallel conditioning of the sensors; (v) Sawtooth waveform for the temperature sensing circuit which will be described in the next chapter. The idea is to measure one sensor and at the same time connect the other sensors to the conditioning circuits that keeps them ready for the measurement. Therefore, while only one sensor can be measured at any given time, other (two) sensors can be conditioned for CV or CA with appropriate voltage waveforms.

Biosensors usually need long-time to be conditioned. During the conditioning phase a voltage similar to the measurement voltage is applied to the sensor for a certain amount of time while the current does not need to be measured. Therefore, in order to speed up the measurements, two conditioning circuits are also integrated into ARIC to condition the biosensors for either CV or CA methods (Conditioning 1 and Conditioning 2 in Fig. 4.12). In this way, when one WE is connected to the measurement circuit, the other WEs can go through the conditioning phase to be ready for measurement afterwards.

The *sample and hold* (SH) circuits are used to enable DDS sharing when different voltage profiles are needed at the same time. Proper switching is applied to the SH while the digital input of the DAC is changed in order to keep the right value on the right SH. The required control signals to refresh the SHs (signals SHx Cntrl in Fig. 4.12) are generated on-chip through the digital control unit. The control unit itself receives and processes the commands - regarding the measurement type and waveform information- from the user.

The sensor current is converted into voltage, amplified, and goes through a $\Sigma\Delta$ modulator and a *cascaded integrator-comb* (CIC) filter to be digitized. The readout circuit consists of a unified measurement block for CV, CA and pH readout followed by the $\Sigma\Delta$ ADC which are described in the following sections.

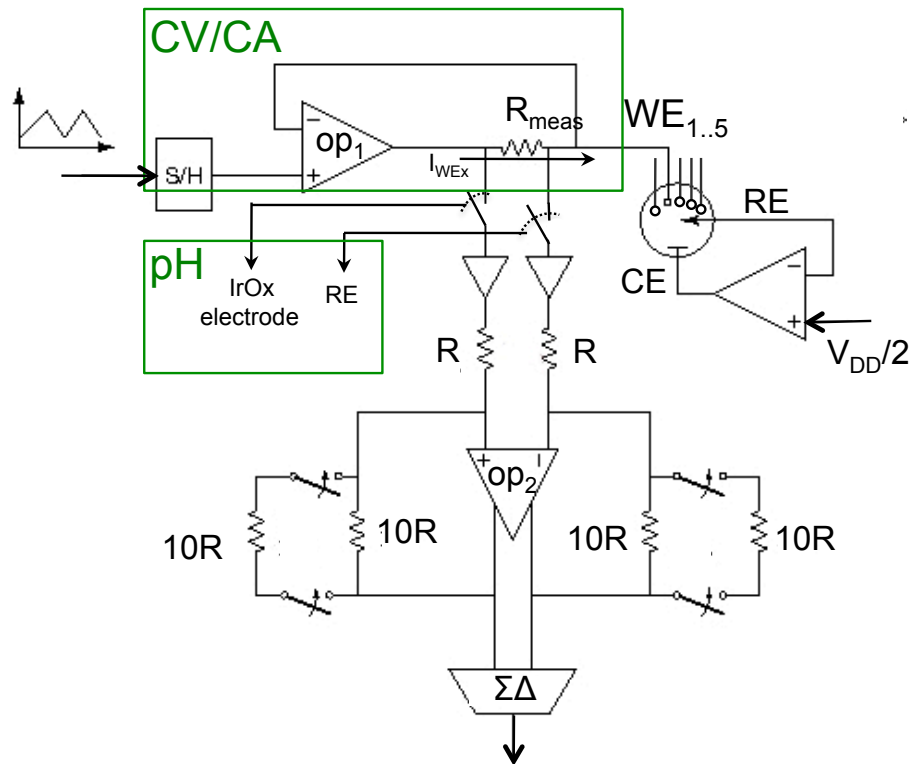


Figure 4.13: The schematic view of the circuit for CV, CA and pH readout. A fixed or triangular waveform is applied to the WEx and the resulting current is measured through R_{meas} and amplified before going through the ADC. Reprinted from [11].

Unified circuit for CV and CA readout

The readout core is capable of CV and CA, as well as potentiometry measurement. The schematic of the circuit is shown in Fig. 4.13.

CV measurement is performed by keeping a fixed voltage (e.g. $V_{DD}/2$) on RE through the potentiostat while a triangular waveform is applied to the WE of interest through OP_1 . A switch bank is used to connect one of the WEs to the circuit and is controlled through commands which are described later in this chapter. Once a WE is connected to the circuit, the switch bank doesn't change during the measurement unless commanded. There is a time difference of few minutes between measurements of the different WEs. Therefore, despite using switches at the WEs, no switching noise is introduced in the measurements.

In the most common scenario the triangular waveform sweeps the voltage from 0.4 V to 1.4 V with a slope of 20 mV/sec. Note that when the voltage at the WE is at its maximum, the current flows out of OP_1 . This results in a voltage that is higher than 1.4 V at the output of OP_1 . To insure linear measurement of the sensor current, the value of the resistance is chosen such

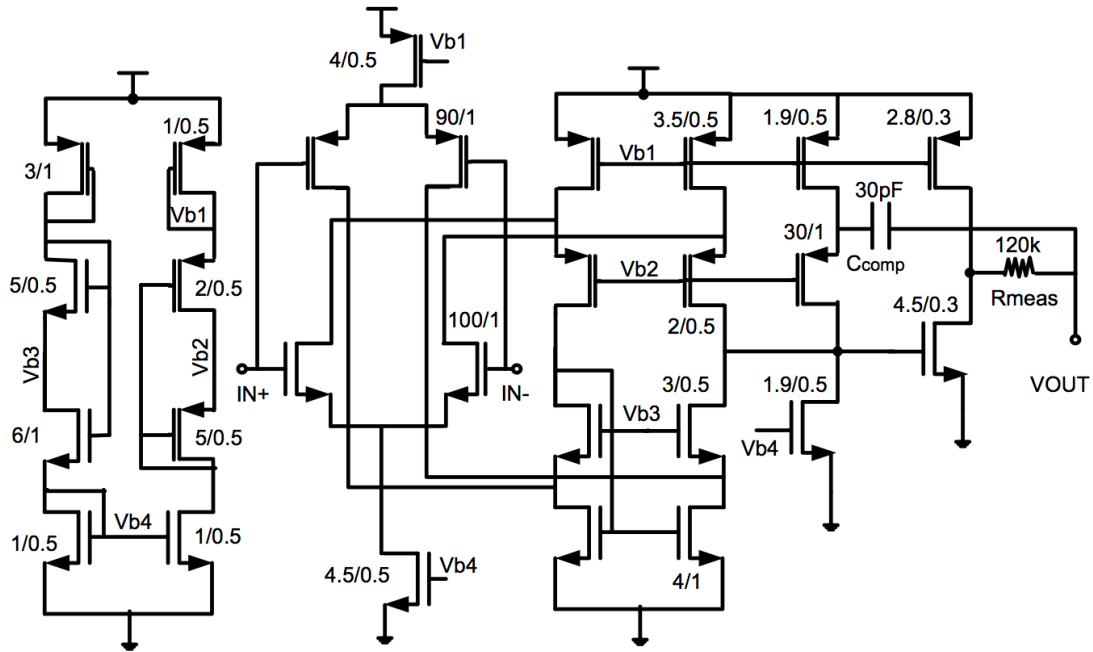


Figure 4.14: The schematic view of the compensated opamp for CV and CA readout (OP_1 in Fig. 4.13). It remains stable for $C_{load} \geq 500 \text{ pF}$.

that the maximum voltage drop across it is less than 300 mV .

As discussed in Section 4.1.1 folded cascode structure is chosen for the first stage of all opamps in ARIC because of its high gain, good PSRR (due to high output resistance), and wide input dynamic range. The OP_1 is a two stage amplifier compensated for a wide range of load capacitors and its schematic is shown in Fig. 4.14. The conventional compensation method (based on Miller effect) for a two stage amplifier is to connect a capacitor between the outputs of the two stages. Some modifications can be applied to the connection point of the capacitor to the first stage to remove the right-plane zero [103]. In OP_1 the the compensation is further improved: the compensation capacitor is now connected to the WE_x instead of the OP_1 output. This modification is effective because in the presence of R_{meas} the dominant pole is no more located at the output of the second stage but at the other terminal of R_{meas} (i.e. $VOUT$ in Fig. 4.14). Simulations show that the phase margin is higher than 45° for any load capacitor larger than 500 pF . Fig. 4.15 shows the simulated input to output gain and phase shift of OP_1 for a load capacitor of 1 nF .

The sensor current (I_{WE_x} in Fig. 4.13), which is the signal of the biosensor and carries the information about the concentration and type of the target molecules, flows into the resistance R_{meas} . The voltage across R_{meas} is buffered using two full-swing amplifiers. The buffered differential voltage is amplified using the differential amplifier OP_2 . The output of OP_2 goes

4.2. ARIC to readout amperometric and potentiometric sensors

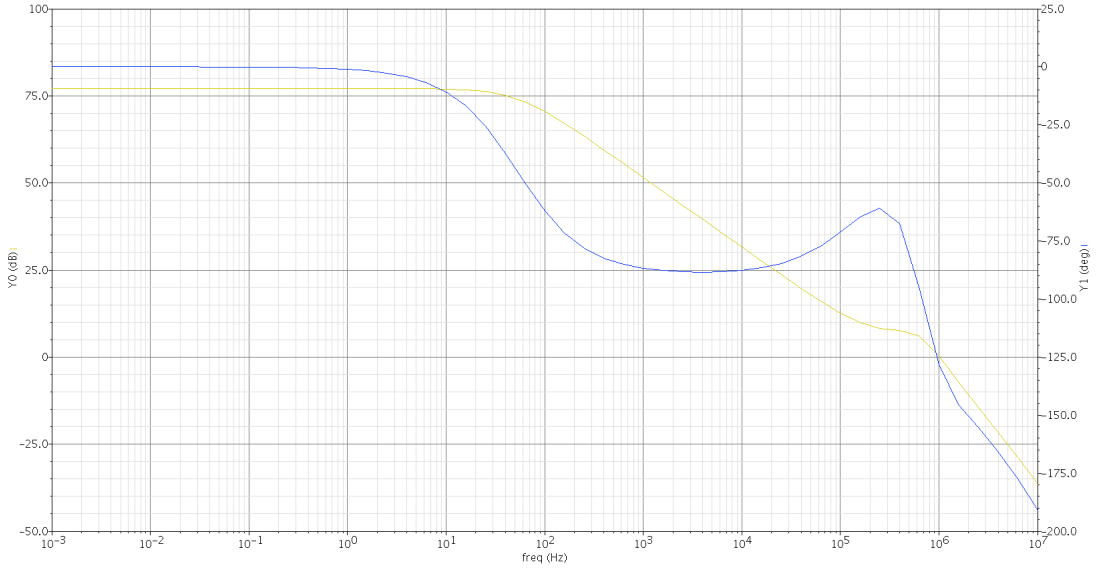


Figure 4.15: The gain (20dB) in green and phase in blue of OP_1 for $C_L = 1 \text{ nF}$.

Table 4.5: The specifications of the opamps in ARIC

Opamp	Gain(dB)	Phase margin($C_L = 1 \text{ nF}$)	-3dB Bandwidth (Hz)	PSRR (dB)
OP_1	77	55°	50	99
OP_2	52	86°	8500	192
Potentiostat	78	65°	110	72

through a $\Sigma\Delta$ ADC to be digitized. The OP_2 also plays the role of the anti-aliasing filter for the ADC. OP_2 is a folded cascade amplifier with common mode feedback. Its schematic is shown in Fig. 4.16. Two NMOSs at the bottom of the cascades are biased in the weak inversion and work as source degeneration resistors controlled by the output common-mode voltage. The gain and -3dB bandwidth of OP_2 are 52 dB and 8.5 kHz , respectively. The specifications of the opamps in ARIC are summarized in Table 4.5.

pH measurement is realized by disconnecting the buffers from the R_{meas} and connecting one of them to RE and the other one to an IrOx coated electrode that has been designed for pH sensing. The voltage difference between this electrode and RE changes linearly with the pH of the sensor wet interface [4].

Simulations on the CV and CA readout are done using the RC-equivalent model of the biosensor [5], [81]. A summary of the circuit specifications is presented in Table 4.6. According to [4], the open circuit voltage at of the pH sensor varies from -30 mV to $+120 \text{ mV}$ for pH from 5 to 8. Therefore, assuming an ideally linear pH sensor, our circuit is able to detect an equivalent pH from 1.5 to 13.5 units with 0.0003 resolution.

Table 4.6: Simulation results on the circuit for CV, CA, and pH readout

Readout	Linear range (5%)	Integrated noise (1 μHz to 1 Hz)
CV, CA	$\pm 2.3 \mu A$	125 pA (input referred current noise)
pH	$\pm 300 mV$	16 μV (input referred voltage noise)

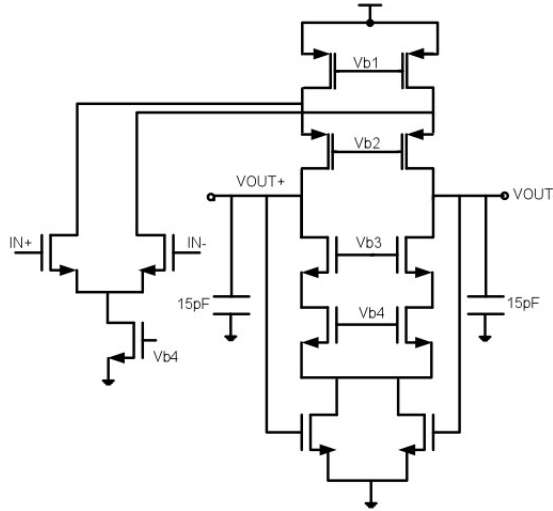


Figure 4.16: Schematic view of OP_2 in the unified circuit for CV,CA and pH measurement

$\Sigma\Delta$ ADC

A 13-bit ADC is required to convert the sensor signal into digital. This is to digitize the sensor current which is in the range of $\pm 0.4 \mu A$ with a minimum detectable change of 100 pA . The bandwidth of the signal is considered to be less than 1 KHz and the desired data-rate is 13 $kbps$ corresponding to one sample per millisecond. Possible options for the ADC are then $\Sigma\Delta$ ADC and *Successive Approximation* ADC (SAR ADC). In this research $\Sigma\Delta$ ADC is chosen due to several advantages it provides: (i) high precision at DC inputs; (ii) relax requirement on the analog anti-aliasing filter; (iii) lower sensitivity to mismatch and opamp offset.

A second order $\Sigma\Delta$ modulator is designed to digitize the measured data. The capacitors in the first and second integrator are chosen such that the modulator gives 14-bit accuracy for a signal bandwidth of 1 kHz with a clock frequency of 512 kHz . The schematic view of the $\Sigma\Delta$ modulator is shown in Fig. 4.17. $S_1, S_2, S_3,$ and S_4 are non-overlapping clock signals, generated by an on-chip clock generator block, to control the switches. The amplifiers are realized with a folded-cascade stage (see Fig. 4.18) to provide high output impedance for capacitive load. The switch-capacitor common mode feedback method from [112] is used to set the output common-mode voltage of the amplifiers at $V_{DD}/2$.

The common mode voltage of the differential amplifiers as well as the common mode voltage of the integrators (VCM in Fig. 4.17) are provided on-chip by a bandgap reference circuit which

4.2. ARIC to readout amperometric and potentiometric sensors

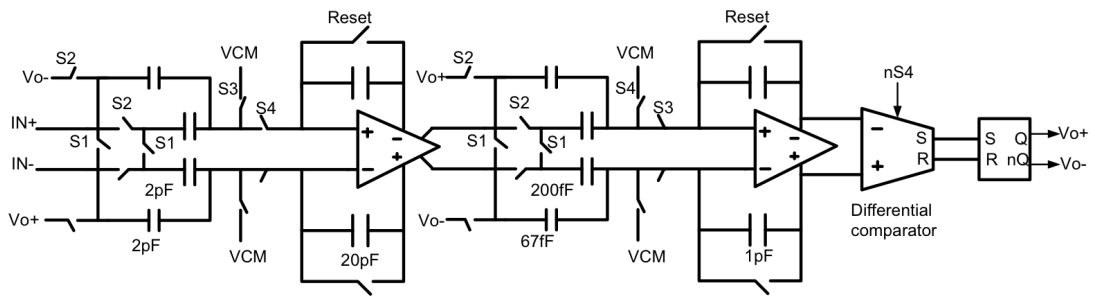


Figure 4.17: The schematic view of the second order $\Sigma\Delta$ modulator. The capacitors are chosen such that the modulator gives 14-bit accuracy. Reprinted from [11]

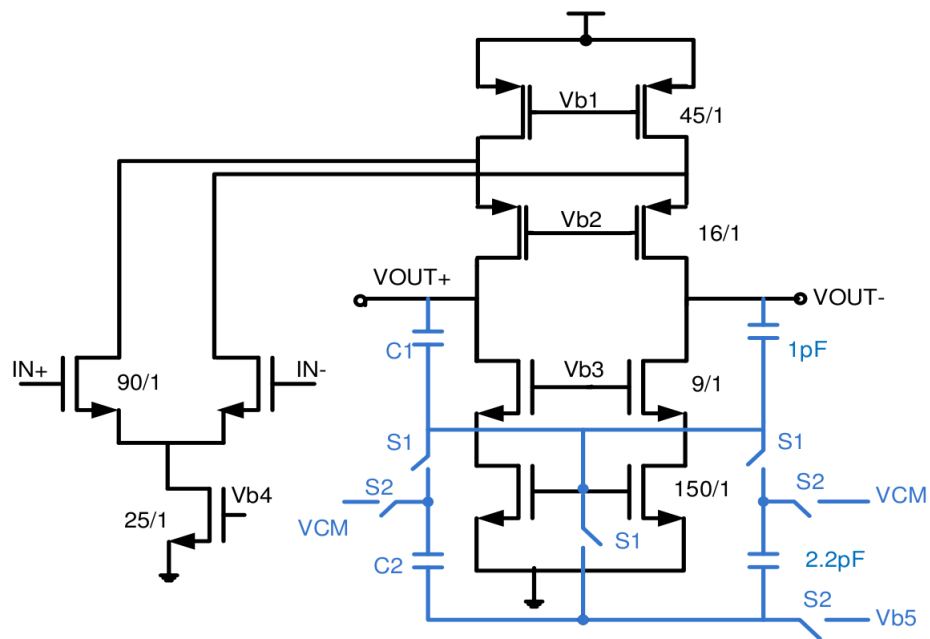


Figure 4.18: The opamp of the integrators in the $\Sigma\Delta$ modulator. A switched-capacitor common-mode-feedback is implemented to set the differential bias point. The bias circuit is similar to the one shown in Fig. 4.14.

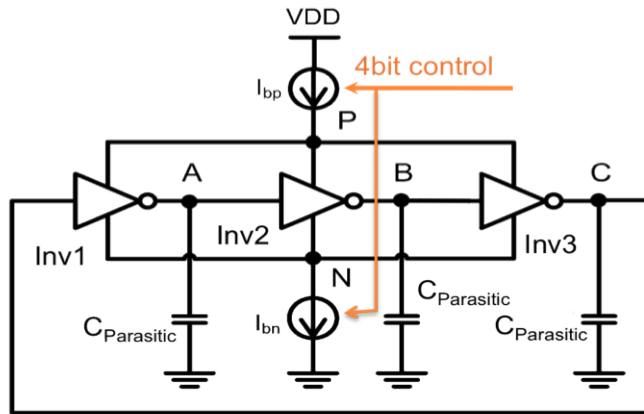


Figure 4.19: Schematic view of the three-stage current starved ring oscillator

is designed similar to [113] to generate $V_{DD}/2$. Simulation results on the bandgap reference circuit in different corners and temperatures from 30°C to 80°C show less than $20\ \mu\text{V}$ variation in the generated voltage.

A three-stage current starved ring oscillator is designed to provide the clock frequency to the $\Sigma\Delta$ modulator and the digital blocks of the IC. The schematic view of the oscillator is shown in Fig. 4.19. Simulations in different corners and temperatures range of 40°C to 60°C have shows that a 4 bit control over the current source is enough to get a better than 5% drift in the center frequency of the oscillator.

In sampling systems like the ADCs, the timing jitter of the clock frequency is one of the most important factors that limit their signal-to-noise ratio (SNR) as well as the dynamic range (DR). However, the effect is not severe if the input signal has low frequency and lo bandwidth. Moreover, one of the main advantages of the discrete-time $\Sigma\Delta$ modulator is its tolerance to the clock jitter which is shaped with the loop filter. Therefore, the effect of clock jitter on the SNR of the ADC is neglected in this research.

The output *power spectral density* (PSD) of the $\Sigma\Delta$ modulator is simulated after extracting the parasitic resistances and capacitances from the layout and is shown in Fig. 4.20. We can calculate the effective number of bits, n , in the signal bandwidth of $1\ \text{kHz}$ for differential input voltage, $V_{in} = 0.8\ \text{V}$ according to the equation [114]:

$$SNR_{dB} = 6.02n + 1.761 \quad (4.4)$$

From Fig. 4.20 we can see the SNR is $83.3\ \text{dB}$ that results in 13.5 bits for $V_{in} = 0.8\ \text{V}$, which corresponds to 14.6 bits for the full-scale input (i.e. $V_{in} = 1.8\ \text{V}$).

4.2. ARIC to readout amperometric and potentiometric sensors

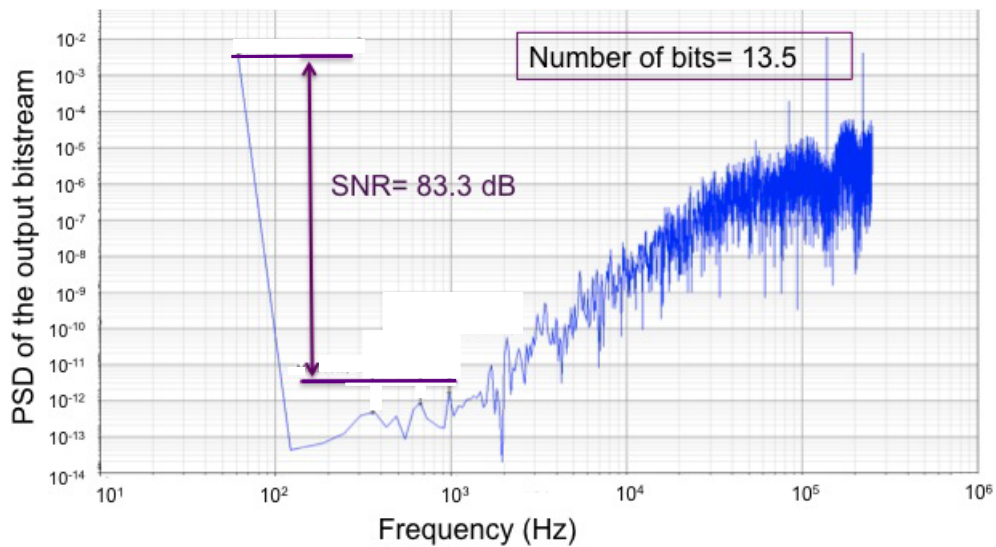


Figure 4.20: PSD of the $\Sigma\Delta$ modulator output (post-layout simulation). Reprinted from [11].

4.2.2 Commands

The instruction set of ARIC consists of three main commands (as shown in Fig. 4.21), each having a length of two bytes: (i) *Configuration*; (ii) *Execution*; and (iii) *Read*. The *Tx/Rx Interface* unit samples the voltage on the *Commands* pin to extract the commands.

The instruction *Configuration* is used to define the measurement parameters. Two types of measurements can be performed by the biosensor array: *CA* and *CV*. *Configuration*[13:10] selects the measurement type and the parameter to set. The parameter is set to *Configuration*[8:0]. In case of *CV* measurement, four parameters can be set: the maximum voltage, the minimum voltage, the scan rate, and the number of periods of the triangular waveform applied to the WE. In case of *CA* measurement, the applied voltage to the WE can be set. The circuits *Conditioning 1* and *Conditioning 2* are used to condition the electrodes when used for the first time and they can be configured in either *CA* or *CV* with configurable parameters. The connection of the five WEs and the RE with the measurement circuit and the conditioning circuits is also determined by the *Configuration* command. The *command unit* writes the parameters into the dedicated registers. The *Refresh unit* generates the digital data for the DAC as well as for the SH control signals.

The instruction *Execution* is used to begin/stop a *CV*, *CA*, or conditioning by applying/removing the appropriate voltage profile to the sensor. The stop command turns also off the $\Sigma\Delta$ modulator and the CIC filter. The instruction *Read* requests the readout IC to send back a certain number of measured data.

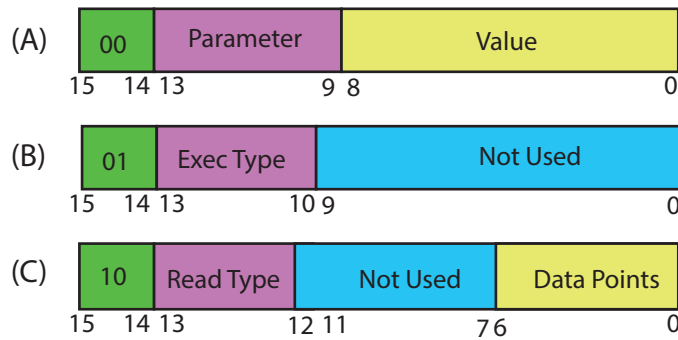


Figure 4.21: Three different commands for ARIC: (A) Configuration; (B) Execution; (C) Read.

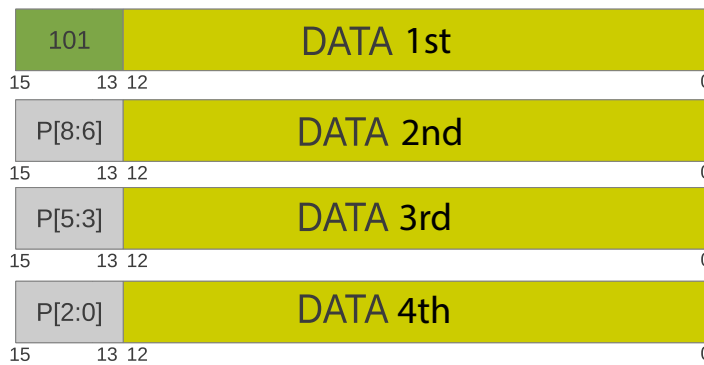


Figure 4.22: The pattern of the data as ARIC prepares it for communication. P[8:0] corresponds to the applied voltage to the WE. Data 1st to 4th are the output of the CIC filter.

4.2.3 Data transmission

The 13 bit output of the CIC filter is given to the *Tx/Rx interface* to prepare for transmission. If a *Read* command is received, the IC sends out the requested number of data. In case of CA or CV measurement, *Data*[12:0] contains the output of the $\Sigma\Delta$ ADC (i.e. the sensor current), while *Data*[15:13] of four consequent *Data* gives the 9-bit applied voltage (to the selected WE) preceded by a 3-bit starting pattern. An 8b/10b channel encoding is used in the *Tx/Rx unit* to convert the *Data* in order to achieve DC-balancing and avoid long sequences of the same logic value. The pattern of the data is shown in Fig. 4.22.

4.2.4 Electrical measurements

ARIC is implemented in $0.18 \mu\text{m}$ CMOS technology. It measures $3 \times 1.5 \text{ mm}$ and consumes $0.93 \mu\text{W}$ from 1.8 V supply voltage. Its micro-photograph is shown in Fig. 4.23.

A FPGA board (Xilinx Virtex-5) is used to send the commands to ARIC, and receive the data back from the IC. The data bit-stream is 8b/10b decoded by the FPGA to extract the current and voltage values. Fig. 4.24 shows the applied voltage on three different WEs by the IC, when

4.2. ARIC to readout amperometric and potentiometric sensors

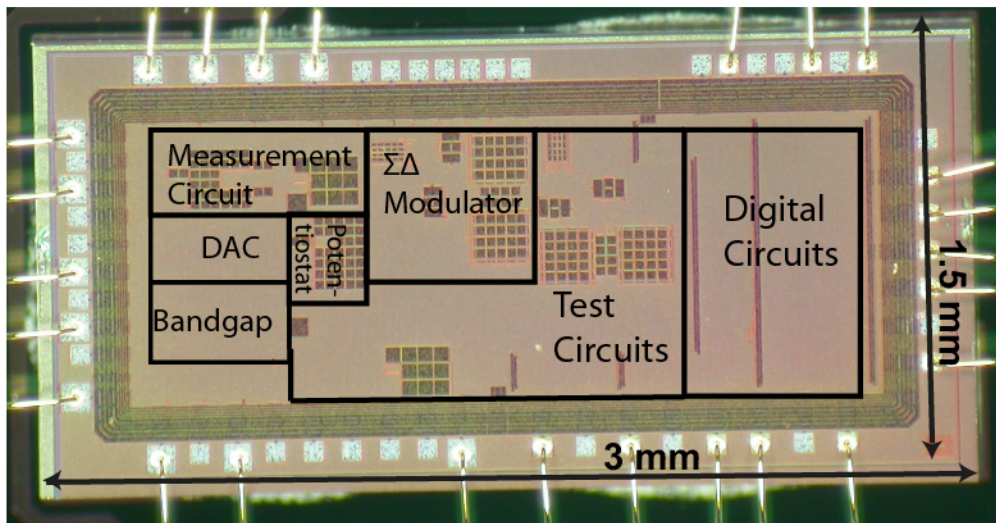


Figure 4.23: The microphotograph of ARIC in $0.18 \mu m$ technology.

the IC is configured for CA measurement on WE1, and CV conditioning with different slopes on WE1 and WE2. As shown in Fig. 4.24 a fixed voltage and two triangular voltages with different slopes are applied to the WEs, at the same time, by the single waveform generator.

Measurements showed that the waveform generator is able to provide different fixed voltages for the CA in the range of $300 mV$ to $1.5 V$ to be applied to the RE or to the WE. However, the waveform generator does not generate the triangular waveform with the slope of less than $2 V/S$. To overcome this, the IC is commanded to work in the CA mode, and the slow triangular voltage is generated by sending a configuration command to the IC that changes the voltage of the WE, for every step in the voltage. A sub-Hertz triangular waveform generated this way is shown in Fig. 4.25.

The output PSD of the $\Sigma\Delta$ modulator in absence of any input (input terminals short connected) is shown in Fig. 4.26. From Fig. 4.26 we can see that at the bandwidth of $1 kHz$ the noise floor is $-109 dB$, which matches with the post-layout simulation results shown in Fig. 4.20.

The *signal to noise ratio* (SNR) of the modulator in different input voltages is shown in Fig. 4.27. The maximum SNR is $76 dB$ which corresponds to an effective number of bits of 12.3 according to Eq. 4.4. Measurements showed that connecting the input voltage increases the noise-floor of PSD by $14 dB$. This is due to the injected noise by the voltage generator into the $\Sigma\Delta$ modulator. Considering this effect, and correcting the result for this, results in the actual number of bits (n) of 14.3 which is close to the simulation results shown in Fig 4.20. It came to our attention during the measurements that the modulator has $24 dB$ attenuation that when combined with the CIC filter reduces the resolution to 9 bits.

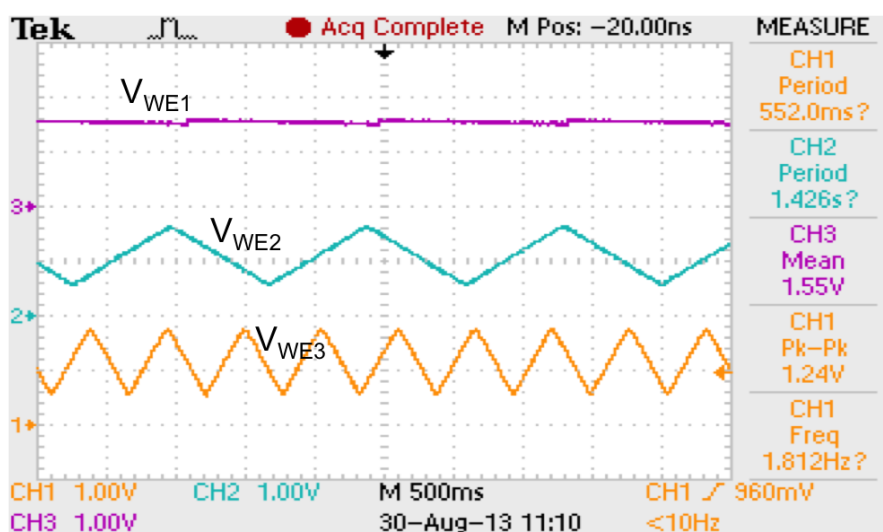


Figure 4.24: Generated voltages on the WE1 (purple), WE2 (blue), and WE3 (orange) by the voltage generator on ARIC.

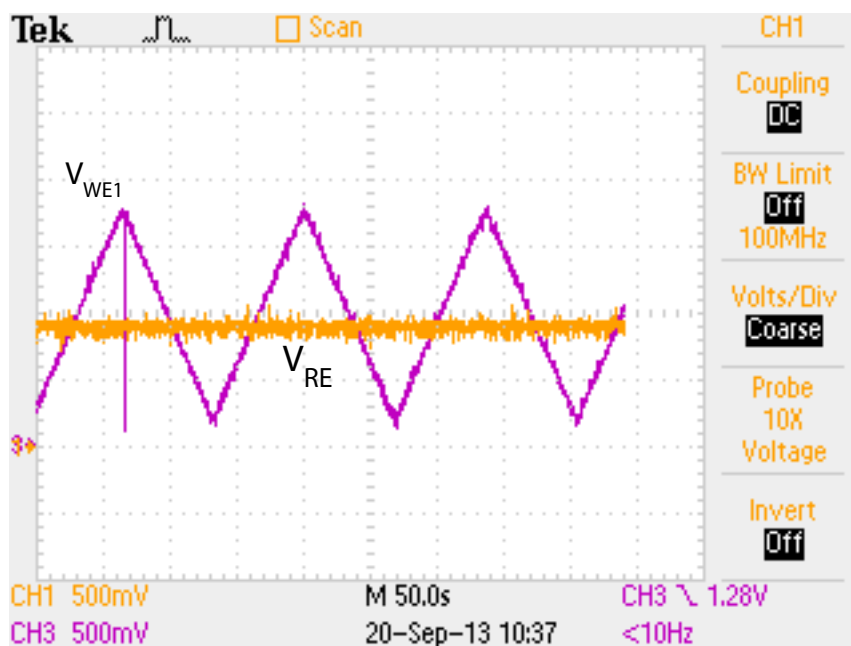


Figure 4.25: The slow triangular waveform on WE1 (purple), and the fixed voltage on RE (orange) generated by ARIC for CV measurement. In this measurement ARIC is configured in CA mode and the applied voltage is changed at each voltage step by sending a command. (The glitch in V_{WE1} is due to the communication error between the FPGA and ARIC.)

4.2. ARIC to readout amperometric and potentiometric sensors

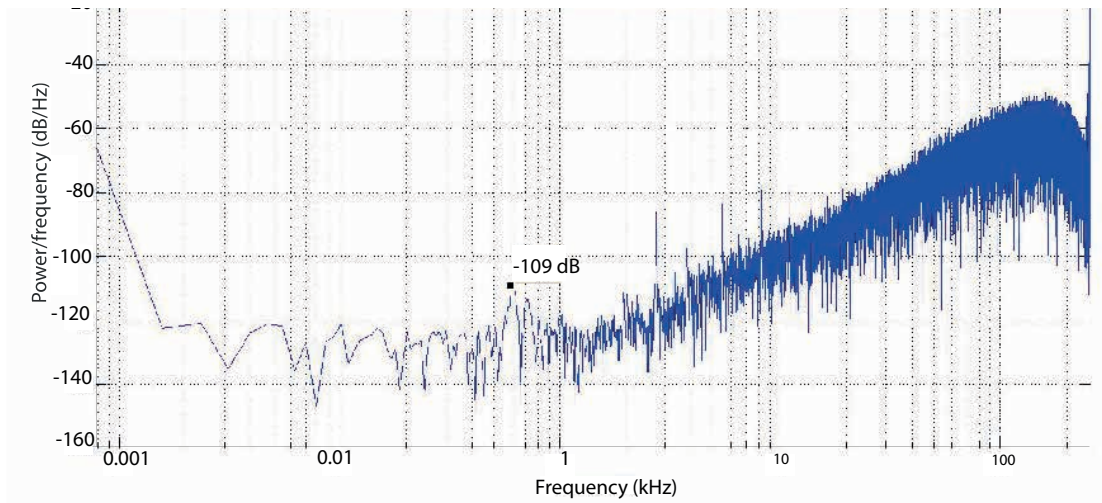


Figure 4.26: The PSD of the output bit stream of the $\Sigma\Delta$ modulator. The noise floor in the signal bandwidth of 1 kHz is -109dB when the input voltage is zero (i.e. the differential inputs of the modulator are short connected).

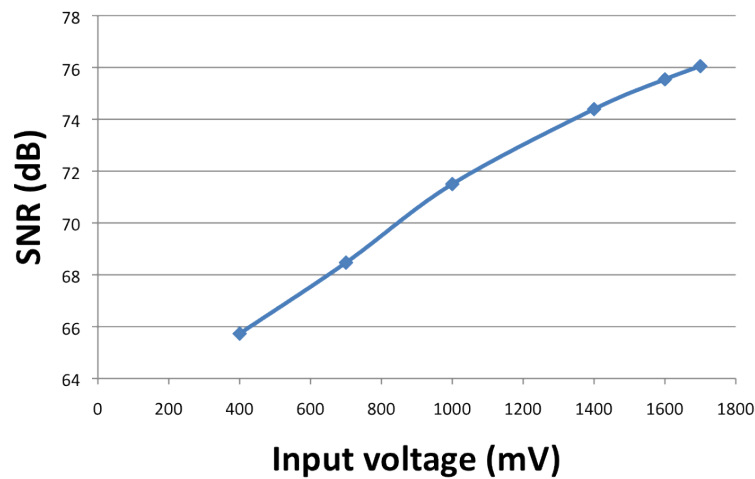


Figure 4.27: SNR of the $\Sigma\Delta$ modulator versus input voltage amplitude. The input voltage is at DC frequency. By connecting the input voltage source, the noise floor changes by 14dB. This can be attributed to the injected noise at the input by the power supply equipment. Correcting for this effect gives the effective number of bits of the $\Sigma\Delta$ modulator which is 14.3.

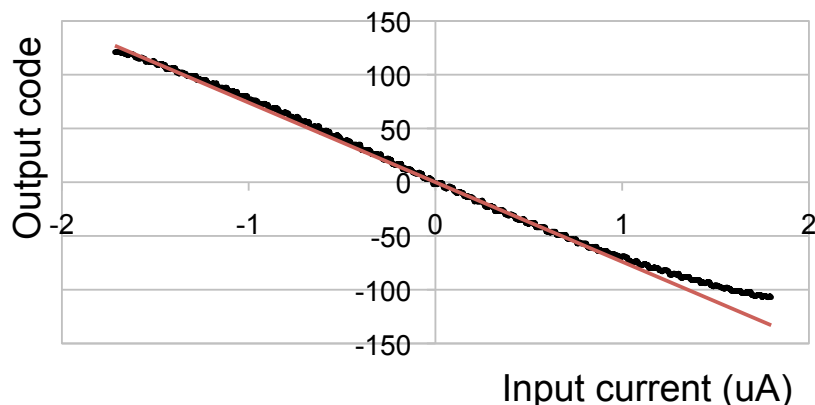


Figure 4.28: The measured input-output characteristics of the current readout chain which includes the TIA, the gain stage, and the $\Sigma\Delta$ ADC (black), and the simulated characteristics (red). In both lines the offset is removed.

To characterise the readout chain, the FPGA board sends commands to ARIC, and receive the data back from the IC. The readout circuit is characterized by configuring the IC for CV measurement. The proper *Configuration* commands are sent to the IC to generate and apply a triangular voltage waveform to WE1 with a maximum of 1.5 V, minimum of 0.5 V, and slope of 4.5 V/s. The circuit is electrically characterized by using a resistor (267 k Ω) between WE1 and a fixed voltage of 900 mV. The input-output characteristics of the readout chain is shown in Fig. 4.28. The current readout chain includes the TIA, the gain stage, and the $\Sigma\Delta$ ADC. Measurements show that the 1-dB compression point in the current readout chain is at ± 1650 nA, while the readout resolution is 8 bits within this range.

As explained before, the pH readout chain is similar to the biomolecular readout chain, except that it does not include the TIA. The measured input-output characteristics of the pH readout chain is shown in Fig. 4.29. Its 1-dB compression point is at the OCP voltage of ± 0.3 V and its dynamic range is 8.8-bits which corresponds to a resolution of 1.35 mV.

4.2.5 Electrochemical measurements

ARIC is validated with electrochemical sensors shown in Fig. 4.8. Potassium ferricyanide ($K_4Fe(CN)_6$) and hydrogen peroxide (H_2O_2) are chosen as target molecules. The first compound is chosen because it has a well-defined response and highly reversible electrochemistry [25]. Therefore, it is a valid benchmark for cyclic voltammetry. The hydrogen peroxide, instead, is selected because it is an extremely significant and fundamental molecule in the biomedical field. Many analytes can be detected by using oxidases. These enzymes usually promote a redox reaction, where the H_2O_2 is the main by-product [104]. Then, since hydrogen peroxide is an electrochemically active molecule, it can be directly detected through amperometric measurements.

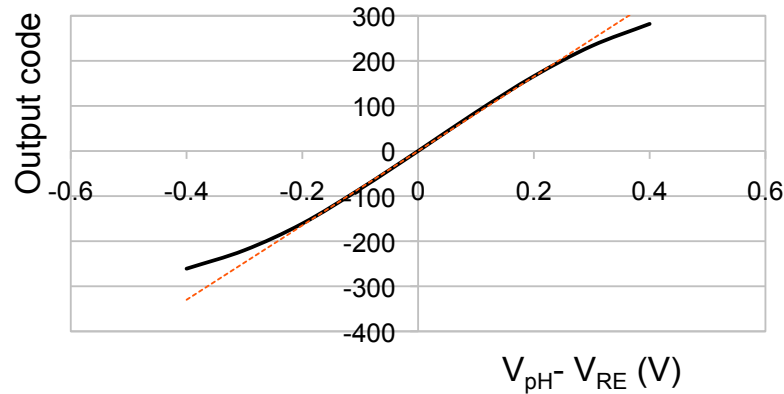


Figure 4.29: The measured input-output characteristics of the pH readout chain which consist of the Gain stage and the $\Sigma\Delta$ ADC (black), and the simulated characteristics (red). In both lines the offset is removed.

Cyclic voltammetry

For each measurement, a drop of buffer saline solution with different concentration of potassium ferricyanide is placed on top of the WE, as well as the RE and the CE. A triangular voltage waveform with a maximum of 1.5 V, minimum of 0.5 V, and the slope of 10 mV/sec is applied to WE1 while 0.7 V is applied to RE. CV performed by ARIC in the presence of potassium ferricyanide at different concentrations is plotted in Fig. 4.30. The measured sensor current is calculated from the output code of the readout IC and the measured characteristics of the IC in Fig. 4.28. A 50-point moving average low-pass filter is used to reduce the noise while displaying the data in Fig. 4.30. The position of the peaks agree well with literature [115].

Chronoamperometry

The CA of H_2O_2 at +650 mV is reported in Fig. 4.31. The sensor current is measured in time while the concentration of the H_2O_2 is increased in steps of 0.2 mM or 0.4 mM. Since the CV and CA readout circuits are exactly the same, the IC output code in CA is converted to current using the same characteristics shown in Fig. 4.28. Table 4.7 summarizes the measurement results.

Potentiometry

The potentiometry readout circuit is used to measure the pH with the pH sensor (an IrOx pH sensor described in [4]) and an external silver reference electrode at room temperature. The measured OCP ($V_{pH} - V_{RE}$) is plotted versus the pH in Fig. 4.32 for three consequent runs. In each run, we changed the pH from 5 to 9 by adding proper amount of NaOH solution of 5 M concentration. We measured the pH separately using an external pH meter (VWR). Then we

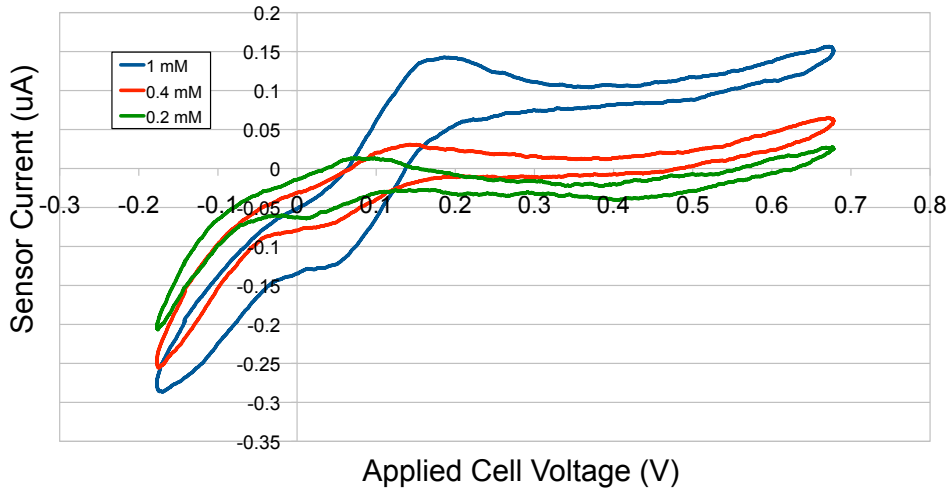


Figure 4.30: Cyclic voltammetry of potassium ferricyanide at different concentrations with ARIC. Reprinted from [12].

Table 4.7: Measured Specifications of ARIC

<i>Parameter</i>	<i>Value</i>
Current consumption of analog part	462 μA
Static current consumption of digital part	56 μA
Control voltage range	0.1 – 1.7 V
Minimum control voltage step	3.5 mV
Linear input current range	± 1650 nA
Minimum resolvable input current	13 nA
Sensitivity to pH	76.84 ± 3.89 mV/pH
PH resolution	0.02

decreased the pH from 9 to 5 by adding the *HCl* solution of 3 M concentration to the solution and repeated the process two more times.

In these measurements a fixed voltage is applied to the reference electrode through an off-chip voltage source. Without controlling the voltage on the reference electrode, we observed that the measured OCP is not stable for a fixed pH. This voltage is chosen at $V_{DD}/2 = 900$ mV so that the OCP of ± 900 mV is measurable by the circuit. Any other voltage within the range of 0 to V_{DD} could be applied instead of $V_{DD}/2$ but it may result in a smaller interval of detectable pH in the following way. Indeed the best voltage to apply to the reference electrode (i.e. V_{RE}) is a voltage that at $pH = 7$ makes $V_{pH} = V_{DD}/2$ so that pH variation in 0 to 14 results in an OCP range that is centred around $V_{DD}/2$ where the opamps have maximum linearity. However, since this voltage drifts from one measurement to the other, a fixed voltage of $V_{RE} = V_{DD}/2$ is finally chosen and applied.

Measurements show that the average sensitivity of the potentiometric sensor to pH is 77 mV/pH which agrees very well with literature [116]. The existence of the drift in the measured voltage

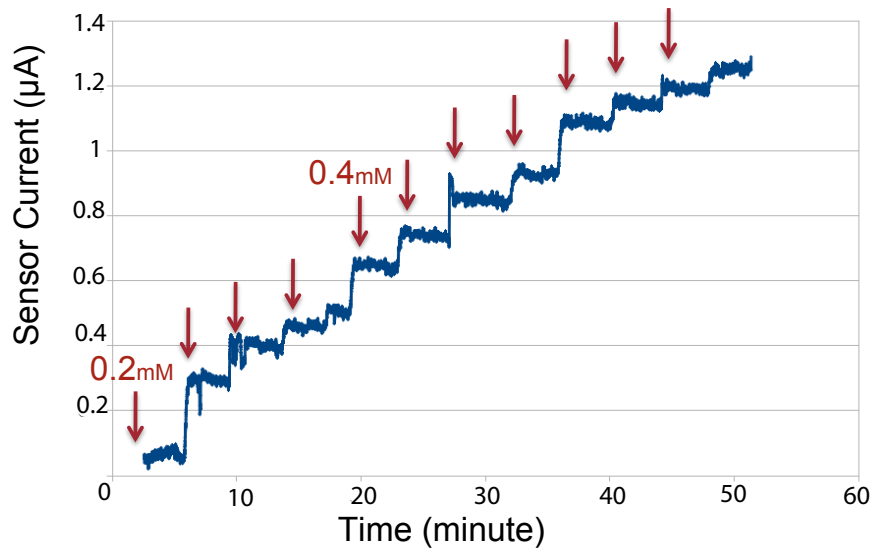


Figure 4.31: Chronoamperometry of hydrogen peroxide using the proposed IC. Successively injections of 0.2 mM and 0.4 mM of H_2O_2 show that the IC is able to correctly readout the current. Reprinted from [12].

between different runs is also reported in other works and is an important characteristic of IrOx electrode [116]. This phenomenon is identified in the literature as hysteresis of the sensor response. To reduce it the pH microelectrodes could be prepared for use after they are soaked in a universal buffer of pH 7.0 for 2 days [117]. This also ensures that OCP measurements are repeatable. However, optimization of the pH sensor was beyond the context of this research and has been addressed by my fellow students [3, 4].

The potentiometry circuit of ARIC was modified in a later design to make stable measurement without the external voltage source. This circuit is shown in Fig. 4.33 and is fabricated in 0.35 μm . This circuit applies a fixed voltage (VCM) to the RE through an on-chip buffer amplifier. Through the multiplexer three different Ion sensors can be read out. The voltage difference between the RE and the Ion sensitive sensors is given to the ADC to be digitized.

4.3 Chapter contributions and summary

Two fully-integrated circuits (LOPHIC and ARIC) have been presented to readout and control amperometric and potentiometric sensors. They were fabricated in 0.18 μm and are designed to control and readout an array of five biosensors.

LOPHIC includes a current to frequency converter for CA readout. Measurements show excellent linearity of the current to frequency converter in $sub - \mu A$ range. The novelties of LOPHIC are:

- Low total power consumption (220 μW). The most similar IC to LOPHIC (and ARIC) is

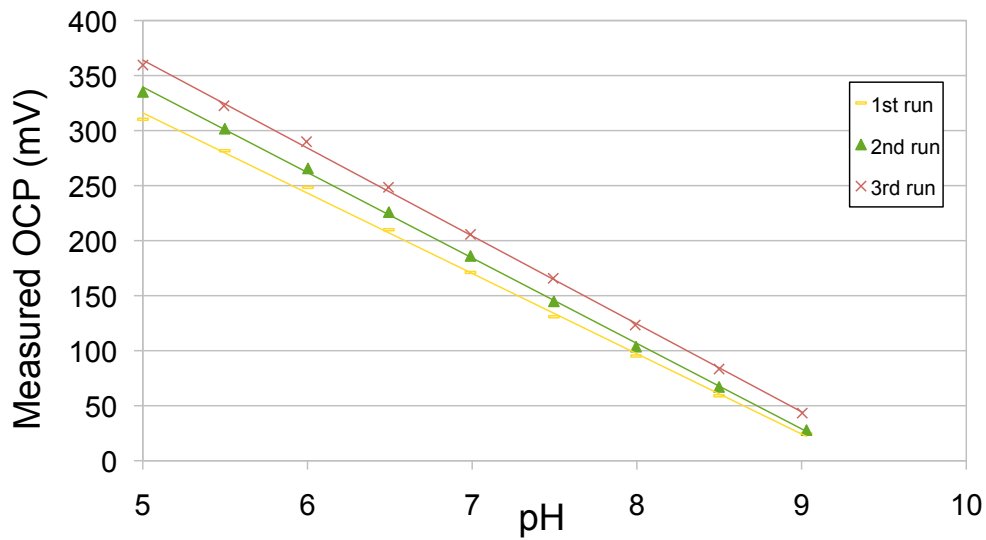


Figure 4.32: The measured output of the pH readout circuit for different values of the pH. The same measurement repeated three times.

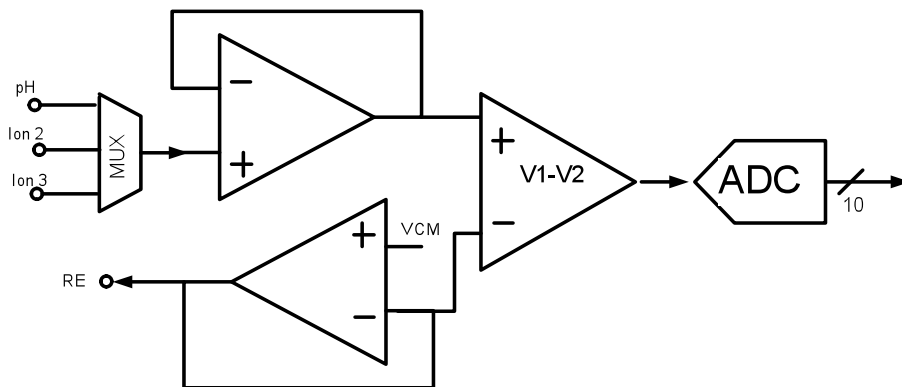


Figure 4.33: The circuit to measure the open circuit potential between an Ion sensor and a reference electrode.

presented in [9] which consumes 21.5 *mW*.

- Mixed-mode ramp generator and its combination with the CV readout circuit. The CV readout circuit applies the ramp waveform to a WE and reads the bidirectional current at the same electrode with a supply voltage of 1.8 *V*.
- the opamp OP_1 in the CV readout circuit (in Fig. 4.1) is stable for a wide range of loads. This is highly necessary because the load of this opamp is the biosensor which has a time and concentration dependent RC-equivalent model.

Glucose and lactate CA measurements with LOPHIC are successfully performed. Etoposide CV measurement is achieved by applying the on-chip triangular waveform to the sensor. The oxidation current peak position and height agree well with the measurements performed with the commercial equipment.

ARIC is an autonomous and reconfigurable circuit that generates different voltage profiles to control CV and CA by using a fully on-chip waveform generator. The novelties of ARIC are:

- This is the first fully-integrated readout circuit for multi-metabolite detection with different measurement techniques that enables also the calibration with pH and temperature.
- ARIC is programmable through 16-bit serial commands and can be reconfigured for different measurements on each sensing site of the sensor array
- The waveform generator that is designed such that it can provide multiple voltage profiles at the same time. In particular it saves both energy and area.
- The parallel conditioning circuits to speed-up the measurement.

ARIC reads out the electrochemical sensors and streams out the digitized measured data. Electrochemical measurements including CA, CV, and potentiometry measurements have been successfully performed on H_2O_2 , potassium ferricyanide, and Iridium oxide pH sensor, respectively.

Both ARIC and LOPHIC consume sub-mW power which makes them suitable for remotely powered implantable applications [118]. ARIC consumes more power than LOPHIC. This difference is mainly due to the $\Sigma\Delta$ modulator and other functionalities that are added to ARIC and are absent in LOPHIC. On the other side, ARIC has a fully digital output as well as all necessary bias and clock generator circuit blocks. It receives commands to start, configure, and stop the measurements and is fully autonomous. Therefore, it is ready to be integrated within heterogeneous sensing platforms for implantable or low-cost portable applications. Such integration is discussed in Chapter 6.

5 ASICs to readout resistance-temperature-detectors

Recall from Section 2.5.2 that the calibration of the biosensors for environmental variables like pH and temperature is required for precise monitoring [29]. The response of a non-calibrated-sensor to a change in temperature may be accounted for a non-real change of the target molecule concentration. Therefore, a thermometer must be placed close to the sensors to accurately monitor the temperature of the sensing environment.

Resistance thermometers, also called resistance temperature detectors (RTDs), are sensors used to measure temperature by correlating the resistance of the RTD element with temperature. Common RTD sensing elements are constructed of platinum, copper or nickel. They have a repeatable resistance versus temperature relationship (R vs. T) and operating temperature range. The R vs. T relationship is defined as the amount of resistance change of the sensor per degree of temperature change. The temperature coefficient of RTD varies only slightly over the useful range of the sensor.

Platinum was proposed by Sir William Siemens as an element for resistance temperature detector in 1871 [119]. It is the best metal for RTDs because it follows a very linear resistance-temperature relationship and it follows the R vs. T relationship in a highly repeatable manner over a wide temperature range. The unique properties of Platinum make it the material of choice for temperature standards and is used in the sensors that define the International Temperature Standard, ITS-90.

Moreover, Platinum is a biocompatible metal that does not cause body reaction if implanted inside the body. Therefore, it is a perfect candidate for temperature measurement in bio-environments where the bio-compatibility is important.

A CMOS circuit is therefore needed to measure the off-chip platinum RTD to be integrated into the interface IC of the IMD. The target feature and specifications of the RTD readout circuit are as following: (i) It should be fully integrated; (ii) It should measure a single off-chip resistor; (iii) The temperature resolution should be better than 0.2°C ; (iv) It should measure temperature range of 35°C to 45°C (Possible human body temperature) or wider; (v) It should

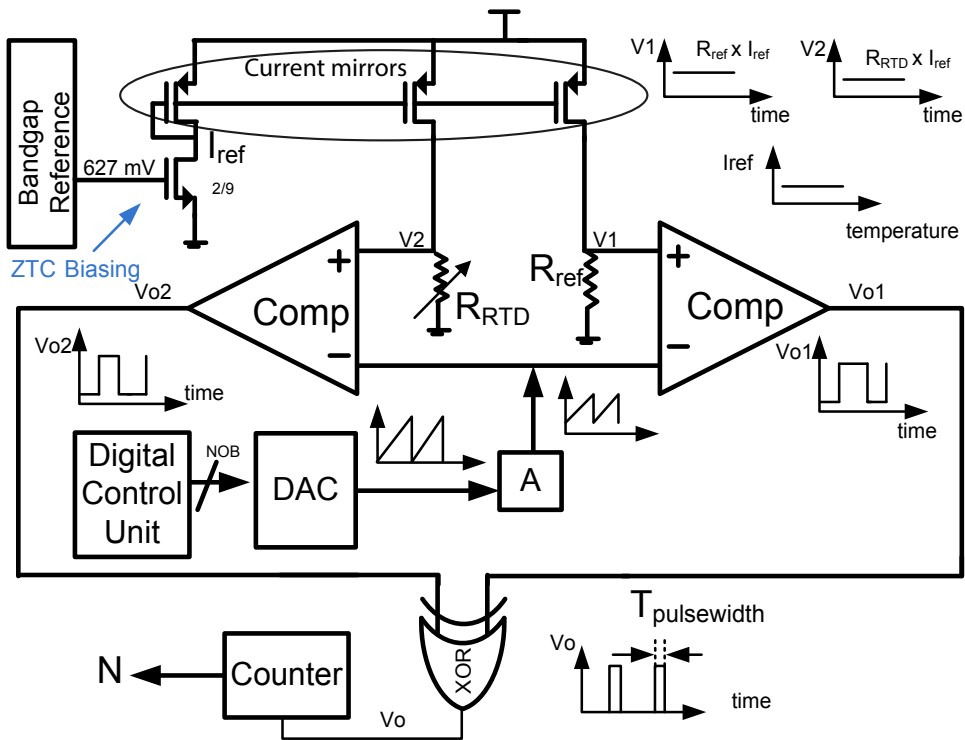


Figure 5.1: The schematic view of the R2PC circuit for temperature measurement using an off-chip Pt-RTD. The circuit converts the resistance difference into pulsewidth and then into digital.

consume low power typically much less than a miliWatt.

The state-of-the-art of circuits for RTD measurement is presented Section 3.4, where that to readout a single off-chip resistor through a fully integrated IC. In this chapter two circuits are presented which are the first fully-integrated circuits to readout off-chip RTDs. They both generate a constant current that passes through the resistor. The voltage across the resistor is then compared with a reference value and the result is converted into pulse-width or digital. The first circuit converts the difference between the Pt-RTD and an on-chip reference resistance into pulse-width. The circuit gives an equivalent resolution of $1^\circ C$ while consumes $12 \mu W$. The second circuit is highly improved with respect to the first circuit in terms of the resolution ($0.03^\circ C$) while consumes more power ($330 \mu W$). It converts the Pt-RTD into voltage that is later digitized through an ADC. In the following section these circuits are explained in details.

5.1 Resistance to pulsewidth converter (R2PC)

5.1.1 Circuit architecture

The *Resistance to pulse-width converter* (R2PC) circuit is based on the comparison of a Pt-RTD with an on-chip reference resistor, R_{ref} . The schematic of the circuit as well as the voltage and current values of different nodes are shown in Fig. 5.1. The circuit includes two comparators the threshold voltages of which are set to $R_{RTD} \times I_{ref1}$ and $R_{ref} \times I_{ref2}$, where I_{ref1} and I_{ref2} are mirrored currents of a reference current, I_{ref} . The difference in the threshold voltage of the comparators is linearly proportional to the difference of R_{RTD} and R_{ref} , and therefore to the temperature. High-doped Poly-resistor with low temperature coefficient is used for R_{ref} .

The R_{ref} may change from die to die due to process variation. This leads to different voltages on V_1 and V_2 when the temperature difference between R_{RTD} and R_{ref} is zero and induces offset in the output. Calibration is needed to remove the offset from the output. In order to remove the offset, either R_{ref} or the gain of the current mirrors can be tuned. This is implemented in the R2PC circuit presented in the next section.

A sawtooth waveform is generated on-chip and applied to the common terminal of the comparators. Any difference in the threshold voltages translates into different transition times in the output of the comparator. This time difference is detected by the XOR gate and can be calculated by:

$$T_{pulsewidth} = \frac{V_2 - V_1}{A \cdot V_{step,sawtooth}} \times T_{clk} = \frac{I_{ref}(R_{RTD} - R_{ref})}{A \cdot \frac{V_{DD}}{2^{NOB}}} \times T_{clk} \quad (5.1)$$

$$= \frac{I_{ref}(R_{RTD} - R_{ref})}{A \cdot V_{DD}} \times T_{Sawtooth} \quad (5.2)$$

Where T_{clk} is the clock period that runs the counter and is equal to $T_{sawtooth}/2^{NOB}$. $T_{sawtooth}$ is the period of the sawtooth waveform and NOB is the DAC's number of bits. The voltage step of the sawtooth waveform on its rising edge, $V_{step,sawtooth}$, is $V_{DD}/2^{NOB}$. The attenuation factor, called A , is applied to the sawtooth waveform to make smaller voltage steps at the input of the comparators and hence increase the sensitivity of the circuit to the changes of R_{RTD} .

The pulse-width is measured on-chip using a digital counter that works with a period of T_{clk} . Finally the output of the counter is proportional to the resistance difference and independent from the clock frequency :

$$N = \left[\frac{T_{pulsewidth}}{T_{clk}} \right] = \left[\frac{2^{NOB} I_{ref}(R_{RTD} - R_{ref})}{A \cdot V_{DD}} \right] = \left[\frac{2^{NOB} I_{ref}(\alpha \cdot \Delta T \cdot R_{RTD})}{A \cdot V_{DD}} \right] \quad (5.3)$$

Where α is the temperature coefficient of the R_{RTD} , and ΔT is the difference in the temperature of R_{RTD} and R_{ref} with respect to a temperature T_0 at which R_{RTD} and R_{ref} are equal. The design values for V_{DD} , I_{ref} , A , NOB , R_{ref} and α are 1.8 V, 2.3 μA , 1, 9, 400 k Ω (equal to the nominal value of R_{RTD}) and 0.00385, respectively. According to Eq. 5.3 this results in a nominal temperature resolution of 1°C.

Current source design

The current source, I_{ref} , is designed using an NMOS biased in its *zero temperature coefficient* (ZTC) bias point. The gate-source voltage of the NMOS transistor in its ZTC is provided by the bandgap reference circuit. The current I_{ref} is therefore independent from the temperature (in the typical technology corner, tt).

5.1.2 Simulation results

The simulated output of the digital counter versus the difference of R_{RTD} and R_{ref} is plotted vs. the equivalent temperature difference in Fig.5.2. The simulations were repeated in fast (ff), typical (tt), and slow (ss) corners. While the linearity of the output-input characteristics is held in different corners, the equivalent sensitivity to the temperature, which is the slope of the lines in Fig. 5.2 changes. The resulted resolution in fast, typical and slow corners are 0.74°C, 0.96°C, and 1.28°C respectively. The main reason for different sensitivities at different corners is the current source (I_{ref} in Eq. 5.3). Indeed while the current source is temperature-independent (in tt corner) it depends on the technology corner. In the fast corner (ff) the higher electron mobility results in a higher I_{ref} for a fixed gate voltage.

5.1.3 Measurement results

R2PC is fabricated together with ARIC (which is presented in the previous chapter) on a single Silicon chip in 0.18 μm technology and shares the bandgap and the DDS with ARIC.

The measurements on R2PC is acquired vs. different values of off-chip RTDs and plotted in Fig. 5.3. The measurements were repeated with 9 ICs to make statistics. In this plot the offsets of the lines- which is due to the deviation of R_{ref} from the nominal value- are removed. The measured minimum resolvable change in the resistor is 1.67 k Ω which corresponds to an equivalent temperature resolution of 1.080°C with a standard deviation of 0.048°C. This can be easily improved by increasing the attenuation factor, A , according to Eq. 5.3.

The equivalent temperature range can be calculated in theory by dividing the measurable R_{RTD} from Fig. 5.3 (i.e. $R_{ref} \pm 300 k\Omega$) to the temperature coefficient of the Pt-RTD. However, in this research we express the input range in the domain of resistance instead of temperature to correspond with the measurements.

5.1. Resistance to pulsewidth converter (R2PC)

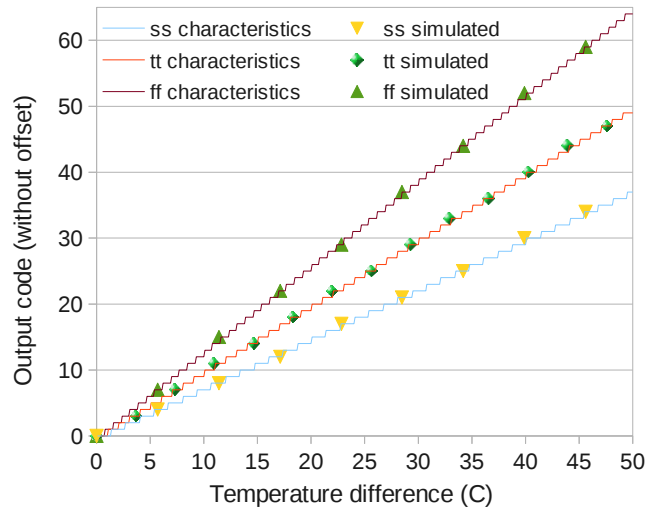


Figure 5.2: Characteristics of the temperature sensor in fast (ff), typical (tt), and slow (ss) corners. The markers represent the simulated points and the lines are interpolated characteristics of the circuit for each corner.

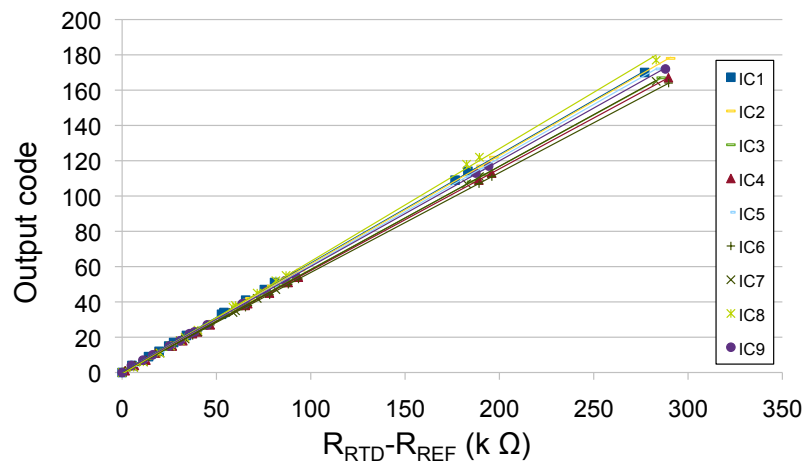


Figure 5.3: The measured output of the temperature readout in nine different ICs versus the difference between the off-chip RTD, R_{RTD} , and the on-chip R_{REF} .

5.2 Resistance to voltage converter (R2VC)

5.2.1 Circuit architecture

The R2PC circuit enables the measurement of resistors within a wide range ($R_{ref} \pm 300k\Omega$) while provides a limited resolution ($1.67k\Omega$ or $1.080^\circ C$). Moreover, the on-chip reference resistor R_{ref} introduces an offset in the measurements which is different from chip to chip. A second circuit is designed within this research to enhance the resolution. This is achieved by improving the design of the current source and removing the on-chip reference resistor, R_{ref} . The architecture of the circuit is shown in Fig. 5.4. The circuit converts the *resistance value into voltage* (R2VC). This is achieved through a precision current reference circuit with low temperature and supply sensitivity and without any external component.

The circuit consists of three main parts: (i) The first part is a bandgap reference circuit with a *proportional to absolute temperature* (PTAT) coefficient that generates voltage V_r ; (ii) The second one is a quasi-constant beta multiplier in which the resistor in conventional one has been replaced by an NMOS transistor M1; (iii) The third part includes the current mirror and the output stage. The first two parts create a constant current source (CCS) which flows into the Pt-RTD. The architecture of the CCS is inspired from [120]. The difference between the voltage drop across the Pt-RTD and the reference voltage is amplified and given to an ADC to be digitalized. The description of the three parts is given in this section.

In the R2VC shown in Fig. 5.4 the drain-source voltage of M1 is controlled by V_r in a negative feedback loop established by the OP_2 . The voltage V_r is less than drain-source saturation voltage of M1. Therefore, M1 operates in triode region. Assuming M1 and M2 have adequately long channel length, we can write the square law current equations for M1 (in triode) and diode connected M2 (in saturation). For $\frac{W_1}{W_2} = 2$ and $L_1 = L_2$, the output current I_{out} is obtained as follows:

$$\begin{aligned}
 I_{M1} &= I_{M2} = I_{out} \Rightarrow \\
 \beta_1 \times ((V_{gs1} - V_{th}) \times V_r - V_r^2/2) &= 1/4 \times \beta_1 \times (V_{gs1} - V_{th})^2 \Rightarrow \\
 (1/2 \times (V_{gs1} - V_{th}) - V_r)^2 &= 1/2 \times V_r^2 \Rightarrow \\
 V_{gs1} - V_{th} &= V_r \times (2 - \sqrt{2}) \Rightarrow \\
 I_{out} &= (6 - 4\sqrt{2})\beta_1 \times V_r^2 \approx 0.34 \times \beta_1 V_r^2
 \end{aligned} \tag{5.4}$$

Where $\beta = \mu_n C_{ox} W/L$ has a negative temperature constant due to the mobility factor μ_n . The μ_n is inversely proportional to temperature:

$$\mu_n = \mu_0 \times \left(\frac{T_0}{T}\right)^{3/2} \tag{5.5}$$

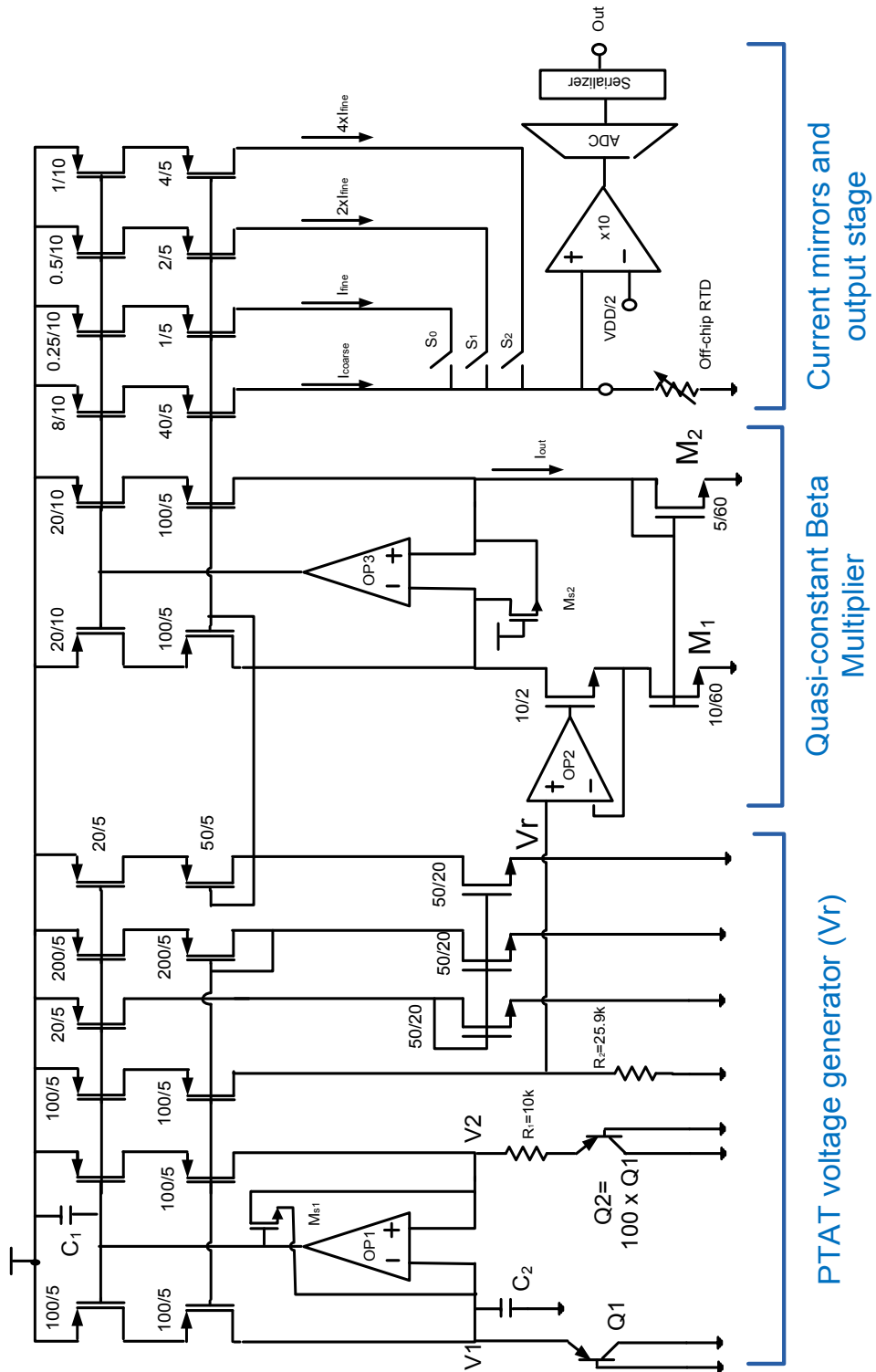


Figure 5.4: The schematic of the resistance to voltage converter (R2VC) circuit. A PVT independent current source is designed through a PTAT voltage generator and a quasi-constant beta-multiplier.

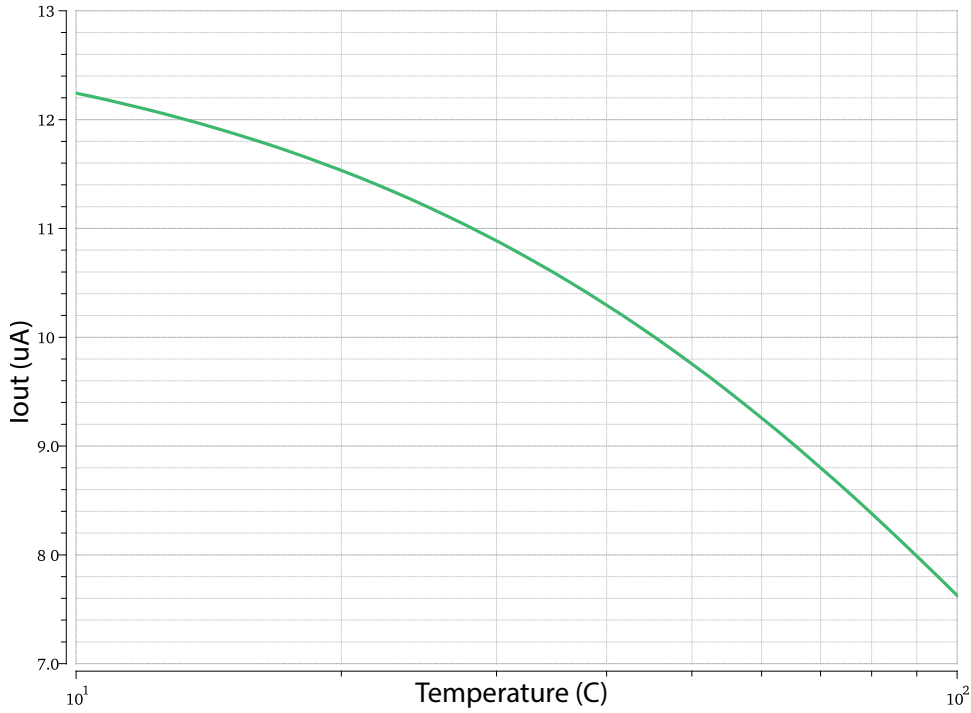


Figure 5.5: The variation of I_{out} with temperature when $V_r = 310 \text{ mV}$.

The variation of I_{out} versus the temperature for a constant V_r is sketched in Fig. 5.5. The circuit is simulated with connecting the positive terminal of OP_2 to a fixed temperature-independent supply voltage $V_r = V_{supply} = 310 \text{ mV}$. The value of the voltage supply is chosen such that a nominal current of $10 \mu\text{m}$ is achieved at I_{out} .

To make I_{out} independent of temperature, the V_r has to have positive temperature coefficient. This is achieved through the the PTAT voltage generator where the opamp OP_1 constitutes a feedback loop through which the voltages V_1 and V_2 are forced to be equal. As a consequence, the current through R_1 is proportional to the difference of the emitter-base voltages (V_{EB}) of Q_1 and Q_2 which has a positive temperature coefficient:

$$\begin{aligned}
 V_r &= \frac{(V_2 - V_{EB2})}{R_1} \times R_2 = \frac{(V_{EB1} - V_{EB2})}{R_1} \times R_2 \\
 &= (V_T \text{Ln}(N_{area})) \times \frac{R_2}{R_1}
 \end{aligned} \tag{5.6}$$

Where $V_T = KT/q$ is the thermal voltage (K is the Boltzmann constant, q is the charge of a single electron, and T is temperature), and N_{area} is the ratio of the emitter area of Q_1 and Q_2 .

The OP_1 , OP_2 and OP_3 are PMOS-input folded cascode opamps [121]. The PMOS input stage is proper for low level input voltages, it is used in the quasi beta multiplier. To push the PTAT

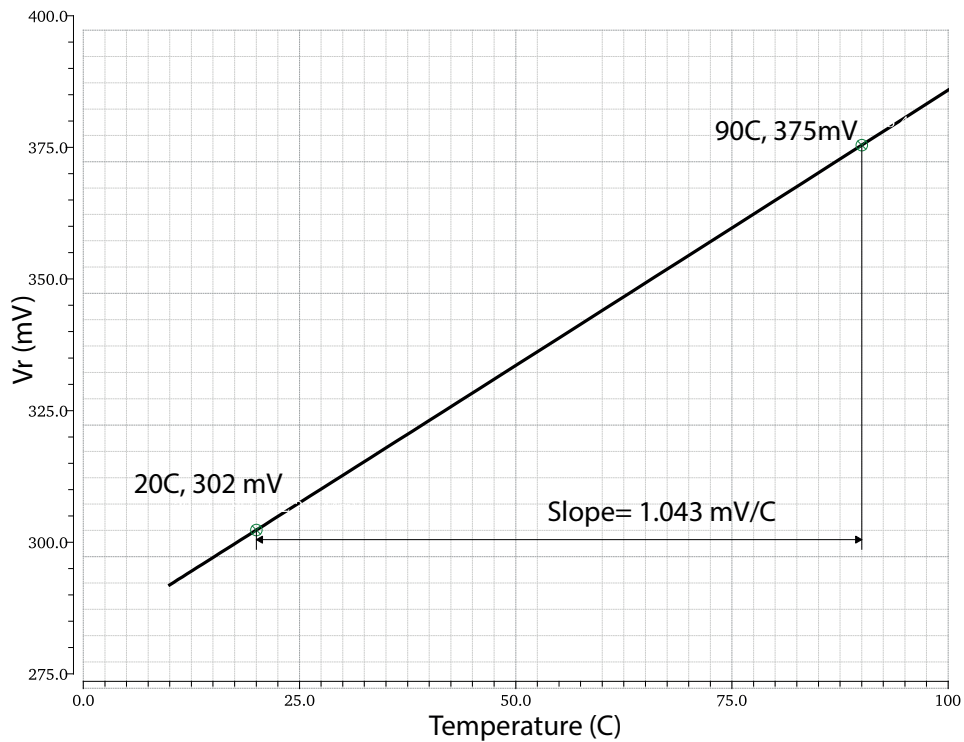


Figure 5.6: The V_r change in temperature that cancels the effect of μ_n in I_{out} .

voltage generator and the Quasi-constant Beta multiplier out of the unwanted zero bias at circuit start-up, The NMOS transistors Ms1 and Ms2 are added to the circuit.

5.2.2 Simulation results

The values of N and the ratio of $\frac{R_2}{R_1}$ are calculated from the simulation to achieve a temperature independent I_{out} . These are $N=100$ and $\frac{R_2}{R_1} = 25.9$. The resulted V_r and I_{out} versus temperature are plotted in Fig. 5.6 and Fig. 5.7, respectively. Simulations show that I_{out} varies only by 0.2% in the temperature range of 10 to 100°C. The integrated noise of the circuit in the frequency of 1 mHz to 1 kHz at the input of the ADC is 20 mV. Therefore, the equivalent temperature resolution of R2VC is 0.03°C.

The measured resistance of ten RTD samples (shown in Fig. 2.9) falls in the range of $(342 \pm 7) k\Omega$. And the temperature range of interest is 20 – 50°C in biological samples with a resolution of 0.03°C. This implies that the output voltage should fall within 300 digital values, and a 9 bit ADC is adequate to get this resolution. We used the 10-bit ADC available in the technology. A reference voltage of $V_{DD}/2$ for VCM in Fig. 5.4. Assuming a constant I_{out} and VCM, the change of the Pt-RTD from sample to sample introduces a systematic and variable offset at the output. In order to keep this offset within the linear range of the amplifier and the ADC, the current through the Pt-RTD has to stay between 4.54 μA and 5.2 μA . To achieve this and also to remove the process-dependant offset, the final current through the Pt-RTD is divided

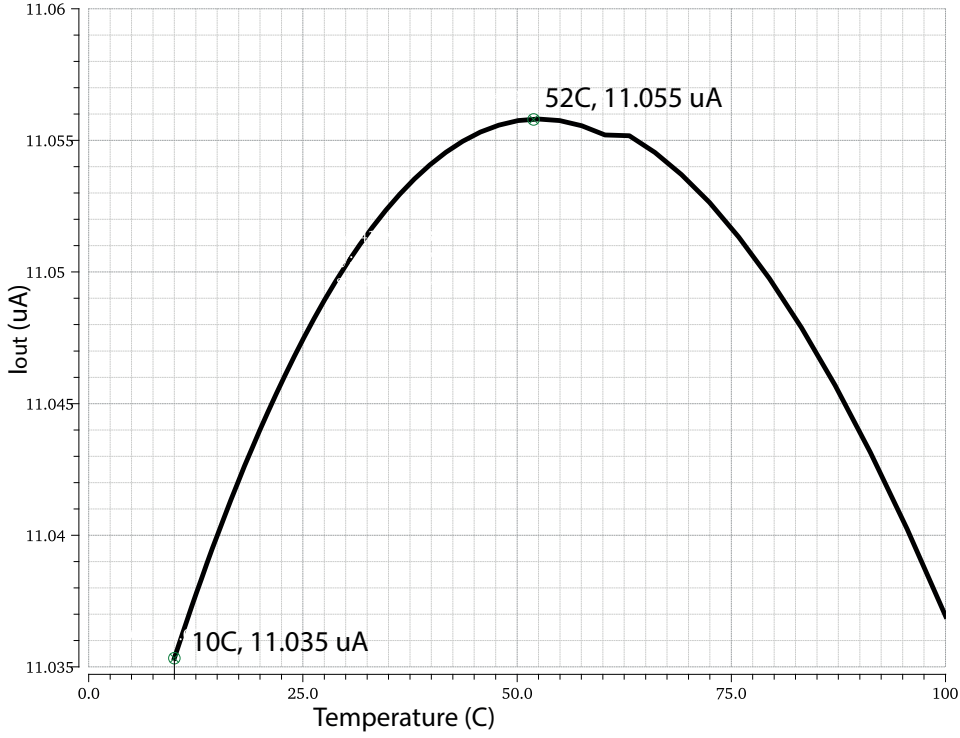


Figure 5.7: The variation of I_{out} with temperature when V_r is generated through the PTAT voltage generator.

Table 5.1: The characteristics of R2PC and R2VC circuits in the worst case scenario and comparison with state-of-the-art

Circuit name	R2PC	R2VC	[101]	[98]
Nominal Pt-RTD resistance ($k\Omega$)	400	342 ± 7	NA	NA
Detectable resistor range ($k\Omega$)	100 – 700	20 – 50	NA	NA
Min resolvable change in temperature ($^{\circ}C$)	1.08 (measured)	0.03 (simulated)	0.04	0.0001
Technology	UMC 0.18 μm	AMS 0.35 μm	0.18 μm	0.18 μm
Supply voltage (V)	1.8	3.3	1.8	3.3
Power consumption (μW)	12	330 (w/o ADC)	30	13000

into a fixed $I_{coarse} = 4.5 \mu A$ and adjustable $n \times I_{fine}$. Where n can be selected from 0 to 8 and $I_{fine} = 100 nA$. Both I_{coarse} and I_{fine} are driven from the I_{out} by the current mirrors. The simulated I_{coarse} in different corners is shown in Fig. 5.8.

$$I_{Pt-RTD} = I_{coarse} + n \times I_{fine} \tag{5.7}$$

The R2VC circuit is sent for fabrication in AMS 0.35 μm technology.

5.2. Resistance to voltage converter (R2VC)

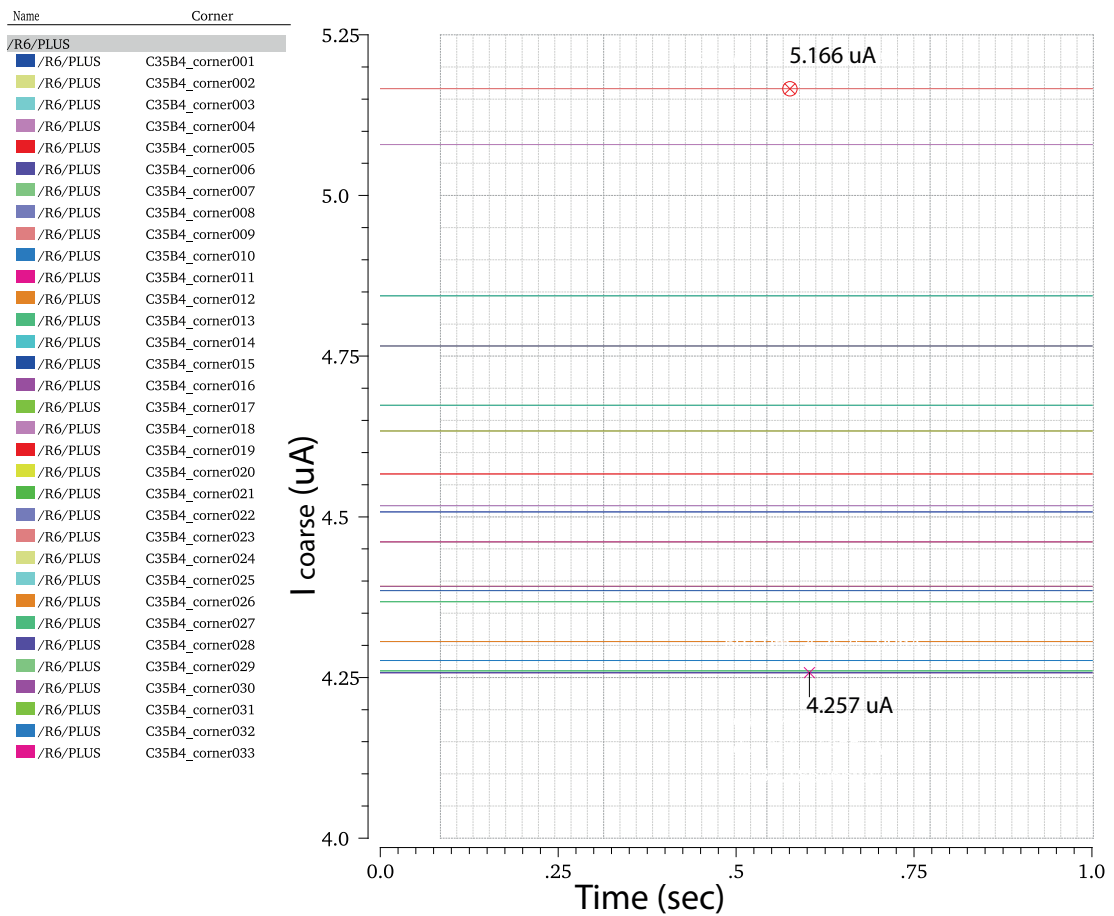


Figure 5.8: Simulated I_{coarse} in different process corners including Temperature= 30, 100; V_{Supply} = 3, 3.3, 3.6 V; CMOS model= ws wo wp wz; and resistor model= wp, ws.

5.3 Chapter contributions and summary

Two novel circuits are presented to readout off-chip Pt-RTD. The specifications of the circuits are summarized in Table 5.1. The R2PC and R2VC circuits are implemented in $0.18\ \mu\text{m}$ and $0.35\ \mu\text{m}$ technologies, respectively. R2PC offers wide dynamic-range for the input resistance while consumes little power and coarse resolution. R2VC instead measures a narrower range of temperature with an excellent resolution at the price of higher power consumption. These are the first circuits that measure a single off-chip resistor. In particular the novelty in these circuits is the design of the fully-on-chip temperature-independent current sources to drive the RTD.

6 Application of ARIC in remotely-powered implantable medical devices

In this chapter, the application of the *autonomous reconfigurable IC* (ARIC) in two *implantable medical devices* (IMDs) for *health-care monitoring* (HEM) and *personalized therapy* (PET) is presented. Tiny battery-less IMDs are developed to monitor multiple metabolites in the body. As described in Chapter 1, HEM-IMD aims for monitoring humans with chronic conditions while PET-IMD targets personalized therapy in laboratory animals like mice.

In addition to ARIC, the IMDs include a sensing platform and a powering system. In this chapter different parts and aspects of the IMDs as well as the integration and final validation of the IMDs are presented.

6.1 Application of ARIC in IMDs for HEM

The *health-care monitoring IMD* (HEM-IMD), as described in Chapter 1, is a wireless and battery-less device for multi-metabolite detection in the human body. The device is placed under the skin in the interstitial tissue. It reacts to the presence of certain bio-compounds (e.g. glucose, lactate, and ATP) in the fluid, detects and measures them and sends the measured data to a bandage like patch that is located on top of the skin. The patch sends power to the implant through the inductive link and receives the measurement data from HEM-IMD and sends them via blue-tooth to a more powerful device like an ipad or a smart-phone for processing and display. The conceptual diagram of the system is shown in Fig. 6.1. In this section the designs of the patch and different parts and aspects of HEM-IMD are presented.

6.1.1 The patch

The patch was designed by Jacopo Olivo at EPFL and is fabricated on a flexible FR4 platform [122]. Its photo is shown in Fig. 6.2. The patch is able to transmit up to 7 mW to HEM-IMD from a distance of 1 cm. The patch is a wearable device to power on HEM-IMD by means of an inductive link. It measures $69 \times 40 \text{ mm}^2$, and designed to be embedded into a skin patch and located over the implantation area. Downlink communication (patch sends commands to

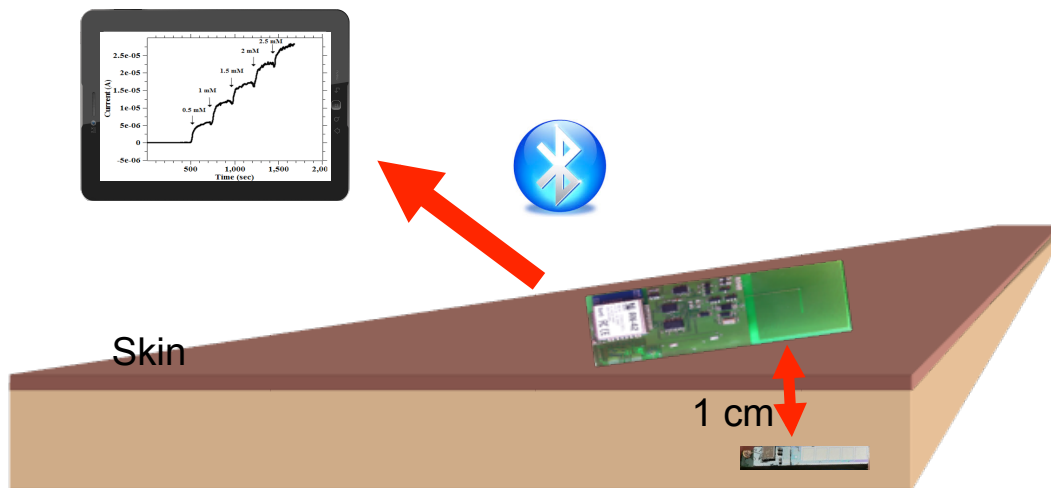


Figure 6.1: The conceptual diagram of the health-care monitoring system. The HEM-IMD measures multiple metabolites in the interstitial tissue and sends the results to the patch. The patch communicates the results to a more powerful device for processing, storage and display.

HEM-IMD) can be performed at 100 *kbps* by amplitude modulation. Uplink communication (patch receives data from HEM-IMD) is performed at 66.6 *kbps* by using load modulation. Long range communication between the system and remote devices is enabled by a blue-tooth module. The patch is powered by two rechargeable lithium-ion polymer batteries and has an autonomy of 10 hour in stand-by mode and 1.5 hour in transmitting mode [122]. Details on the design of the patch can be found in [122].

6.1.2 HEM-IMD

The conceptual diagram of the HEM-IMD is shown in Fig. 6.3. It consists of a sensor array to detect different metabolites. A pH and a temperature sensor are also placed for calibration of the biosensors. The design of the HEM-biointerface is discussed in details in Chapter 2 (Section 2.4). An inductor (i.e. receiving coil in Fig. 6.3) is placed on the bottom of the device for power and data transmission. In order to ensure a minimum-size HEM-IMD, the inductor size is minimized by adopting a multi-layer design approach [123]. Moreover, a single antenna is used for both data and power transmission. Finally, the front-end electronics rectifies and regulates the power received through the inductive link, controls and reads out the sensors, and transmits the data back to the patch through the inductive link.

Front-end electronics

The schematic view of the front-end electronics is shown in Fig. 6.4. It includes two ASICs: ARIC and *Health-care monitoring power management IC* (HEM-PMIC). The HEM-PMIC includes the voltage regulator and the load modulator. In this figure the parts coloured in blue



Figure 6.2: The wearable patch to transmit power and commands to the HEM-IMD and to receive measured data from it. It is powered by two lithium batteries. A blue-tooth module on the patch transmits the data to a more powerful device.

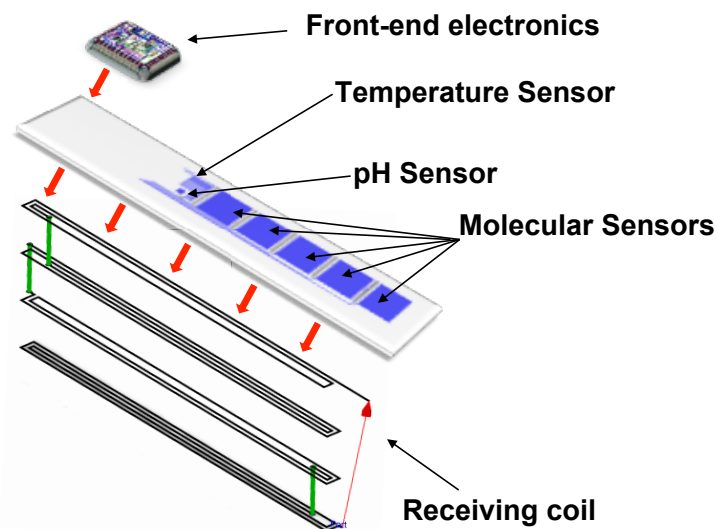


Figure 6.3: The conceptual diagram of the HEM-IMD for health-care monitoring. It includes five biomolecular sensors, a pH and temperature sensor for biomolecular calibration, a multi-layer inductor for power and data transmission, and front-end electronics to readout the sensors.

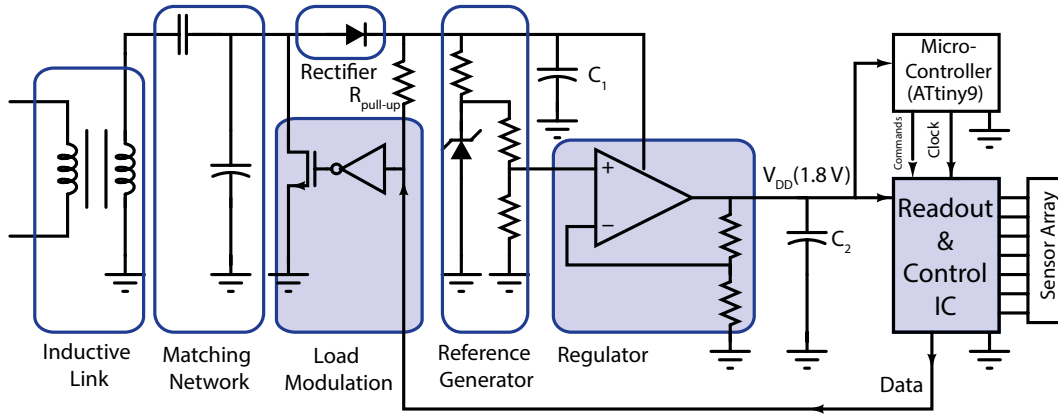


Figure 6.4: The schematic view of the front-end electronics of the HEM-IMD. The blocks coloured in blue are fully-integrated in ARIC and HEM-PMIC where HEM-PMIC includes the load modulator and the regulator. The rest of the blocks are realized by off-the-shelf components.

(ARIC, the regulator and the load modulation blocks) are integrated on-chip and the rest are of-the-shelf components. A purely capacitive matching network is used for impedance matching. The regulator is designed to deliver 1.8 V supply voltage to the circuits. C_1 and C_2 are placed to reduce the ripple of the V_{DD} . The inductive link, the HEM-PMIC, and the rectifier are designed by Jacopo Olivo and are presented in details in [123] and [124].

Finally, a tiny micro-controller (ATtiny9) is programmed to send the commands to the readout IC as soon as the system is powered on. This commands were originally planned to be sent to the implant through the patch. However due to synchronization problem in command communication between HEM-PMIC and the patch (due to the absence of a clock recovery circuit), the micro-controller is added to HEM-IMD to send the commands to ARIC. Three set of commands are sent to ARIC from the micro-controller: (i) set the CA measurement voltage to +650 mV; (ii) start the measurement; (iii) and send out data. In order to keep ARIC and the micro-controller synchronized, the clock of ARIC is also provided by the micro-controller. The micro-controller is $2 \times 2 \text{ mm}^2$ and, once programmed, its measured power consumption is 400 μW power from 1.8 V supply voltage.

Measurement results

The power and data communication between HEM-IMD and the patch are measured in the following way. The patch is placed 6 mm away from the receiving coil and sends power via the inductive link to HEM-IMD. The induced voltage at the receiving coil is rectified and regulated and given to ARIC and the micro-controller (V_{DD} in Fig. 6.4). As soon as ARIC and the micro-controller turn on, the micro-controller starts sending the commands to ARIC. This

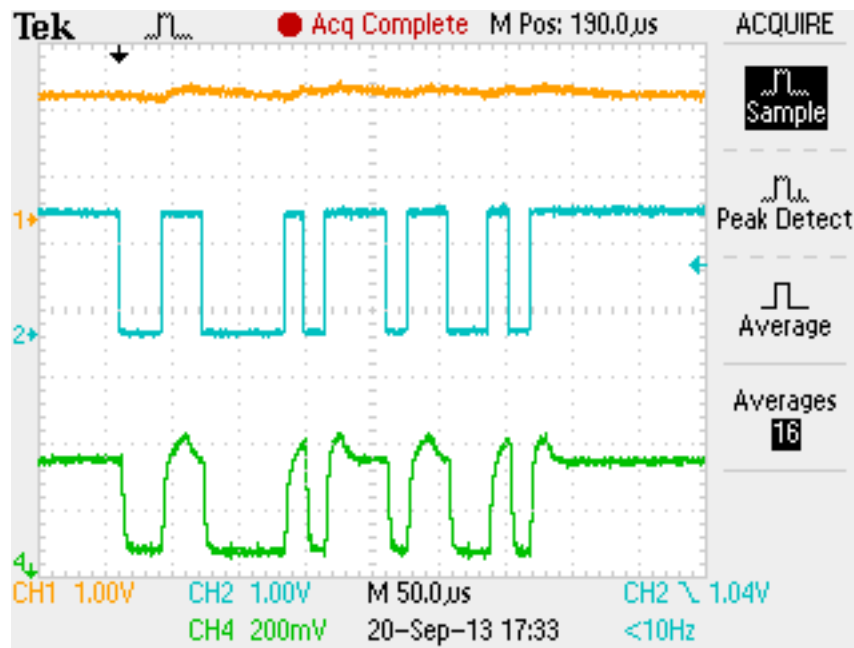


Figure 6.5: The measured signals in HEM-IMD and the patch. In orange: The induced voltage at the multi-layer receiving coil after it is rectified and regulated. In green: the data bit-stream at the output of ARIC. This data is given to the load modulator and is transmitted to the patch via backscattering. In blue: The received signal on the patch.

configures ARIC for a chronoamperometry measurement on one working electrode while it applies $+650\text{ mV}$ to it. ARIC streams out the measurement data to the load modulator. The load modulator transmits the bit-stream out of HEM-IMD by short-circuiting the receiving coil for the bits which equal zero (see *Data* in Fig. 6.4). The load modulation of the inductive link is detected on the patch, where data is reconstructed. The measured received signal at the patch, the transmitted data and the regulated voltage (i.e. the supply voltage of ARIC and the micro-controller) are shown in Fig. 6.5. Measurements also show that the regulator delivers more than 2 mW to its load which is enough for the energy demand of ARIC and the micro-controller. The bit rate of the data is 58 Kbps and the micro-controller sends the commands to the IC with a bit rate of 100 Kbps .

Final integration

Fig. 6.6 shows the fully-integrated HEM-IMD on a silicon substrate. The device measures $5 \times 25\text{ mm}$ and presents two main areas: the sensing area with all the electrodes and measurement area with the electronic components sketched in Fig. 6.4. ARIC and HEM-PMIC are placed in the measurement area and wire-bonded on the pads on the silicon substrate. They are then covered by (black) insulate rubber to protect the wire-bonding. The micro-controller is programmed and placed on the platform. The other off-the-shelf components are placed

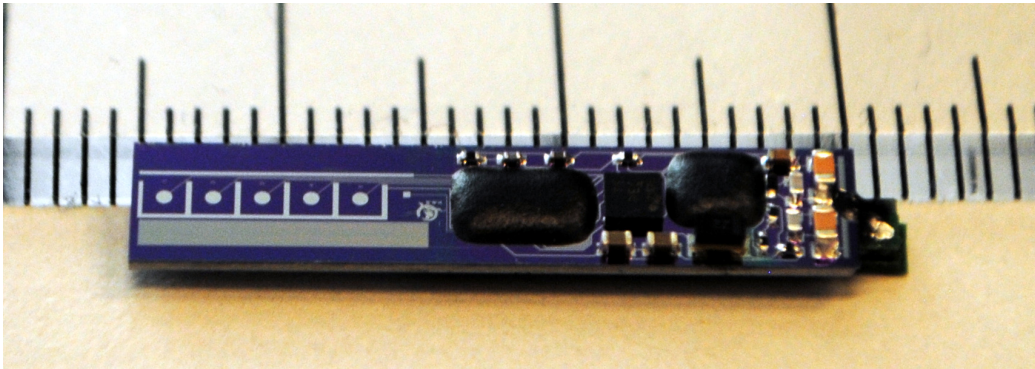


Figure 6.6: The photograph of the fully-integrated HEM-IMD with two main parts: the sensing area on the left and the front-end electronics on the right. The multi-layer inductor is placed on the bottom of the device and wire-bonded to the pads on the top.

and soldered in the dedicated areas. Finally, the multi-layer inductor is glued on the bottom side of the silicon platform and wire-bonded to the pads on the top for power and data transmission.

On the final test of the fully-integrated HEM-IMD, the start-up process was challenging. The main reason is the NMOS at the load modulator that creates a path to ground when *Data* is zero at the start-up. This short-circuits the receiving coil and turns-off the HEM-IMD. The pull-up resistor, $R_{pull-up}$ was added to turn off the NMOS during the start-up. This solution provided a proper start-up for HEM-IMD in the PCB level, where the resistor could be tuned to achieve a correct start-up. However, this solution was not effective when HEM-IMD was fully-integrated which hindered the integrated HEM-IMD characterisation. A possible solution to be applied during the design time is to remove the inverter from the load modulator in HEM-PMIC while also redesigning *Data* at the output of ARIC to be active-high (instead of active-low).

6.2 Application of ARIC in IMDs for PET

The healthcare system and the pharmaceutical research are demanding highly sensitive implantable devices for monitoring endogenous (i.e. glucose, lactate, ATP) and exogenous (i.e. drugs) metabolites to improve and personalize a therapy [125]. Small rodents are commonly used animals for developing new treatments and research applications, as they are low-cost models of mammalian regulator functions [126]. Because of the small size of the animal, IMD has to be small and light-weight. Therefore, we realized a fully implantable device with a remote powering system for monitoring glucose and drugs in small animals. The scheme of the PET is shown in Fig. 6.7.

PET-IMD is implanted in a laboratory mice and is powered through the inductive link. The

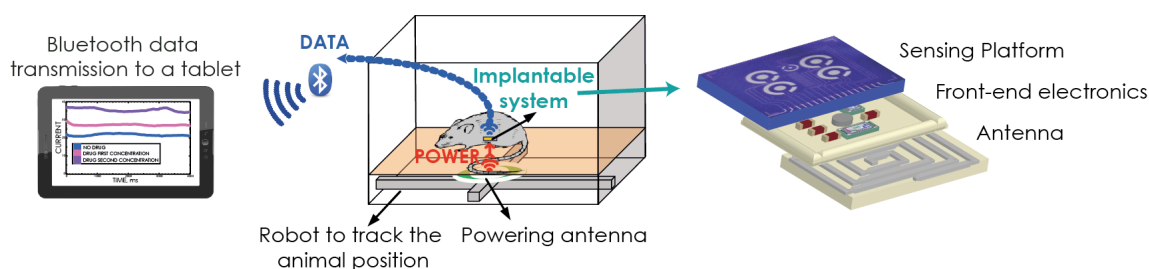


Figure 6.7: Scheme of the PET system with the data transmission via Blue-tooth to an Android interface (left), and the scheme of PET-IMD (right). PET-IMD is implanted in a laboratory mice and is powered through the inductive link. The external inductor is placed on a robot arm controlled with a servo-controlled system which moves it according to the position of mice to ensure constant powering of PET-IMD while the mice is moving.

external inductor is placed on the *external reader* (EXER) on a robot arm. The robot arm moves the EXER according to the position of mice to ensure constant powering of PET-IMD while the mice is moving inside the cage. The block diagram of PET-IMD and EXER is shown in Fig. 6.8. PET-IMD measures the metabolite and transmits the data to the EXER through a different carrier frequency. The data is then transferred via blue-tooth from the external reader to an iPad for filtering, display in real-time, and further storing.

Different parts and aspects of the system are presented in this section, followed by the full-system characterization with in-vitro glucose and paracetamol measurements.

6.2.1 PET-IMD

PET-IMD consists of three layers as shown in Fig. 6.7. The bottom layer hosts an antenna to receive power from the magnetic field. The middle layer hosts the front-end electronics. Finally the sensor array is placed on the top layer to measure glucose and drugs in the surrounding fluid.

The front-end electronics consists of two custom designed ICs: ARIC and the *PET power-management IC* (PET-PMIC). The same micro-controller (ATtiny9) described in the previous section is used here to send commands to ARIC.

Sensor array

The sensing platform is designed to monitor biological parameters of the body and is placed on top of the implant in order to be exposed to the fluid. The photograph of the sensor array is shown in Fig. 6.9. It hosts four working electrodes (WEs) with 1 mm or 0.5 mm diameter, sharing a common counter electrode (CE) and a reference electrode (RE), with the addition of a Pt-RTD as a temperature sensor and an Iridium-oxide pH sensor. The choice of the pH and temperature sensor is justified in Chapter 2 (Section 2.4). The sensor array measures

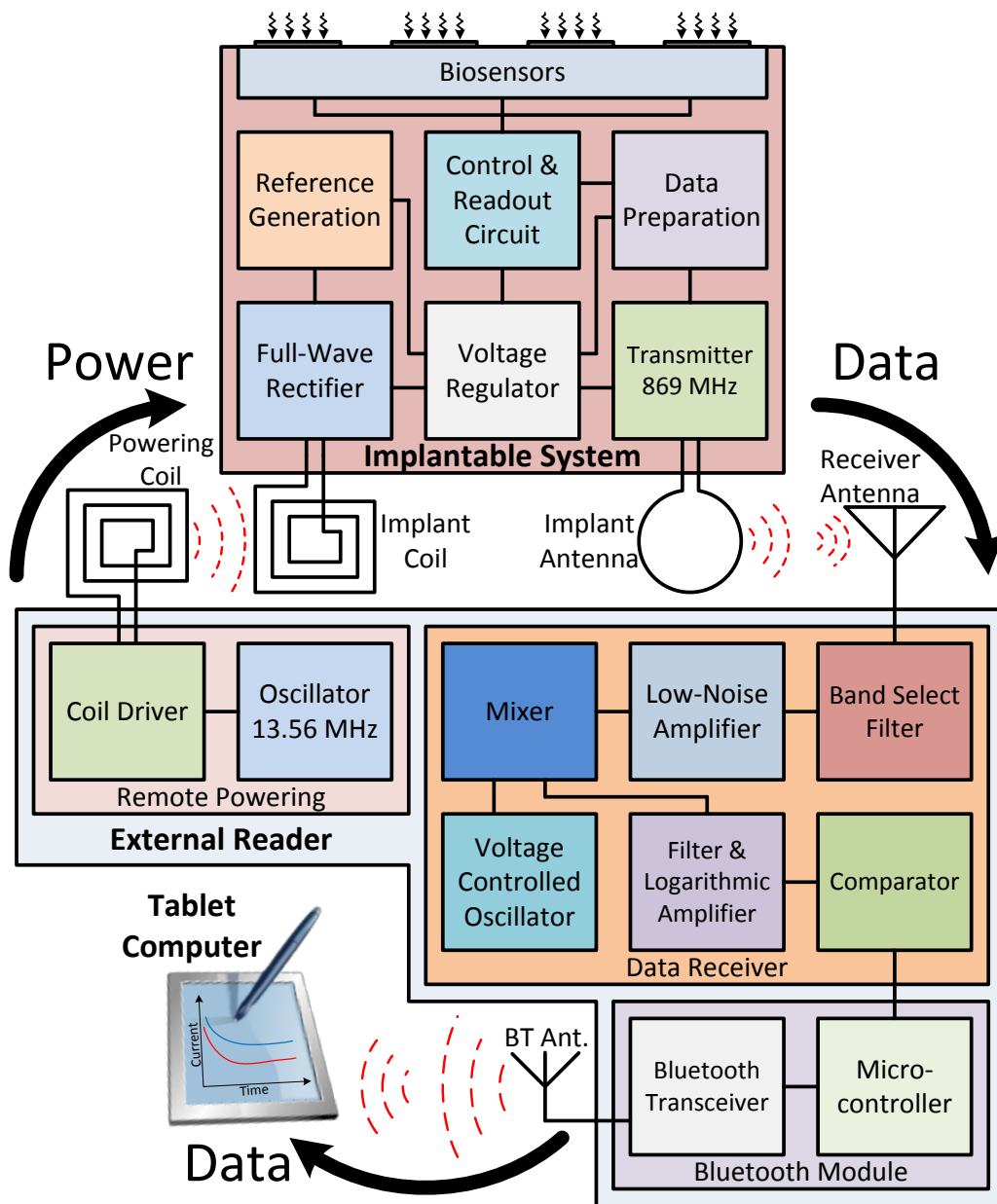


Figure 6.8: Block diagram of the PET system. It consists of PET-IMD on the top, the external reader (EXER) on the bottom and the tablet on bottom-left. The external reader sends power to PET-IMD at 13.56 MHz, and receives the OOK-modulated data at 869 MHz. The data is validated and sent to an Android device by the EXER.

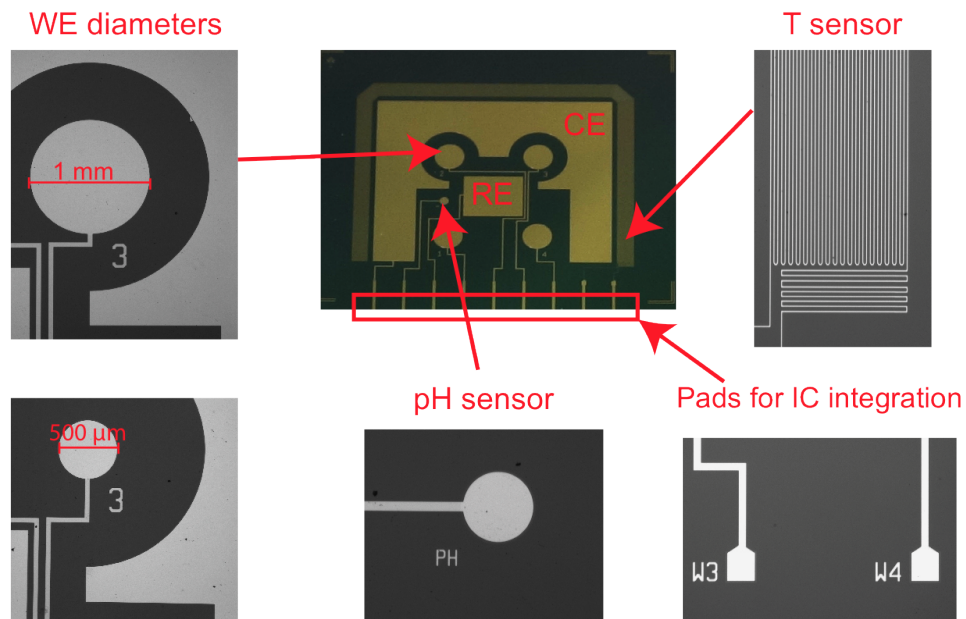


Figure 6.9: The micro-fabricated sensing platform of the PET-IMD. Reprinted from [13].

12x11 mm in order to fit the size of the coil (12 × 12 mm) and the wire bonding. Metallizations are made in Pt and passivation in Al_2O_3 by Camilla Baj-Rossi at EPFL. Details on the process flow can be found in [4].

PET-PMIC

The *PET power-management IC* (PET-PMIC) includes a passive full-wave rectifier to create a DC voltage from the induced AC voltage on the receiving coil. The block diagram of PET-IMD is shown in Fig. 6.8 with emphasis on PET-PMIC. PET-PMIC also includes a low drop-out voltage regulator, a reference voltage generator, and a transmitter. The regulator follows the rectifier to create a noiseless and stable 1.8 V voltage supply for PET-IMD. The reference generator circuit creates 0.9 V reference voltage for the voltage regulator.

A low-power transmitter is implemented using a free running LC-tank oscillator working at 869 MHz. The inductance of the oscillator acts also as the transmitting antenna. ARIC streams the data out to PET-PMIC to modulate the transmitter. The communication is then achieved by *on-off keying* (OOK) data modulation and is read on the receiver antenna on the EXER.

PET-PMIC is designed by Enver Gurhan Kilinc, at EPFL [127]. Some important specification of the circuits in PET-IMD are as follows. The rectifier has 80% of measured power efficiency for 2 mW load. The *power supply rejection ratio* (PSRR) of the voltage regulator is more than 60 dB at 27.12 MHz. The measured bit-error-rate of data communication is less than $15 \cdot 10^{-5}$

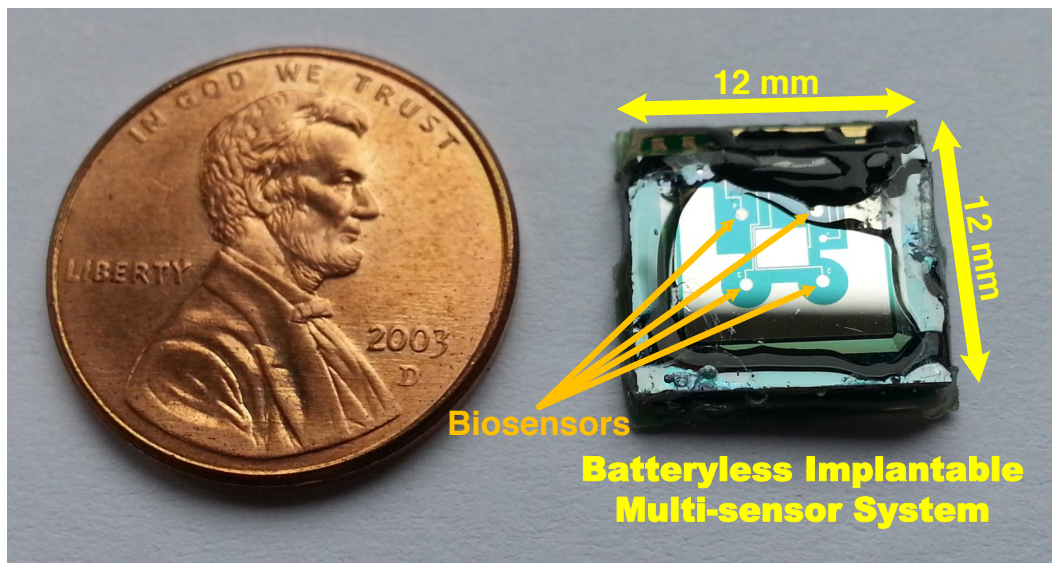


Figure 6.10: fully-integrated PET-IMD covered with bio-compatible glue. PET-IMD is a batteryless IMD for multiple-metabolite detection in laboratory animals.

for 30 *cm* communication distance at 1 *Mbps* data-rate. More details about PET-PMIC can be found in [127] and [128].

Final integration

The epoxy adhesive (EP42HT-2Med system) was used to assemble the three layers of PET-IMD. The interconnections between the platinum pads on the top layer and the gold pads on the middle layer were realized with Aluminium wire bonding and were protected with a glob top protection of 0.3 *mm*. A 10 μm layer of Parylene C was deposited by chemical vapour deposition using a Comelec C-30-S Parylene Deposition System. Parylene C was used to cover the whole device except the sensor array that needs to be in contact with fluids. A biocompatible Silicone (NuSil MED-6233), was used to cover the edges and to fill the empty space between the layers. *In-vivo* experiments were performed to verify the biocompatibility of the package once implanted for 30 days in mice [13]. The low inflammation level at the implant site proved that the host has accepted the implant. Fig. 6.10 shows the photograph of the assembled implantable device.

6.2.2 EXER and Android interface

The EXER transfers power to PET-IMD at 13.56 *MHz*, and receives data from it at 869 *MHz*. Two different channels were designed for data and power transmission to achieve reliable communication [127]. The external reader (i.e. the EXER) is shown in Fig. 6.8. It has three main blocks: (i) a remote powering unit to drive the inductive link and send power to PET-IMD (ii) a custom designed data receiver to receive the data from the implant; (iii) a blue-tooth module

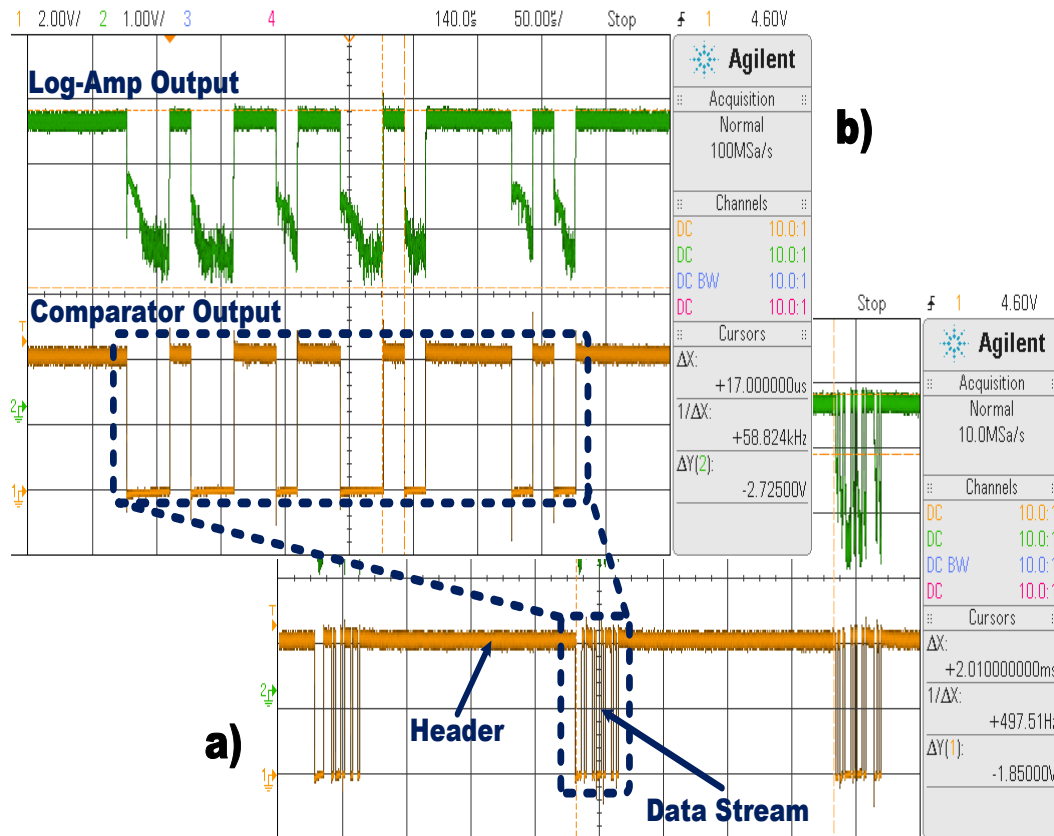


Figure 6.11: (a) Transmitted data out of ARIC on PET-IMD; (b) received data at the output of the logarithmic amplifier on the EXER (in green) and on the EXER comparator (in orange).

to communicate with a more powerful device for data storage and display. A class-E power amplifier is chosen due to its high drain efficiency to drive the powering inductive link. It is optimized at 13.56 MHz to achieve maximum power transfer [127].

As explained before, the implant uses an OOK transmitter implemented with an LC tank oscillator. Since the operation frequency of such oscillator drifts with the temperature and process corner, the custom-designed data receiver is implemented to compensate the frequency drifts in the transmitter. A super-heterodyne receiver is designed together with a custom dipole receiver antenna. A band-select filter with a large bandwidth is placed after the antenna to compensate the frequency drift. A low-noise amplifier is used to amplify the received RF signal followed by a mixer to down-convert the received signal to lower frequency where the filter has better quality factor. A logarithmic amplifier changes its output according to its RF input power level. In this way, the logarithmic amplifier converts the received RF burst to a corresponding DC voltage which creates the bit "1". Finally the logarithmic amplifier drives a comparator to regenerate the data bit-stream. Fig. 6.11 shows the sensor data together with the received bit-stream on the logarithmic amplifier and the comparator.

The data is then transmitted to the blue-tooth module. The blue-tooth module validates

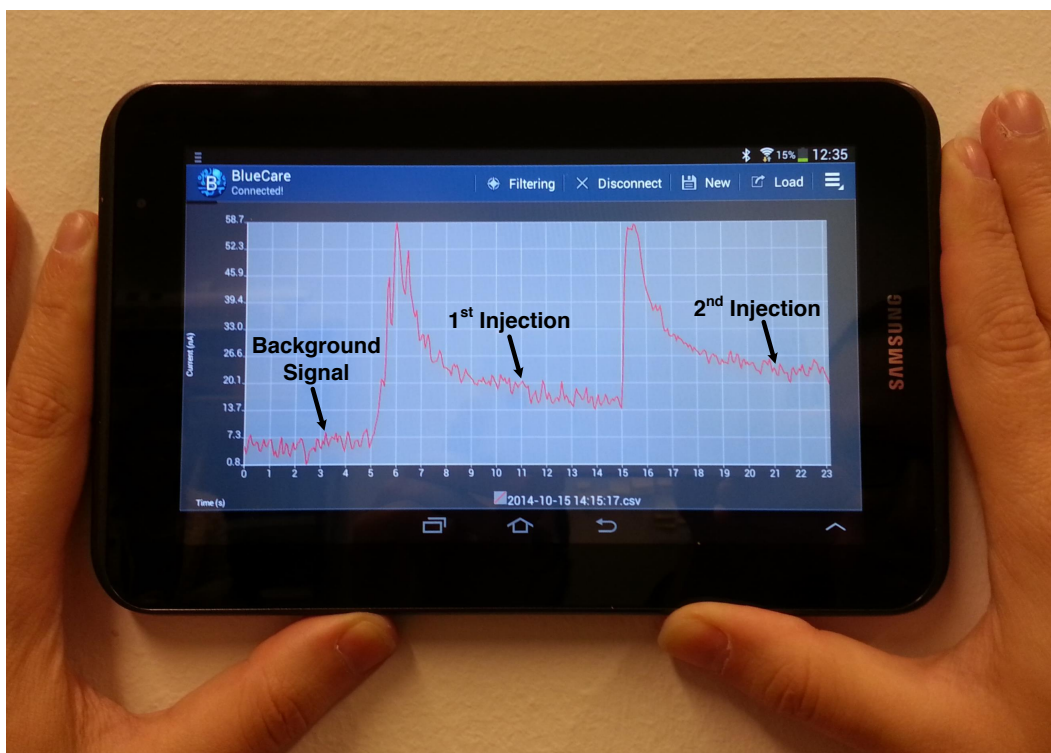


Figure 6.12: Continuous bio-monitoring application on the Android interface during the measurement of Paracetamol with PET-IMD. Two injections of Paracetamol are distinguishable.

and transmits the data to an iPad or any other Android device (e.g. a smart-phone). The data validation is done by a micro-controller that is programmed to sample each bit of the received data, decode it and determine if a transmission error has occurred. The data is then transmitted by UART protocol to a commercial blue-tooth transceiver. The blue-tooth transceiver communicates with an iPad that is driven by an Android interface to filter and display the data in real-time.

In order to allow continuous monitoring of the target metabolite, the Android interface is chosen because it is open-source and used for a wide range of mobile devices.

The communication and the data transmission between the Android interface and the EXER is achieved through Blue-tooth technology. The algorithm and design of the Android application is designed by Jacopo Olivo and Lorenzo Foglia, and optimized by Gregoire Surrel and Francesca Stradolini (all in LSI at EPFL) and presented in details in [129]. The application provides noise filtering possibilities of real-time data (moving average, median value, IIR filter, etc.). The application can, therefore, receive and plot a large amount of data by optimizing space occupation in the external memory of the device, which could be added to any tablet or smart phone. Fig. 6.12 shows the continuous monitoring on the Android interface during the detection of Paracetamol.

6.2.3 Servo-controlled system for wireless power transfer

Previous studies have presented remote powering systems for a moving animal with an array of coils under the animal's cage [130–132]. These systems are based on tracking the animal inside the cage and turning on the closest powering coil to the animal's location. However, the power transfer efficiency decreases drastically when the animal moves towards the edges of the powering coils. Moreover, the power transfer to IMD interrupts when the animal moves from one powering coil to another powering coil. In order to avoid the interrupts, the number of the powering coils is increased to recover the dead-zones (i.e. zones where the power transfer efficiency is less than 1%). However, adding more powering coils creates undesired coupling between the powering coils and degrades the wireless power transfer efficiency.

We designed a servo-controlled system to ensure continuous power transmission to PET-IMD when the animal is moving. The servo-controlled system tracks the animal inside the living space and moves the powering coil accordingly. Fig. 6.13 shows the photograph of this servo-controlled system designed and implemented by Enver Gurhan Kilinc at EPFL. A permanent magnet is placed in the middle layer of PET-IMD to create a magnetic field which can be sensed by the magnetic field sensors on the servo-controlled system. The magnetic sensors data is processed and then used to monitor the animal position. According to this, servo-controlled x and y rails move the powering coil in order to keep the coupling between PET-IMD and powering coil at the maximum level. The distance between PET-IMD and the powering coil is 3 cm for which the powering and the implant coils are optimized for maximum power transfer efficiency. The optimized sizes of the powering and the implant coils are 80x80 cm and 12x12 cm, respectively [127].

6.2.4 Measurement results

The performance of PET-IMD is validated by the *in-vitro* test set-up as shown in Fig. 6.13. The permanent magnet is installed in PET-IMD to track the IMD. The servo-controller system locates PET-IMD and moves the powering coil accordingly to ensure continuous power transmission to the IMD. To test the system, we moved PET-IMD randomly to emulate the moving of the animal. The test showed that the servo-controller system tracks the PET-IMD and transfers the power to it when it is moving efficiently. To perform a bio-measurement, the metabolites were injected on the PET-IMD while it was fixed.

PET-IMD is tested *in-vitro* by chronoamperometry measurements of paracetamol and glucose. Measurements related to paracetamol detection are acquired by depositing a drop of 100 μl of *Phosphate-buffered saline* (PBS) solution covering all the electrodes on top of PET-IMD. Paracetamol is then injected at fixed concentration (0.5 mM). Paracetamol (Acetaminophen) is a well-known anti-inflammatory drug [133]. Moreover, it is an electro-active species that can be oxidized at a constant voltage of +650 mV. At this voltage Paracetamol is transformed into its oxidized form, *N-acetyl-p-benzoquinone-imine* [133]. The initial current value (background signal) related to PBS is considered as the baseline, so that the successive values of current are

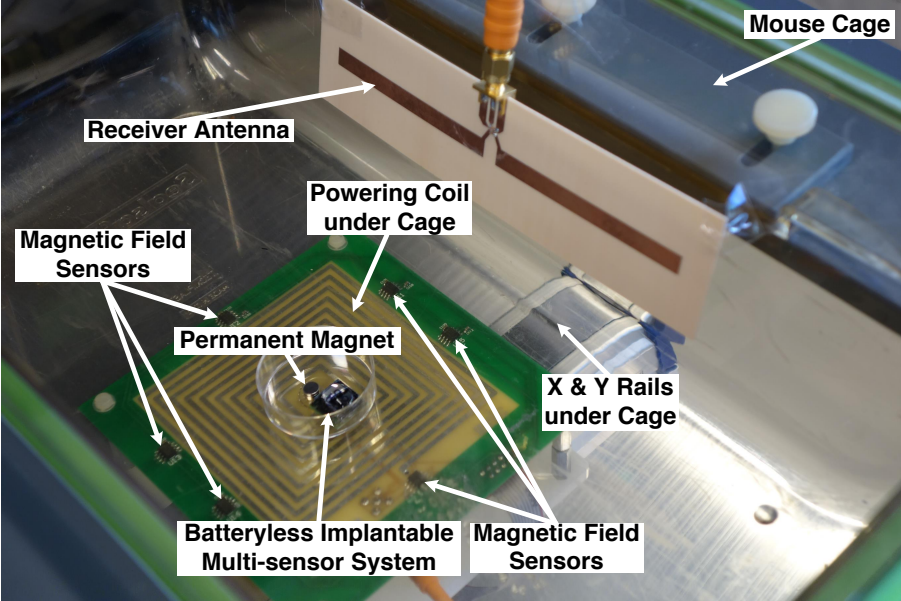


Figure 6.13: The in-vitro test set-up for the measurement of Paracetamol and glucose with PET-IMD and the servo-controlled system.

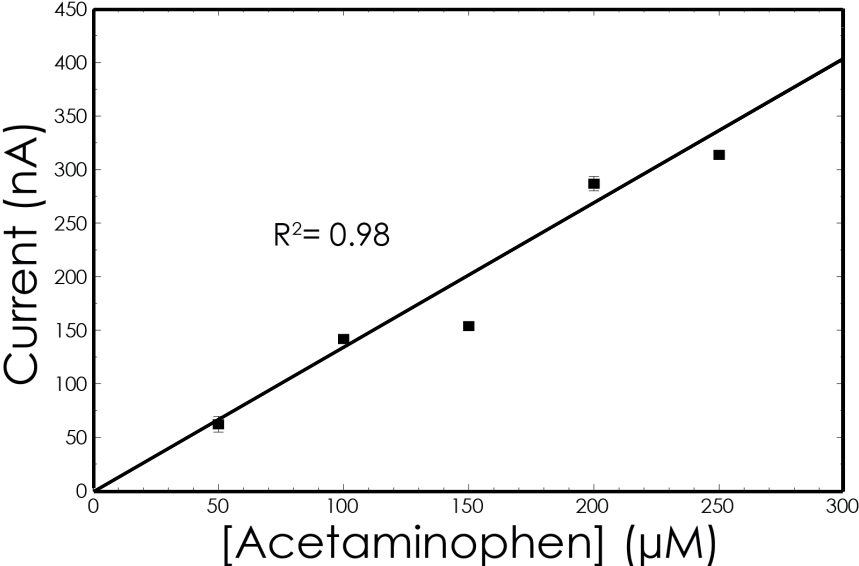


Figure 6.14: Calibration curve obtained during the in-vitro measurements of paracetamol with PET-IMD.

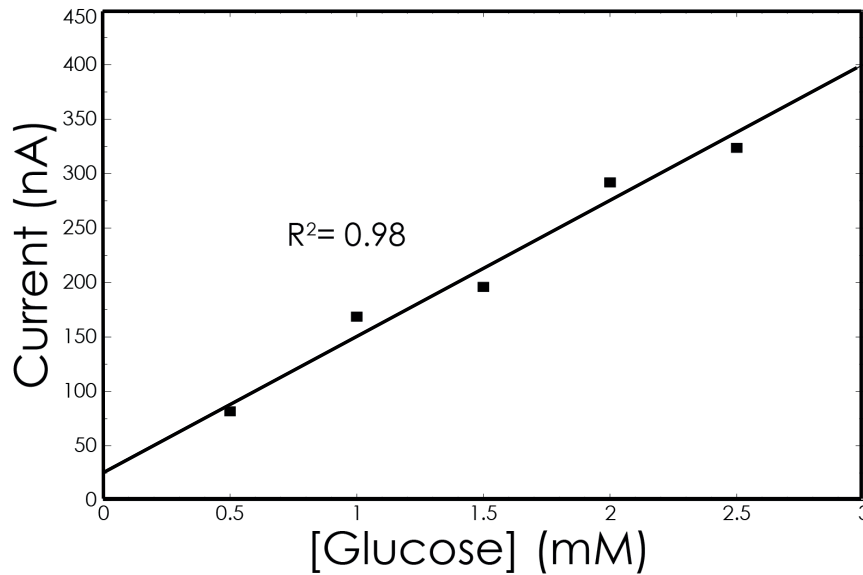


Figure 6.15: Calibration curve obtained during the in-vitro measurements of glucose with PET-IMD.

referred to the baseline value (i.e. the offset is removed). Fig. 6.14 shows the calibration curve calculated during the detection of paracetamol at different concentrations. Two successive injections of the same amount of paracetamol result in a similar increase of the current with respect to the baseline. The obtained sensitivity of the system to paracetamol is $66 \pm 21 \frac{\mu A}{mM \times cm^2}$ and the LOD (calculated according to the definition in Chapter 2) is $34 \pm 11 \mu M$.

We repeated the same measurement procedure with glucose instead of Paracetamol. The measured calibration curve is shown in Fig. 6.15. The resulted sensitivity to the glucose is $38 \pm 11 \frac{\mu A}{mM \times cm^2}$ and the LOD is $0.6 \pm 0.3 mM$ which is relevant in many clinical applications. Although the calibrations are non perfectly linear, we can conclude that the PET-IMD can autonomously receive power, actuate the sensors to measure glucose and Paracetamol within the physiological range, read the data and transmit them to an external reader. The detectable glucose concentration is less than $3 mM$ in this measurement which corresponds to the hypoglycaemia condition. Indeed, the functionalized glucose sensor in this measurement saturates at higher concentration. The addition of a selective and compatible membrane to the sensor expands the linear range of the detectable glucose concentration into the physiological range[110].

6.3 Chapter contributions and summary

In this chapter the application of ARIC in IMDs for health-care monitoring and personalized therapy is discussed, where ARIC provides the control and readout of the electrochemical sensor array of the IMDs. The IMD for health-care monitoring (HEM-IMD) is a battery-less

Chapter 6. Application of ARIC in remotely-powered implantable medical devices

and wireless tiny device with a sensor array to measure multiple-metabolites in the human body. ARIC is powered through the inductive link, controls and reads out the electrochemical sensors, and streams out the measured data to a load modulator that transmits the data to the patch. The implant is a heterogeneous system that includes a number of custom-designed (ARIC and HEM-PMIC) and commercial (e.g. micro-controller) components. The power and data transmission between the implant and the patch is validated by measurements at PCB-level.

Another IMD aimed for drug- and metabolite- monitoring in laboratory animals was developed, in which ARIC stimulates and reads out the sensors. This is an autonomous and fully-integrated tiny ($12 \times 12 \text{ mm}$) device, that includes three different layers: sensor, electronics and antenna. This fully integrated PET-IMD is successfully tested in-vitro to perform glucose and paracetamol measurements. The measured current of the sensor is displayed on an ipad in real-time thanks to the custom-designed Android application.

As a line of future work, we will consider to monitor other relevant metabolites and drugs such as Lactate, Mitoxantrone, and Ifosfamide with PET-IMD, as well as in-vivo measurements of metabolites (such as glucose and paracetamol) in mice.

I contributed to both PET and HEM systems with *(i)* ARIC; *(ii)* program and successfully testing the ATtiny9 micro-controller with ARIC for both PET- and HEM-IMDs; design and successfully testing the PCB-level connections of the front-end electronics of HEM- and PET-systems, in particular *(iii)* ARIC and HEM-PMIC and *(IV)* ARIC and PET-PMIC.

7 A lightweight cryptographic system for implantable medical devices

The development of new *Implantable Medical Devices* (IMD) has allowed blood tests to be performed in the patient's body anywhere and at any time instead of in the laboratories. However, the increased reliance on the IMD technology, especially in the case of potentially life-saving therapies introduces difficult trade-offs in reliability and security. Personal health information that was once restricted to the confines of a medical laboratory, can now potentially be accessible to various unauthorized parties.

Recent examples of IMD include injectable subcutaneous devices that are remotely powered by a bandage-like patch that also provides a data link to a higher level wearable device, possibly a body area network or, eventually, a higher-level health information system. An example of such IMD is in the PET-system described in Chapter 6 which is re-sketched in Fig. 7.1. The wireless communication with the IMD allows sensor data and control commands to be transferred and become unprecedented exposed.

IMDs require a special set of security and privacy. A key problem with fully implanted sensors is that small infrequent wireless transmission poses a greater privacy risk than large or continuous transmissions. For example, a sensor may take several minutes to complete measurement, then deliver only a few bytes of data; giving this information a high value per bit that may make it an attractive target. Short data transmissions necessitate careful use of a cipher, especially if the data measured by the IMD take only a few different values. On the other hand, when a biosensor includes a patch that is meant to pair with the sensor, additional risks arise. For example, the patch of an unconscious patient can be removed and replaced by another patch to access the data of the implant without authorization. Other challenges are low-power and low-cost implementation, potential side-channel attacks, and key management issues. Conventional key management schemes can be used to allow access to the data by authorized parties from physicians, to insurance providers, emergency personnel, and even the user.

To address the need for a more secure IMD, we have designed a *lightweight cryptographic system* (LCS) for subcutaneous IMDs that provides security and privacy for the sensor data [14]. The LCS is designed in collaboration with Prof. Wayne Burleson (from University of

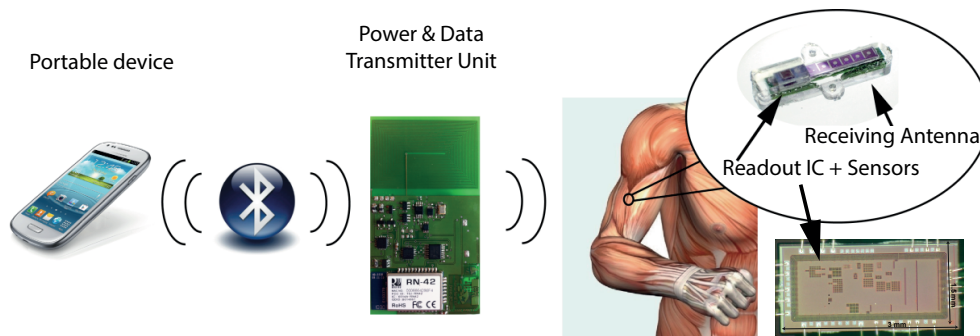


Figure 7.1: Fully implantable subcutaneous medical device powered by a patch located on top of the skin. The patch is wirelessly connected to a smart phone for further data analysis and decision-making.

Massachusetts at Amherst) and Dr. Tolga Yalcin (from University for Information Science and Technology, Ohrid, Macedonia). LCS is integrated into ARIC described in Chapter 4 as a part of the two IMDs introduced in the previous chapter: HEM-IMD and PET-IMD. The resulting heterogeneous system provides a unique and fundamental capability by immediately encrypting and signing the sensor data upon its creation within the body [14].

LCS uses the recently standardized Keccak [134] secure hash function implemented in an authenticated encryption mode. Keccak, the winner of the SHA-3 competition, is the best known and most analyzed sponge-based secure hash function. Moreover, Keccak allows various block sizes and different modes of operation.

The following section describes the threat models and the attacks to be prevented by LCS. Section 8.2 presents the position of the LCS block in ARIC and more in general in the IMD's front-end electronics. Section 7.3 gives an overview of previous researches on IMD security. Finally, the design of LCS as well as the simulation results on the synthesized system in *UMC 0.18 μm* are presented in Sections 7.4 and 7.5, respectively.

7.1 Threat models

Personal health data has the potential to be misused for financial gain, discrimination, tracking or violence among others [135]. However the implementation of strong security is at odds with the low-cost and low-power system described. Hence we take a somewhat non-traditional and asymmetric approach by relying on the trust of standard key distribution in higher levels of the system where cost is not so important.

The key classes of IMD vulnerabilities that researchers have identified are control vulnerabilities, in which an unauthorized person can gain control of an IMD's operation or even disable its therapeutic services, and privacy vulnerabilities, in which an IMD exposes patients

data to an unauthorized party. Both kinds of vulnerability may be harmful to patients' health outcome, and are avoidable [136].

Two threat scenarios we consider are: (i) trusted patch is removed and placed on a rogue implant (e.g. falsified data for insurance fraud) (ii) rogue patch is used to extract data from a trusted implant. (e.g. stealing of personal health data)

Our scheme also avoids potential weaknesses in the patch or in the Bluetooth link and higher levels. The patch is a low-cost device that cannot afford expensive tamper-proofing. Thus we must avoid storing secrets on the patch that could be somehow extracted and then used to clone the patch or otherwise impersonate the patch. The lightweight Bluetooth link does not need to be secure in our scenario either. Our approach avoids the need for two-way authentication by automatically encrypting and signing all outgoing data. This avoids potential replay or relay attacks, both recently demonstrated in automotive and smart-card applications [137]. We do not protect against potentially malicious control of the device. This is a topic for future research, but we expect standard authentication techniques to be used as a defence. Malicious control could either destroy or falsify biosensor data.

By selecting the newly standardized Keccak scheme, we benefit from the large amount of analysis and testing performed during the standardization process. In contrast, proprietary cryptographic schemes are often quickly broken due to their lack of exposure to the academic community.

7.2 System overview

The encryption and authentication system is implemented and integrated into ARIC so that the sensor data is signed and encrypted upon its creation inside the body. ARIC controls and reads out the sensor array and transmits the measured data back to the patch (see Fig. 7.1). The detailed description of all parts of ARIC, except LCS, is already presented in Chapter 4. The block diagram of ARIC including the LCS block and connections is shown in Fig. 7.2. The control and readout unit perform different types of electrochemical measurements on different sensing sites of the sensor array. The data is then digitized by an *analog to digital converter* (ADC) and goes through the data preparation unit to form a 16-bit long data. This data then goes through the Encryption/Decryption unit. The encryption unit takes four consequent data to form a 64-bit plaintext, and outputs a 64-bit ciphertext. The ciphertext, which is also divided in four words, is streamed out by the Tx/Rx interface. The parameters of the Encryption/Decryption unit (i.e. LCS) can be set through a standard test access port and boundary-scan architecture called *Joint Test Action Group* (JTAG).

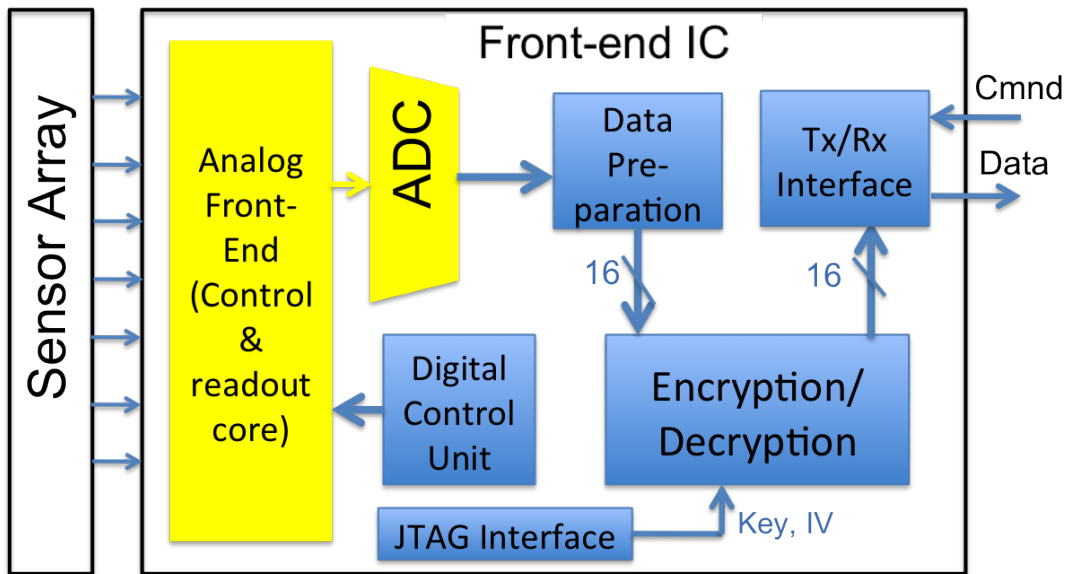


Figure 7.2: The block diagram of ARIC including LCS. The analog blocks are coloured in yellow and the digital blocks in blue, reprinted from [14].

7.3 Background

Given the security issues involving the IMDs, several solutions were proposed in the literature to enhance their security. In [138, 139], a hardware implementation (on FPGA and micro-controller) of the stream-cipher Hummingbird is presented. In [140], the use of block ciphers in IMD security is investigated. In [141] a mutual authentication protocol allowing a secure access to the IMD in regular situation as well as in emergency situations is presented. In [142] a lightweight wireless protocol for IMDs is presented that leverages well-studied wireless and cryptographic technologies. Recently, use of sponge-based hash functions for authenticated encryption of IMDs was introduced [143]. However in both works [142, 143] the actual power results and cryptanalysis, which are essential when proposing a new security protocol is not provided. LCS is the first ASIC-implemented cryptographic system for implantable biosensors, to the best of our knowledge.

Then, in [144] a system architecture was proposed for IMDs where security and medical functionalities are decoupled by running them on two separate cores while LCS is realized in a single core with the readout IC. Moreover, their proposed security core consumes more than $200 \mu W$ power which is higher than the power consumption of the LCS ($7 \mu W$). To guarantee security and safety through the proposed security protocol in [144], they proposed a system architecture for the whole IMD. A comparison between the proposed architecture in [144] and our target IMDs is not so straightforward, because the IMD in [144] is large and battery powered, while LCS targets mm-size and battery-less IMDs.

7.4 Security module

Security of biosensor data has to be guaranteed in various levels: During measurement and processing, from outside observers (also known as side-channel attackers [145]), during communication, and during storage from unauthorized users. There are several algorithms and standards designed and extensively analysed to achieve these goals. The internationally accepted *Advanced Encryption Standard*, AES, is perhaps the most widely used encryption algorithm. It is very well-analysed and proved to be secure. However, encryption alone is not enough. Authentication is another important operation that has to be performed on the secure data which is also very well-established and standardized by the *National Institute of Standards and Technology* (NIST). Authenticated encryption combines both authentication and encryption in order to provide confidentiality, integrity and authenticity of the data, simultaneously. It is proven to be much more effective, especially on resource-limited devices, than simultaneous use of an encryption algorithm and an authentication algorithm.

Block cipher based special modes of operation [146] are the most popular authenticated encryption schemes. More recently, use of sponge-based hash functions as authenticated encryption primitives has been proposed [147]. A sponge function or a sponge construction is a class of algorithms with finite internal state that takes an input bit stream of any length and produces an output bit stream of any desired length. It is built from three components: (i) *A state memory, S*, containing b bits which is divided into two parts, R of size r bits and C of size $c = b - r$ bits. The parameter r is called the bitrate and c is the capacity. (ii) *A function, f* , of fixed length that permutes or transforms the state memory. (iii) *A padding function P* : it appends enough bits to the input string so that the length of the padded input is a whole multiple of the bitrate, r . The padded input can thus be broken into r -bit blocks.

With its arbitrarily long input and output sizes, the sponge construction enables us to construct various cryptographic primitives such as hash function, stream cipher or message authentication code [148]. Keccak is the best known and most thoroughly analysed sponge-based hash function [134] and it offers a very lightweight construction, especially for hardware implementations [149]. Keccak can also be tweaked to operate with reduced state size, which makes it even more lightweight and the ideal choice for our application.

We use Keccak in DuplexSponge configuration, which is based on the SpongeWrap run in duplex mode [143]. In this mode, the key and the *Initialization Vector* (IV) are added to the zero initial state as a whole or in chunks. This process is known as the initialization phase, where the internal state of the cipher is initialized with both non-secret IV secret key. Following this phase, duplex operation begins, where the incoming plaintext is processed in blocks defined by the bit rate, r . The sponge function absorbs the incoming data blocks into its internal state, while the corresponding ciphertext block is generated in parallel. Upon completion of processing of all plaintext data, the authenticated tag is squeezed from the internal state in the finalization phase [14].

The generalized scheme is illustrated in Fig. 7.3, where *crop* and *pad* functions are simple

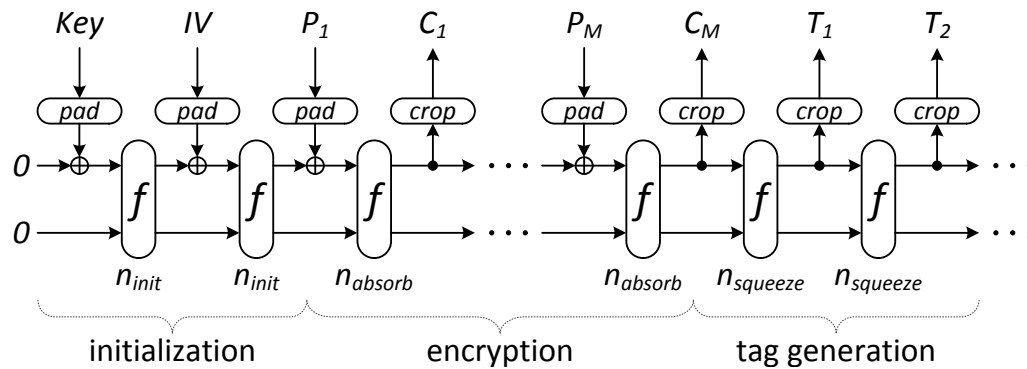


Figure 7.3: DUPLEXSPONGE construction for authenticated encryption, reprinted from [14].

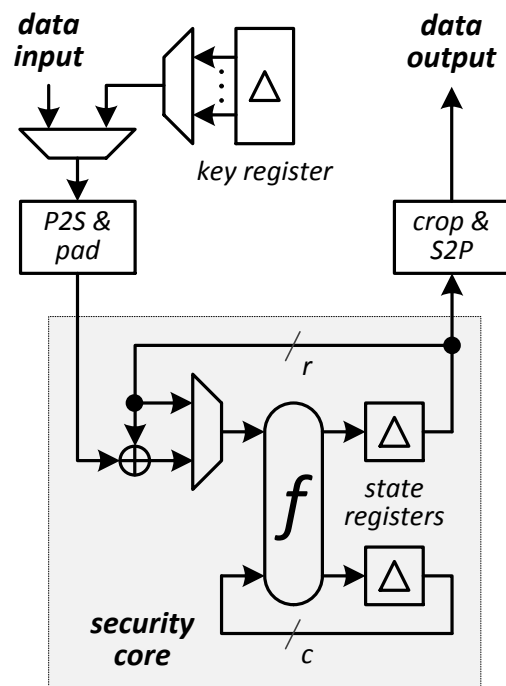


Figure 7.4: The implementation of the biosensor security module: permutation based authenticated encryption, reprinted from [14]

Table 7.1: Design parameters

<i>Parameter</i>	<i>Value</i>
Key size	80 bits
IV size	48 bits
Data (plaintext/ciphertext) size	64 bits
Tag size	32 bits
Sponge state size (b)	100 bits
Bitrate (without padding and parity)	4 bits
Bitrate (r)	7 bits
Capacity (c)	93 bits
First order preimage attack security	86 bits
Second order preimage attack security	46 bits

functions for bit removal and bit addition, respectively. In modified forms of the scheme, such as donkeySponge or monkeyDuplex [134], it is also possible to use the whole state input size b rather than the bitrate r for key and IV absorption. These specific forms even support different round counts for n_{init} , n_{absorb} and $n_{squeeze}$ in order to increase the average throughput [14]. In our design, we have used the same number of rounds for all in order to guarantee the security claim of the Keccak proposal.

However, instead of using the standard sizes for bitrate and capacity, we reduced the overall state size in order to achieve a compact implementation with a security level that would not have been possible at this cost with any other authenticated encryption scheme. The state size and data block size are selected as 100 and 4 bits, respectively. Together with 2 bits of padding and one bit of parity, this corresponds to a datarate $r = 7$, which provides first order preimage security of 86 bits ($= b - 2 \times r$) and second order preimage security of 46 bits ($= (b - r)/2$) [14]. The corresponding round number is chosen as 16, as stated in the Keccak specification. The design parameters are summarized in Table 7.1.

The block diagram of LCS is shown in Fig. 7.4. It consists of the security core and the interface wrapper. Upon start, the 80-bit parallel key is read from the key register in 4-bit packages. It then starts receiving 16-bit data packages (48-bit initialization vector, IV, followed by 64-bit sensor data) from the readout circuitry, which it also processes in 4-bit packages. The key, IV and plaintext data are absorbed into the sponge state. IV and ciphertext are sent to the transmitter. Finally, the internal state is squeezed from the security core in 4-bit packages in order to extract the 32-bit message authentication tag. All the 4-bit extracted data are converted to 16-bit parallel data at the output of the serial-to-parallel converter.

In order to achieve low power, we opted for a low bandwidth tweak of the Keccak secure hash function used in authenticated encryption mode. We also made aggressive utilization of bit-serial architectures in order to reduce combinational logic and minimize switching activity.

Table 7.2: Design specifications and performance

<i>Parameter</i>	<i>Value</i>
Clock frequency	500 <i>kHz</i>
Latency	1120 clock cycles
Throughput	100 kbps
Technology	0.18 μm
Power consumption(static+dynamic)	12 μW
Gate count (security core only)	1550
Total gate count (including wrapper)	2280

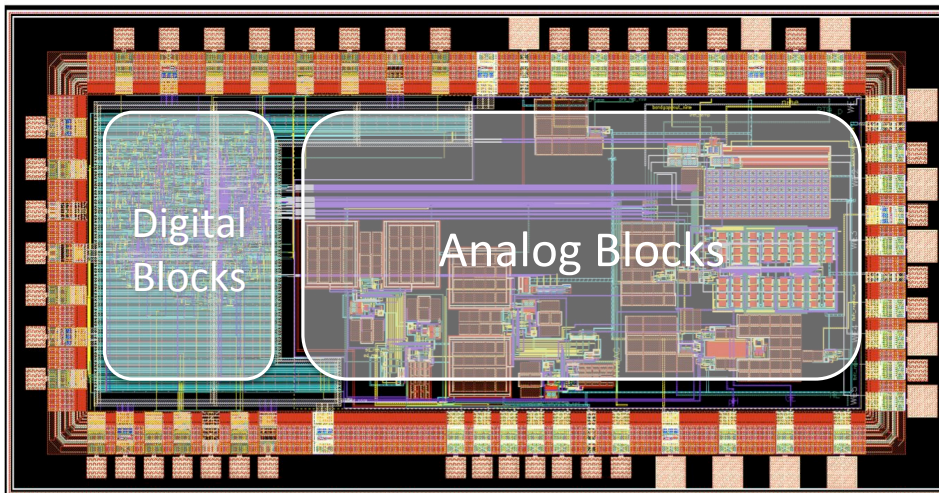


Figure 7.5: Layout of ARIC in 0.18 μm technology. LCS is synthesized together with other digital blocks of ARIC.

7.5 Simulation results

The behavioural model of LCS is simulated with random inputs on the encrypted/decrypted data while all other inputs (control signals, keys, etc) constant as is for verification. Then LCS was synthesised and parasitic information were extracted from this synthesis. The simulations were run again using these parasitics and actual gates (and their consumption).

The security core alone occupies only 1550 gate-equivalents (GE), which is the smallest authenticated encryption core reported up-to-date. Together with the interface wrapper, total area becomes 2280 *GE*. The simulated (static plus dynamic) power consumption of the whole design is below 12 μW at 500 *kHz* system clock. According to simulations, only 0.02% of this is static power. Since this is a low leakage technology, it is to be expected. Processing of each 4-bit block takes 20 clock cycles, resulting in a total of 640 cycles for initialization, 320 cycles for encryption and 160 cycles for tag generation. Specifications of the design and performance

results are summarized in Table 7.2.

Finally, LCS is synthesized together with other digital circuits in ARIC. The layout of ARIC in $0.18 \mu\text{m}$ technology is shown in Fig. 7.5, where the digital part and the analog circuits are depicted.

7.6 Chapter contributions and summary

To protect the wireless data transmission and to provide security and privacy for the IMD information, we designed and implemented a lightweight cryptographic system that uses a tweaked version of the Keccak secure hash function implemented in an authenticated encryption mode. LCS is implemented in $0.18 \mu\text{m}$ standard CMOS technology. It consumes only $12 \mu\text{W}$, which is 30-times less GEs of the only other implemented security core in [144], and it occupies 50 times less area. The implemented cryptosystem takes into consideration the unique threat models and constraints of the implantable biosensors. Therefore, it is a suitable cryptosystem to be integrated into the future IMDs to avoid vulnerabilities in both control and privacy.

8 Measurement of noise in amperometric electrochemical sensors

A better understanding of noise sources in electrochemical sensing is necessary to design the next generation devices for high sensitivity bio-sensing applications. Such understanding is also very useful to develop new models for the electrochemical sensors that can improve chip design simulations.

In general, the noise fluctuations found in nature falls into three classes according to their spectral densities: thermal noise; shot noise; and flicker noise [150]. Shot noise is a type of electronic noise, which originates from the discrete nature of electric charge. Shot noise is temperature and frequency independent, in contrast to thermal noise, which is proportional to temperature, and flicker noise, which is frequency-dependant. Flicker noise, or $1/f$ noise, is a process with a frequency spectrum such that the power spectral density of the noise is proportional to the reciprocal of frequency. The $1/f$ noise is the dominant noise source in low frequencies for the devices that exhibits this kind of noise.

We experimentally studied the noise of biosensors under different conditions in the domain of low frequencies [16]. The effect of the applied voltage and the analyte concentration on the noise level is investigated as well as effect of introducing CNTs on the electrode surface.

The noise in CNTs and sensors were already characterised separately in [30–32] and [33, 34], respectively. This is the first time that the noise in sensors incorporating CNTs is studied.

8.1 Material and methods

8.1.1 Preparation of electrodes

Nano-structured *screen printed electrodes* (SPE) were prepared by using *multi-walled CNT* (MWCNT) (see Fig. 8.1). To prepare the MWCNT modified SPEs, 30 μL of MWCNT Chloroform solution was deposited by drop-casting in the steps of 6 μL onto the working electrode and dried. All the samples were freshly prepared and used the same day.

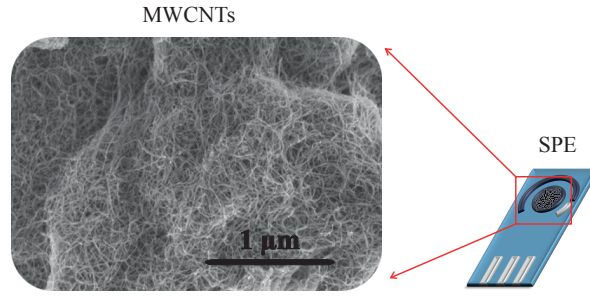


Figure 8.1: The screen printed electrode functionalized with CNTs. Reprinted from [15].

8.1.2 Apparatus

Two different target molecules, i.e. H_2O_2 and Potassium Ferrocyanide are chosen because of their popularity in electrochemical detection of biocompounds.

Chronoamperometry measurements of H_2O_2 and Ferrocyanide were carried out on bare graphite SPE and were repeated using SPE with drop-casted MWCNT. There are four variables to each measurement: (i) the applied voltage; (ii) the analyte concentration; (iii) the type of the analyte; and (iv) the presence of the MWCNT on the electrode. The sensor area would also affect both the signal and the noise of the sensor. However, in this study we keep the sensor area constant and only discuss the effect of the aforementioned four variables on the measured noise. To do this, we investigate the noise in frequency domain. The frequency spectrum of the noise is acquired by calculating the Fourier transform of the noise in time domain using the FFT algorithm. The time domain noise is extracted from the measurement data by subtracting the average sensor current from the measured current.

Fig. 8.2 shows a sample chronoamperometry measurement of Ferrocyanide in PBS solution using bare graphite electrodes. Consequent increasing of the current is obtained by injecting the proper amount of the Ferrocyanide into the solution. The applied voltage to the electrochemical cell, is kept at 300 mV in this measurement. The average current is considered the signal level of the biosensor. We assume that at low frequencies (i.e. less than 10 Hz) the dominant noise source is flicker noise. This is a reasonable assumption because the curve fitting with both flicker and white noise components gives negligible white noise compare to flicker noise, and hardly changes the flicker noise parameters. Thus noise PSD is fitted to the flicker formula in order to extract the values of noise coefficients, A and α in

$$N_{flicker} = S(f) = \frac{A \times I_{Avg}^2}{f^\alpha} \quad (8.1)$$

Where f is the frequency, I_{Avg} is the average current of the biosensor. The noise coefficient, A , and the frequency power, α , are estimated from the PSD of the measured noise using the

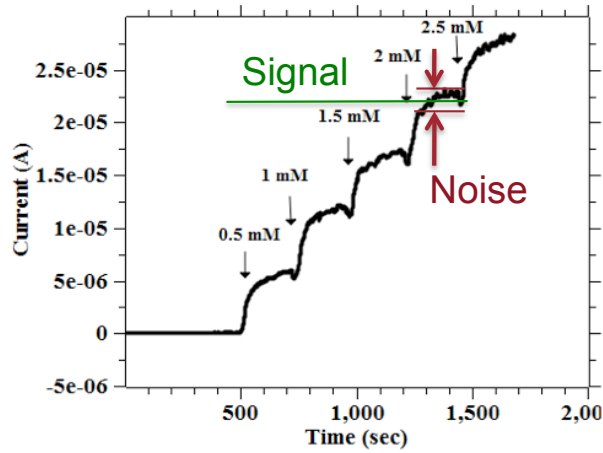


Figure 8.2: Chronoamperometry measurement using MWCNT- functionalized SPE at 300 *mV* with five subsequent additions of 0.5 *mM* Ferrocyanide in PBS with the indication of the noise and signal level.

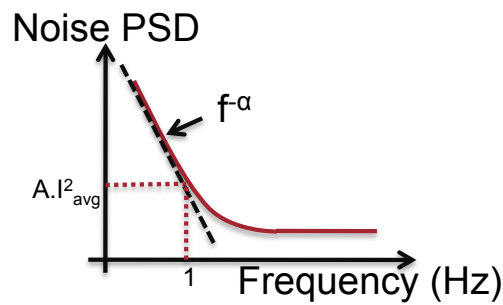


Figure 8.3: The PSD of noise at low frequencies in the presence of flicker noise

non-linear least-mean-square fitting method in Matlab. The power of the average current is considered to be equal to two when MWCNTs are used [31, 32, 151] as well as when there are no MWCNTs on the electrodes. The SNR of the measurement at a given frequency, F , can be calculated in the following way:

$$SNR_{@F} = \frac{I_{Avg}^2}{\int_0^F N_{flicker} df} = \frac{1}{A \int_0^F f^{-\alpha} df} \quad (8.2)$$

To avoid improper integral (which is the case when α is greater than one), we introduce a modified definition for SNR (mSNR) which that is calculated in the following way:

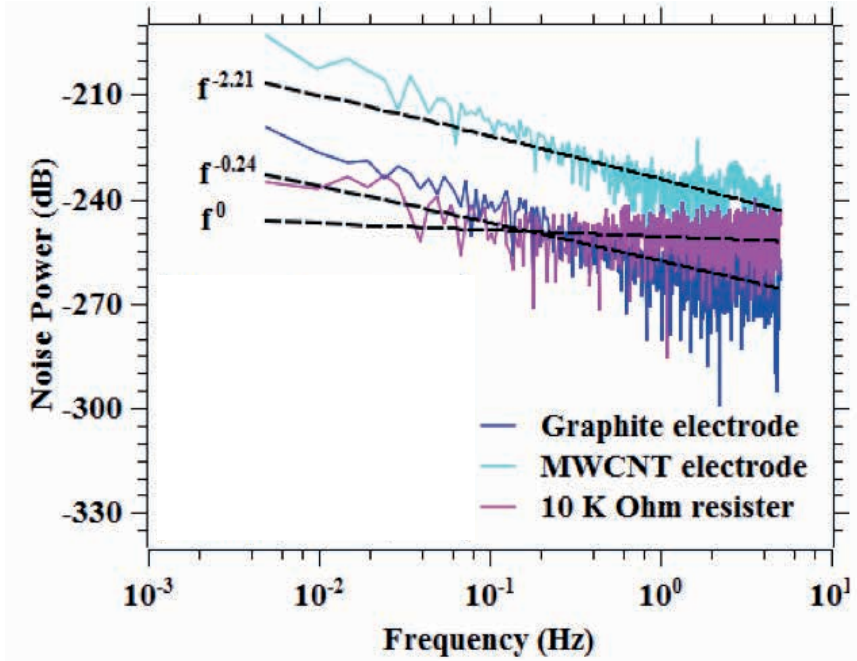


Figure 8.4: Noise PSD in chronoamperometry measurement with bare and MWCNT-functionalized electrodes and a 10 k Ω resistor. The H_2O_2 concentration is kept at 2 mM and the applied voltage is 650 mV. The dashed lines represent the fits to Eq. 8.1. Reprinted from [16].

$$mSNR_{@F} = \frac{I_{Avg}^2}{N_{flicker@F}} = \frac{1}{AF^\alpha} \rightarrow mSNR_{@1Hz} = A^{-1} \quad (8.3)$$

The mSNR is used as an alternative for SNR in this study. Moreover, since the $mSNR_{@1Hz}$ only depends on A, using it makes the comparisons among different measurements much easier in this research.

Fig. 8.4 shows the noise PSD of three different measurements: (i) chronoamperometry measurement on the detection of H_2O_2 using bare graphite electrode, and (ii) MWCNT-functionalized electrode (at a fixed voltage of 650 mV and a fixed concentration of 2 mM); (iii) the same voltage is applied across a resistance and the resulted noise PSD is drawn for comparison. The primary result of this measurement is that the noise is much higher in electrodes with MWCNT than bare electrodes. The value of α is given for each PSD plot. It is zero for the measurement with the resistor, which means the instrument does not add any considerable flicker noise.

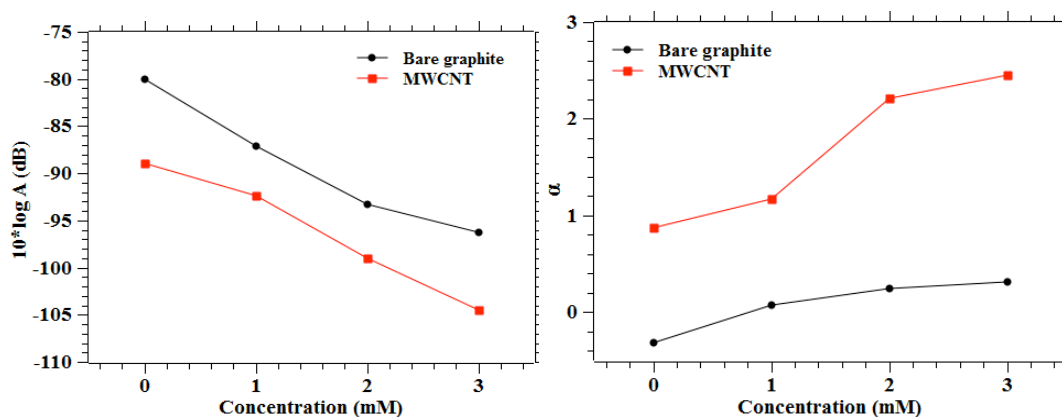


Figure 8.5: Estimated values of parameters A (left) and α (right) in Eq. 8.1 versus concentration in H_2O_2 measurement with both bare electrodes and MWCNT-functionalized electrodes. The applied voltage is 650 mV in these measurements. Reprinted from [16].

8.2 Results

8.2.1 Effect of the analyte concentration and MWCNT

We measured the noise PSD of different H_2O_2 concentrations with bare electrode and MWCNT-functionalized electrodes. The estimated values of A and α are plotted in Fig. 8.5 versus the H_2O_2 concentration.

According to Fig. 8.5-right, the α increases with concentration for MWCNT-functionalized electrodes. While the bare electrodes does not show any flicker noise (α is zero). In the case of MWCNT-functionalized electrodes higher α means that noise PSD decreases with a sharper slope in frequency. From Eq. 8.3 and Fig. 8.5 we can conclude that SNR increases more rapidly by concentration in the case of MWCNT-functionalized electrodes than in the case of bare electrode. This is shown qualitatively in Fig. 8.6. We can also see that the $mSNR_{@1Hz}$ (i.e. A^{-1}) is about one order of magnitude higher when MWCNT are used. Moreover, an increase in the SNR is achieved by increasing the concentration for both electrodes.

8.2.2 Effect of the applied voltage

In order to investigate the dependence of A and α on the applied voltage, a voltage between 550 mV to 750 mV is applied to the cell. The analyte concentration is set to 2 mM and both bare and MWCNT-functionalized electrodes were investigated. The estimated values of A and α are presented in Fig. 8.7. The results show an increase in α with the applied voltage for both kinds of electrodes. The $mSNR_{@1Hz}$ (i.e. A^{-1}) also increases significantly with increasing the applied voltage. Interestingly we observe the presence of flicker noise for the bare electrode at high applied voltages.

Chapter 8. Measurement of noise in amperometric electrochemical sensors

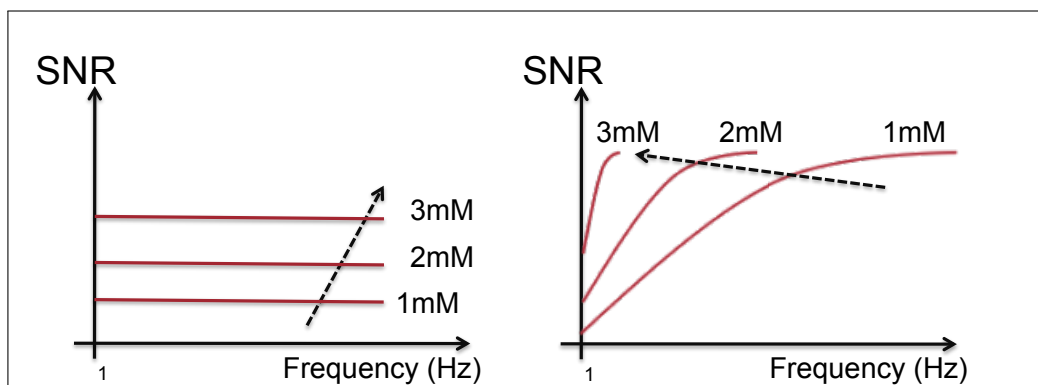


Figure 8.6: The qualitative change of SNR in bare (left) and MWCNT-functionalized (right) sensors for different concentrations of H_2O_2 . The SNR increases with concentration.

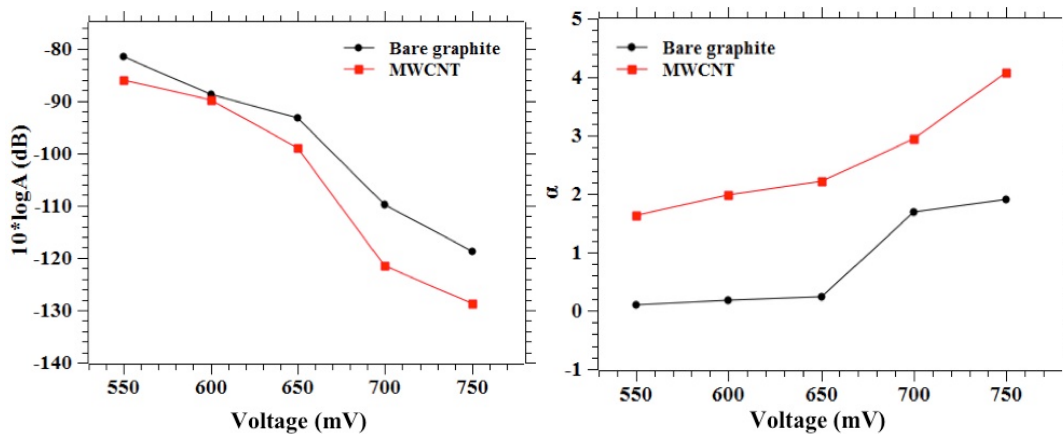


Figure 8.7: Estimated values of parameters A (left) and α (right) in Eq. 8.1 versus the applied voltage. H_2O_2 concentration is 2 mM and both bare and MWCNT-functionalized electrodes are used for comparison. Reprinted from [16].

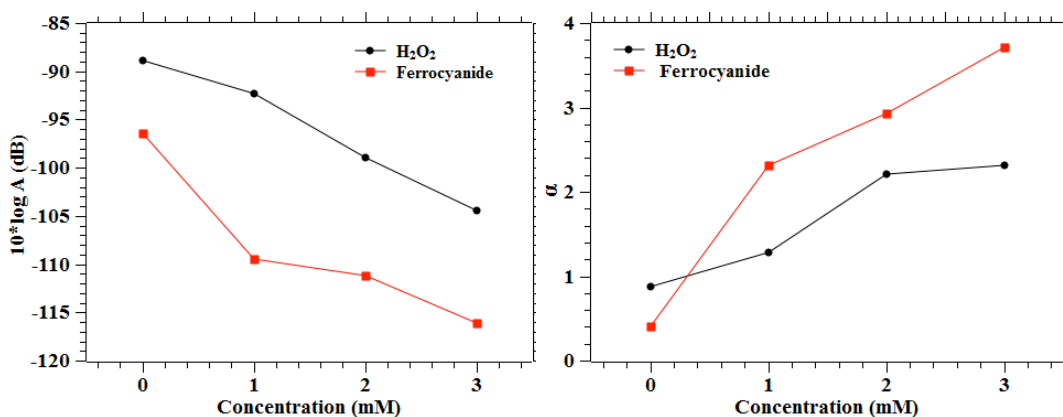


Figure 8.8: Estimated values of parameters A (left) and α (right) versus concentration in H_2O_2 and Ferrocyanide measurement. MWCNT-functionalized electrode is used and the applied voltage is 650 mV. Reprinted from [16].

8.2.3 Effect of the target Molecule

Fig. 8.8 shows parameters A and α extracted from H_2O_2 and Ferrocyanide measurement by MWCNT-functionalized electrodes at different concentrations. We can see that the $mSNR_{@1Hz}$ (i.e. A^{-1}) is higher with Ferrocyanide than with H_2O_2 while for both molecules an increase in the SNR is achieved by increasing the concentration. According to Fig. 8.8-right, the α increases with concentration for both target molecules. Both the average value of α and its increase rate with concentration is higher in the case of Ferrocyanide. In addition to having a higher $mSNR_{@1Hz}$ (i.e. A^{-1}), noise with Ferrocyanide has a higher corner frequency (assuming the same amount of thermal noise for both H_2O_2 and Ferrocyanide).

8.3 Chapter contributions and summary

We performed several experiments in order to characterise the dependence of the noise parameters of electrochemical sensors on the physical parameters of the sensor. We have demonstrated that the current noise fluctuations originates from the amount of analyte in the solution, type of electrode material used and the applied voltage. In particular the presence of the CNT on the sensor on the noise and mSNR of the measurements is studied.

We observed that the bare graphite electrode has much smaller noise amplitude and α than their MWCNT counterparts. This could be attributed to higher mobility and higher charge fluctuations in MWCNTs. It is also possible that the difference in the measured noise is due to the interaction of analytes with different electrode materials used. Indeed, when there is no charge transfer process occurring at the interface, only thermal noise is anticipated [34]. Measurements with H_2O_2 showed more noise compared to Ferricyanide, which could be due to the faster electron transfer, and hence lower charge transfer resistance (R_{ct}) in H_2O_2 . The complexity of the analyte being used and the redox reactions occurring at the interface and the ionic charges being transferred are one of the reasons for the higher noise. Indeed, charge transfer and mass transfer processes occurring at the electrode surface-interface are responsible for the $1/f$ noise.

On the other side, measurements show that using MWCNTs increases the mSNR of the in all cases we studied. We have also demonstrated that the mSNR of the measurement significantly increases with analyte concentration and the applied voltage. In summary, the use of highest possible voltage, highest possible frequency, as well as the use of MWCNTs results in a higher mSNR in chronoamperometry measurement. As a part of future work, we will investigate the effect of the electrode area in the mSNR. Moreover, we will develop a new model for the noise in electrochemical sensors that includes these dependencies.

9 Differential readout IC for amperometric sensors

In this chapter a *pseudo-differential readout IC* (DIRIC) is presented to readout amperometric electrochemical sensors. This circuit uses switched-capacitor technique and reads out on-chip and off-chip sensors in differential mode. DIRIC is able to measure currents in the wide range of $\pm 100 \mu A$ with more than $120 dB$ dynamic range.

9.1 Motivation

In most cases, the cyclic voltage employed in CV measurement generates a large periodic background current due to charging and discharging of the double layer capacitance at the electrode-electrolyte interface [152, 153]. In particular, when CNTs are involved in the electrochemical sensor, this background current is typically much larger than the redox current. An example of a voltammogram measured in presence of CNT on the sensor is shown in Fig. 9.1, where the small current peak at $400 mV$ represents the redox current which while the background current at this voltage is almost ten times higher than the redox current.

In general, the presence of any other electro-active molecule in the solution can also cause large unwanted interference current. Moreover, the background current increases in presence of the nano-structures on the sensor. Examples are when gold or other nano-particles are introduced into the sensing area to increase the sensitivity of the sensor [154, 155]. In all these cases, the presence of a large background current when reading out the small redox current in presence of large background current requires a high resolution ADC.

DIRIC measures the difference in the currents of two *working electrodes* (WEs): (i) the main WE (WE_M) that is covered by a nano-structure and a selective enzyme. (ii) A compensation WE (WE_C) similar to the main WE except that it is not covered by the selective enzyme. Therefore, WE_M conducts both the background current and the redox current while the WE_C conducts only the background current. DIRIC measures the difference between the current of the two electrodes which is only the redox current. DIRIC measures, amplifies, and digitize the redox current and sends it serially out of the IC. By removing the large background current, DIRIC

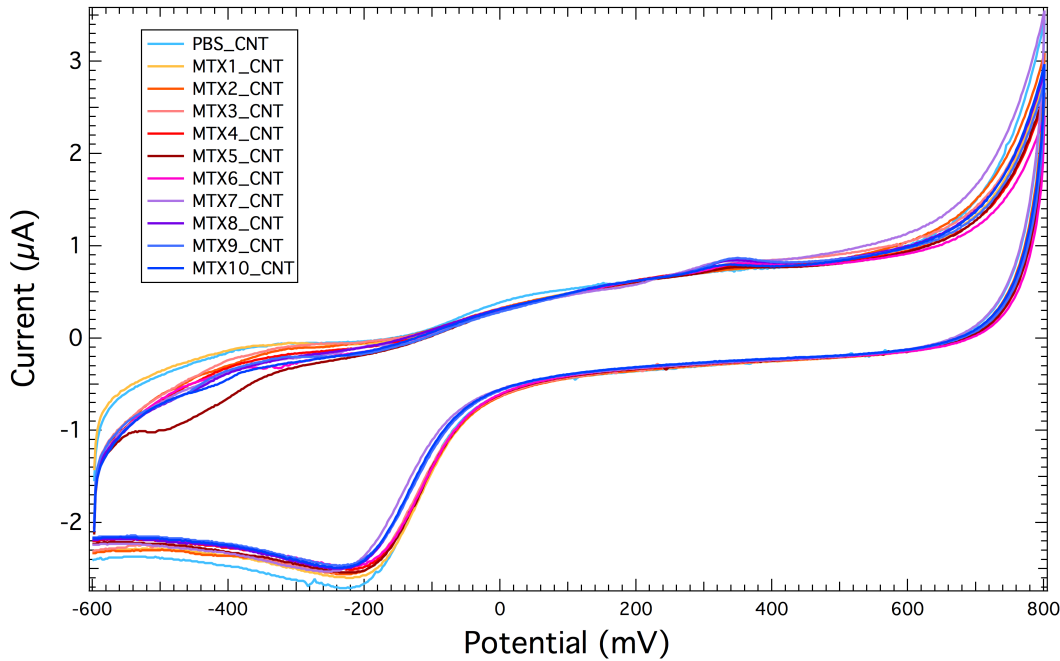


Figure 9.1: The measured voltammogram during the measurement of Mitoxantrone in different concentration [13] with a WE incorporating CNTs. The small current peak at around +400 mV represents the redox current that should be measured in presence of the large background current.

eliminates the need for an unnecessary high resolution ADC.

As presented in Chapter 3 (Section 3.2.3), few differential readout circuits have been reported in literature [90–92]. However, they are either not fully-integrated [90], not capable of differential measurement [76] or are not completely differential systems as the output still shows the background current [91]. DIRIC is a fully-integrated readout circuit that completely removes the effect of the background current from the output. Moreover, DIRIC samples the input currents at the same time as opposed to [91] and potentially results in more accurate background current removal.

9.2 DIRIC architecture

The schematic view of DIRIC is shown in Fig. 9.2. The circuit consists of four main building blocks:

(i) two identical integrators convert the sensor currents into voltages; The *main integrator* reads WE_M , which has both background and redox currents. The *reference integrator* reads the WE_C , that only conducts background current. I will show later in this chapter that using two multiplexer at the input of the integrators both on-chip and off-chip sensor arrays can be

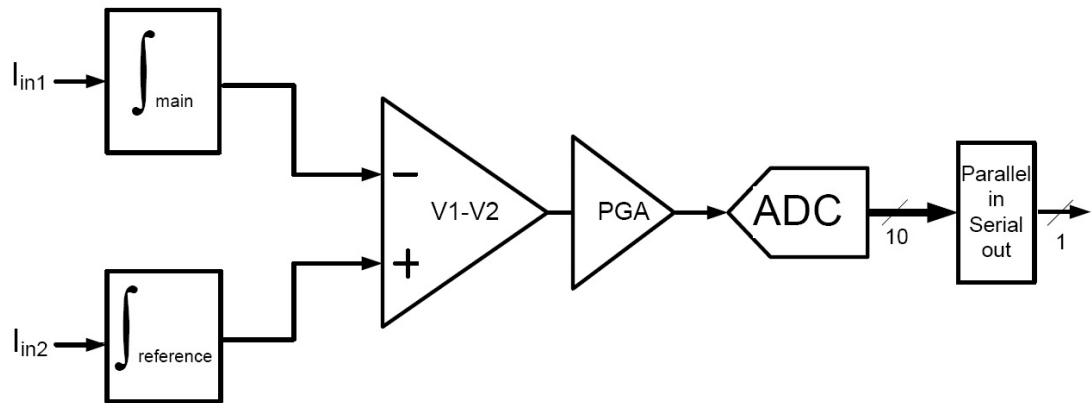


Figure 9.2: The readout circuit in DIRIC to measure the sensor currents differentially. Two integrators at the front integrate the current of the sensors and transforms them into voltages. The difference of these two voltages is amplified through the PGA and given to the ADC. A serializer is designed and placed after the ADC to reduce the PAD-cost.

measured by DIRIC.

(ii) a difference amplifier subtracts the output of the *reference integrator* from the *main integrator*. It converts the differential voltage into a single one with a unity-gain and adjusts the common mode voltage; This is where the effect of the background current is removed from the main current.

(iii) a *programmable gain amplifier* (PGA) amplifies the voltage difference between the *main integrator* and the *reference integrator*. The gain of the PGA can be set to any integer value between 1 and 15.

(iv) the output stage includes a 10 bit-SAR ADC and a serializer. The SAR ADC is taken from the standard library of the AMS 0.35 μ m technology. The serializer is built from the flip-flops provided in this technology.

The detailed description of the circuits are described in this section.

9.2.1 The integrator

The switch-capacitor(SC) based integrator is chosen over a resistor-based TIA as the first stage of the readout circuit. The main advantages of SC integrator are: (i) The sensor current (i.e. I_{in}) is low-pass filtered straight away, which removes the high frequency noise in the electro-chemical process; (ii) Changing the clock or the capacitor ratio enables the measurement of I_{in} in a wide dynamic range with an accurate gain. However, the accuracy of the readout is limited by the the noise and leakage of the op-amps and the switches, which can be minimised by proper design and sizing of the devices. The switching noise may also affect the sensor

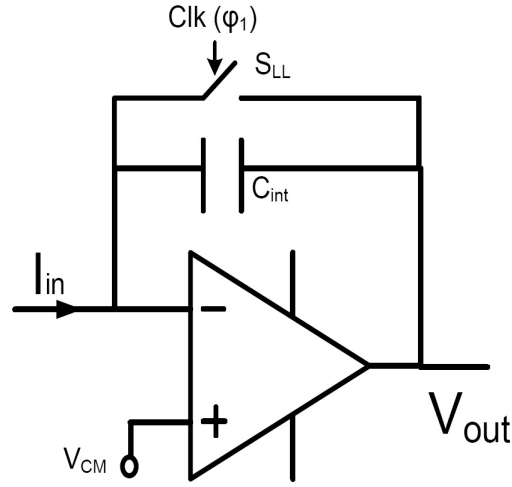


Figure 9.3: The switch-capacitor current integrator. This is the first stage of the readout chain. S_{LL} is a low leakage switch that enables accurate readout of pA-currents.

operation (i.e. the electrochemical reaction) by unbalancing the charge on the electrode at the switching time. This effect will be investigated by measurements.

The SC integrators are realized with an opamp, a capacitor and a switch as shown in Fig. 9.3. In the INTEGRATION phase ($\phi_1 = 0$) the sensor current, I_{in} , charges the capacitor C_{int} while a fixed voltage, V_{CM} , is applied to the WE through the negative feedback. The output voltage of the integrator is calculated as follows:

$$V_{out,integ}(t) = \int_0^t \frac{I_{in}}{C_{int}} dt \quad (9.1)$$

In the RESET phase ($\phi_1 = 1$) the switch, S_{ll} , closes to discharge C_{int} . In this phase, the voltage V_{CM} is kept on the WE while I_{in} flows through S_{LL} . The clock frequency to control the INTEGRATION and RESET phases depends on the absolute value of I_{in} . Its value is chosen for each current range such that the maximum voltage drop across C_{int} is 1 V. This is to ensure the linear operation of the amplifier. Assuming a symmetrical clock that provides equal INTEGRATION and RESET cycles, the output voltage of the integrator at the end of the n th INTEGRATION phase is

$$V_{out,integ}(nT + T/2) = \frac{T \times I_{in}}{2C_{int}} \quad (9.2)$$

Where T is the period of the clock.

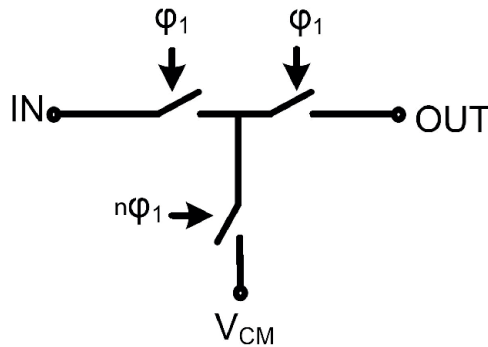


Figure 9.4: The low leakage switch, S_{LL} , consists of three complementary sub-switches. When S_{LL} is open (i.e. $\phi_1 = 0$), the voltage drop across the the left sub-switch is zero ($V_{IN} = V_{CM}$) to prevent the off-state leakage current.

Low leakage switch

A low leakage switch is used as S_{LL} to prevent discharging of C_{int} through the switch in the INTEGRATION mode. The schematic of S_{LL} is shown in Fig. 9.4. It consists of two series-connected complementary sub-switches with their common terminal connected to the V_{CM} through a third sub-switch. This third switch closes when S_{LL} is open (i.e. $\phi_1 = 0$) in order to keep the voltage drop on the series switch at zero to eliminate the off-state leakage current of S_{LL} .

9.2.2 Differential to single converter (D2SC)

A differential switched-capacitor amplifier is designed similar to [156] to take the difference of the voltages at the output of the integrators. The switch-capacitor technique is chosen over a resistor-based difference amplifier, because the output of the integrator is only valid at an instance (i.e. end of the INTEGRATION phase) and needs to be sampled right away.

The D2SC circuit is shown in Fig. 9.5 and has several advantages. It cancels the clock-feed-through and op-amp offset voltage. Moreover, it samples the two inputs at the same time and does not require the output to slew to ground each time the amplifier is reset [156]. The input of the D2SC follows the output of the integrators during the INTEGRATION phase. During this time C_3 is connected in feedback around the opamp which causes the output to change only by the opamp input offset voltage. This is a much smaller change than that required without the usage of C_3 where the output has to slew to a potential close to V_{CM} each time the amplifier is reset. Since the output does not have to change as much, its slew rate requirement is greatly reduced [156].

The output of the D2SC is valid when $\phi_1 = 1$. To get a unity gain, C_1 , C_2 , and C_3 have similar values (1 pF). The output voltage of the D2SC at the end of ϕ_1 can be calculated as a function

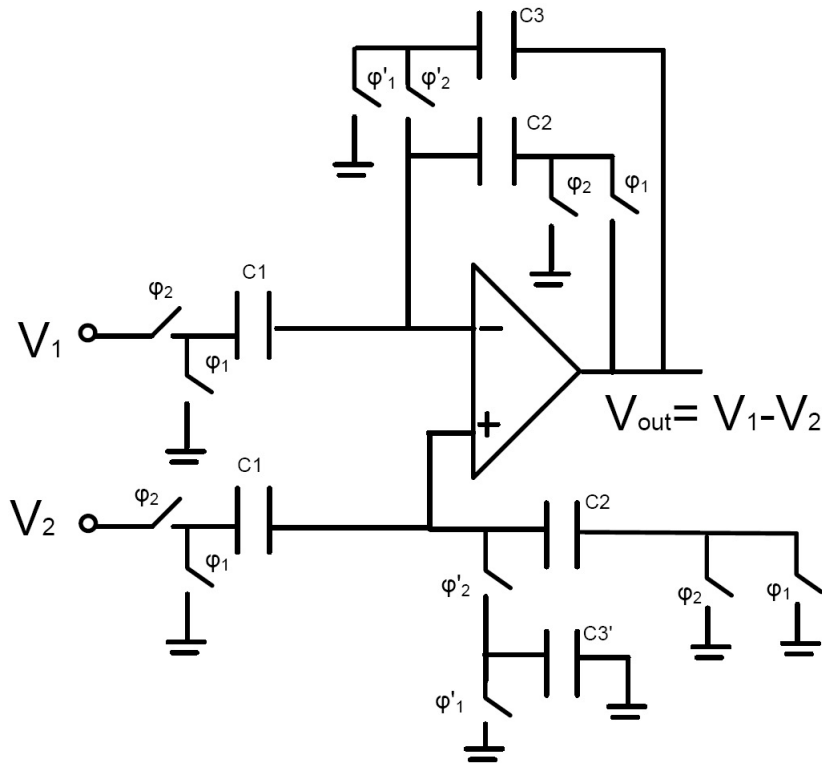


Figure 9.5: The differential voltage to single voltage converter circuit (D2SC)

of its input voltages (V_1 and V_2) and subsequently the input currents to the integrators:

$$V_{out,D2SC}(nT+T) = V_1 - V_2 = V_{out,integ1}(nT+T/2) - V_{out,integ2}(nT+T/2) = \frac{T \times (I_{in1} - I_{in2})}{2C_{int}} \quad (9.3)$$

The clock waveforms with the primed superscripts change before the non-primed waveforms in order to prevent charge from escaping through C_3 and C_3' . The opamp is left open-loop for this amount of time. However, this has no effect on the ultimate output of the D2SC circuit except for causing glitches at the clock transitions. All clock waveforms are generated on-chip by the clock generator circuit.

9.2.3 Clock generator

The clock generation circuit used is shown in Fig. 9.6 where the inverted outputs were used to drive the PMOS transistors in the complementary switches. ϕ_1 and ϕ_2 are non-overlapping clock cycles. The actual amount of the delay between the clock phases and their primed version is determined by the capacitor C_{delay} and is nominally 10 ns for $C_{delay} = 0.5$ pF.

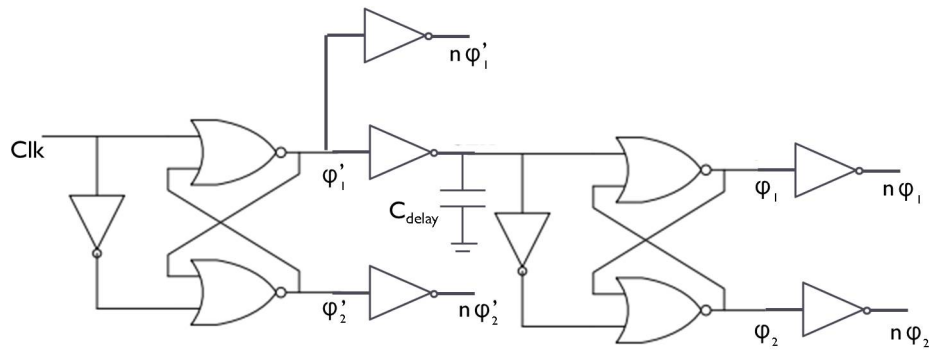


Figure 9.6: The clock generator circuit

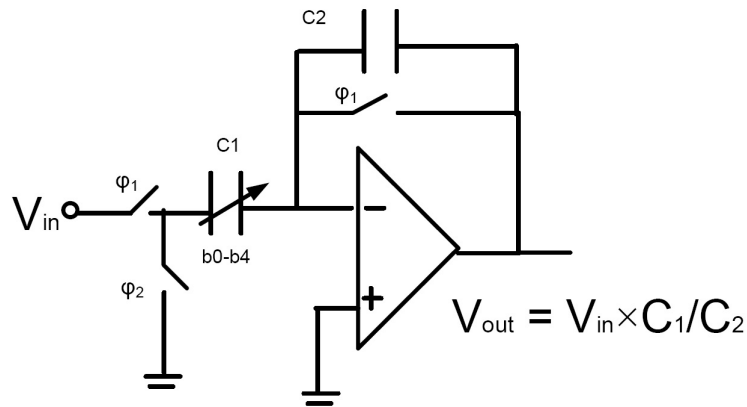


Figure 9.7: The programmable gain amplifier based on opamp, switches and a programmable capacitor array

9.2.4 Programmable gain amplifier

The PGA is realized in a switched-capacitor architecture as shown in Fig. 9.7. The gain of the PGA is equal to the ratio of the capacitors C_1 and C_2 . The capacitor C_1 is a programmable capacitor array with a unit capacitor equal to C_2 and four bit dynamic range as shown in Fig. 9.8. Therefore, the gain of the PGA can be programmed from 1 to 15 through $b < 0:3 >$. The output voltage of the PGA can be calculated as a function of the input currents:

$$V_{OUT,PGA}(nT + 3T/2) = \frac{C_1}{C_2} \times V_{out,D2SC}(nT + T) = \frac{C_1}{C_2} \times \frac{T(I_{in1} - I_{in2})}{2C_{int}} \quad (9.4)$$

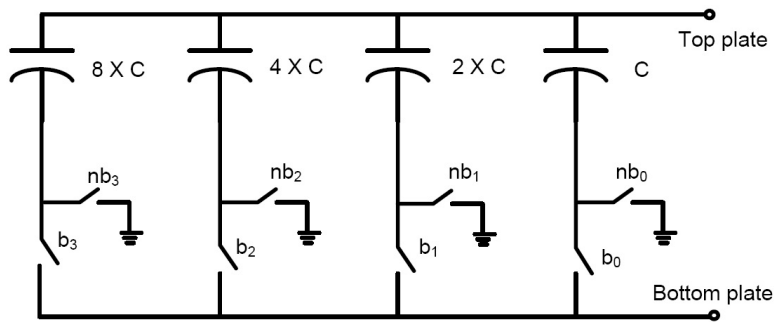


Figure 9.8: The programmable capacitor array

9.3 Potentiostat

The potentiostat in DIRIC applies a voltage to the RE and provides current for the CE . This is achieved through a negative feedback around the opamp shown in Fig. 9.9 when it comes in contact with the sensor. The potentiostat applies a programmable voltage waveform to the sensor. This is achieved by placing a *digital to analog converter* (DAC) before the amplifier which is driven by an off-chip micro-controller through a *serial to parallel converter and hold* (SPCH). DAC converts the digital input into an analog voltage (V_{RE}) and applies it to the positive terminal of the opamp. Therefore, V_{RE} is applied to the RE when it comes in contact with the sensor (to close the negative feedback loop). The voltage on the WE is instead fixed at $V_{CM} = V_{DD}/2$ by the integrators. Therefore, the micro-controller can be programmed to generate the equivalent digital value of V_{RE} that is needed to initiate CV, CA, impedance spectroscopy, square wave voltammetry, etc.

9.3.1 SPCH

SPCH receives a serial input from the off-chip micro-controller, converts it into parallel ($P < 0 : 9 >$) and sends it to DAC. SPCH keeps its output value until the next input is received from the micro-controller. This is achieved through the enable signal (EN) that is generated by micro-controller. The EN activates each time the micro-controller sends the serial data to the SPCH. This signalling can be easily implemented with the SPI port of a commercial micro controllers.

The schematic view of SPCH is shown in Fig. 9.10. It consists of 20-*flipflops* (FFs) that are taken from the digital library of the AMS 0.35 μm CMOS technology. The FFs have a synchronized serial input (IN_S) in addition to the normal D-input. The FFs in the bottom row convert the serial input to parallel and drive the FFs on the top row. To prevent glitches on the output of SPCH when the input is changing. The FFs on the top change their output only when the bottom FFs have the correct value at their outputs. This is achieved through the negated EN that drives the top FFs.

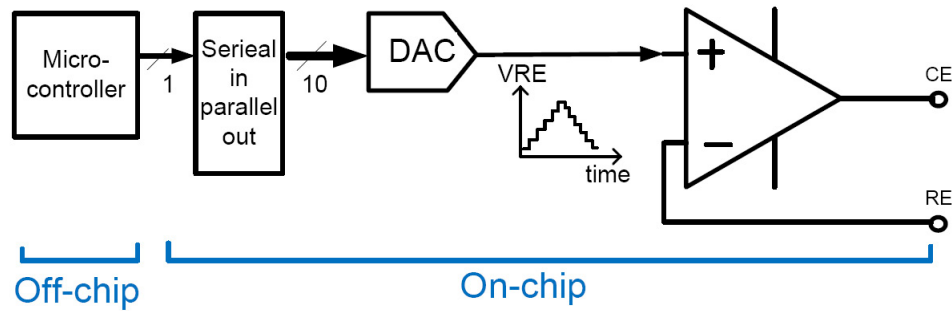


Figure 9.9: The Potentiostat generates the voltage to apply to the RE. It is driven from a serial port to generate arbitrary waveform like: triangular, square wave and fixed voltages. An off-chip micro-controller controls the voltage level of V_{RE} .

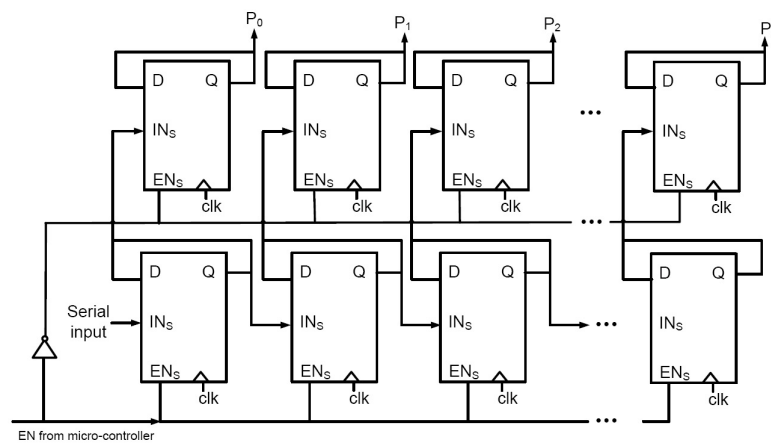


Figure 9.10: The serial to parallel converter and hold

Table 9.1: Design specifications of the amplifiers

Parameter	$OP_{Integ,D2SC}$	OP_{PGA}	$OP_{Potentiostat}$
Gain (dB)	82.7	83.5	71.5
-3dB bandwidth (kHz)	8.4	4.3	45
Phase margin (@ $C_L = 1pF$)	53°	60°	59°
Power consumption (mW)	1.67	0.46	2.18
Output current (μA)	126	35	207
Offset (mV, monte-carlo simulated)	1.64	1.63	1.65
CMRR (dB)	126.7	124	112
PSRR (dB)	84.4	84.6	72.5
Input-referred noise (μV , integrated in 1MHz)	11	14	14.2

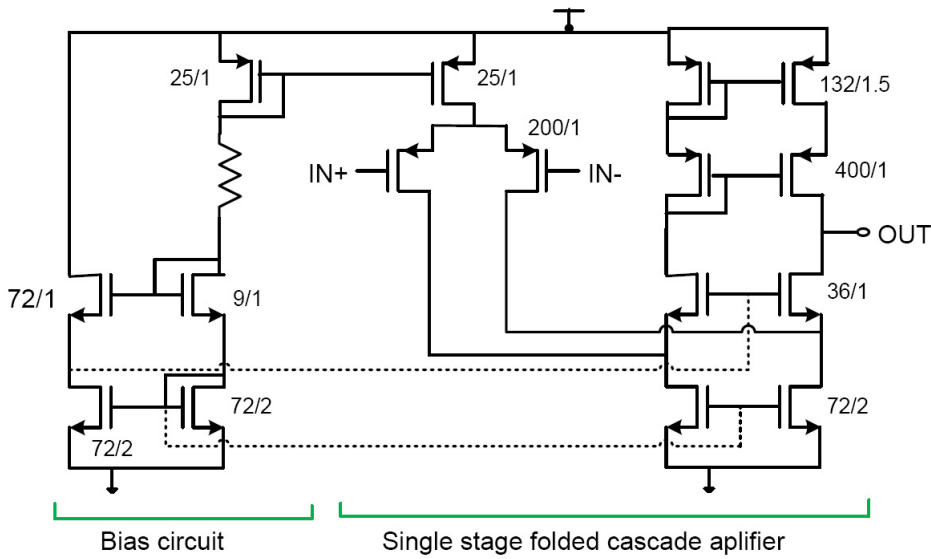


Figure 9.11: The schematic of the single-stage folded-cascode amplifier used in the integrator, D2SC, PGA, and the potentiostat. The given transistor sizes are valid for the opamps used in the integrators.

9.4 Amplifiers

The amplifiers in the integrators, D2SC, PGA, and the potentiostat are all realized with PMOS-input folded-cascode architecture as shown in Fig. 9.11. Single-stage amplifier is chosen for the integrators and the potentiostat to ensure the stability of the amplifier for any unknown load (i.e. the sensor). Single-stage amplifier is also chosen for the PGA and D2SC over two-stage amplifiers to ensure short settling-time of the amplifier and low power consumption. The folded-cascode structure is chosen due to its higher gain among single-stage amplifiers. To decrease the noise and the mismatch of the amplifiers, large PMOS transistors are used for the input pair as well as for the current mirror.

The only difference of the opamps of the integrator, D2SC, PGA and potentiostat is their maximum output current. The potentiostat has to provide twice the current of the integrator to its load (i.e. the CE), because later in this chapter CE is shown to be common for both the WE_C and WE_M . Instead the opamp in the PGA should only satisfy the speed requirement of the system. The output of the opamp should settle within half of the fastest clock period. It is shown later in this chapter that the fastest clock is 2 MHz. The simulated specifications of the opamps are listed in Table 9.1. Monte-carlo simulation is used to find the input offset of the amplifiers.

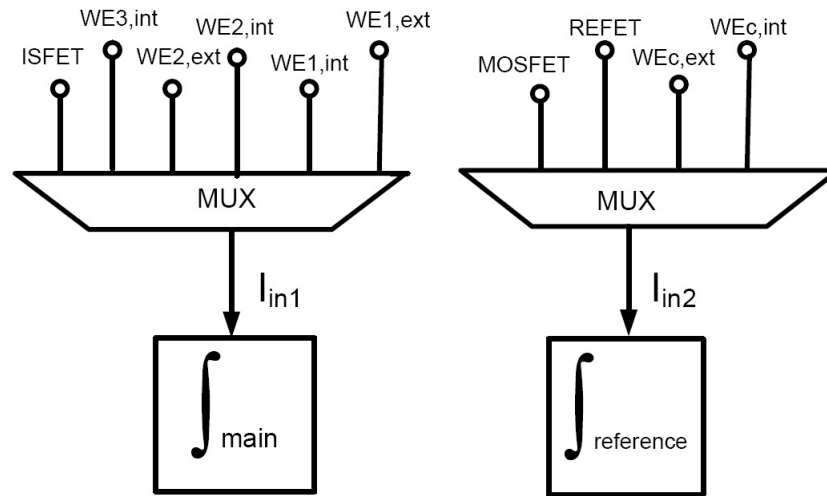


Figure 9.12: Two multiplexers integrated to DIRIC to configure the interface of the readout circuit in Fig. 9.2 with the internal sensors ($WE_{1,int}$, $WE_{2,int}$, $WE_{3,int}$, $WE_{C,int}$, ISFET, REFET, MOSFET) or external sensors ($WE_{1,ext}$, $WE_{2,ext}$, $WE_{C,ext}$).

9.5 Sensor array

Together with DIRIC, an on-chip sensor array is designed with multiple sensing sites to measure glucose, lactate and ATP in both differential and single mode measurements. DIRIC can also be coupled with off-chip amperometric sensors. This is achieved through two multiplexers that are added at the inputs of the *reference integrator* and *main integrator* as shown in Fig. 9.12.

The multiplexer at the *main integrator* connects it to one of the on-chip WE_M s, off-chip WE_M s or the drain of an ISFET. The multiplexer at the *reference integrator* connects it to one of the on-chip WE_C , off-chip WE_C s, the drain of a REFET or a MOSFET.

The differential- or single mode- operations can be set through the *reference integrator* where the single-mode measurement means no sensor is connected to it. The single-mode is embedded in the system without any extra cost to provide further possibilities to study the background current.

The plot of the on-chip sensor array is shown in Fig. 9.13. It includes four $100 \times 100 \mu m$ WEs (one of which serves as WE_C , the rest are WE_M s), a common RE, and a common CE to measure three metabolites: glucose, lactate and ATP. The WE_1 and WE_C are placed symmetrical with respect to the RE and CE and aimed for differential glucose measurement. To study the effect of symmetry between WE_C and WE_M in accuracy of background current removal, WE_3 and WE_4 are placed asymmetrically with respect to RE and CE, when compared to WE_C .

An ISFET is added to the on-chip sensor array for pH measurement to calibrate the biosensors. A REFET and a MOSFET with the exact same size are added to the sensor array to provide

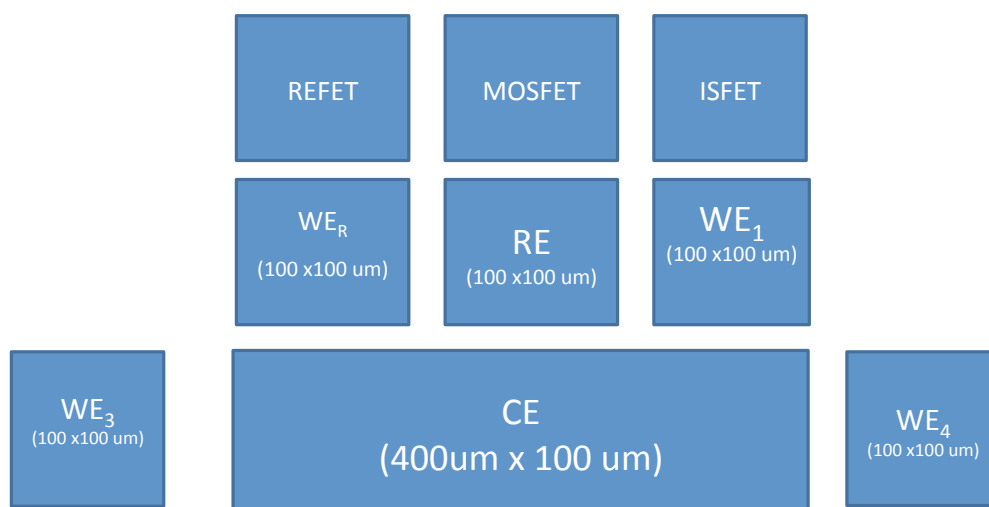


Figure 9.13: The plot of the on-chip sensors. The array includes three main WEs (WE_1 , WE_3 , WE_4), a common WE_C , a common RE, and a common CE, as well as a set of ISFET, MOSFET and REFET for pH measurement

electrochemical and electrical reference for the ISFET, respectively. The design procedure of the ISFET, REFET and the MOSFET is presented here.

9.5.1 ISFET Design

Ion sensitive field effect transistor (ISFET) based chemical sensors are becoming increasingly popular for the creation of miniature, highly scalable, intelligent and cheap sensing systems owing to their implementation on unmodified CMOS [157]. This is possible because of the pH sensing capability of the CMOS passivation layer, which happens to be silicon nitride. To create ISFETs in unmodified CMOS, the standard MOSFET from the technology is used with an extended floating gate to the passivation to sense ionic changes on the insulator [157]. The gate bias of the device is now applied using an external reference electrode, typically Ag/AgCl (See Fig. 9.14). The threshold voltage of the ISFET, V_{th} changes linearly with the pH of analyte in contact with:

$$V_{th} = V_{th0} + \alpha \times \Delta pH \quad (9.5)$$

Where V_{th0} is the threshold voltage of the device at a reference pH and ΔpH is the change in the pH from the reference pH. The parameter α is the coefficient of proportionality.

ISFET readout circuits require that the chemical information that led to the variation of the threshold voltage V_{th} be transduced into a form which can be further processed. This is achieved by biasing two of the three variable parameters of the ISFET (the voltage on the

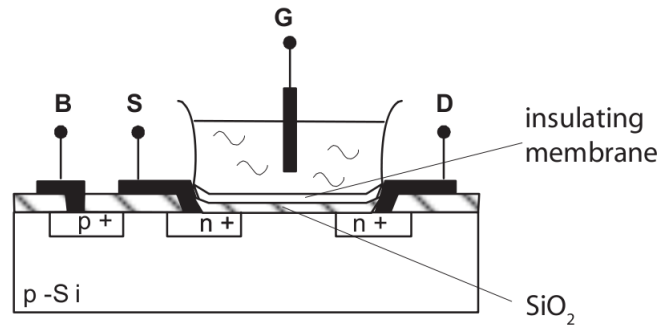


Figure 9.14: The ISFET. Reprinted from [17].

reference electrode (V_R), V_{DS} or I_{DS}) with a constant source and reading the third to follow changes in V_{th} .

There are two typical ways to measure the variation of the V_{th} of an ISFET: (i) constant-current method [158]; and (ii) constant-voltage method [159]. The constant-current method is achieved by fixing V_R , V_{DS} , and I_{DS} of the ISFET and measuring the source voltage of the device, V_S . In this method the circuit operates in a source follower configuration and V_{th} can be monitored by observing the source voltage of the device. The constant-voltage method is achieved by fixing the V_{RS} and V_{DS} and measuring I_{DS} . Then V_{th} can be calculated from the I_{DS} depending on the operation mode of the ISFET.

We selected the constant-voltage method, in order to be compatible with DIRIC acquisition system. We also chose the weak inversion region for biasing the ISFET, to get a higher transconductance efficiency (i.e. g_m/I_{DS}) [17]. The weak inversion region is desired also because I_{DS} is exponentially related to the change in V_{th} . By using the logarithmic relation of $pH = -\log[H^+]$ we can get a linear relationship between the I_{DS} and concentration of the hydrogen ions.

To bias the ISFET, a constant voltage is applied to the external reference electrode of the ISFET, the source voltage is grounded, and the V_{DS} is held at a constant voltage. Therefore any change in ion concentration in the solution changes the output current of the ISFET. In the weak inversion region the drain-source current of a normal MOSFET is

$$I_{DS} = I_{DS0} e^{\frac{V_{GS} - V_{th}}{nV_T}} \quad (9.6)$$

Where I_{DS0} is the current when $V_{GS} = V_{th}$. V_T is the thermal voltage, KT/q , in which T is the absolute temperature, K is the Boltzman constant, and q is the charge of an electron. Finally,

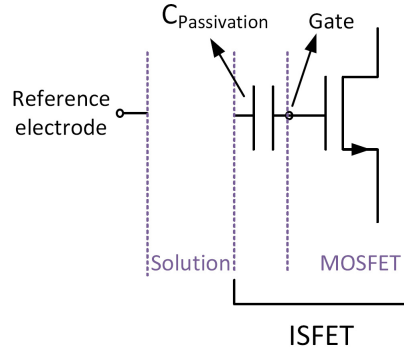


Figure 9.15: The ISFET fabricated in unmodified CMOS technology.

n is the slope factor given by:

$$n = 1 + \frac{C_D}{C_{OX}} \quad (9.7)$$

C_D is the capacitance of the depletion layer and C_{OX} is the capacitance of the oxide layer. For an ISFET, the effect of the passivation layer in the slope factor should be taken into account:

$$n_{ISFET} = \frac{C_{pass} + \frac{C_{ox} + C_D}{C_{OX} C_D}}{C_{pass}} \times n \quad (9.8)$$

Where C_{Pass} is the passivation capacitance between the solution and the last metal layer of the ISFET (see Fig. 9.15), and depends on the chemical size of the ISFET. The chemical size (i.e. $(W/l)_{chem}$) of the ISFET is the extended area of the ISFET gate in the last metal layer covered with the passivation layer that is exposed to the solution. We define parameter $A = n_{ISFET} \times V_T$. Therefore, the I_{DS} of an ISFET biased in the weak inversion is:

$$I_{DS} = I_{DS0} e^{\frac{V_{RS} - V_{th}}{A}} \quad (9.9)$$

Where V_{RS} is the voltage difference between the external reference electrode and the source of the ISFET. Eq. 9.9 is a simplified equation for the current of the ISFET which is enough for our calculations in this chapter. The interested reader is referred to [17, 160, 161] for detailed model of the ISFET current and threshold voltage in the weak inversion region.

Assuming ISFET is biased in the weak inversion region and V_{RS} and V_{DS} are fixed and equal,

for two different ISFET currents, I_{DS1} and I_{DS2} , we can write:

$$\ln \frac{I_{DS2}}{I_{DS1}} = \frac{V_{th1} - V_{th2}}{A} \Rightarrow \ln\left(1 + \frac{\Delta I_{DS}}{I_{DS}}\right) = \frac{-\Delta V_{th}}{A} \quad (9.10)$$

The goal is to measure the pH from 0 to 14 with a resolution of 0.1 unit. Here we calculate the electrical dimension (i.e. $(W/l)_{elec}$) of the ISFET to achieve this with DIRIC. We choose $(W/L)_{Chemical} = 100/100 \mu m$ which results in $C_{Pass} \approx 100 fF$ [160]. For an ISFET in the selected technology (AMS $0.35 \mu m$), the coefficient α in Eq. 9.5 is equal to $32 mV/pH$ [160]. Therefore, a 0.1 unit change in pH leads to $\Delta V_{th} \approx 3.5 mV$. Replacing this into Eq. 9.10 results in:

$$\Delta pH = 0.1 \Rightarrow \Delta V_{th} = 3.2 mV \Rightarrow \ln\left(1 + \frac{\Delta I_{DS}}{I_{DS}}\right) = \frac{3.2 mV}{A} \quad (9.11)$$

Assuming the minimum-detectable change in current is $0.5 nA$, we can rewrite Eq. 9.11:

$$I_{DS} \geq \frac{\min(\Delta I_{DS})}{e^{\frac{3.2 mV}{A}} - 1} = \frac{0.5 nA}{e^{\frac{3.2 mV}{A}} - 1} \quad (9.12)$$

which gives a lower limit on I_{DS} .

On the other side, assuming α remains constant over the whole pH range, a 14 unit change in pH results in $\Delta V_{th} \approx 448 mV$. Therefore, according to Eq. 9.10:

$$I_{DS,max} = I_{DS,min} \times e^{\frac{448 mV}{A}} \quad (9.13)$$

which gives an upper limit on I_{DS} .

Both $I_{DS,min}$ and $I_{DS,max}$ should be in the weak inversion region to ensure the logarithmic behaviour of the device. Their values depend on A and consequently the electrical and chemical gate size of the ISFET. DC simulations were performed to find the ISFET electrical size and the voltage on the external electrode that satisfies the criteria in Eqs. 9.12 and 9.13. Fig. 9.16 shows the simulated $I_{DS}-V_{GS}$ characteristics of the ISFET that satisfies both Eq. 9.12 and Eq. 9.13 for $(W/L)_{elec} = 20/10 \mu m$. The results of ISFET design are summarized in Table 9.2. The external reference voltage to bias the ISFET in the weak inversion can be also calculated from Eq. 9.10 and Fig.9.16. This is the gate voltage that corresponds to the current at the

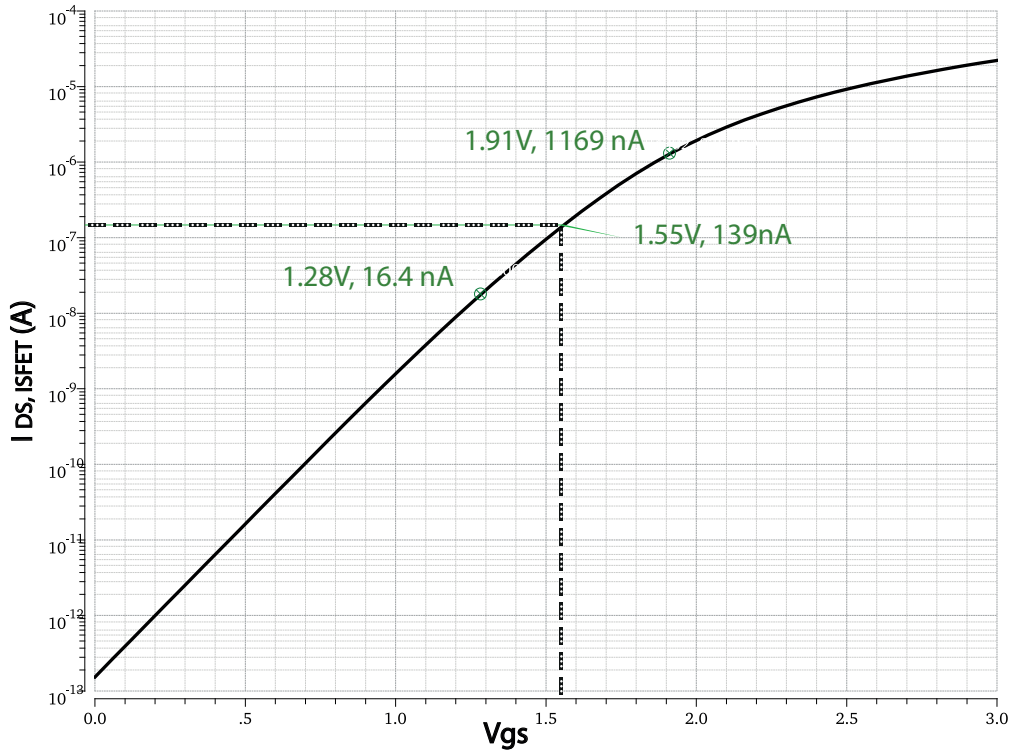


Figure 9.16: The simulated I_{DS} - V_{GS} characteristics of the ISFET with $(W/L)_{elec} = 20/10$ and $(W/L)_{chem} = 100/100$. The source is grounded and V_{DS} is fixed at 1.65 V. V_G is the voltage of the external reference electrode.

reference pH (i.e. $pH = 7$). The current at $pH = 7$ is

$$I_{DS,ref} = I_{DS,min} \times e^{\frac{224 \text{ mV}}{A}} = 139 \text{ nA} \quad (9.14)$$

The corresponding V_{GS} can be found from Fig.9.16 and is 1.55 V.

Differential ISFET measurement

A REFET which is the duplicate of the ISFET is placed in the array to provide an electrochemical reference for the ISFET. The envisaged differential measurement is through two separate chambers each containing one of the ISFET or REFET. The chamber with the REFET is to be exposed to a solution with a known pH (i.e. 7) while the other chamber is exposed to the target analyte with unknown pH (i.e. x). The output of the readout circuit is proportional to the

Table 9.2: Design specifications of the ISFET

<i>Parameter</i>	<i>Value</i>
$(W/l)_{elec}$	$20 \mu m / 10 \mu m$
$(W/l)_{chem}$	$100 \mu m / 100 \mu m$
$C_{Passivation}$	$100 fF$ [160]
$Min(I_{ISFET})$	$16.4 nA$
$Max(I_{ISFET})$	$1169 nA$
A	$105 mV / \log(A)$

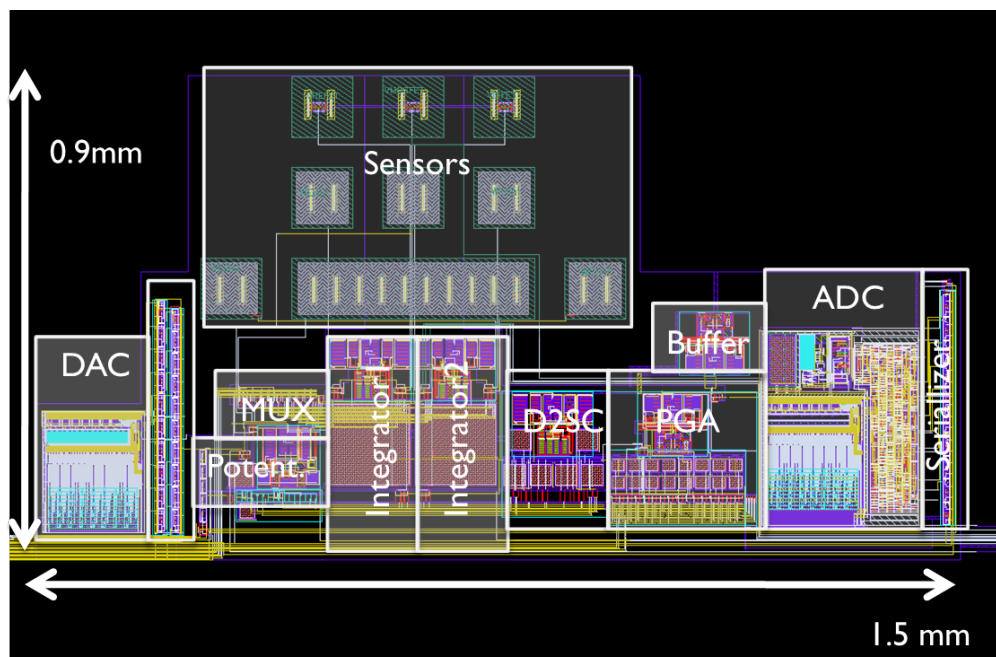


Figure 9.17: The layout of the readout IC with the on-chip sensors

difference in the currents:

$$V_{out} \propto I_{DS,ISFET} - I_{DS,REFET} = I_{DS0} \times \left(e^{\frac{V_{RS,ISFET} - V_{th,ISFET}}{A}} - e^{\frac{V_{RS,REFET} - V_{th,REFET}}{A}} \right) \quad (9.15)$$

where A , $V_{RS,REFET}$, $V_{RS,ISFET}$ and $V_{th,REFET}$ are known. Therefore with some calculations, $V_{th,REFET}$ can be found calculated the measured V_{out} . Alternatively, $V_{RS,REFET}$ can be tuned to result in a zero output voltage, V_{out} . At this point according to Eq. 9.15:

$$V_{RS,ISFET} - V_{RS,REFET} = V_{th,ISFET} - V_{th,REFET} = V_{th,ISFET} |_{pH=x} - V_{th,ISFET} |_{pH=7} = \alpha(x-7) \quad (9.16)$$

which shows that the difference in the V_{RS} voltages of the ISFET and REFET is now linearly proportional to the difference of the pH in the two chambers. This provides another means to investigate the pH of the unknown analyte and the characteristics of the ISFET.

To provide an electrical reference for the ISFET, a MOSFET with a similar size is added to the array. It is connected through the multiplexer to the reference integrator, and its gate voltage is accessible on-chip. Therefore, With a similar argument, the V_{GS} of the MOSFET can be tuned to result in a zero output at DIRIC. In this case:

$$\frac{V_{RS,ISFET} - V_{th,ISFET}}{n_{ISFET}} = \frac{V_{GS,MOS} - V_{th,MOS}}{n} \quad (9.17)$$

9.6 Simulation results

The layout of DIRIC and the on-chip sensors is shown in Fig. 9.17. DIRIC alone occupies 0.6 mm^2 , and the sensor array measures $0.7 \text{ mm} \times 0.4 \text{ mm}$. It works with 3.3 V supply voltage and consumes 9.9 mW power.

The last metal layer is used for the on-chip sensors. The ISFET, MOSFET and REFET use the passivation layer as discussed before as the pH-sensitive layer. For the other sensors a pad opening layer is used to remove the last passivation and make the electrodes exposed to the solution and for further nano-structuring and development.

After the fabrication, all the chip surface except the sensor array will be encapsulated using glob topping epoxy. The sensor array is placed in the middle of the chip to ensure more than 0.5 mm distance from the edges of the fabricated IC. This is to ensure a proper encapsulation

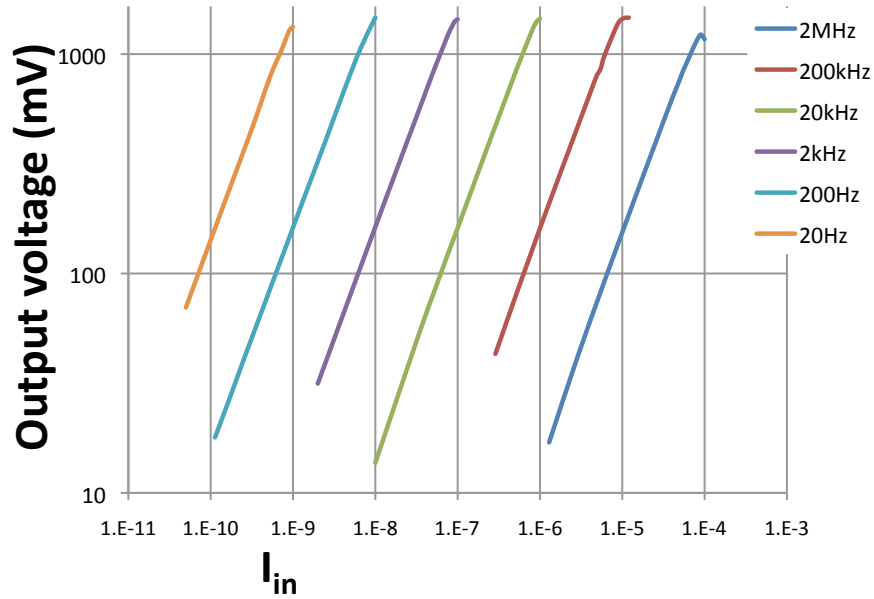


Figure 9.18: The input-output characteristics of the readout circuit for a wide range of input currents in different frequency settings. The whole range of 0.1 nA to $100 \text{ }\mu\text{A}$ can be covered by three clock frequencies: 200 Hz , 20 kHz , and 2 MHz .

Table 9.3: Design specifications and performance of the amplifier

<i>parameter</i>	<i>value</i>
Current range	$\pm 100 \text{ }\mu\text{A}$
Input current dynamic range	124 dB
Input referred current noise	150 pA
maximum input referred leakage current	38 pA
Voltage step size	3.3 mV
Technology	$0.35 \text{ }\mu\text{m}$
Supply voltage	3.3 V
Power consumption	9.9 mW
Area	0.9 mm^2

of the chip and opening in the sensor area.

The simulated input-output characteristics of the readout circuit in the single-mode operation is shown in Fig. 9.18 for a wide input current range. The current range can be divided into three sub-ranges: 0.1 nA to 10 nA , 10 nA to $1 \text{ }\mu\text{A}$, and $1 \text{ }\mu\text{A}$ to $100 \text{ }\mu\text{A}$. Fig. 9.18 shows that these sub-range can be covered by only three clock frequencies: 200 Hz , 20 kHz , and 2 MHz . The minimum detectable current is limited by the noise of the system as well as the input-dependant leakage current of the capacitor and the switches of the main integrator. Both effects are simulated for different input current ranges using periodic steady-state simulation

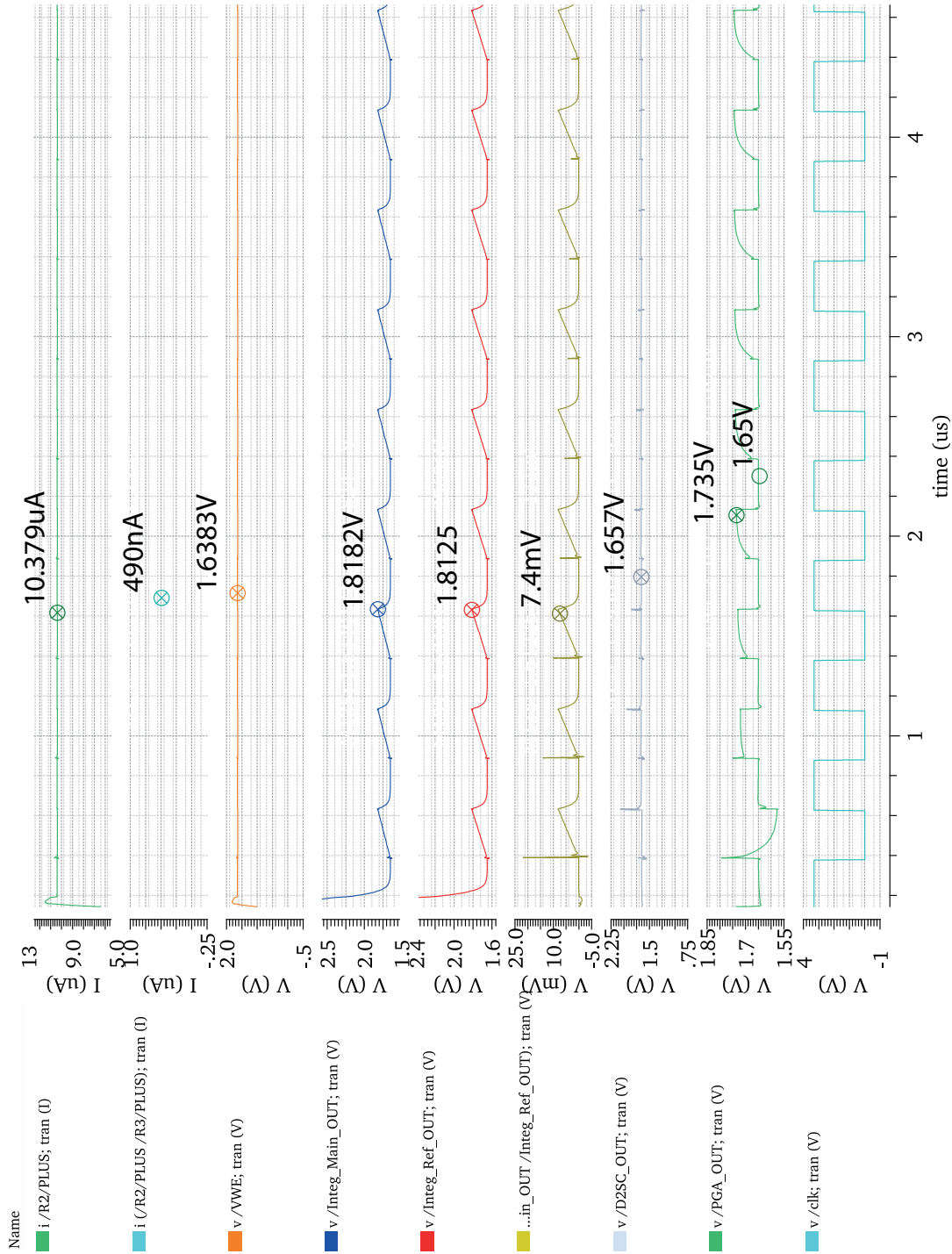


Figure 9.19: The simulated voltages of different nodes in the readout circuit for $I_{in} = 10 \mu A$, $\Delta I_{in} = 0.5 \mu A$, $f_{clk} = 2 MHz$, and $PGA = 15$.

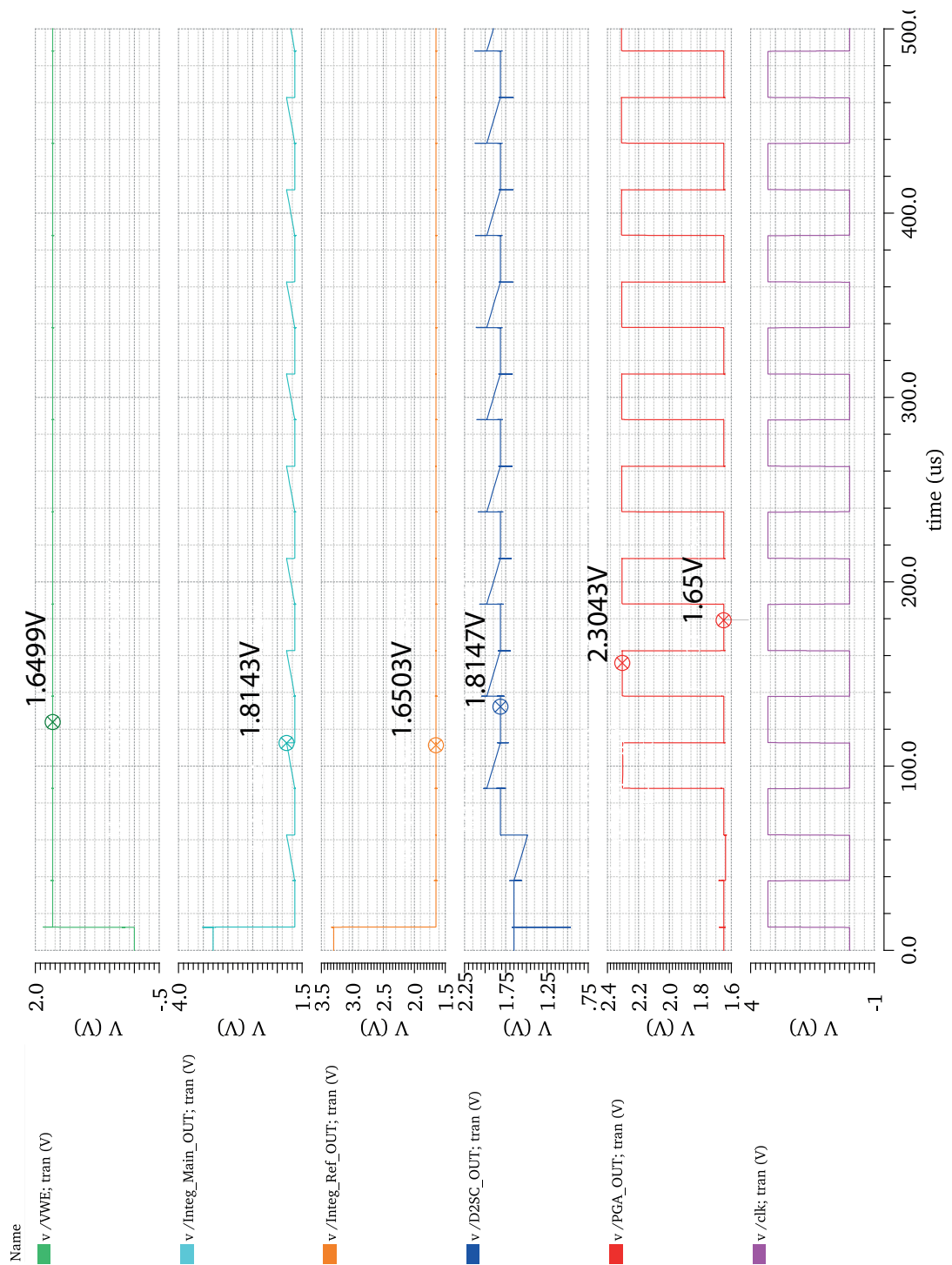


Figure 9.20: The simulated voltages of different nodes in the readout circuit for $I_{in} = 100 \text{ nA}$, $f_{clk} = 20 \text{ kHz}$, and $PGA = 4$.

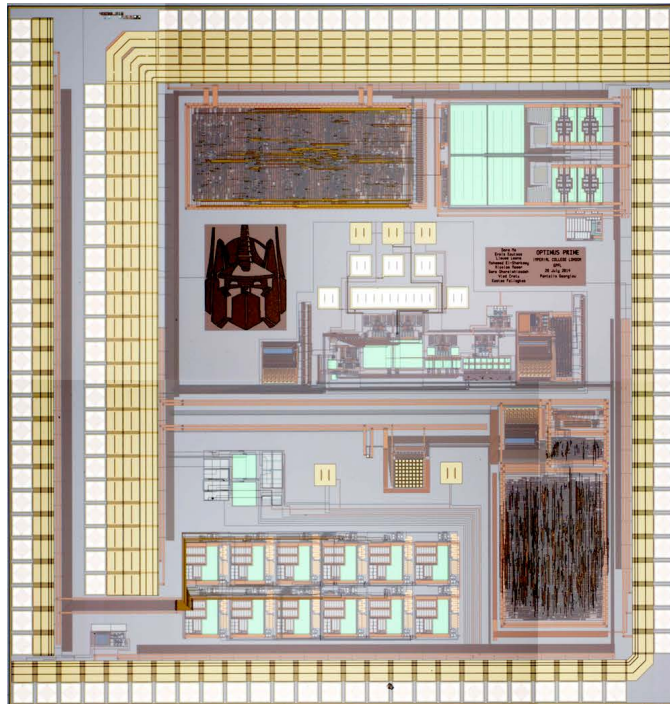


Figure 9.21: The microphotograph of the $3.3 \times 3.3 \text{ mm}$ IC fabricated in AMS $0.35 \mu\text{m}$. It includes DIRIC and the on-chip sensor array in the middle.

and results are reported in Table 9.3.

An example of the transient simulation of different nodes in the readout circuit is shown in Fig. 9.19. In this simulation the output voltages of the integrator, the D2SC, and the PGA are simulated in the differential-mode when $I_{in1} = 10.5 \mu\text{A}$, $I_{in2} = 10 \mu\text{A}$, $f_{clk} = 2 \text{ MHz}$, and PGA gain is set to 15.

An example of the single-mode measurement is also shown where the input current is 100 nA , $f_{clk} = 20 \text{ kHz}$ and the gain of the PGA is 4. The simulated waveforms are shown in Fig. 9.20.

The circuit is fabricated in miniasic AMS $0.35 \mu\text{m}$ technology. The micro-photograph of the fabricated IC is shown in Fig. 9.21 which includes DIRIC.

9.7 Chapter contributions and summary

In this chapter, DIRIC is presented for differential measurement of on-chip and off-chip amperometric sensors. DIRIC is the first complete and fully-integrated readout circuit that removes the background current from the sensor current, amplifies the redox current and digitize it. Therefore, the output of DIRIC eliminates the effect of the background current. Moreover, DIRIC is the first fully-integrated differential IC that samples the input currents at the same time.

The on-chip sensor array includes three sensing sites for metabolite sensing (glucose, lactate, and ATP) and an ISFET for pH measurement. An on-chip WE_C , a REFET and a MOSFET provide the reference for the measurements. Differential readout is achieved through a chain of switched-capacitor circuits followed by an ADC to digitalize the data. The advantage of differential measurement is the elimination of the background current during the amperometric measurements. The system is designed and fabricated in $0.35\ \mu m$ technology. Simulation results show that the readout circuit can measure currents in $\pm 100\ \mu A$ range with $150\ pA$ resolution. Preliminary measurements on the fabricated IC agreed well with the simulations.

10 Conclusions and future work

This dissertation introduces new approaches for the development of potentiostats for amperometric electrochemical biosensors. Electrochemical detection of biological agents is important in several domains, including the medical practice, the discovery of biological mechanisms and monitoring the environment. Electrochemical detection of biocompounds has been extremely popular in the last two decades and a large number of commercial devices are based on enzyme-based biosensors. A notable case is the family of FDA-approved devices for glucose monitoring.

Continuous monitoring of human metabolism is of crucial importance for personalized medicine. Many metabolic diseases may be monitored by means of different endogenous metabolites (i.e. glucose, lactate, ATP). On the other hand, metabolism of exogenous compounds (i.e. anti-cancer drugs) can enhance the outcome of a therapy according to the individual patient. To this aim, bio-monitoring can be effectively used to tune the dosage of a therapy.

Implantable medical devices (IMDs) are emerging as a valid alternative for continuous monitoring. They eliminate the need for blood sampling and decrease the test costs. IMDs have to be small to be minimally invasive, and low power. Moreover, they should be able to detect a specific group of key metabolites and/or drugs within a single platform, to accurately monitor the health condition of the patient and to enable personalized therapy. Finally, the IMD requires the full-integration of the biosensors together with the electronic circuits to control and readout them.

The readout circuits in IMDs require the integration of several electrochemical detection techniques to enable multi-metabolite detection. Moreover, the need for calibration of the biosensors for environmental variables such as pH and temperature, necessitates the co-design of the sensors and circuits to achieve precise and accurate bio-monitoring. To achieve a low-power and small IMD, self-contained readout circuits are designed in this thesis that perform several measurements techniques with little energy and area budgets.

10.1 Thesis summary and contribution

The contributions of this dissertation were presented as follows:

- The design, implementation, characterization, and validation of two sub-mW ICs (LOPHIC and ARIC) are presented. The ICs are designed to control and readout electrochemical sensors, and they extend significantly the state-of-the-art of potentiostat for multi-metabolite sensing.
- ARIC is reconfigurable and can be commanded from outside to perform different types of measurement on different sensors. In addition to providing biosensor control and readout, it enables the calibration of the biosensor with pH and temperature. ARIC is the first IC that provides temperature measurement through off-chip RTD.
- Two novel circuits to measure off-chip resistors (RTDs) are presented, one of which is embedded into ARIC to enable the calibration of the biosensors with temperature. Innovative temperature-independent current sources were designed in these circuits.
- The application of ARIC in two IMDs aimed for health-care monitoring (HEM-IMD) and personalized therapy (PET-IMD) is showed where glucose and paracetamol were successfully measured by ARIC while it was remotely powered. This is the first remotely-powered IMD that measures both glucose and drugs.
- The first implemented cryptographic-system that provides security and privacy for the subcutaneous IMDs is presented. The system is integrated into ARIC and prevents low level attacks to the system while consumes little energy ($7 \mu W$). The implemented cryptosystem takes into consideration the unique threat models and constraints of the implantable biosensors. Therefore, it is suitable to be integrated into the future IMDs to avoid vulnerabilities in both control and privacy.
- The effect of introducing CNTs into the sensors on the noise and SNR of the measurements is studied for the first time. This is the first time that the noise of the sensors incorporating the CNTs is studied. The outcome of the measurements proved that the use of highest possible voltage, highest possible frequency, as well as the presence of CNTs results in a higher SNR in chronoamperometry measurement of both Hydrogen peroxide (H_2O_2) and Ferricyanide.
- A fully-integrated circuit is presented to eliminate the effect of the background current through differential measurement. This is in particular important for sensors incorporating CNTs. DIRIC outputs a digital value which is only proportional to the redox current. together with the DIRIC, an on-chip sensor array is designed to measure multiple metabolites as well as pH.

10.2 Future work

ARIC has been tested and validated and the results are promising for further work and experiments to perform. However, some improvements can be still implemented to enhance the autonomy of the IMDs system. As discussed in Chapter 6, the commands to configure ARIC are sent by the micro-controller instead of the patch in the HEM-system or EXER in PET-system. This was mainly due to the complexity of downlink communications from the external unit to the IMD. As a line of future work, the micro-controller can be embedded into ARIC. Alternatively, a start-up mode could be defined in which ARIC performs a certain set of measurements as soon as it is powered-on. This would also reduce the size of the IMDs.

The power consumption of DIRIC could be further reduced by optimizing the design of the opamps. Moreover, an automatic-gain-control can be developed to automatically change the clock frequency of the readout circuit according to the input current.

Regarding the sensor noise characterisation, more measurements on other sensors, such as glucose sensor, in both low and high frequencies could be performed to study the effect of the enzymes on the SNR as well. The noise in other types of electrochemical measurements such as cyclic voltammetry could be studied as well. These are in particular important to develop closed-form models for the noise of bio-nano-sensors. Such models not only help in understanding the noise dependency on the physical and chemical properties of the sensor, but can also be used in the simulations of the readout ICs.

While LCS provides lightweight cryptosystem that can be easily integrated to the IMDs, further improvements are needed for the key setting and management. This has to be addressed in a way to ensure the autonomy of the device once it is fabricated. Instead of using the JTAG to set the key, *Physical unclonable function* (PUF) technology might be used [162, 163]. PUF is a physical entity that is embodied in a physical structure and is easy to evaluate but hard to predict. Such structure can be designed and embedded into the next-generation ARIC.

Further validation experiments can be carried out with PET-IMD. We may consider to monitor other relevant metabolites and drugs such as Lactate, Mitoxantrone, and Ifosfamide. An algorithm can be developed to calibrate the bio-measurements with the measured temperature. This can be integrated into the user interface to directly provide the calibrated data to the user.

Finally, despite all the benefits of the remote powering of the IMD, the in-vitro tests showed a higher noise compare to the PCB-level measurements. The main reason is the absence of a solid ground in the fully-integrated IMD. A possible solution to reduce the noise is to integrate all the front-end electronics, in particular, ARIC, PMICs and the micro-controller, into a single IC to shorten the wiring and to reduce the noise on the IMD's ground.

I hope you enjoyed reading my PhD dissertation, the story of my engineered scientific-life over the last 1638 days!

Bibliography

- [1] C. Boero, S. Carrara, G. Del Vecchio, L. Calzà, and G. De Micheli, “Highly sensitive carbon nanotube-based sensing for lactate and glucose monitoring in cell culture,” *NanoBioscience, IEEE Transactions on*, vol. 10, no. 1, pp. 59–67, 2011.
- [2] S. Ghoreishizadeh, C. Baj-Rossi, S. Carrara, and G. De Micheli, “Nano-sensor and circuit design for anti-cancer drug detection,” in *Life Science Systems and Applications Workshop (LISSA)*, 2011, pp. 28–33.
- [3] A. Cavallini, “An implantable biosensor array for personalized therapy applications,” Ph.D. dissertation, École Polytechnique Fédérale de Lausanne (EPFL), 2013.
- [4] A. Cavallini, C. Baj-Rossi, S. Ghoreishizadeh, G. De Micheli, and S. Carrara, “Design, fabrication, and test of a sensor array for perspective biosensing in chronic pathologies,” in *Biomedical Circuits and Systems Conference (BioCAS), 2012 IEEE*, Nov 2012, pp. 124–127.
- [5] M. Ahmadi and G. Jullien, “Current-mirror-based potentiostats for three-electrode amperometric electrochemical sensors,” *Circuits and Systems I: Regular Papers, IEEE Transactions on*, vol. 56, no. 7, pp. 1339–1348, July 2009.
- [6] S. Sutula, J. Pallares Cuxart, J. Gonzalo-Ruiz, F. Xavier Munoz-Pascual, L. Teres, and F. Serra-Graells, “A 25 μ w all-mos potentiostatic delta-sigma adc for smart electrochemical sensors,” *Circuits and Systems I: Regular Papers, IEEE Transactions on*, vol. 61, no. 3, pp. 671–679, March 2014.
- [7] V. Balasubramanian, P.-F. Ruedi, Y. Temiz, A. Ferretti, C. Guiducci, and C. Enz, “A 0.18 μ m biosensor front-end based on 1/f noise, distortion cancelation and chopper stabilization techniques,” *Biomedical Circuits and Systems, IEEE Transactions on*, vol. 7, no. 5, pp. 660–673, Oct 2013.
- [8] G. De Micheli, S. Ghoreishizadeh, C. Boero, F. Valgimigli, and S. Carrara, “An integrated platform for advanced diagnostics,” in *Design, Automation Test in Europe Conference Exhibition*, 2011, pp. 1–6.

Bibliography

- [9] L. Li, X. Liu, W. Qureshi, and A. Mason, "CMOS amperometric instrumentation and packaging for biosensor array applications," *Biomedical Circuits and Systems, IEEE Transactions on*, vol. 5, no. 5, pp. 439–448, Oct 2011.
- [10] S. Ghoreishizadeh, C. Baj-Rossi, A. Cavallini, S. Carrara, and G. De Micheli, "An integrated control and readout circuit for implantable multi-target electrochemical biosensing," *Biomedical Circuits and Systems, IEEE Transactions on*, vol. PP, no. 99, pp. 1–1, 2014.
- [11] S. Ghoreishizadeh, S. Carrara, and G. De Micheli, "A configurable ic to control, readout, and calibrate an array of biosensors," in *Circuit Theory and Design (ECCTD), 2013 European Conference on*, Sept 2013, pp. 1–4.
- [12] S. Ghoreishizadeh, C. Boero, A. Pullini, C. Baj-Rossi, S. Carrara, and G. De Micheli, "Sub-mw reconfigurable interface ic for electrochemical sensing," in *Biomedical Circuits and Systems Conference (BioCAS), 2014 IEEE*, Oct 2014, pp. 232–235.
- [13] C. Baj-Rossi, E. Kilinc, S. Ghoreishizadeh, D. Casarino, T. Jost, C. Dehollain, F. Grassi, L. Pastorino, G. De Micheli, and S. Carrara, "Full fabrication and packaging of an implantable multi-panel device for monitoring of metabolites in small animals," *Biomedical Circuits and Systems, IEEE Transactions on*, vol. 8, no. 5, pp. 636–647, Oct 2014.
- [14] S. S. Ghoreishizadeh, T. Yalcin, A. Pullini, G. De Micheli, W. Burtleson, and S. Carrara, "A lightweight cryptographic system for implantable biosensors," in *Biomedical Circuits and Systems Conference (BioCAS), 2014 IEEE*, Oct 2014, pp. 472–475.
- [15] S. Ghoreishizadeh, I. Taurino, S. Carrara, and G. De Micheli, "A current-mode potentiostat for multi-target detection tested with different lactate biosensors," in *Biomedical Circuits and Systems Conference (BioCAS), 2012 IEEE*, Nov 2012, pp. 128–131.
- [16] S. Ghoreishizadeh, G. Nanda, S. Carrara, and G. De Micheli, "Empirical study of noise dependence in electrochemical sensors," in *Advances in Sensors and Interfaces (IWASI), 2013 5th IEEE International Workshop on*, June 2013, pp. 36–39.
- [17] P. Georgiou, "Chemical bionics - a novel design approach using ion sensitive field effect transistors," Ph.D. dissertation, Imperial College of Science, Technology and Medicine, University of London, 2008.
- [18] C. Hiemke, "Clinical utility of drug measurement and pharmacokinetics – therapeutic drug monitoring in psychiatry," *European Journal of Clinical Pharmacology*, vol. 64, no. 2, pp. 159–166, 2008. [Online]. Available: <http://dx.doi.org/10.1007/s00228-007-0430-1>
- [19] P. D'Orazio, "Biosensors in clinical chemistry- 2011 update," *Clinica Chimica Acta*, vol. 412, no. 19, pp. 1749–1761, 2011.

- [20] A. S. Gross, "Best practice in therapeutic drug monitoring," *British journal of clinical pharmacology*, vol. 46, no. 2, pp. 95–99, 2002.
- [21] F. Valgimigli, F. Lucarelli, C. Scuffi, S. Morandi, and I. Sposato, "Evaluating the clinical accuracy of glucomen® day: a novel microdialysis-based continuous glucose monitor," *Journal of diabetes science and technology*, vol. 4, no. 5, pp. 1182–1192, 2010.
- [22] A. Poscia, D. Messeri, D. Moscone, F. Ricci, and F. Valgimigli, "A novel continuous subcutaneous lactate monitoring system," *Biosensors and bioelectronics*, vol. 20, no. 11, pp. 2244–2250, 2005.
- [23] S. Carrara, L. Bolomey, C. Boero, A. Cavallini, E. Meurville, G. De Micheli, T. Rezzonico, M. Proietti, and F. Grassi, "Single-metabolite bio-nano-sensors and system for remote monitoring in animal models," in *Sensors, 2011 IEEE*. IEEE, 2011, pp. 716–719.
- [24] A. Cavallini, G. De Micheli, and S. Carrara, "Comparison of three methods of biocompatible multi-walled carbon nanotubes confinement for the development of implantable amperometric adenosine-5-triphosphate biosensors," *Sensor Letters*, vol. 9, no. 5, pp. 1838–1844, 2011.
- [25] A. J. Bard and L. R. Faulkner, *Electrochemical Methods: Fundamentals and Applications*. John Wiley & Sons, Inc, Dec. 2001. [Online]. Available: <http://www.wiley.com/WileyCDA/WileyTitle/productCd-0471043729.html>
- [26] S. Carrara, C. Baj-Rossi, C. Boero, and G. De Micheli, "Do carbon nanotubes contribute to electrochemical biosensing?" *Electrochimica Acta*, vol. 128, pp. 102–112, 2014.
- [27] Y. Liu, Y. Zhao, B. Sun, and C. Chen, "Understanding the toxicity of carbon nanotubes," *Accounts of Chemical Research*, vol. 46, no. 3, pp. 702–713, 2012.
- [28] S. Arens, U. Schlegel, G. Printzen, W. Ziegler, S. Perren, and M. Hansis, "Influence of materials for fixation implants on local infection an experimental study of steel versus titanium dcp in rabbits," *Journal of Bone & Joint Surgery, British Volume*, vol. 78, no. 4, pp. 647–651, 1996.
- [29] K. B. Koller and F. M. Hawkrige, "The effects of temperature and electrolyte at acidic and alkaline ph on the electron transfer reactions of cytochrome c at in₂o₃ electrodes," *Journal of Electroanalytical Chemistry and Interfacial Electrochemistry*, vol. 239, pp. 291–306, 1988.
- [30] M. Briman, K. Bradley, and G. Gruner, "Source of 1/f noise in carbon nanotube devices," *Journal of Applied Physics*, vol. 100, no. 1, pp. 013 505–013 505–5, Jul 2006.
- [31] D. Kingrey and P. G. Collins, "Noise in carbon nanotube electronics," in *SPIE Third International Symposium on Fluctuations and Noise*. International Society for Optics and Photonics, 2005, pp. 92–100.

Bibliography

- [32] P. G. Collins, M. Fuhrer, and A. Zettl, "1/f noise in carbon nanotubes," *Applied Physics Letters*, vol. 76, no. 7, pp. 894–896, 2000.
- [33] A. Hassibi, H. Vikalo, and A. Hajimiri, "On noise processes and limits of performance in biosensors," *Journal of applied physics*, vol. 102, no. 1, p. 014909, 2007.
- [34] A. Hassibi, R. Navid, R. W. Dutton, and T. H. Lee, "Comprehensive study of noise processes in electrode electrolyte interfaces," *Journal of applied physics*, vol. 96, no. 2, pp. 1074–1082, 2004.
- [35] K. Rajeshwar and J. G. Ibanez, *Environmental electrochemistry: Fundamentals and applications in pollution sensors and abatement*. Academic Press, 1997.
- [36] F.-G. Banica, *Chemical sensors and biosensors: fundamentals and applications*. John Wiley & Sons, 2012.
- [37] F. Valgimigli *et al.*, "Evaluating the clinical accuracy of glucomenday: A novel microdialysis-based continuous glucose monitor," *Journal of Diabetes Science Technology*, vol. 4, pp. 1182–1192, 2010.
- [38] M.-C. Tsai and Y.-C. Tsai, "Adsorption of glucose oxidase at platinum-multiwalled carbon nanotube-alumina-coated silica nanocomposite for amperometric glucose biosensor," *Sensors and Actuators B: Chemical*, vol. 141, no. 2, pp. 592 – 598, 2009.
- [39] M. R. Romero *et al.*, "Design and optimization of a lactate amperometric biosensor based on lactate oxidase cross-linked with polymeric matrixes," *Sensors and Actuators B: Chemical*, vol. 131, no. 2, pp. 590 – 595, 2008.
- [40] A. Salimi *et al.*, "Fabrication of a sensitive cholesterol biosensor based on cobalt-oxide nanostructures electrodeposited onto glassy carbon electrode," *Electroanalysis*, vol. 21, no. 24, pp. 2693–2700, 2009.
- [41] Y. Hu *et al.*, "Direct measurement of glutamate release in the brain using a dual enzyme-based electrochemical sensor," *Brain Research*, vol. 659, no. 1-2, pp. 117 – 125, 1994.
- [42] M. Antonini *et al.*, "Preliminary electrochemical characterisation of cytochrome P4501A2 clozapine interaction," *IEE Proceedings on Nanobiotechnology*, vol. 150, no. 1, pp. 31–34, june 2003.
- [43] N. R. Hendricks *et al.*, "Microsomal cytochrome P450-3A4 (CYP3A4) nanobiosensor for the determination of 2,4-dichlorophenol—an endocrine disruptor compound," *Electrochimica Acta*, vol. 54, no. 7, pp. 1925–1931, 2009.
- [44] A. Ignaszak *et al.*, "Novel therapeutic biosensor for indinavir—a protease inhibitor antiretroviral drug," *Journal of Pharmaceutical and Biomedical Analysis*, vol. 49, no. 2, pp. 498–501, 2009.

- [45] S. Carrara *et al.*, "Screen-printed electrodes based on carbon nanotubes and cytochrome p450scc for highly sensitive cholesterol biosensors," *Biosensors and Bioelectronics*, vol. 24, pp. 148–150, 2008.
- [46] V. V. Shumyantseva *et al.*, "A new format of electrodes for the electrochemical reduction of cytochromes p450," *Journal of Inorganic Biochemistry*, vol. 100, no. 8, pp. 1353–1357, 2006.
- [47] —, "Direct electron transfer of cytochrome P450 2B4 at electrodes modified with nonionic detergent and colloidal clay nanoparticles," *Analytical Chemistry*, vol. 76, no. 20, pp. 6046–6052, 2004.
- [48] S. Liu *et al.*, "Electrochemistry of cytochrome P450 enzyme on nanoparticle-containing membrane-coated electrode and its applications for drug sensing," *Analytical Biochemistry*, vol. 375, no. 2, pp. 209–216, 2008.
- [49] L. Peng *et al.*, "Electrochemistry of cytochrome P450 2B6 on electrodes modified with zirconium dioxide nanoparticles and platinum components," *Electroanalysis*, vol. 20, no. 7, pp. 803–807, 2008.
- [50] D. Johnson *et al.*, "Electrochemical characterisation of the human cytochrome P450 CYP2C9," *Biochemical Pharmacology*, vol. 69, no. 10, pp. 1533–1541, 2005.
- [51] A. Fantuzzi *et al.*, "Direct electrochemistry of immobilized human cytochrome P450 2E1," *Journal of the American Chemical Society*, vol. 126, no. 16, pp. 5040–5041, 2004.
- [52] B. R. Eggins, *Chemical sensors and biosensors*, LTD, Ed. John Wiley & sons, 2009, pp. 125-169.
- [53] S. M. J. Mocak, A.M. Bond and G. Scollary, "A statistical overview of standard (iupac and acs) and new procedures for determining the limits of detection and quantification: application to voltammetric and stripping techniques," *Pure and Applied Chemistry*, vol. 69, no. 2, pp. 297–328, 1997. [Online]. Available: <http://www.mdpi.com/1424-8220/12/5/6520>
- [54] D. R. Thevenot *et al.*, "Electrochemical biosensors: recommended definitions and classification," IUPAC, Tech. Rep., 1999.
- [55] P. Childs, J. Greenwood, and C. Long, "Review of temperature measurement," *Review of scientific instruments*, vol. 71, no. 8, pp. 2959–2978, 2000.
- [56] T. Thamaraiselvi and S. Rajeswari, "Biological evaluation of bioceramic materials-a review," *Carbon*, vol. 24, no. 31, p. 172, 2004.
- [57] S. Carrara, M. D. Torre, A. Cavallini, D. De Venuto, and G. De Micheli, "Multiplexing pH and temperature in a molecular biosensor," in *Biomedical Circuits and Systems Conference (BioCAS), 2010 IEEE*. IEEE, 2010, pp. 146–149.

Bibliography

- [58] A. P. Li, D. L. Kaminski, and A. Rasmussen, "Substrates of human hepatic cytochrome p450 3a4," *Toxicology*, vol. 104, no. 1, pp. 1–8, 1995.
- [59] S. Carrara, V. V. Shumyantseva, A. I. Archakov, and B. Samorì, "Screen-printed electrodes based on carbon nanotubes and cytochrome p450scc for highly sensitive cholesterol biosensors," *Biosensors and Bioelectronics*, vol. 24, no. 1, pp. 148–150, 2008.
- [60] S. Carrara, C. Boero, and G. De Micheli, "Quantum dots and wires to improve enzymes-based electrochemical bio-sensing," in *Nano-Net*. Springer, 2009, pp. 189–199.
- [61] S. Carrara, A. Cavallini, V. Erokhin, and G. De Micheli, "Multi-panel drugs detection in human serum for personalized therapy," *Biosensors and Bioelectronics*, vol. 26, no. 9, pp. 3914–3919, 2011.
- [62] P. Kurzweil, "Metal oxides and ion-exchanging surfaces as ph sensors in liquids: State-of-the-art and outlook," *Sensors*, vol. 9, no. 6, pp. 4955–4985, 2009.
- [63] S. Cherevko, T. Reier, A. R. Zeradjanin, Z. Pawolek, P. Strasser, and K. J. Mayrhofer, "Stability of nanostructured iridium oxide electrocatalysts during oxygen evolution reaction in acidic environment," *Electrochemistry Communications*, vol. 48, no. 0, pp. 81 – 85, 2014. [Online]. Available: <http://www.sciencedirect.com/science/article/pii/S1388248114002823>
- [64] W. Agnew, T. Yuen, D. McCreery, and L. Bullara, "Histopathologic evaluation of prolonged intracortical electrical stimulation," *Experimental neurology*, vol. 92, no. 1, pp. 162–185, 1986.
- [65] M. S. H. James D Weiland, David J Anderson, "In vitro electrical properties for iridium oxide versus titanium nitride stimulating electrodes," *Biomedical Engineering, IEEE Transactions on*, vol. 49, no. 12, pp. 1574–1579, 2002.
- [66] W. Olthuis, M. Robben, P. Bergveld, M. Bos, and W. Van Der Linden, "ph sensor properties of electrochemically grown iridium oxide," *Sensors and Actuators B: Chemical*, vol. 2, no. 4, pp. 247–256, 1990.
- [67] B. Baker, "Temperature sensing technologies," AN679, *Microchip Technology Inc*, 1998.
- [68] H. Narula and J. Harris, "A time-based vlsi potentiostat for ion current measurements," *Sensors Journal, IEEE*, vol. 6, no. 2, pp. 239–247, April 2006.
- [69] S. Hwang and S. Sonkusale, "CMOS VLSI potentiostat for portable environmental sensing applications," *Sensors Journal, IEEE*, vol. 10, no. 4, pp. 820–821, April 2010.
- [70] S. Ayers, K. Gillis, M. Lindau, and B. Minch, "Design of a CMOS potentiostat circuit for electrochemical detector arrays," *Circuits and Systems I: Regular Papers, IEEE Transactions on*, vol. 54, no. 4, pp. 736–744, April 2007.

- [71] A. Zeki and H. Kuntman, "Accurate and high output impedance current mirror suitable for CMOS current output stages," *Electronics Letters*, vol. 33, no. 12, pp. 1042–1043, Jun 1997.
- [72] H. Jafari and R. Genov, "Chopper-stabilized bidirectional current acquisition circuits for electrochemical amperometric biosensors," *Circuits and Systems I: Regular Papers, IEEE Transactions on*, vol. 60, no. 5, pp. 1149–1157, May 2013.
- [73] Y.-T. Liao, H. Yao, A. Lingley, B. Parviz, and B. Otis, "A 3 μW CMOS glucose sensor for wireless contact-lens tear glucose monitoring," *Solid-State Circuits, IEEE Journal of*, vol. 47, no. 1, pp. 335–344, Jan 2012.
- [74] R. Turner, D. Harrison, and H. Baltes, "A CMOS potentiostat for amperometric chemical sensors," *Solid-State Circuits, IEEE Journal of*, vol. 22, no. 3, pp. 473–478, Jun 1987.
- [75] A. Manickam, A. Chevalier, M. McDermott, A. Ellington, and A. Hassibi, "A CMOS electrochemical impedance spectroscopy (EIS) biosensor array," *Biomedical Circuits and Systems, IEEE Transactions on*, vol. 4, no. 6, pp. 379–390, Dec 2010.
- [76] R. Genov, M. Stanacevic, M. Naware, G. Cauwenberghs, and N. Thakor, "16-channel integrated potentiostat for distributed neurochemical sensing," *Circuits and Systems I: Regular Papers, IEEE Transactions on*, vol. 53, no. 11, pp. 2371–2376, Nov 2006.
- [77] M. Roham, D. Covey, D. Daberkow, E. Ramsson, C. Howard, B. Heidenreich, P. Garris, and P. Mohseni, "A wireless ic for time-share chemical and electrical neural recording," *Solid-State Circuits, IEEE Journal of*, vol. 44, no. 12, pp. 3645–3658, Dec 2009.
- [78] M. Mollazadeh, K. Murari, G. Cauwenberghs, and N. Thakor, "Wireless micropower instrumentation for multimodal acquisition of electrical and chemical neural activity," *Biomedical Circuits and Systems, IEEE Transactions on*, vol. 3, no. 6, pp. 388–397, Dec 2009.
- [79] M. Stanacevic, K. Murari, A. Rege, G. Cauwenberghs, and N. Thakor, "Vlsi potentiostat array with oversampling gain modulation for wide-range neurotransmitter sensing," *Biomedical Circuits and Systems, IEEE Transactions on*, vol. 1, no. 1, pp. 63–72, March 2007.
- [80] C. Yang, Y. Huang, B. Hassler, R. Worden, and A. Mason, "Amperometric electrochemical microsystem for a miniaturized protein biosensor array," *Biomedical Circuits and Systems, IEEE Transactions on*, vol. 3, no. 3, pp. 160–168, June 2009.
- [81] P. Levine, P. Gong, R. Levicky, and K. L. Shepard, "Active CMOS sensor array for electrochemical biomolecular detection," *Solid-State Circuits, IEEE Journal of*, vol. 43, no. 8, pp. 1859–1871, Aug 2008.
- [82] A. Hassibi and T. Lee, "A programmable 0.18 μm CMOS electrochemical sensor microarray for biomolecular detection," *Sensors Journal, IEEE*, vol. 6, no. 6, pp. 1380–1388, Dec 2006.

Bibliography

- [83] Y.-J. Huang, T.-H. Tzeng, T.-W. Lin, C.-W. Huang, P.-W. Yen, P.-H. Kuo, C.-T. Lin, and S.-S. Lu, "A self-powered CMOS reconfigurable multi-sensor soc for biomedical applications," *Solid-State Circuits, IEEE Journal of*, vol. 49, no. 4, pp. 851–866, April 2014.
- [84] M. Haider, S. Islam, S. Mostafa, M. Zhang, and T. Oh, "Low-power low-voltage current readout circuit for inductively powered implant system," *Biomedical Circuits and Systems, IEEE Transactions on*, vol. 4, no. 4, pp. 205–213, Aug 2010.
- [85] S. Martin, T. Strong, and R. Brown, "Design, implementation, and verification of a CMOS-integrated chemical sensor system," in *MEMS, NANO and Smart Systems, 2004. ICMENS 2004. Proceedings. 2004 International Conference on*, Aug 2004, pp. 379–385.
- [86] S. Martin, F. Gebara, B. Larivee, and R. Brown, "A CMOS-integrated microinstrument for trace detection of heavy metals," *Solid-State Circuits, IEEE Journal of*, vol. 40, no. 12, pp. 2777–2786, Dec 2005.
- [87] S. Martin, F. Gebara, T. Strong, and R. Brown, "A fully differential potentiostat," *Sensors Journal, IEEE*, vol. 9, no. 2, pp. 135–142, Feb 2009.
- [88] V. Shenoy, S. Jung, Y. Yoon, Y. Park, H. Kim, and H.-J. Chung, "A CMOS analog correlator-based painless nonenzymatic glucose sensor readout circuit," *Sensors Journal, IEEE*, vol. 14, no. 5, pp. 1591–1599, May 2014.
- [89] M. Vergani, M. Carminati, G. Ferrari, M. Sampietro, L. Amato, A. Heiskanen, M. Dimaki, W. Svendsen, and J. Emneus, "Compact potentiostat for cellular electrochemical imaging with 54 parallel channels," in *Biomedical Circuits and Systems Conference (BioCAS), 2012 IEEE*, Nov 2012, pp. 136–139.
- [90] A. Hassibi and T. Lee, "A programmable electrochemical biosensor array in 0.18 μm standard CMOS," in *Solid-State Circuits Conference, 2005. Digest of Technical Papers. ISSCC. 2005 IEEE International*, Feb 2005, pp. 564–617 Vol. 1.
- [91] M. Augustyniak, C. Paulus, R. Brederlow, N. Persike, G. Hartwich, D. Schmitt-Landsiedel, and R. Thewes, "A 24x16 CMOS-based chronocoulometric DNA microarray," in *Solid-State Circuits Conference, 2006. ISSCC 2006. Digest of Technical Papers. IEEE International*, Feb 2006, pp. 59–68.
- [92] J. Aziz, K. Abdelhalim, R. Shulyzki, R. Genov, B. Bardakjian, M. Derchansky, D. Serletis, and P. Carlen, "256-channel neural recording and delta compression microsystem with 3d electrodes," *Solid-State Circuits, IEEE Journal of*, vol. 44, no. 3, pp. 995–1005, March 2009.
- [93] E. Santos and I. Vasconcelos, "RTD-based smart temperature sensor: Process development and circuit design," in *Microelectronics, 2008. MIEL 2008. 26th International Conference on*, May 2008, pp. 333–336.

- [94] S. Hu, K. Wu, H. Wang, and J. Chen, "Electrical conductivity measurement method in seawater desalination based on variable frequency excitation," in *Electronic Measurement Instruments, 2009. ICEMI '09. 9th International Conference on*, Aug 2009, pp. 1–810–1–813.
- [95] S. Pop, V. Bande, D. Pitica, and I. Ciascai, "Dynamic measurement circuit for the resistive transducers," in *Design and Technology in Electronic Packaging (SIITME), 2012 IEEE 18th International Symposium for*, Oct 2012, pp. 259–262.
- [96] Y. Qian, Z. Luo, Z. Liu, H. Zhao, C. Li, Y. Song, D. Nan, and J. Wei, "Application of RTD sensor in the real time measurement and wireless transmission," in *Instrumentation and Measurement, Computer, Communication and Control (IMCCC), 2014 Fourth International Conference on*, Sept 2014, pp. 658–662.
- [97] J. W. Lee, T. I. Oh, S. M. Paek, J. S. Lee, and E. J. Woo, "Precision constant current source for electrical impedance tomography," in *Engineering in Medicine and Biology Society, 2003. Proceedings of the 25th Annual International Conference of the IEEE*, vol. 2, Sept 2003, pp. 1066–1069 Vol.2.
- [98] M. Perrott, J. Salvia, F. Lee, A. Partridge, S. Mukherjee, C. Arft, J. Kim, N. Arumugam, P. Gupta, S. Tabatabaei, S. Pamarti, H. Lee, and F. Assaderaghi, "A temperature-to-digital converter for a MEMS-based programmable oscillator with $< \pm 0.5$ ppm frequency stability and 1ps integrated jitter," *Solid-State Circuits, IEEE Journal of*, vol. 48, no. 1, pp. 276–291, Jan 2013.
- [99] P. Park, K. Makinwa, and D. Ruffieux, "A resistor-based temperature sensor for a real time clock with 2ppm frequency stability," in *European Solid State Circuits Conference (ESSCIRC), ESSCIRC 2014 - 40th*, Sept 2014, pp. 391–394.
- [100] M. Shahmohammadi, K. Souri, and K. Makinwa, "A resistor-based temperature sensor for MEMS frequency references," in *ESSCIRC (ESSCIRC), 2013 Proceedings of the*, Sept 2013, pp. 225–228.
- [101] D. Ruffieux, F. Krummenacher, A. Pezous, and G. Spinola-Durante, "Silicon resonator based $3.2\mu w$ real time clock with ± 10 ppm frequency accuracy," *Solid-State Circuits, IEEE Journal of*, vol. 45, no. 1, pp. 224–234, Jan 2010.
- [102] S. Ghoreishizadeh, E. Kilinc, C. Baj-Rossi, C. Dehollain, S. Carrara, and G. De Micheli, "An implantable bio-micro-system for drug monitoring," in *Biomedical Circuits and Systems Conference (BioCAS), 2013 IEEE*, Oct 2013, pp. 218–221.
- [103] B. Ahuja, "An improved frequency compensation technique for CMOS operational amplifiers," *Solid-State Circuits, IEEE Journal of*, vol. 18, no. 6, pp. 629–633, Dec 1983.
- [104] I. Taurino, R. Reiss, M. Richter, M. Fairhead, L. Thöny-Meyer, G. D. Micheli, and S. Carrara, "Comparative study of three lactate oxidases from aerococcus viridans for

Bibliography

- biosensing applications,” *Electrochimica Acta*, vol. 93, no. 0, pp. 72 – 79, 2013. [Online]. Available: <http://www.sciencedirect.com/science/article/pii/S0013468613001126>
- [105] A. Biedler, S. Schneider, F. Bach, S. Soltész, W. Wilhelm, S. Ziegeler, and S. Kreuer, “Methodological aspects of lactate measurement—evaluation of the accuracy of photometric and biosensor methods,” *Open Anesthesiology Journal*, vol. 1, pp. 1–5, 2007.
- [106] D. B. Pyne, T. Boston, D. T. Martin, and A. Logan, “Evaluation of the lactate pro blood lactate analyser,” *European journal of applied physiology*, vol. 82, no. 1-2, pp. 112–116, 2000.
- [107] M. Florescu and C. M. A Brett, “Development and evaluation of electrochemical glucose enzyme biosensors based on carbon film electrodes,” *Talanta*, vol. 65, no. 2, pp. 306–312, 2005.
- [108] V. H. Routh, “Glucose-sensing neurons: are they physiologically relevant?” *Physiology & behavior*, vol. 76, no. 3, pp. 403–413, 2002.
- [109] M. J. Markuszewski, K. Otsuka, S. Terabe, K. Matsuda, and T. Nishioka, “Analysis of carboxylic acid metabolites from the tricarboxylic acid cycle in *Bacillus subtilis* cell extract by capillary electrophoresis using an indirect photometric detection method,” *Journal of Chromatography A*, vol. 1010, no. 1, pp. 113–121, 2003.
- [110] S. S. G. S. R. G. S. F. S. C. B. G. D. M. E. G. K. C. D. Sandro Carrara, Camilla Baj-Rossi, “Full system for translational studies of personalized medicine with free-moving mice,” *in preparation*.
- [111] J. Holthuis, W. Van Oort, F. Römkens, J. Renema, and P. Zuman, “Electrochemistry of podophyllotoxin derivatives: part I. oxidation mechanism of etoposide (pp 16–213),” *Journal of Electroanalytical Chemistry and Interfacial Electrochemistry*, vol. 184, no. 2, pp. 317–329, 1985.
- [112] O. Choksi and L. Carley, “Analysis of switched-capacitor common-mode feedback circuit,” *Circuits and Systems II: Analog and Digital Signal Processing, IEEE Trans. on*, vol. 50, no. 12, pp. 906–917, 2003.
- [113] H. Banba, H. Shiga, A. Umezawa, T. Miyaba, T. Tanzawa, S. Atsumi, and K. Sakui, “A CMOS bandgap reference circuit with sub-1-V operation,” *Solid-State Circuits, IEEE Journal of*, vol. 34, no. 5, pp. 670–674, 1999.
- [114] B. Razavi, *Principles of Data Conversion System Design*. IEEE Press, 1995.
- [115] G. Perenlei, T. W. Tee, N. A. Yusof, and G. J. Kheng, “Voltammetric detection of potassium ferricyanide mediated by multi-walled carbon nanotube/titanium dioxide composite modified glassy carbon electrode,” *Int. J. Electrochem. Sci*, vol. 6, pp. 520–531, 2011.

- [116] I. A. Ges, B. L. Ivanov, D. K. Schaffer, E. A. Lima, A. A. Werdich, and F. J. Baudenbacher, "Thin-film IrOx pH microelectrode for microfluidic-based microsystems," *Biosensors and Bioelectronics*, vol. 21, no. 2, pp. 248–256, 2005.
- [117] S. A. Marzouk, S. Ufer, R. P. Buck, T. A. Johnson, L. A. Dunlap, and W. E. Cascio, "Electrodeposited iridium oxide pH electrode for measurement of extracellular myocardial acidosis during acute ischemia," *Analytical chemistry*, vol. 70, no. 23, pp. 5054–5061, 1998.
- [118] J. Olivo, S. Carrara, and G. De Micheli, "Energy harvesting and remote powering for implantable biosensors," *IEEE Sensors Journal*, vol. 11, no. EPFL-ARTICLE-152140, pp. 1573–1586, 2011.
- [119] W. Siemens, *On the Increase of Electrical Resistance in Conductors with Rise of Temperature, and Its Application to the Measure of Ordinary and Furnace Temperatures*. The Bakerian Lecture (Royal Society), 1871.
- [120] R. Dehghani and S. M. Atarodi, "A new low voltage precision CMOS current reference with no external components," *Circuits and Systems II: Analog and Digital Signal Processing, IEEE Transactions on*, vol. 50, no. 12, pp. 928–932, 2003.
- [121] B. Razavi, *Design of Analog CMOS Integrated Circuits*. McGraw-Hill, 2000.
- [122] J. Olivo, S. Carrara, and G. De Micheli, "Ironic patch: A wearable device for the remote powering and connectivity of implantable systems," in *Instrumentation and Measurement Technology Conference (I2MTC), 2012 IEEE International*, May 2012, pp. 286–289.
- [123] —, "A study of multi-layer spiral inductors for remote powering of implantable sensors," *Biomedical Circuits and Systems, IEEE Transactions on*, vol. 7, no. 4, pp. 536–547, 2013.
- [124] J. Olivo, "Remote powering and communication of implantable biosensors through inductive link," Ph.D. dissertation, École Polytechnique Fédérale de Lausanne (EPFL), 2013.
- [125] S. P. Nichols, A. Koh, W. L. Storm, J. H. Shin, and M. H. Schoenfisch, "Biocompatible materials for continuous glucose monitoring devices," *Chemical reviews*, vol. 113, no. 4, pp. 2528–2549, 2013.
- [126] I. Macrae, "Preclinical stroke research—advantages and disadvantages of the most common rodent models of focal ischaemia," *British journal of pharmacology*, vol. 164, no. 4, pp. 1062–1078, 2011.
- [127] E. Kilinc, M. Ghanad, F. Maloberti, and C. Dehollain, "A remotely powered implantable biomedical system with location detector," *Biomedical Circuits and Systems, IEEE Transactions on*, vol. 9, no. 1, pp. 113–123, Feb 2015.

Bibliography

- [128] E. G. Kilinc, K. Kapucu, F. Maloberti, and C. Dehollain, "Servo-controlled remote powering and low-power data communication of implantable bio-systems for freely moving animals," in *Biomedical Circuits and Systems Conference (BioCAS), 2014 IEEE*. IEEE, 2014, pp. 508–511.
- [129] J. Olivo, L. Foglia, M. A. Casulli, C. Boero, S. Carrara, and G. De Micheli, "Glucose and lactate monitoring in cell cultures with a wireless android interface," in *Biomedical Circuits and Systems Conference (BioCAS), 2014 IEEE*, Oct 2014, pp. 400–403.
- [130] D. M. Russell, D. McCormick, A. J. Taberner, S. Malpas, and D. Budgett, "A high bandwidth fully implantable mouse telemetry system for chronic ecg measurement," in *Engineering in Medicine and Biology Society, EMBC, 2011 Annual International Conference of the IEEE*. IEEE, 2011, pp. 7666–7669.
- [131] E. G. Kilinc, B. Canovas, F. Maloberti, and C. Dehollain, "Intelligent cage for remotely powered freely moving animal telemetry systems," *Power*, vol. 16, p. 24cm, 2012.
- [132] B. Lee, M. Kiani, and M. Ghovanloo, "A smart homecage system with 3d tracking for long-term behavioral experiments," in *Engineering in Medicine and Biology Society (EMBC), 2014 36th Annual International Conference of the IEEE*. IEEE, 2014, pp. 2016–2019.
- [133] D. Nematollahi, H. Shayani-Jam, M. Alimoradi, and S. Niroomand, "Electrochemical oxidation of acetaminophen in aqueous solutions: kinetic evaluation of hydrolysis, hydroxylation and dimerization processes," *Electrochimica Acta*, vol. 54, no. 28, pp. 7407–7415, 2009.
- [134] B. G., P. M. Daemen J., and V. A. G. The keccak sponge function family. [Online]. Available: <http://keccak.noekeon.org>
- [135] W. Bursleson, S. S. Clark, B. Ransford, and K. Fu, "Design challenges for secure implantable medical devices," in *Proceedings of the 49th Annual Design Automation Conference*. ACM, 2012, pp. 12–17.
- [136] W. Bursleson and S. Carrara, *Security and Privacy for Implantable Medical Devices*. Springer, 2013.
- [137] A. Francillon, B. Danev, S. Capkun, S. Capkun, and S. Capkun, "Relay attacks on passive keyless entry and start systems in modern cars." in *NDSS*, 2011.
- [138] X. Fan, H. Hu, G. Gong, E. M. Smith, and D. Engels, "Lightweight implementation of hummingbird cryptographic algorithm on 4-bit microcontrollers," in *Internet Technology and Secured Transactions, 2009. ICITST 2009. International Conference for*. IEEE, 2009, pp. 1–7.
- [139] X. Fan, G. Gong, K. Lauffenburger, and T. Hicks, "FPGA implementations of the hummingbird cryptographic algorithm," in *Hardware-Oriented Security and Trust (HOST), 2010 IEEE International Symposium on*. IEEE, 2010, pp. 48–51.

- [140] C. Beck, D. Masny, W. Geiselmann, and G. Bretthauer, "Block cipher based security for severely resource-constrained implantable medical devices," in *Proceedings of the 4th International Symposium on Applied Sciences in Biomedical and Communication Technologies*. ACM, 2011, p. 62.
- [141] N. Ellouze, M. Allouche, H. Ben Ahmed, S. Rekhis, and N. Boudriga, "Securing implantable cardiac medical devices: Use of radio frequency energy harvesting," in *Proceedings of the 3rd International Workshop on Trustworthy Embedded Devices*, ser. TrustED '13. New York, NY, USA: ACM, 2013, pp. 35–42. [Online]. Available: <http://doi.acm.org/10.1145/2517300.2517307>
- [142] S. Hosseini-Khayat, "A lightweight security protocol for ultra-low power asic implementation for wireless implantable medical devices," in *Medical Information & Communication Technology (ISMICT), 2011 5th International Symposium on*. IEEE, 2011, pp. 6–9.
- [143] G. Bertoni, J. Daemen, M. Peeters, and G. Assche, "Permutation-based encryption, authentication and authenticated encryption," *Directions in Authenticated Ciphers (July 2012)*, 2012.
- [144] C. Strydis, R. M. Seepers, P. Peris-Lopez, D. Siskos, and I. Sourdis, "A system architecture, processor, and communication protocol for secure implants," *ACM Trans. Archit. Code Optim.*, vol. 10, no. 4, pp. 57:1–57:23, Dec. 2013. [Online]. Available: <http://doi.acm.org/10.1145/2555289.2555313>
- [145] S. Mangard, E. Oswald, and T. Popp, *Power analysis attacks: Revealing the secrets of smart cards*. Springer, 2008, vol. 31.
- [146] M. Dworkin, "Recommendation for block cipher modes of operation. methods and techniques," DTIC Document, Tech. Rep., 2001.
- [147] G. Bertoni, J. Daemen, M. Peeters, and G. Van Assche, "Duplexing the sponge: single-pass authenticated encryption and other applications," in *Selected Areas in Cryptography*. Springer, 2012, pp. 320–337.
- [148] M.-J. O. Saarinen and D. Engels, "A do-it-all-cipher for rfid: Design requirements (extended abstract)," *Cryptology ePrint Archive*, Report 2012/317, 2012, <http://eprint.iacr.org/>.
- [149] L. Henzen, P. Gendotti, P. Guillet, E. Pargaetzi, M. Zoller, and F. K. Gürkaynak, "Developing a hardware evaluation method for sha-3 candidates," in *Cryptographic Hardware and Embedded Systems, CHES 2010*. Springer, 2010, pp. 248–263.
- [150] R. Voss, "1/f (flicker) noise: A brief review," in *33rd Annual Symposium on Frequency Control*. 1979, May 1979, pp. 40–46.

Bibliography

- [151] M. Briman, K. Bradley, and G. Gruner, "Source of 1/f noise in carbon nanotube devices," *Journal of applied physics*, vol. 100, no. 1, p. 3505, 2006.
- [152] D. J. Michael and R. M. Wightman, "Electrochemical monitoring of biogenic amine neurotransmission in real time," *Journal of pharmaceutical and biomedical analysis*, vol. 19, no. 1, pp. 33–46, 1999.
- [153] D. L. Robinson, B. J. Venton, M. L. Heien, and R. M. Wightman, "Detecting subsecond dopamine release with fast-scan cyclic voltammetry in vivo," *Clinical chemistry*, vol. 49, no. 10, pp. 1763–1773, 2003.
- [154] H. Jafari, K. Abdelhalim, L. Soleymani, E. Sargent, S. Kelley, and R. Genov, "Nanostructured CMOS wireless ultra-wideband label-free pcr-free dna analysis soc," *Solid-State Circuits, IEEE Journal of*, vol. 49, no. 5, pp. 1223–1241, May 2014.
- [155] C. Baj-Rossi, G. D. Micheli, and S. Carrara, "Electrochemical detection of anti-breast-cancer agents in human serum by cytochrome p450-coated carbon nanotubes," *Sensors*, vol. 12, no. 5, pp. 6520–6537, 2012. [Online]. Available: <http://www.mdpi.com/1424-8220/12/5/6520>
- [156] K. Martin, L. Ozcolak, Y. Lee, and G. C. Temes, "A differential switched-capacitor amplifier," *IEEE Journal of Solid-State Circuits*, vol. 22, pp. 104–106, 1987.
- [157] J. Bausells, J. Carrabina, A. Errachid, and A. Merlos, "Ion-sensitive field-effect transistors fabricated in a commercial CMOS technology," *Sensors and Actuators B: Chemical*, vol. 57, no. 1, pp. 56–62, 1999.
- [158] B. Palán, K. Roubík, M. Husak, and B. Courtois, "CMOS ISFET-based structures for biomedical applications," in *Microtechnologies in Medicine and Biology, 1st Annual International, Conference On. 2000.* IEEE, 2000, pp. 502–506.
- [159] L. Shepherd, P. Georgiou, and C. Toumazou, "A novel voltage-clamped CMOS ISFET sensor interface," in *Circuits and Systems, 2007. ISCAS 2007. IEEE International Symposium on.* IEEE, 2007, pp. 3331–3334.
- [160] Y. Liu, P. Georgiou, T. Prodromakis, T. Constandinou, and C. Toumazou, "An extended CMOS ISFET model incorporating the physical design geometry and the effects on performance and offset variation," *Electron Devices, IEEE Transactions on*, vol. 58, no. 12, pp. 4414–4422, Dec 2011.
- [161] L. Shepherd and C. Toumazou, "Weak inversion isfets for ultra-low power biochemical sensing and real-time analysis," *Sensors and Actuators B: Chemical*, vol. 107, no. 1, pp. 468–473, 2005.
- [162] G. Suh and S. Devadas, "Physical unclonable functions for device authentication and secret key generation," in *Design Automation Conference, 2007. DAC '07. 44th ACM/IEEE*, June 2007, pp. 9–14.

- [163] D. Lim, J. Lee, B. Gassend, G. Suh, M. van Dijk, and S. Devadas, “Extracting secret keys from integrated circuits,” *Very Large Scale Integration (VLSI) Systems, IEEE Transactions on*, vol. 13, no. 10, pp. 1200–1205, Oct 2005.

Sara Ghoreishizadeh

Personal information

Birth Sep. 1985, Iran
Phone +44 7948 212458
Email sghoreishizadeh@gmail.com

Research interests

- **Integrated system design for sensor interfaces and implantable devices**
- **Integrated circuit design for**
 - low-power and low-noise sensor front-ends
 - data converters: sigma-delta modulators, SAR
 - power management and reference circuits
- **Digitally-assisted analog circuit design**

Education

Oct. 2010- **PhD**, École Polytechnique Fédérale de Lausanne (EPFL), Switzerland
March 2015 Thesis title: *Intergated electronics to control and readout biosensors in implantable applications*,
Thesis supervisors: Giovanni De Micheli & Sandro Carrara,
Sep. 2007- **Master of Science**, Sharif University of Technology (SUT), Iran,
Dec. 2009 Major: Electronics, Minor: Microelectronics Circuits, *GPA: 17.03/20*
Thesis title: *Design and implementation of a two-dimensional test-socket in low temperature (77K)*
Sep. 2003- **Bachelor of Science**, SUT, Iran,
Sep. 2007 Major: Electrical Engineering, Minor: Electronics, *GPA: 17.96/20*
Thesis title: *Using TMS320-C6416 DSP board in simulating the H.264/AVC video standard*
Sep. 1999- **High school diploma**, National Organization for Development of Exceptional
Sep. 2003 Talents (NODET), Iran, Major: Mathematics and Physics

Honours and awards

Feb. 2015 **Junior Research Fellowship**, Imperial College London, UK. The award provides salary plus 30k GBP research grant for three years.
Jun. 2007 **Ranked 32** out of 10,000 in "national entrance examination for M.Sc. in electrical engineering", Iran
Aug. 2003 **Ranked 53** out of 450,000 in "national university entrance examination", Iran

Professional experiences

- Dec. 2015-
Nov. 2018 **Research fellow**, Centre for Bio-Inspired Technology (CBIT), Imperial College London, UK
- April 2015-
Nov. 2015 **Research associate**, CBIT, Imperial College London, UK
- May 2014-
Aug. 2014 **Exchange PhD candidate**, CBIT, Imperial College London, UK
I have designed a readout IC based on switched-capacitor opamp integrators in collaboration with Dr. Pantelis Georgiou. In particular, I have designed and implemented the fully-integrated IC for differential electrochemical biosensing. The IC supports a dynamic range of 120 dB and is able to readout different on-chip and off-chip sensors.
- Oct. 2010-
Mar 2014 **PhD candidate and research assistant**, Integrated Systems Laboratory (LSI), EPFL
During my PhD studies I designed and implemented low-power analog/ mixed-signal ICs for health-care monitoring. In particular, I designed ICs to control, readout, and calibrate electrochemical sensor arrays. I have been in charge of closing an interdisciplinary project which aimed to develop an implantable and wireless device for human metabolite sensing. I collaborated in another interdisciplinary project with six colleagues from different disciplines. We are currently finalizing the project which aims to develop an implantable system for metabolite detection in animals. More specifically, during my Phd, I
- implemented analog and digital integrated circuits in 0.18 μm technology;
 - verified my ASICs with glucose, lactate and anti-cancer drug sensors;
 - creatively solved the problems in the final integration of an interdisciplinary project;
 - communicated on a weekly basis with colleagues from different disciplines;
 - designed and fabricated PCBs and embedded systems;
 - employed FPGA boards to test and analyze integrated digital circuits;
 - programmed microcontrollers and developed microcontroller-based circuits;
 - measured and modeled the noise in electrochemical sensors;
 - took or audited several intensive courses, including: *Low-power circuit design, sigma-delta ADC, Electrochemical nano-bio-sensing and bio/CMOS interfaces power management circuit design, mixed-signal circuit design, neuroscience I.*
- May 2010-
Sep. 2010 **VLSI design engineer**, LSI, EPFL
- During a 4-month internship, I designed a sub-Hertz waveform generator with mixed-signal CMOS circuits in 0.18 μm technology. The large-signal sub-Hertz voltage waveform is needed to control the electrochemical sensors.
- Sep. 2007-
Dec. 2009 **Microelectronics engineer**, Integrated System Design Laboratory (ISDL), SUT
During my M.Sc thesis in ISDL, I designed two readout ICs in 0.18 μm and 0.5 μm technologies. The ICs were designed to measure the current in the range of pA to μA . I successfully tested the ICs at room temperature and 77K. Moreover, I took several intensive courses about analog and digital design, including: CMOS circuits, RFIC, MMIC, data converters, and digital electronics. I met the project deadlines while also taking intensive courses and being course TA.

- Sep. 2003- **Electrical and Electronics engineer**, B.Sc., SUT
Sep. 2007 I took several courses including *analog circuit design*, *microcontroller*, *microprocessor*, *C++*, and *filters*. During my B.Sc. thesis I wrote a C++ code to implement H.264/AVC video standard on a DSP board.

Teaching and dissemination experiences

Teaching assistant for

- 2014 *Bio-nano-chip design* - EPFL, Switzerland
- I taught M.Sc. students how to design front-end electronics for biosensors.
- I designed problem sets, exam questions, and graded them.
- 2012 *Lab in EDA based design* - EPFL, Switzerland
- I guided M.Sc. students through full-custom and semi-custom digital design.
- 2009 *Electronics Lab*, Sharif University of Technology, Iran
- I guided B.Sc. students through circuit design with off-the-shelf components and measurements with commercial equipment.
- I designed problem sets, exam questions, and graded them.
- 2008 *Electronics II*, Sharif University of Technology, Iran
- I taught weekly classes.
- I designed the material for the classes.

Reviewer for

2011-present BioCAS, ISCAS, IEEE Sensors

Seminar talks

- Dec. 2013 Imperial College London, Department of Electrical and Electronic
Nov. 2013 University of Zurich, Institute of Neuroinformatics Engineering
In both seminars, I talked about "sub-mW reconfigurable CMOS IC to control, readout, and calibrate multi-target biosensors in implantable applications".

Press

- BBC News [Under the skin blood-testing device developed](#)
Sky News [Mini blood labs can predict a heart attack](#)

Computer skills

- CAD Tools Cadence Virtuoso, Mentor Modelsim, Synopsis Design Compiler, Cadence SoC Encounter, Altium (PCB design)
Programming MATLAB, C++, Labview, Verilog, VHDL, Assembly (AVR studio)

Languages

- Persian Native/ mother tongue
English Full professional proficiency
French Limited professional working proficiency
Arabic Basic words and phrases

Publications

Journal papers

- *An integrated control and readout circuit for implantable multi-target electrochemical biosensing*, **S. Ghoreishizadeh**, C. Baj-Rossi, A. Cavallini, S. Carrara, G. De Micheli, IEEE Transactions on Biomedical Circuits and Systems (TBCAS), vol.8, no.6, pp. 891-898, 2014
- *A subcutaneous biochip for remote monitoring of human metabolism: packaging and biocompatibility assessment*, A. Cavallini, T. Rezzonico Jost, **S. Ghoreishizadeh**, J. Olivo, M. Op de Beeck, B. Gorissen, B.; F. Grassi, G. De Micheli, and S. Carrara, IEEE Sensors Journal, vol. 15, no. 1, pp. 417-424, 2015
- *Fully integrated biochip platforms for advanced healthcare*, S. Carrara, **S. Ghoreishizadeh**, J. Olivo, I. Taurino and C. Baj-Rossi et al., Sensors journal, pp. 11013-11060, 2012
- *Electrochemical Biochip for wireless and batteryless monitoring of free-moving mice* Camilla Baj-Rossi, Enver G. Kilinc, **S. Ghoreishizadeh**, D. Casarinoz, T. Rezzonico Jost, C. Dehollain, F. Grassi, L. Pastorino, G. De Micheli and S. Carrara, Accepted in IEEE TBCAS.
- *An integrated differential potentiostat for multi-target biosensor arrays* **S. Ghoreishizadeh**, P. Georgiou, S. Carrara, and G. De Micheli, In preparation.
- *Fully-integrated implantable sensor for personalized therapy* **S. Ghoreishizadeh**, C. Baj-Rossi, S. Carrara, and G. De Micheli, In preparation.

Conference papers

- *Sub-mW reconfigurable interface IC for electrochemical sensing*, **S. Ghoreishizadeh**, C. Boero, A. Pullini, C. Baj-Rossi, S. Carrara, and Giovanni De Micheli, IEEE Biomedical Circuits and Systems Conference (BioCAS), 2014.
- *A Lightweight cryptographic system for implantable biosensors* **S. Ghoreishizadeh**, T. Yalcin, A. Pullini, G. De Micheli, W. Burleson, and S. Carrara, Accepted in BioCAS, 2014.
- *A configurable IC to control, readout, and calibrate an array of biosensors*, **S. Ghoreishizadeh**, S. Carrara and G. De Micheli, IEEE European Conference in Circuit Theory and Design (ECCTD), Germany, 2013
- *An implantable bio-micro-system for drug monitoring*, **S. Ghoreishizadeh**, E. G. Kilinc, C. Baj-Rossi, C. Dehollain, S. Carrara, and Giovanni De Micheli, IEEE BioCAS, the Netherlands, 2013.
- *Empirical study of noise dependence in electrochemical Sensors*, **S. Ghoreishizadeh**, G. Nanda, S. Carrara, and G. De Micheli, IEEE International Workshop on Advances in Sensors and Interfaces (IWASI), Italy, 2013.
- *A current-mode potentiostat for multi-target detection tested with different lactate biosensors*, **S. Ghoreishizadeh**, I. Taurino, S. Carrara, G. De Micheli, IEEE BioCAS, Taiwan, 2012
- *Nano-sensor and circuit design for anti-cancer drug detection*, **S. Ghoreishizadeh**, C. Baj-Rossi, S. Carrara, G. De Micheli, IEEE/NIH 5th Life Science Systems and Applications (LiSSA) Workshop, USA, 2011

- *Circuit design for human metabolites biochip*,
S. Ghoreishizadeh, S. Carrara, G. De Micheli,
IEEE BioCAS, USA, 2011
- *Full-system for translational studies of personalized medicine with free-moving mice*,
S. Carrara, C. Baj-Rossi, S. Ghoreishizadeh, S. Riario, G. Surrel, F. Stradolini, C. Boero, G. De
Micheli, E. G. Kilinc, C. Dehollain
Accepted in IEEE international symposium on circuits and systems(ISCAS), 2015
- *Fabrication and packaging of a fully implantable biosensor array*,
C. Baj-Rossi, E. G. Kilinc, S. Ghoreishizadeh, D. Casarinoz, T. Rezzonicox, C. Dehollain, F.
Grassix, L. Pastorinoz, G. De Micheli and S. Carrara,
IEEE BioCAS, 2013
- *Electronic implants: power delivery and management*,
J. Olivo, S. Ghoreishizadeh, S. Carrara, G. De Micheli,
Design Automation and Test in Europe Conference and Exhibition (DATE), France, 2013
- *Developing highly-integrated subcutaneous biochips for remote monitoring of human metabolism*,
S. Carrara, A. Cavallini, S. Ghoreishizadeh, J. Olivo, G. De Micheli,
IEEE Sensors, Taiwan, 2012
- *Design, fabrication, and test of a sensor array for perspective biosensing in chronic pathologies*,
A. Cavallini, C. Baj-Rossi, S. Ghoreishizadeh, G. De Micheli, S. Carrara,
IEEE BioCAS, Taiwan, 2012
- *An integrated platform for advanced diagnostics*,
G. De Micheli, S. Ghoreishizadeh, C. Boero, F. Valgimigli and S. Carrara,
DATE, France, 2011